Field-induced magnetic phase transitions and correlated electronic states in the hexagonal RAgGe and RPtIn series

by

Emilia Morosan

A dissertation submitted to the graduate faculty

in partial fulfillment of the requirements for the degree of

DOCTOR OF PHILOSOPHY

Major: Condensed Matter Physics

Program of Study Committee:
Paul C. Canfield, Major Professor
Sergey L. Bud'ko
Bruce N. Harmon
Steven D. Kawaler
Matthew J. Kramer

Iowa State University

Ames, Iowa

2005

Graduate College
Iowa State University

This is to certify that the doctoral dissertation of

Emilia Morosan

has met the dissertation requirements of Iowa State University

Major Professor

For the Major Program

TABLE OF CONTENTS

LIST OF TABLES

LIST OF FIGURES

IS-T 2235

Foreword

Little do we pause in our every day life, to wonder how the microwave oven works, what happens with the gasoline as our automobile takes us places, how our computer instantly sends e-mails half-way across the world, or what lies behind the magic of modern medicine. Even less attention do we pay to the discoveries preceding these 'modern marvels' which make our lives safer, faster, better.

Even though these days the compass is mostly encountered as a keychain, a thousand years ago it became a ubiquitous navigation instrument. It took a few more centuries until Dr. W. Gilbert's "De Magnete" explained the ability of the compass needle to point north on the basis that the Earth itself was magnetic. A few centuries later, electricity and magnetism were linked to each other, and numerous discoveries related to electromagnetism followed: the electric force and the capacitor, Galvani's discovery of electrical current, the resistance and the inductance, Morse's electric telegraph, the great discovery by Faraday of electromagnetic induction, the DC motor, followed by the invention of the now omni-present telephone, incandescent light, Tesla's alternating current motor, the wireless telegraph invented by Marconi, and so on. These were accompanied by the theoretical developments of Kirchoff's laws, Coulomb's laws, Maxwell's equations of the electromagnetic field, Einstein's theory of relativity.

At the dawn of the twentieth century, the magnetic properties of the rare earth elements were discovered. Later, Spedding's production of pure rare earth single crystals, together with the developing neutron scattering experiments, allowed for the progressive elucidation of the magnetic structures of the rare earths. A standard model of rare earth magnetism was formulated, followed by the development of the Ruderman-Kittel-Kasuya-Yoshida (RKKY) description of the exchange interaction between the local moments of the rare earths. Stevens

invented his operator equivalents method for the treatment of crystal field effects, the primary source of magnetic anisotropy in rare earth-based materials. These are only a few of the early steps that led to our understanding of the apparently complex magnetism of the rare earths.

An example of the great impact of magnetism on our society is the development of permanent magnets, particularly in the last couple of centuries: the Alnico magnets (aluminium, cobalt and nickel-based alloys) were the first modern permanent magnets; the cobalt-platinum magnets had improved properties over the Alnico's, and corrosive resistance, being ideal candidates for biomedical applications. Next, various iron oxides were fabricated and widely used as commercial magnets in the last decades. Rare earth-based hard magnets were later discovered ($SmCo_5$ [1966], Sm_2Co_{17} [1972], and $Nd_2Fe_{14}B$ [1984]), of which the Sm-based ones were rather costly, but the Nd-based ones are currently widely used, especially in applications where miniaturisation is an important design criteria.

Motivated by the anticipated complexity of the properties of rare earth compounds, the present work represents a small step into the ongoing investigation of magnetism of such systems.

CHAPTER 1. Introduction

Rare earth intermetallic compounds provided rich grounds for investigating the properties of both local moment and strongly correlated, hybridized moment systems. These areas have been intensively explored mostly on cubic and tetragonal intermetallic compounds, and relatively less work existed on materials with lower symmetry. Moreover, a large number of Ce-based heavy fermion compounds have been studied, whereas the analogous Yb-based ones are much rarer. We thus wanted to study local moment metamagnetism and Yb-based heavy fermion physics in hexagonal systems, *i.e.*, still with relatively high symmetry, but with added complexity compared to the more symmetric cubic or tetragonal compounds.

The Fe_2P structure class of hexagonal compounds allowed us to perform such studies on both local moment and strongly correlated, hybridizing moment systems. Two ternary series of compounds (RAgGe and RPtIn) belonging to this family particularly attracted our attention. Having a ZrNiAl-type crystal structure, an ordered variant of the aforementioned Fe_2P family, each of the two series displays complex physical properties. In addition they provide two related examples of how these properties arise as an effect of the hexagonal crystal structure with the rare earths in orthorhombic point symmetry.

The magnetic RAgGe (R = Tb - Lu) and the RPtIn (R = Y, Gd - Lu) compounds display anisotropic temperature and field dependent magnetization due to the crystalline electric field (CEF) splitting of the Hund's rule ground state multiplet. In the former series, this strong CEF anisotropy confines the magnetic moments along the c-axis in TbAgGe; across the series, this is followed by a progression towards an almost isotropic case for the R = Ho member, whereas for R = Er - Yb the easy axis lies in the ab-plane, with TmAgGe being extremely anisotropic. In the RPtIn series, no strong anisotropy in the paramagnetic state is observed

for the R = Gd member, whereas TbPtIn is extremely anisotropic, with planar magnetization, very similar to the case of TmAgGe.

Antiferromagnetic ordering can be inferred for most of the RAgGe compounds, with values of T_N between 28.5 K for TbAgGe, and 1.0 K for YbAgGe. DyAgGe appears to be the only exception, by showing a ferromagnetic component of the magnetization parallel to the c axis. However, for all of the above RAgGe compounds, their ordering temperatures scale fairly well with the deGennes factor $dG = (g_J\text{-}1)^2\ J\ (J + 1)$, where g_J is the Landé g factor, and J is the total angular momentum of the R^{3+} ion Hund's rule ground state: the anticipated behavior for rare earth intermetallic compounds. A more curious behavior occurs across the RPtIn series, where the ordering temperatures for all magnetic compounds also scale well with the deGennes factor: TbPtIn and TmPtIn have larger planar than axial susceptibilities in the paramagnetic state, and order antiferromagnetically around 46 K, and 3 K respectively, whereas the ordered states in the R = Gd, Dy - Er compounds have axial ferromagnetic components. Although, at a first glance, these appeared as rather unusual discontinuities for a magnetically ordering local moment series, we show (in Chapter 7) that the hexagonal crystal structure of these compounds, with three R ions in the unit cell occupying unique orthorhombic point symmetry sites, is of crucial importance in explaining the moment configurations and magnetic ordering in these RPtIn materials.

The anisotropic M(H) measurements of the RAgGe systems indicate one or more metamagnetic transitions when the external field is applied in the c direction (for R = Tb) or perpendicular to it (for R = Ho - Tm), or even in both orientations as is the case of DyAgGe. No evident metamagnetic transitions can be observed in the ferromagnetic RPtIn compounds, but they exist in the two antiferromagnetic ones: TbPtIn and TmPtIn.

TmAgGe and TbPtIn represent special examples of complex metamagnetism, very similar despite the different rare earth ions and different ligands in the two compounds. Due to their extreme planar anisotropy, the nature of the magnetic order changes abruptly, with both the magnitude and the orientation of the applied field even within the basal plane. This allowed us to perform a study of the angular dependent planar magnetism in each of the two compounds,

and also to determine net distribution of the magnetic moments using the *three co-planar Ising-like systems model.*

The YbAgGe and YbPtIn compounds have some properties distinct from the rest of their respective series. YbAgGe has a low magnetic ordering temperature ($\sim$ 1 K) and an enhanced electronic specific heat coefficient 150 mJ/mol K^2 $\leq$ γ $\leq$ 1000 mJ/mol K^2. The magnetic entropy at 1 K is only 5 % of the expected R ln 2 for a ground state doublet, suggesting small moment ordering in this compound. All these observations, and detailed $C_p(T,H)$ and $\rho(T,H)$ measurements allow us to classify YbAgGe as new stoichiometric, Yb-based heavy fermion material with a magnetic field-induced quantum critical point QCP. Furthermore, Hall resistivity measurements are consistent with the presence of a QCP in this material, and indicate that YbAgGe behaves similarly to other heavy fermion materials, and is very similar to the extensively studied $YbRh_2Si_2$ (Trovarelli, 2000; Gegenwart 2002; Ishida 2002; Paschen 2003; Paschen 2004).

A more complex situation is encountered in the case of YbPtIn, given the observed site-disorder that occurs in the flux-grown single crystals of this material. The small Pt-deficiency in the flux-grown crystals greatly affects the magnetic transition temperatures and the critical field values, in comparison with the analogous values for the stoichiometric, on-line grown YbPtIn single crystals. However, both these systems exhibit enhanced electronic specific heat coefficients ($\gamma \geq$ 550 mJ/mol K^2), quantum critical point and non-Fermi liquid like behavior at low temperatures outside the ordered state, very similar to the YbAgGe and $YbRh_2Si_2$ compounds. Having an even higher ordering temperature (T_N = 2.1 K for the Pt-deficient system, and 3.4 K for the ordered one) and magnetic entropy at T_N about $0.6 * R$ ln 2, YbPtIn seemed a good candidate to further study this progression from small towards reduced moment ordering in Yb-based heavy fermion compounds, with field-induced quantum critical point.

This work will be presented as follows: first I will review the physics of rare earth intermetallic compounds, including magnetism and magnetic ordering, de Gennes scaling, crystal electric field CEF effects, metamagnetism, heavy fermions and quantum criticality. Next I will introduce the motivation for studying hexagonal compounds, in particular the Fe_2P-type ones,

with hexagonal unit cell and three rare earth ions sitting at sites with orthorhombic point symmetry. The following chapter is dedicated to details of crystal growth from high-temperature solution, with emphasis on the particular procedures used for growing the RAgGe and RPtIn single crystals; it also includes a review of the measurement techniques used in characterizing these systems. Chapter 5 presents a thorough compound-by-compound analysis of the basic thermodynamic and transport properties of the RAgGe series, along with a discussion of trends across the series. Chapter 6 will be dedicated to the study of the angular dependent metamagnetism in TbPtIn and TmAgGe; the measured data is presented by comparison to *the three co-planar Ising-like systems model*, and the features common to the two compounds will be emphasized. An appropriate version of this model, enhanced to three dimensions, is than introduced in an attempt to explain the unusual trends of the magnetic ordering across the RPtIn series, which are discussed compound by compound, in the following chapter. Chapters 8 and 9 present the YbAgGe, and the YbPtIn and $YbPt_{0.98}In$ heavy fermion systems respectively, all of which exhibit field-induced quantum critical points. A final chapter will attempt to summarize the results of this work, and outline directions for further investigations.

CHAPTER 2. Overview of physics of Rare Earth Compounds

2.1 General properties

2.1.1 4f Electrons and Local Moment Magnetism

The starting point for the understanding of the rare earths' magnetism is the description of their electronic state, particularly of the 4f electrons. The rare earth ions are almost always trivalent, with the exception of some which can also be di- or tetra-valent. All of the trivalent rare earth ions are comparable in size, with virtually identical outermost electron shells with the $5s^2 5p^6$ configuration. As a result, their chemical properties are fairly similar. Even in metals, the 4f core retains its integrity and its atomic properties. Therefore, series of compounds can often be synthesized, which differ only in the choice of lanthanide element. This valuable ability allows for systematic studies of the physics of rare earth intermetallic compounds. By studying a whole series of compounds, the effects of the crystal electric field CEF, interactions between ions, and other physical characteristics may be separated from each other. Finally, the analysis of trends across the series aids in the understanding of the physics of the individual members.

Fig. 2.1 shows the radial densities of the electrons of the Gd^{3+} free ions (or Gd^{3+} ions in hard insulators). As seen in the figure, the 4f electrons are much more localized than the 5s, 5p, and 6s electrons. Furthermore, these 4f electrons are shielded by the completely filled $5s^2$ and $5p^6$ shells. Therefore, the 4f electrons may be considered part of the electronic core, not directly interacting with the rest of the electronic system. Since a partially filled 4f shell will have a large magnetic moment, it is imperative to determine the electronic configuration of the 4f electrons. However, this picture needs to be changed in the case of metals, to include

the effect of the Fermi level position on the radial extent of the electronic orbitals.

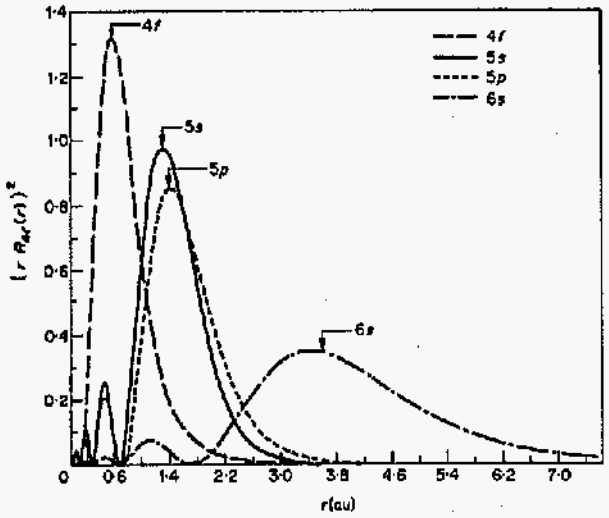

Figure 2.1 Radial densities of the electrons of Gd from Hartree-Fock calculations (after Taylor, 1972).

2.1.2 Hund's Rules

The total spin **S**, total orbital momentum **L** and total angular momentum **J** quantum numbers are crucial for the theoretical determination of the magnetic properties of a material. In the case of the rare earth ions, their values are determined by the ground state configuration of the 4f electrons. For a given angular momentum l, there are $2l + 1$ possible values for l_z, and 2 possible spin orientations for each l_z. This results in a multiply degenerate ground state, with a total of $2\ (2l + 1)$ possible states. However, most of this degeneracy is lifted by electron-electron Coulomb interaction and through spin-orbit coupling (Mattis, 1981), such that the ground state configuration of a partially filled shell will then be governed by Hund's

rules (Ashcroft, 1976):

- The ground state has the largest value of total spin S that is consistent with the exclusion principle.
- For the maximum possible S value, the electrons are distributed between all possible states in accordance with the exclusion principle, and such that the resulting L value is maximum.
- For shells that are less than half-filled, the total angular momentum is given by $\mathbf{J} = |\mathbf{L} - \mathbf{S}|$. For shells that are more than half-filled, $\mathbf{J} = |\mathbf{L} + \mathbf{S}|$.

Using these rules, the quantum numbers of for the lanthanide ions can be determined, and they are shown in Table 2.1. Now that the components of angular momenta are known for the local moments, it is possible to formulate many aspects of the theory of magnetism in rare earth intermetallic compounds.

Table 2.1 Components of the angular momenta L, S, J, and the calculated values of the Landé g factor ($g_J = \frac{3}{2} + \frac{1}{2}\left[\frac{S(S+1)-L(L+1)}{J(J+1)}\right]$), saturated moment ($M_{sat} = g_J\ J\ \mu_B$), effective moment ($p_{eff} = g_J\ [J(J+1)]^{1/2}$), and de Gennes factor ($dG = (g_J - 1)^2\ J(J+1)$) for the trivalent magnetic rare earth ions.

R	L	S	J	g_J	M_{sat}	p_{eff}	dG
Ce	3	0.5	2.5	0.857	2.14	2.54	0.19
Pr	5	1	4	0.800	3.20	3.58	0.80
Nd	6	1.5	4.5	0.727	3.27	3.62	1.84
Pm	6	2	4	0.600	2.40	2.68	3.20
Sm	5	2.5	2.5	0.286	0.71	0.84	4.46
Eu	3	3	0	–	–	–	–
Gd	0	3.5	3.5	2.000	7.00	7.94	15.75
Tb	3	3	6	1.500	9.00	9.72	10.50
Dy	5	2.5	7.5	1.333	10.00	10.64	7.08
Ho	6	2	8	1.250	10.00	10.61	4.50
Er	6	1.5	7.5	1.200	9.00	9.58	2.55
Tm	5	1	6	1.167	7.00	7.56	1.17
Yb	3	0.5	3.5	1.142	4.00	4.54	0.32

2.1.3 Curie law

In general, the contribution of a magnetic moment in an applied field to the total energy is simply the Zeeman term, $E = -\mu_B \mathbf{H}\cdot(\mathbf{L} + g_0 \mathbf{S})$, where $\mu_B = e\hbar / 2mc \approx 5.79 * 10^{-8}$ eV / G is the Bohr magneton, and $g_0 = 2[1 + \alpha / 2\pi + O(\alpha^2) + \cdots] \approx 2$ is the electronic g-factor ($\alpha = e^2/\hbar c \approx 1/137$). This is typically very small compared to all the other energy scales in the system, and therefore the effect of the applied field can be computed as a small perturbation. In order to derive the susceptibility of a system, a second derivative of the energy with respect to field, second-order perturbation theory must be used, where terms up to second order in H are retained in the expansion of energy:

$$\Delta E_n(H) = \mu_B \mathbf{H}\cdot \langle n \mid \mathbf{L} + g_0 \mathbf{S} \mid n\rangle + \sum_{m\neq n} \frac{|\langle n \mid \mu_B \mathbf{H}\cdot(\mathbf{L} + g_0 \mathbf{S}) \mid m\rangle|^2}{E_n - E_m} \qquad (2.1)$$

The second term in eq.(2.1) yields the Van Vleck paramagnetic susceptibility (Ashcroft and Mermin, 1976), which is typically small in the rare earth ions with partially filled f-shells. When the first term is non-zero (*i.e.*, for $J \neq 0$), it dominates the energy correction; in this case, the ground state energy can be written in a simpler form by using the Wigner-Eckart theorem:

$$\langle JLSJ_z \mid \mathbf{L} + g_0 \mathbf{S} \mid JLSJ'_z\rangle = g_J(JLS)\langle JLSJ_z \mid \mathbf{J} \mid JLSJ'_z\rangle \qquad (2.2)$$

where g_J is the Landé g-factor, which can be computed as (taking g_0 to be exactly 2):

$$g_J(JLS) = \frac{3}{2} + \frac{1}{2}\left[\frac{S(S+1) - L(L+1)}{J(J+1)}\right]. \qquad (2.3)$$

This allows us to determine the magnetization of a system with N ions occupying a volume V, as:

$$M = -\frac{N}{V}\frac{\partial F}{\partial H} \qquad (2.4)$$

where F is the free energy of the system with only the lowest $2J + 1$ states being thermally excited with appreciable probability; using eq.(2.3), and the free energy F given by

$$e^{-\beta F} = \sum_{J_z=-J}^{J} e^{-\beta(g_J \mu_B H) J_z}, \quad \beta = \frac{1}{k_B T} \tag{2.5}$$

the above magnetization becomes:

$$M = -\frac{N}{V} g_J \mu_B J B_J(\beta g_J \mu_B J H) \tag{2.6}$$

where $B_J(x)$ is the known Brillouin function.

In the low temperature limit ($k_B T \ll g_J \mu_B H$), the magnetization reaches its saturation value (*i.e.*, each moment is completely aligned with the field and $| J_z | = J$):

$$M_{sat} = g_J \mu_B J. \tag{2.7}$$

These g_J and M_{sat} values are summarized in Table 2.1 for all trivalent rare earth ions, together with the S,L and J quantum numbers of their Hund's rules ground states. This information is useful in the analysis of new rare-earth intermetallic compounds, since it allows the theoretical saturated moments to be compared to the measured values. Under certain circumstances, this comparison may then be used to determine the amount of rare earth element present in an unknown compound. In addition, knowledge of the theoretical saturated moment may also be used to identify easy and hard magnetic axes arising from the crystalline electric field, discussed below. Finally, this theoretical result may allow an estimate of the net distribution of moments in materials exhibiting metamagnetic transitions, which will be discussed in detail in Chapter 6.

When we analyze the temperature-dependence of the magnetization (2.6) in the high temperature limit ($k_B T \gg g_J \mu_B H$), one can determine the molar susceptibility as:

$$\chi = \frac{\partial M}{\partial H} = N_A \frac{(g_J \mu_B)^2}{3} \frac{J(J+1)}{k_B T} = \frac{C}{T}. \tag{2.8}$$

This variation of the susceptibility as the inverse of temperature is also known as Curie's law, where the Curie constant C can be written as a function of the "effective Bohr magneton number" p_{eff}:

$$C = N_A \frac{(g_J \mu_B)^2}{3} \frac{J(J+1)}{k_B} = N_A \frac{p_{eff}^2 \mu_B^2}{3k_B}. \quad (2.9)$$

2.1.4 Curie-Weiss law

The above Curie law has been derived within the hypothesis of negligible interactions between the magnetic moments; within mean field theory, these interactions are taken into account by considering that, in addition to the external applied field H, an effective field H_{eff} acts on each local moment. Such an effective field arises from the thermal average of the surrounding moments, and is proportional to their magnetization M: $H_{eff} = \alpha M$.

Consequently, since the temperature-dependent magnetization follows Curie's law (2.8), the magnetization in this case will result from the equation:

$$M = \frac{C}{T}(H + H_{eff}) = \frac{C}{T}(H + \alpha M). \quad (2.10)$$

Solving for M and the susceptibility, one gets the Curie-Weiss law:

$$\chi = \frac{C}{T - \alpha C} = \frac{C}{T + \theta_W}. \quad (2.11)$$

where $\theta_W = \alpha C$ representing the paramagnetic Weiss temperature. From its proportionality to α, the Weiss temperature comes out to be of the form:

$$\theta_W \propto \frac{S(S+1)}{k_B^2}. \quad (2.12)$$

Like the saturated moment, this result is extremely useful in the characterization of new rare earth intermetallic compounds, since at high temperatures, the slope of a plot of the inverse susceptibility $(1/\chi)$ versus temperature is the Curie constant C. From the determination of the Curie constant, the molar mass of the measured compound may be calculated if g_J and J are known from the choice of the rare earth element in the compound. The theoretical values of the effective Bohr magneton values are listed in Table 2.1, together with the other already mentioned characteristic quantities for the rare earth ions.

2.1.5 deGennes scaling

Another important outcome of the mean field theory is the scaling of the Weiss temperatures θ_W with what is known as the de Gennes factor dG:

$$dG = (g_J - 1)^2 J(J+1). \tag{2.13}$$

The Weiss temperature θ_W given by 2.12 can be expressed in terms of the total angular momentum of the 4f-electrons, **J**, by making use of the Wigner-Eckart theorem (2.2): replacing the S (S + 1) term in (2.12) with $\frac{1}{3}\ (g_J - 1)^2 J(J+1)$ yields an equivalent form for θ_W:

$$\theta_W \propto \frac{1}{3}\ \frac{(g_J - 1)^2 J(J+1)}{k_B^2}\ \propto\ dG\ \frac{1}{3\ k_B^2}, \tag{2.14}$$

Within mean field theory, the Curie temperature T_C (for ferromagnetic ordering) or Néel temperature T_N (for antiferromagnetic order) are given by the magnitude of the Weiss temperature; consequently the magnetic ordering temperatures are also expected to scale with the de Gennes factor.

The values of the de Gennes factor for each rare earth ion are listed in Table 2.1; since this is largest for Gd, compounds containing this element can be expected to have the highest ordering temperature. Likewise, compounds containing Pr, or Tm, should order magnetically at much lower temperatures.

2.1.6 The RKKY interaction

As can be inferred from Fig. 2.1, the overlap between the 4f-orbitals of neighboring rare earth sites is extremely small, drastically reducing the possibility for direct exchange interaction between the rare earth ions. Therefore in metals the primary interaction between the magnetic moments is indirect, via the polarization of the conduction electrons. Specifically, the localized spin of the 4f electrons interacts with the spin of the conduction electrons, resulting in a polarization of the conduction electrons. This polarization then interacts with the spin of the 4f electron localized on another rare earth ion. This is known as the Ruderman-Kittel-Kasuya-Yoshida (RKKY) interaction. This interaction is long-range and oscillatory, and can couple

the spins either ferromagnetically or antiferromagnetically, depending on the ions' separation and the shape of the Fermi surface. This type of exchange was first proposed by Ruderman and Kittel (1954) and later extended by Kasuya (1956) and Yosida (1957).

The interaction between two magnetic moments at positions $\mathbf{R}_i$ and $\mathbf{R}_J$ is characterized by a coupling constant J given by

$$J(\mathbf{R}_i - \mathbf{R}_J) \sim F(2k_F \mid \mathbf{R}_i - \mathbf{R}_J \mid), \tag{2.15}$$

where k_F is the Fermi wavevector, and F(x) is given by (Elliott 1972):

$$F(x) = \frac{x\cos x - \sin x}{x^4}. \tag{2.16}$$

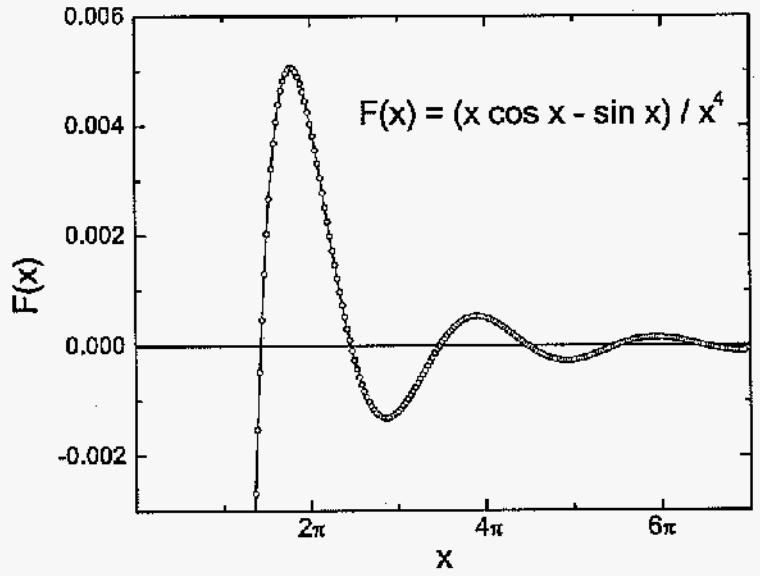

Figure 2.2 The polarization of the conduction electrons via the RKKY interaction (where x = 2 $k_F \mid \mathbf{R}_i - \mathbf{R}_J \mid$).

The RKKY exchange coefficient J oscillates from positive to negative as the separation of

the ions changes, and has the damped oscillatory nature shown in Fig. 2.2. This yields an indirect exchange energy of the form:

$$E = \frac{9n^2\pi\Gamma^2}{2E_F}\sum_{i\neq j}\mathbf{S}_i\cdot\mathbf{S}_J\ F(2k_F\mid \mathbf{R}_i-\mathbf{R}_J\mid) \tag{2.17}$$

where n is the average density of conduction electrons, Γ represents the interaction constant and E_F is the Fermi energy. At low temperatures, k_BT is less than E, and the exchange interaction between the local moments will dominate, causing the magnetic sublattice to order magnetically. Depending on the values of k_F and $\mathbf{R}_i-\mathbf{R}_J$, the exchange between neighboring moments may be positive or negative, which will result in ferromagnetic or antiferromagnetic ordering, respectively.

2.1.7 Crystal Electric Field

2.1.7.1 Overview of Crystal Electric Field CEF effects

Together with the interactions between the magnetic moments, the crystal electric field CEF effect greatly affects the magnetic properties of the rare earth ions, once they are placed in solids. In particular, the CEF is responsible for lifting some or all of the degeneracy of Hund's rule ground state multiplet at low temperatures. In transition metals, where the unfilled 3d-shell is the outermost shell, this effect is very large; however, in the rare earth elements where the 4f shell is screened and highly localized, the crystal field splitting is relatively small and may be treated as a perturbation of the ground state (Hutchings, 1964).

If the surrounding k ions are treated as point charges at positions $\mathbf{R}_i$, the resulting total potential at the rare earth site is the sum of all potentials from such point charges:

$$V(\mathbf{r}) = \sum_i \frac{q_i}{\mid \mathbf{r}-\mathbf{R}_i\mid}. \tag{2.18}$$

After expanding V(r) in Legendre polynomials $P_n^m(\cos\theta)$, and expressing it more conveniently in the tesseral harmonics Z_{nm}:

$$Z^c_{nm} = \left[\frac{2n+1}{2}\frac{(n-m)!}{(n+m)!}\right]^{\frac{1}{2}} P^m_n(\cos\theta)\frac{\cos m\varphi}{\sqrt{\pi}}$$
$$Z^s_{nm} = \left[\frac{2n+1}{2}\frac{(n-m)!}{(n+m)!}\right]^{\frac{1}{2}} P^m_n(\cos\theta)\frac{\sin m\varphi}{\sqrt{\pi}} \tag{2.19}$$

the above potential becomes:

$$V(r,\theta,\varphi) = \sum_n \sum_\alpha r^n \gamma^{c,s}_{n\alpha} Z^{c,s}_{n\alpha}(\theta,\varphi)$$
$$\text{where} \qquad \gamma^{c,s}_{n\alpha} = \sum_{i=1}^{k} \frac{4\pi}{2n+1}\, q_i\, \frac{Z^{c,s}_{n\alpha}(\theta_i,\varphi_i)}{R_i^{n+1}}. \tag{2.20}$$

This potential function should reflect the point symmetry of the lattice site **r**. Consequently, the number of non-vanishing terms in the CEF potential is limited (*i.e.*, the more symmetric the site, the fewer terms occur in the above expansion). Particularly terms with $n > 2\,l$, where l is the orbital quantum number, vanish; thus for the 4f electrons (l = 3), the expansion of the CEF potential (2.20) can only include terms up to **n** = 6.

Since the effects of the CEF are small in rare earth ions compared to the spin-orbit coupling, the potential (2.20) may be treated as a perturbation to the free-ion states. In principle, the eigenvalues of the CEF states may be found by diagonalizing the matrix elements of this potential.

2.1.7.2 Stevens' Equivalent Operators

A much simpler method to calculate the effect of the CEF potential is to introduce the Stevens equivalent operators. It has been shown (Stevens, 1952) that the matrix elements of the crystal field Hamiltonian (2.20) are proportional to a set of operators containing components of the total angular momentum, J.

To illustrate the method, we consider the CEF Hamiltonian given by:

$$H_{CEF} = -\,|\,e\,|\;V(\mathbf{r}) = -\,|\,e\,|\;\sum_i V(x_i,y_i,z_i). \tag{2.21}$$

If the system of coordinates is chosen such that the coefficients $\gamma^a_{n\alpha}$ of the $Z^a_{n\alpha}$ (2.20) are zero, then the CEF potential (2.20) can be rewritten as:

$$V(\mathbf{r}) = \sum_i \sum_{nm} f^c_{nm}(x_i, y_i, z_i) \equiv \sum_{nm} \theta_n \langle r^n \rangle O^m_n \tag{2.22}$$

where θ_n are the multiplicative factors depending on l, and O^m_n are Stevens' equivalent operators, which are tabulated for the most common n and m values. Thus the CEF hamiltonian in this representation becomes:

$$H_{CEF} = \sum_{nm} [A^m_n \langle r^n \rangle \theta_n] O^m_n \equiv \sum_{nm} B^m_n O^m_n. \tag{2.23}$$

where $A^m_n = \gamma^c_{nm} * (- \mid e \mid)$.

The energy splitting of the Hund's rule multiplet may now be calculated by applying the operators and diagonalizing the matrix elements.

$HoNi_2B_2C$ (Cho, 1996a; Gasser 1996) serves as a great example to illustrate the applicability of the Stevens' operators method to determine the CEF parameters in a highly anisotropic tetragonal system, with the rare earth occupying a tetragonal point symmetry position. As can be seen in Fig. 2.3a,b, this compound is extremely anisotropic, with larger susceptibility values for $H \parallel ab$. Moreover, the field-dependent magnetization (Fig. 2.3c) is indicative of in-plane anisotropy, with the [110]-equivalent directions being the easy axes.

Using a CEF Hamiltonian of the form:

$$H_{CEF} = B^0_2 O^0_2 + B^0_4 O^0_4 + B^4_4 O^4_4 + B^0_6 O^0_6 + B^4_6 O^4_6, \tag{2.24}$$

where the O^m_n are Stevens equivalent operators, the CEF parameters B^m_n have been determined from from fitting the inverse susceptibility data of $Ho_xLu_{1-x}Ni_2B_2C$ (Fig. 2.3c). Fig. 2.4 shows the CEF level scheme calculated from the above B^m_n parameters. However, the thermodynamic properties used for the determination of these parameters are less sensitive to the higher temperature details of the CEF level structure. Therefore Gasser *et al.* (Gasser 1996) refined the above CEF parameters to higher energies, by performing inelastic neutron scattering experiments.

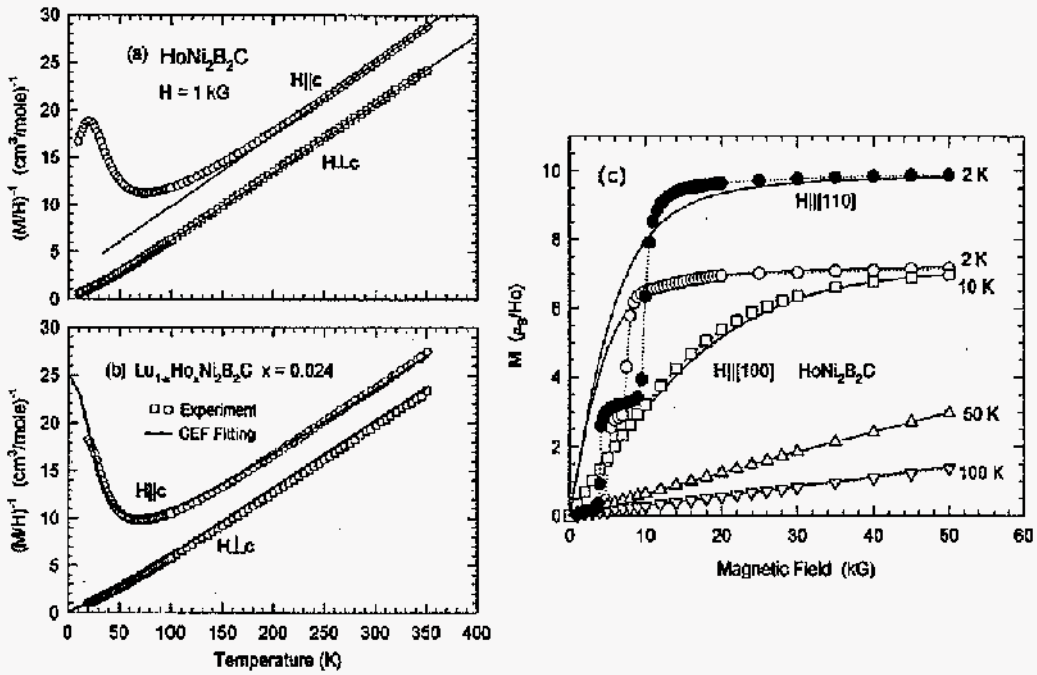

Figure 2.3 Inverse anisotropic susceptibility values for (a) $HoNi_2B_2C$ and (b) $Ho_xLu_{1-x}Ni_2B_2C$ (x $\approx$ 0.024) (symbols); (c) Field-dependent magnetization curves for H applied within the basal plane, along the high symmetry directions: $H \parallel [110]$ (full symbols) and $H \parallel [100]$ (open symbols); the lines in (a) are Curie-Weiss fits to the data above 250 K, whereas in (b) and (c) the CEF calculations, using Stevens' operators method, are shown as solid curves. (Cho, 1996a)

In addition to the specific example shown for tetragonal point symmetry of the magnetic moment, more general calculations of the energy splitting of the Hund's rule multiplet have also been performed in detail for cubic symmetry (Lea, 1962; Taylor,1972). A method to numerically fit the crystal field parameters to experimental data is outlined in MacKeown and Newman (1987). However, the number of available calculations for lower point symmetries is very limited, due to the enhanced degree of difficulty in finding unique level schemes for the

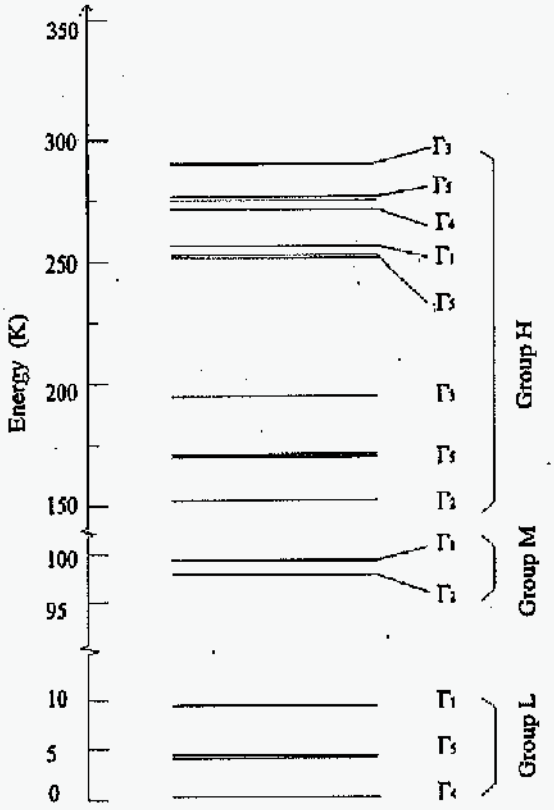

Figure 2.4 Crystalline electric-field energy levels for Ho^{3+} ions in $HoNi_2B_2C$. (Cho, 1996a)

CEF energy splitting, when large number of terms of the Hamiltonian (2.23) are involved in the calculation.

2.1.8 Characteristics of rare earth intermetallic compounds via thermodynamic and transport measurements

Having understood the basic properties of rare earth intermetallic compounds, it is useful to see how they are inferred, in practice, from measurements of various thermodynamic and transport properties.

2.1.8.1 Low-field magnetic susceptibility

In section 2.1.4 we saw that, for high temperatures, the susceptibility of magnetically ordered rare earth compounds is given by Curie-Weiss law (2.11). In addition, section 2.1.7 showed that CEF effects lead to magnetocrystalline anisotropy, which is reflected in anisotropic susceptibility curves measured for field along the three crystallographic directions. Having samples in single crystal form allows one to measure the anisotropic susceptibilities χ_a (H‖a), χ_B (H‖b) and χ_c (H‖c); a polycrystalline average susceptibility χ_{ave} can then be calculated:

$$\chi_{ave} = \frac{\chi_a + \chi_b + \chi_c}{3}, \tag{2.25}$$

which, in turn, can be used to determine the effective moment $\mu_{\rm eff}$ for a given compound.

For high-symmetry compounds (*i.e.*, for which two [tetragonal or hexagonal] or all three [cubic] crystallographic directions are equivalent), it suffices to measure the susceptibility along the non-equivalent directions. An example is shown in Fig. 2.5, illustrating the anisotropic molar susceptibility curves for a tetragonal or hexagonal compound, with an antiferromagnetic ground state. In this case, measurements parallel (χ_{ab}) and perpendicular (χ_c) to the basal plane can be used to calculate the polycrystalline average susceptibility as:

$$\chi_{ave} = \frac{2 * \chi_{ab} + \chi_c}{3}. \tag{2.26}$$

The susceptibility of an antiferromagnetic compound features a fairly sharp peak around the Neél temperature T_N, as seen in Fig. 2.5a. The Neél temperature T_N can be exactly determined (Fisher, 1962) from the peak position in $d(\chi T)/dT$, which is expected to follow the temperature dependence of the specific heat, as well as that of $d\rho/dT$ (Fisher, 1968). From (2.11) it follows that the inverse high-temperature susceptibility is linear in temperature:

$$\frac{1}{\chi} = \frac{T}{C} + \frac{\theta_W}{C}, \tag{2.27}$$

as can be seen in Fig. 2.5b. Linear fits $1/\chi = a\,T + b$ to the high-temperature inverse susceptibility (dotted lines Fig. 2.5b) allow us to experimentally determine the coefficients a

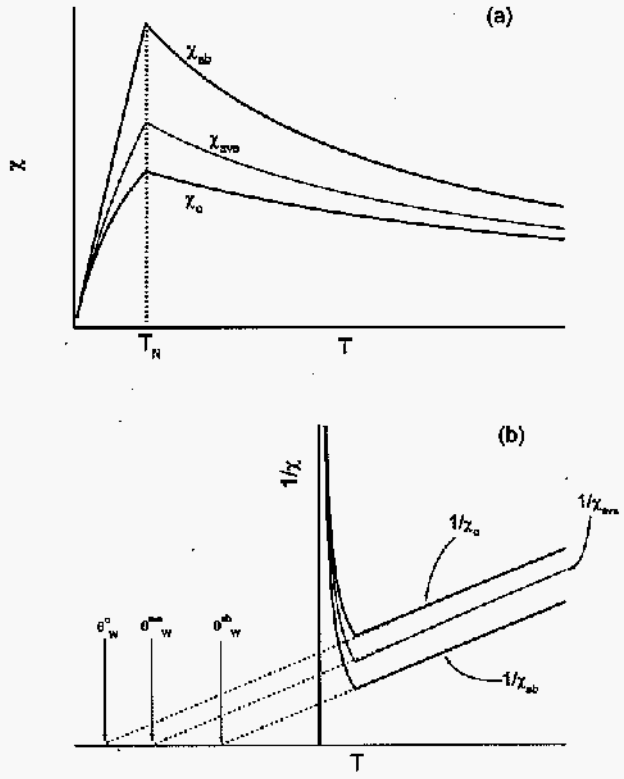

Figure 2.5 Anisotropic (a) susceptibility and (b) inverse susceptibility curves, for an antiferromagnetic tetragonal or hexagonal system. The dotted line in (a) marks the ordering temperature T_N, whereas in (b) the dotted lines are extrapolations to $1/\chi = 0$ of the high-temperature data, from which the anisotropic Weiss temperatures θ_W (indicated by arrows) are determined.

and b for each orientation of the field, and for the calculated polycrystalline average. According to (2.27), these coefficients can be identified as: a $\equiv$ $1/C$ and b $\equiv$ θ_W/C. Using the expression (2.9) for the Curie constant C, the experimental "effective Bohr magneton" $p_{\rm eff}$ can be calculated from the a coefficient corresponding to the polycrystalline average data:

$$a = \frac{1}{C} = \frac{3\,k_{\rm B}}{N_A\,p_{\rm eff}^2\,\mu_{\rm B}^2} \quad \text{therefore} \quad p_{\rm eff} = \sqrt{\frac{3\,k_{\rm B}}{N_A\,\mu_{\rm B}^2}\,\frac{1}{a}} \approx \sqrt{\frac{8}{a}}. \tag{2.28}$$

The resulting value can then be compared with the theoretical one for the respective rare earth ion, listed in Table 2.1. In the calculated polycrystalline average susceptibility, the CEF anisotropy effects average out (Boutron, 1973; Dunlap, 1983), which is the reason for using the these susceptibility data to estimate p_{eff}.

In a similar manner, the b-coefficients can be used to determine the anisotropic Weiss temperatures θ_W:

$$a = \frac{1}{C} \quad \text{and} \quad b = \frac{\theta_W}{C}, \quad \text{therefore} \quad \theta_W = \frac{b}{a}. \tag{2.29}$$

The θ_W temperatures, determined as described above, are indicated by small arrows in Fig. 2.5, for the two field directions, as well as for the calculated polycrystalline average. It is readily apparent from the above figure, that the θ_W temperatures are expected to be negative for antiferromagnetic compounds. In the case of ferromagnetic materials, similar calculations can be performed, with the θ_W temperatures expected to be positive. The one other noticeable difference apparent in the susceptibility measurements is that the Curie temperature T_C is less clearly defined, as a fairly rapid increase in $\chi(T)$ is expected around the ordering temperature.

2.1.8.2 Specific heat

For both ferromagnetic and antiferromagnetic compounds, specific heat measurements (solid line in Fig. 2.6a) typically feature a well-defined peak at the transition temperature, allowing for a fairly accurate determination of T_{ord}. Moreover, in crystalline, metallic compounds, the low-temperature specific heat is dominated by the free electrons contribution, which is linear in T ($C_p^{el} = \gamma * T$), and the lattice contribution, which is proportional to T^3. Thus the low-T specific heat can be written as:

$$C_p = \gamma T + \beta T^3 \quad \text{or} \quad C_p/T = \gamma + \beta T^2. \tag{2.30}$$

Plotting the specific heat in C_p/T vs. T^2 coordinates (Fig. 2.6b) allows for the determination of both the electronic specific heat coefficient γ (by extrapolation of the linear region down to T = 0) and the phonon term coefficient β (as the slope of the linear $C_p/T(T^2)$).

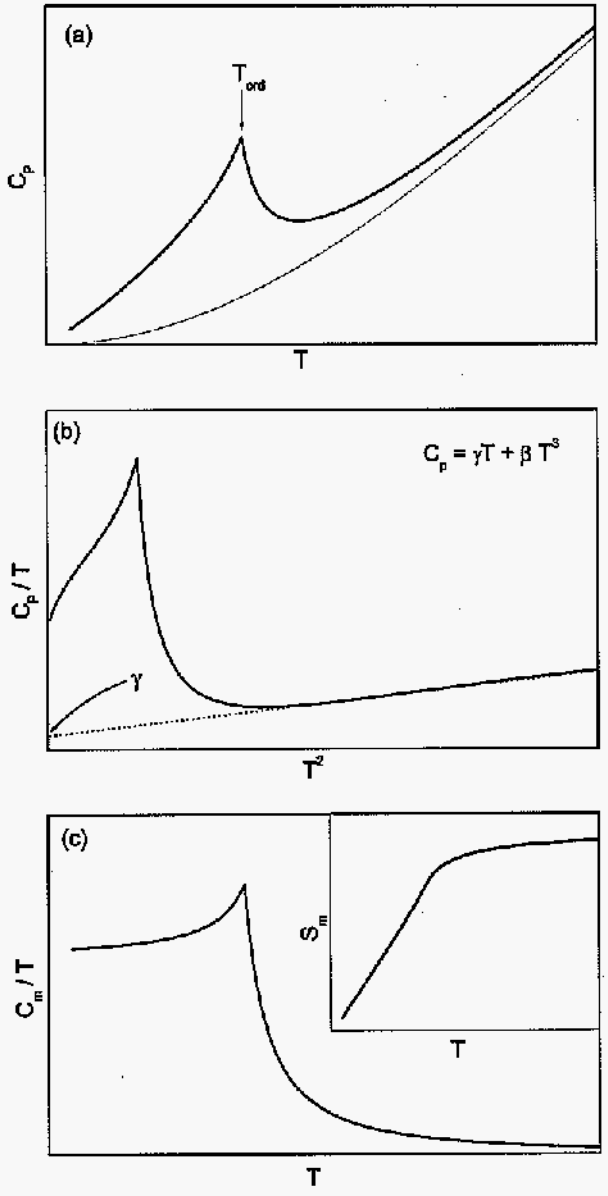

Figure 2.6 (a) Low-temperature specific heat data C_p for a magnetically ordered compound (solid line), with the non-magnetic contribution (dotted line). (b) C_p/T vs. T^2 used to determine the electronic specific heat coefficient γ, the phonon specific heat coefficient β and the Debye temperature Θ_D. (c) The low-T magnetic specific heat, plotted as $C_m/T(T)$, from which the magnetic entropy $S_m(T)$ (inset) can be determined.

Typically, the γ values are $\approx$ 1 $mJ/mol\ K$, but they can be 2 to 3 orders of magnitude larger in compounds known as heavy fermions (see Section 2.3). By using the β coefficient, the Debye temperature Θ_D can be estimated using the Debye model result for the phonon specific heat C_p^{ph}:

$$C_p^{ph} = \beta\, T^3 \equiv \frac{12\pi^4}{5}\, n\, k_{\mathrm{B}} \left(\frac{T}{\Theta_D}\right)^3, \tag{2.31}$$

where n is the number of phonons.

Additional information about magnetically ordered compounds can be extracted from the magnetic specific heat C_m. For rare earth compounds with magnetism due only to the rare earth ions, the R = Y, La and Lu compounds are non-magnetic. Within the Debye model, their specific heat provides fairly good approximations for the non-magnetic contribution to the specific heat of the magnetic compounds (shown as dotted line in Fig. 2.6a), and C_m can be estimated as:

$$C_m(T) = C_p(magn)(T) - C_p(non-magn)(T). \tag{2.32}$$

The integration of $C_m/T(T)$ from 0 up to a given temperature allows us to estimate the magnetic entropy, over the same temperature range. In turn, the magnetic entropy released at T_{ord} is indicative of the degeneracy n of the ground state multiplet, where n can be estimated from:

$$S_m(T_{ord}) \approx R \ln n, \quad \text{where R is the universal gas constant.} \tag{2.33}$$

2.1.8.3 Resistivity

Measurements of the transport properties of new materials frequently corroborate the findings of thermodynamic measurements, but their analysis is typically more difficult than that of magnetization or specific heat. Much of this complexity may be removed through the use of Mathiessen's rule, which states that the total resistivity of a compound is the sum of the individual components of the resistivity (Fig. 2.34):

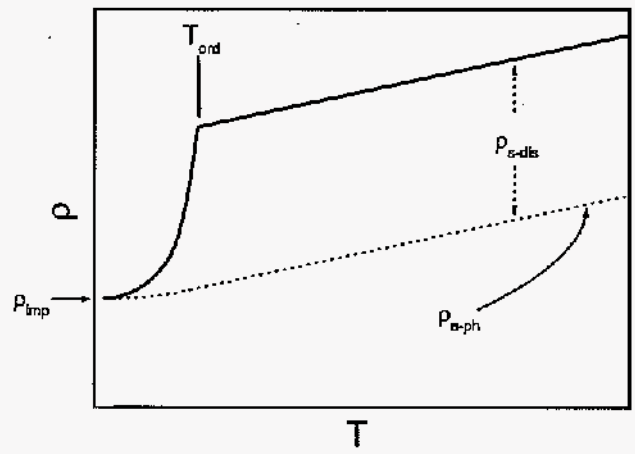

Figure 2.7 Temperature-dependent resistivity of a metallic compound.

$$\rho = \rho_{imp} + \rho_{e-ph} + \rho_{s-dis} + \rho_{e-e} \quad \text{(Ziman, 1967), where:} \tag{2.34}$$

- ρ_{imp} is the term due to scattering off of impurities, dominant at low temperatures and T-independent; the residual resistivity ratio (RRR) of a sample, defined as the ratio of the room-temperature resistance to the resistance extrapolated to 0 K $[\rho(300K)/\rho(0K)]$, or the ratio of $\rho(300K)$ to the resistivity at the lowest measured temperature (e.g., $\rho(300K)/\rho(1.8K)$ in many cases) is an indication of the sample quality (lower residual resistivity yields larger RRR, suggesting better sample quality).

- ρ_{e-ph}: electron-phonon is the dominant scattering process at high temperatures, and this resistivity term increases linearly with temperature;

- ρ_{s-dis} arises from the electrons scattering off of the disordered local magnetic moments in the paramagnetic state (ergo the name of spin-disorder scattering); as the temperature is lowered through T_{ord} (Fig. 2.34), a sudden decrease in the resistivity occurs due to the loss of this spin-disorder.

- ρ_{e-e} is the electron-electron scattering term, which is quadratic in T; this term is negligible around room temperature, and also rapidly decreases as T approaches 0.

2.2 Metamagnetism

2.2.1 General considerations

The concept of metamagnetism was first introduced to describe a field-induced, first-order phase transition from an antiferromagnetic state with low magnetization, to a ferromagnetic state characterized by high magnetization (see Gignoux, 1995, and references therein, for a review). This is driven by the lowering of the total energy of a system via the application of an external magnetic field. Extensive studies of metamagnetic phase transitions have been performed in the past decades, as this concept has been extended to describe not only single-step transitions, but all types of field-induced magnetic phase transitions.

Currently a metamagnetic transition refers to any "anomalous" magnetization with an upward curvature upon increasing field, as opposed to "normal" magnetic behavior (*i.e.*, Brillouin-like), which exhibits downward curvature. Two classes of metamagnetic transitions can be distinguished:

- a sharp (step-like) transition, where the jump in magnetization occurs at almost constant field (Fig. 2.8a);
- a S-shaped transition where the critical field value is associated with an inflection point of the M(H) curve (Fig. 2.8b).

Class 1 transitions are often associated with first-order phase transitions; also, these transitions are typically sharper at low temperatures, and they broaden as temperature is raised, often evolving into class 2 transitions. One given compound may feature both types of metamagnetic transitions on the same M(H) isotherm, or at different temperatures.

Demagnetizing field effects are also responsible for the broadening of the metamagnetic phase transitions. To illustrate this, we consider a simplified picture of an ellipsoidal sample

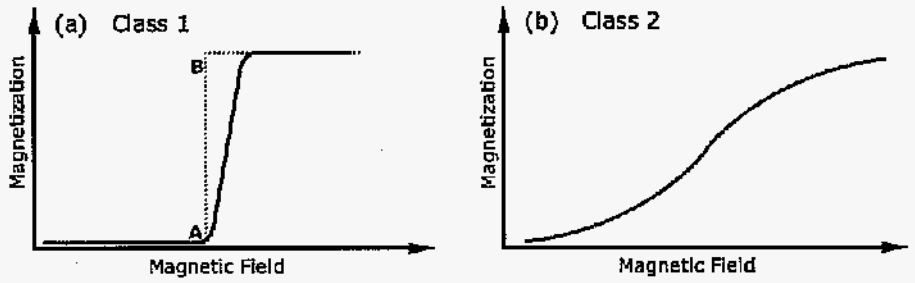

Figure 2.8 Schematic representation of (a) a discontinuous (class (1)), and (b) a continuous (class (2)) metamagnetic transition.

placed in an external applied field H_{ext}; however, due to the magnetization of the sample, the effective internal field experienced by the magnetic ions is reduced to H_{int}:

$$H_{int} = H_{ext} - N_d M = H_{ext} - H_d \tag{2.35}$$

where N_d and H_d are the demagnetizing factor, and the demagnetizing field respectively, dependent on the shape of the sample, and the direction of the applied field. In the case of a first-order phase transition without any hysteresis, at the critical field value of the internal field $H_{c,int}$ the magnetization should jump discontinuously from M_A to M_B (dotted line in Fig. 2.8a). However, the transition can not proceed all at once since, according to eq.(2.35), an increase in magnetization would lead to a decrease in H_{int} below the critical value; therefore the transition must take place at increasing field values, such that

$$\frac{\delta M}{\delta H_{ext}} = \frac{1}{N_d}. \tag{2.36}$$

The resulting magnetization curve has an inclined portion around the transition (solid line in Fig. 2.8a), with a slope inversely proportional to the demagnetizing factor N_d.

The critical field values H_c are generally temperature dependent, and thus each compound

may be characterized by H - T phase diagram. Moreover, these critical values (H_c or T_c), and consequently the H - T phase diagrams, may vary with the orientation of the applied field relative to the crystallographic directions. This is often a direct consequence of the magnetocrystalline anisotropy effect playing an essential role, together with the exchange interactions, in the occurrence of metamagnetism. Strong crystal electric field effects CEF may constrain the magnetic moments to a certain direction (axial anisotropy) or within a given plane (planar anisotropy). Furthermore, the magnetic moments may be constrained to a number of non-collinear easy axes, like the two-fold axes in tetragonal or hexagonal symmetry, or the three-fold axes in cubic symmetry; other such plausible examples are the four-fold axes in tetragonal, or six-fold axes in hexagonal compounds. Weak or intermediate anisotropy may also occur in some systems, leading to the magnetic moments lying anywhere in space.

2.2.2 Different types of metamagnetic phase transitions

Systems where the CEF is the only effect acting on the 4f-shell represent a simple case of metamagnetism. The metamagnetism in such materials occurs because of what is known as level-crossing. For example, as a magnetic field is applied, the excited (*i.e.*, J = 1 in Fig. 2.9) states split into field-dependent states (except for the $J_z = 0$ one). Of these, a subset (i.e., the $J_z = 1$ state) lower their energy as field increases; as a consequence, level-crossing occurs between a low-energy ($E_{J,J_z} = E_{0,0}$) and a high-energy state ($E_{J,J_z} = E_{1,1}$), giving rise to a metamagnetic transition with critical field value H_{crit} given by:

$E_{0,0} = E_{1,1}$, or $\varepsilon_0 = \varepsilon_1$ - g μ_B H_{crit}.

Multiple transitions of this type may, in theory, occur. Examples of compounds for which CEF level-crossing has been theoretically predicted include TmSb (Cooper, 1966), and was experimentally observed in TmSb (Nimori, 1995), Pr metal (McEwen, 1973) and $PrNi_5$ (Ball, 1992).

The level-crossing case considered above corresponds to a paramagnetic system; the metamagnetic behavior is greatly complicated when long range magnetic ordering is also considered.

Particularly in ferromagnetic compounds, metamagnetic transitions occur as the magnetic

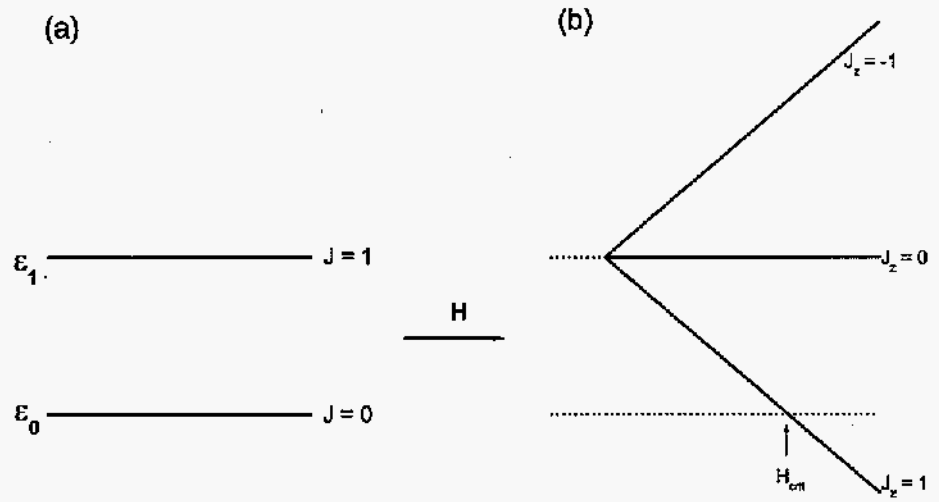

Figure 2.9 The energy levels of an ion with L = 0 and S = 1, in the paramagnetic state: (a) no magnetic field is applied (excited state is degenerate); (b) the degeneracy of the J = 1 state is lifted by the applied magnetic field H, and level-crossing occurs at $H = H_{crit}$.

field is applied parallel to the hard axis (Gignoux, 1995). The transitions are associated with the rotation of the magnetic moments from the easy axis towards the direction of the field, and are typically related to the sudden change of the magnetization at a critical field H_c. Numerous systems show this type of metamagnetism, with RZn, RAl_2, RRu_2 being only a few examples (Gignoux, 1995, and included references).

The case of simple antiferromagnets is of particular interest for studies of metamagnetism, since it often can be understood in terms of simple theoretical models.

A special case of metamagnetism may occur in Gd-based antiferromagnetic compounds, which are expected to be isotropic in the paramagnetic state. However, small anisotropy (mainly of exchange origin) may exist in such compounds, which fixes the zero-field orientation of the magnetic moments in the ordered state. In low applied fields, a spin-flop transition may occur, during which the magnetic moments rotate toward a direction perpendicular to the

applied field. This is a result of the higher perpendicular susceptibility compared to the one for field along the moments' direction. A few examples of Gd-based compounds displaying metamagnetic transitions are $GdCu_6$ (Takayanagi, 1989), $GdCu_2$ (Borombaev, 1987), $GdGa_2$ (Ball, 1993).

As already mentioned in the case of Gd compounds, the susceptibility perpendicular to the moments' direction is larger than the one parallel to it in all rare earth antiferromagnetic compounds. Thus there is a tendency of the moments to align perpendicular to the field direction, even in the case of field initially applied parallel to them. However, for non-Gd based compounds, this effect competes with the magnetocrystalline anisotropy, and, depending on its relative magnitude compared to the exchange energy, two cases can be distinguished:

- for small anisotropy energy, and field parallel to the direction of the moments, when H becomes higher than a critical value the moments flop over to a configuration almost perpendicular to the field. This results in a step in the magnetization; as the field is subsequently increased, the moments continuously rotate towards the direction of the field until saturation is reached.

- in the case of strong anisotropy, for fields parallel to the antiferromagnetic direction, magnetization remains in the same direction. As the field is increased beyond a critical value, some of the magnetic moments antiparallel to the field flip over to becoming parallel. Several such steps can be observed in the magnetization curves, until the field-induced saturated state is reached after all moments have been flipped from their antiparallel to the parallel position.

When field is applied perpendicular to the direction of the moments, the magnetization increases slowly with field towards the saturation value. However, small fields are necessary to reach the saturated state in the case of small CEF anisotropy (and for cases where this is the dominant anisotropy effect), whereas in the large CEF anisotropy limit, the saturation is achieved for fields comparable to the CEF splitting.

Numerous extremely anisotropic systems displaying metamagnetic transitions are currently

known; we can enumerate a few where only two metamagnetic transitions have been observed ($DyCo_2Si_2$ [Iwata, 1990], $ErGa_2$ [Doukouré, 1982], $CeZn_5$ [Gignoux, 1987]). More recently a number compounds have been shown to have several more complex metamagnetic transition, and they are discussed in some detail in the next section.

2.2.3 Metamagnetic transitions in tetragonal compounds with magnetic moments in tetragonal point symmetry

One simple case of an extremely anisotropic antiferromagnetic compound is that of $TbNi_2Ge_2$ (Bud'ko, 1999), a tetragonal compound with Tb ions in tetragonal point symmetry. At low temperatures, the crystalline electric field (CEF) anisotropy confines the local moments along the c ([001]) crystallographic axis (Ising-like system). Up to six metamagnetic transitions are observed, with the critical field values $H_{ci,j}$ having a $1/\cos\theta$ dependence on the angle between the applied field H and the c-axis. It is also shown that the locally saturated magnetization values vary like $M_{i,sat} * \cos\theta$, and from the $M_{i,sat}$ values, the net distribution of moments for each metamagnetic state can be inferred. Both of these angular dependencies are a consequence of the extremely axial nature of the CEF splitting of the $TbNi_2Ge_2$ ground state.

A more complex situation is encountered when the magnetic moments are allowed more degrees of freedom , *i.e.* when the CEF anisotropy constrains them to an easy plane. This is the case in the tetragonal compounds RNi_2B_2C (Cho, 1996b; Canfield, 1997a,b), with R = Tb - Er, and $RAgSb_2$ (Myers, 1999a) for R = Dy. The R ions are again in tetragonal point symmetry and the local moments are confined to four equivalent [110] or [100] crystallographic directions; thus the angular dependent magnetization measurements, when the field is applied in the basal plane, reveal the four-fold anisotropy of the longitudinal magnetization that reflects the symmetry of the unit cell. The angular dependencies of the locally saturated magnetizations $M_{i,sat}$ and the critical fields $H_{ci,j}$ could be treated by simple analysis, and plausible net distribution of moments could be inferred for each metamagnetic phase (Canfield, 1997a,b). As an example, Fig. 2.10a shows a subset of the M(H) T = 2 K isotherms, for various orientations of the applied field within the basal plane. Up to three metamagnetic transitions can be

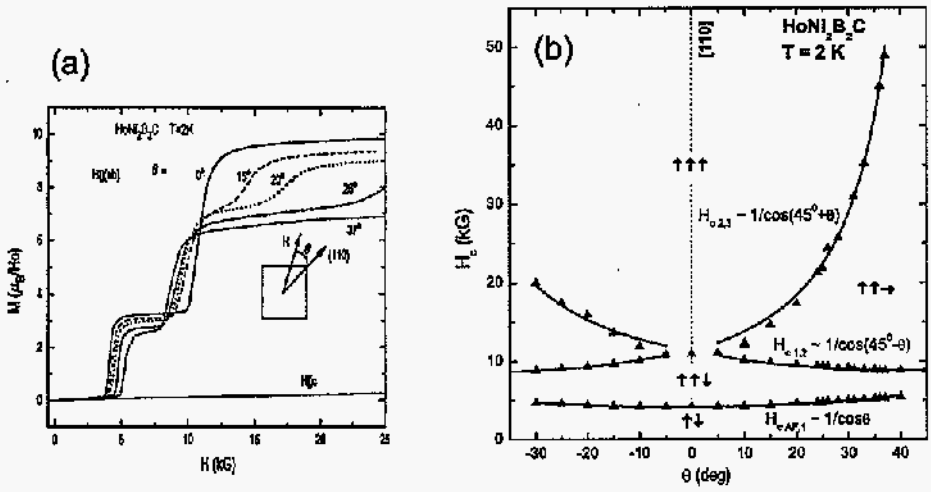

Figure 2.10 (a) $HoNi_2B_2C$ M(H) different field orientations within the ab-plane; (b) H - *theta* phase diagram, with measured data (symbols) and theoretical calculations (lines) based on *the four-position clock model.* (Canfield, 1997b)

observed, and their corresponding critical field values $H_{ci,j}$ are shown as symbols in Fig. 2.10b as a function of the angle θ (with θ being measured from the closest [110] easy direction).

Kalatsky and Pokrovsky (1998) elaborated *the four-position clock model*, which arises directly from the fact that strong CEF anisotropy confines the magnetic moments to four non-collinear directions (*i.e.*, to $\uparrow \longrightarrow \downarrow \longleftarrow$ positions). The angular dependencies of $M_{i,sat}$ and $H_{ci,j}$ calculated based on the above model are described by $cos(\theta \pm \varphi_j)$, and $1 \,/\, cos(\theta \pm \varphi_j)$ respectively, with $\varphi_j = 0^0$, 45^0 or 90^0. These values are integer or half-integer multiples of $360^0 \,/\, n$, where $n = 4$ in our tetragonal system. As can be seen in Fig. 2.10b for $H_{ci,j}$, these calculations agree well with the experimentally determined critical field values in $HoNi_2B_2C$; $DyAgSb_2$ (Myers, 1999a) is another extremely planar tetragonal system with the rare earth ions in tetragonal point symmetry, which is well-described by the same model.

2.3 Heavy fermion compounds

2.3.1 Single ion Kondo effect

Before discussing the heavy fermion systems and their physical properties, it is appropriate to introduce the Kondo problem of a single-magnetic impurity embedded in a non-magnetic host. The extension of this model to the dense Kondo system (*i.e.*, a Kondo lattice) will lead to additional features, especially at low temperatures, but at intermediate temperatures the properties of the Kondo lattices are well-described within the single-ion picture.

A local minimum in the temperature-dependent resistivity of a dilute magnetic alloy (*e.g.*, of Cu, Ag, Au with Cr, Mn or Fe impurities) has been observed experimentally since 1930 (Meissner, 1930). The first theoretical explanation of this minimum (Kondo, 1964) was based on the magnetic impurities which act as scattering centers, hybridizing with the conduction electrons, and leading to the screening of the local moments. Kondo's analysis gives a logarithmic divergence of the low-T resistivity due to magnetic scattering, which competes with the monotonically decreasing phonon contribution as the temperature is lowered. Whereas this picture yields the experimentally observed minimum in resistivity, experimentally the resistivity showed finite values at the lowest temperature, unlike the predicted logarithmic divergency. This constitutes the Kondo problem, and various models have been developed as attempts to account for the observed features down to very low temperatures. One solution to the aforementioned Kondo problem (Yoshimori, 1976; Mihály 1978) yields a quadratic temperature-dependence of the resistivity at very low temperatures, qualitatively illustrated in Fig. 2.11a: the logarithmic increase as the temperature decreases is observed down to a characteristic Kondo temperature T_K, emphasized by the vertical dashed line. Below T_K, the resistivity shows a quadratic saturation as $T \rightarrow 0$. The Kondo temperature T_K separates the local moment regime ($T \gg T_K$) from the compensated magnetic moment regime at low temperatures.

The calculated susceptibility for a diluted Kondo system (Wilson, 1975) yields a cross-over from a quasi-free behavior of the magnetic moments at $T \gg T_K$, to a bound state for $T \ll$

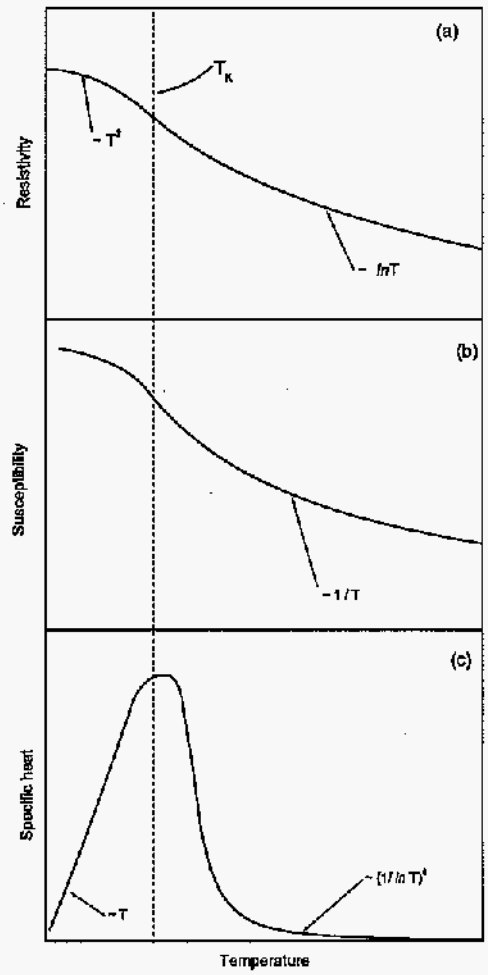

Figure 2.11 Low-temperature behavior of (a) resistivity, (b) susceptibility and (c) specific heat of a diluted Kondo system

T_K (Fig. 2.11b). A full quenching of the magnetic moment in the low temperature regime manifests as a weakly T-dependent susceptibility below T_K.

Rajan (1983) calculated the specific heat of a single-impurity system, and the result is sketched in Fig. 2.11c: a maximum occurs in C_p around a characteristic temperature T_0, which is typically slightly higher than T_K. For diluted systems, the low-temperature specific

heat was shown to be linear in T (Desgranges, 1982). The entropy associated with the impurity contribution tends, for very high temperatures, to R ln 2.

2.3.2 Physical properties of heavy fermions

The heavy fermion materials are a subset of the f-electron intermetallic compounds, associated with multivalent (e.g., capable of hybridizing) rare earth ions, like Ce, Yb and U, and to lesser extent Sm and Eu, and they can be described in terms of a Kondo lattice model. At high temperatures ($T > T_K$), their observed properties may be described based on the single-impurity picture. The relevant physics for the heavy fermions occur at low temperatures, where the local moment is partially or totaly compensated. Their electronic specific heat coefficient γ is anomalously large in the low temperature limit, with correspondingly large Pauli paramagnetic susceptibility χ. The ratio of the magnetic susceptibility to the electronic specific heat coefficient in the limit $T \rightarrow 0$ K, the so-called Wilson-Sommerfeld ratio $R = (\pi^2 k_B^2/\mu_{eff}^2)(\chi(0)/\gamma(0))$, is unity in the case of non-interacting electrons; for heavy fermion systems this ratio is typically closer to 2.

At high temperatures, these compounds exhibit local moment behavior, as indicated by Curie-Weiss susceptibility with Curie constant corresponding to that of the Hund's rule ground state of the f element. The resistivity at high temperature is typical of metallic compounds (~ 100 $\mu\Omega$ cm), but often less temperature dependent than for their non-hybridizing neighbors (i.e., for R = Tm or Lu in the case of Yb-based compounds). A prominent sign of a Kondo lattice state is the fact that, at low temperatures ($T < T_K$), $\rho(T)$ rapidly decreases with temperature, and for very low temperatures (*i.e.*, below a "coherence temperature" T^*), it becomes quadratic in T, characteristic of Fermi-liquid like FL behavior.

As the temperature is lowered, in local moment systems the $R \ln 2$ entropy (for a CEF doublet ground state) is being removed by magnetic ordering; in the limit of strongly correlated, heavy fermion systems (with no magnetic order), the $R \ln 2$ entropy is released continuously below the Kondo temperature (where the magnetic moment is quenched). An interesting behavior is anticipated in-between these extreme cases: around a critical value $(J\ N(E_F))_{crit}$ of the J

$N(E_F)$ parameter, there is a competition between the long-range magnetic order of the uncompensated moments and the low-temperature compensated state (Doniach, 1977a), as illustrated in Fig. 2.12. The exchange interaction between the magnetic moments is characterized by the RKKY temperature $T_{RKKY} \propto J^2 N(E_F)$; the Kondo temperature $T_K \propto e^{-1/|J|N(E_F)}$ increases faster than T_{RKKY}, resulting in a local maximum in the ordering temperature T_N (Fig. 2.12), followed by a drop in T_N around $J\,N(E_F))_{crit}$. This may lead to a quantum phase transition at $T = 0$, with the possibility of tuning the parameter $J\,N(E_F)$ via a number of control parameters (substitution, pressure, magnetic field). Whereas substitution is a discontinuous tuning parameter (pressure being essentially discontinuous as well), the magnetic field offers the advantage that it can be varied continuously.

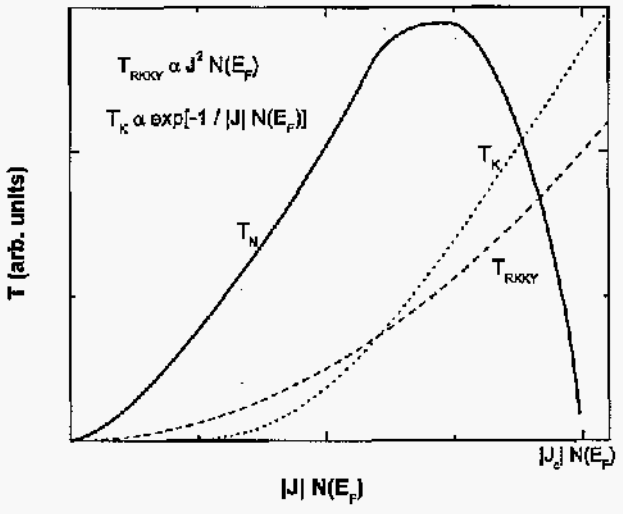

Figure 2.12 Doniach's phase diagram.

2.3.3 Quantum critical phase transitions in heavy fermions

As already mentioned, it is believed that the Kondo lattice picture describes the nonmagnetic ground state, large quasiparticle effective mass (manifested through enhanced γ val-

ues) and curious temperature dependence of the resistivity of heavy fermion compounds (Hewson, 1997). This model describes how the local moment is screened out or partially compensated as the temperature falls below a characteristic Kondo temperature $T_K = D\, e^{1/(N(E_F)J)}$, where D is the conduction electrons band width, $N(E_F)$ is the density of states at the Fermi level, and J is the local spin-conduction electron coupling. A competition between the low-temperature compensated state and the magnetically ordered state of the uncompensated moments is obvious and points toward the possibility of quantum critical phase transitions.

In contrast to a classical phase transition at finite temperatures, driven by temperature as a control parameter with thermal fluctuations, a quantum phase transition is driven by a control parameter C other than temperature (*e.g.*, C = pressure, doping or magnetic field) at T = 0, with quantum mechanical fluctuations. Such a control parameter tunes the system from a magnetically ordered state towards a (magnetically) disordered state, at zero temperature, crossing a quantum critical point. Due to the hybridization of the 4f electrons and the conduction electrons in heavy fermion HF systems, which can be modified by any one of the aforementioned control parameters, the HF compounds are very suitable to study quantum critical behavior. Moreover, close to the critical value C_{crit} which drives the ordering temperature close to zero, pronounced deviations from the Fermi liquid-like FL behavior can occur. This has been observed in a large number of HF systems where C = doping or pressure, and only a few doped systems have been field-tuned through a QCP (Stewart 2001). $YbRh_2Si_2$ (Trovarelli, 2000; Gegenwart, 2002; Ishida, 2002; Paschen, 2003; Paschen, 2004) was the first stoichiometric Yb-based HF compound in which a field-induced quantum critical point QCP has been observed, with only two more such compounds (subject of this study), YbAgGe [Beyermann, 1998; Katoh, 2004; Morosan, 2004; Bud'ko, 2004; Bud'ko 2005] and YbPtIn [Morosan 2005a], known to date.

Non-Fermi liquid like NFL behavior can often be observed in HF systems undergoing a quantum phase transition. Experimentally, such NFL behavior involves logarithmic divergence of the specific heat $C/T \sim -\ln T$, and linear temperature dependence of the resistivity $\Delta\rho \sim T$ at the lowest temperatures, and for intermediate field values (*i.e.*, just above the

critical field of the QCP). For higher fields, the Fermi-liquid state is typically recovered, as the low-T resistivity becomes quadratic in T.

CHAPTER 3. Hexagonal intermetallic compounds

3.1 Search for hexagonal RE-compounds with planar metamagnetism

Initially thought to be improbable, angular dependent metamagnetism in extremely planar systems is now an accepted and understandable event in tetragonal compounds (Canfield, 1997a,b; Budko, 1999; Myers, 1999a); but this has not yet been well studied in hexagonal compounds. This was the motivation for the extensive search for hexagonal compounds suitable for a similar study of angular dependent metamagnetism. We embarked on a search for single crystals of compounds with unique crystallographic site for the rare earth ions and ordered ligand sites. In addition, the compound needed to have extremely planar magnetization with distinct in-plane metamagnetic transitions.

Our numerous attempts to grow single crystals of such systems had mixed results, and they are summarized in Table 3.1. These are only a fraction of the hexagonal compounds which could potentially meet the criteria for our proposed study. As it is readily apparent from the table, we succeeded in growing single crystals of the right phase for a limited number of series we tried, of which very few met our criteria: the R_2Zn_{17}, $RTSn$ (T = Ag, Au), RGa_2 did not show extreme planar anisotropy or anisotropy within the basal plane; TbAuIn was extremely planar, with high T_N ($\sim$ 35 K), but we could not optimize the growth to completely eliminate the growth of a second phase ($TbAu_3$).

The growths of RPtIn and RAgGe produced well-formed single crystals. Since all of the existing reports on these two series were based on polycrystalline samples (Baran, 1998; Gibson, 1996; Watson, 1995; Zaremba, 2001), we have expanded the synthesis of single crystals to include most of their heavy rare earth members, R = Y, Gd - Lu for RPtIn, and R = Tb - Lu for the RAgGe series. The heavy RAgGe and RPtIn compounds are stoichiometric materials,

crystallizing in the hexagonal ZrNiAl structure, space group P $\bar{6}$ 2 m, # 189. This represents an ordered variant of the Fe_2P family, having three rare earth ions in the unit cell positioned at unique sites with orthorhombic point symmetry (m 2 m). Anisotropic physical properties and the existence of metamagnetic transitions in many of these compounds rendered the two series as very interesting for a study of local moment physics. Moreover, the Yb members of both RAgGe and RPtIn series appeared to be promising heavy fermion compounds for studying the properties of strongly correlated electron systems.

Table 3.1 Summary of attempted growths of hexagonal compounds with unique R site having different point symmetries.

Compound	Archetype	Point Symmetry	Results
RCuSn	AlB_2	*Hexagonal*	Unidentified phases
RNi_3Al_9	$ErNi_3Al_9$	*Trigonal*	No crystals; unidentified phase
R_2X_{17} (X = Zn,Fe, Co)	Th_2Ni_{17}/ Th_2Zn_{17}	*Hexagonal*	α/β reported phases, one with 2 R sites in unit cell; ferromagnetic ground state for X = Fe, Co
RInZn	$CaIn_2$	*Hexagonal*	R_2Zn_{17} or RIn_3 (cubic)
RGa_2 RTSn (T = Ag, Au)	LiGaGe	*Trigonal*	No/Reduced in-plane anisotropy Hexagonal plates, no in-plane anisotropy
RCuSi	$InNi_2$	*Trigonal*	Unidentified phases
RPt_2In	YPt_2In	*Hexagonal*	RPt (orthorhombic); dendritic crystals (unidentified)
RAl_2Ge_2	La_2O_3	*Trigonal*	RAlGe (orthorhombic)
RAlNi	$MgZn_2$	*Trigonal*	No crystals; unidentified phase
RTIn (T = Au,Cu, Ni,Pd,Pt,Rh) RAgX (X = Ge,Mg, Pb)	Fe_2P (ZrNiAl)	*Orthorhombic*	T = Pt: **TbPtIn** T = Au: two phases (RAuIn and RAu_3) T = Cu,Ni,Pd,Rh: Cubic crystals X =Ge: **TmAgGe** X = Mg: $R_3Ag_4Mg_3$; RAg_2 X= Pb: R_5Pb_4; unidentified phases

Two isostructural compounds, TbPtIn and TmAgGe, met the requirements for our desired study of angular dependent metamagnetism: unique rare earth site, ordered ligands, extremely planar magnetization, and in-plane anisotropy and metamagnetism. These observations, combined with our experience with *the four position clock model* that was developed

for the tetragonal compounds with rare earths in tetragonal symmetry, lead us to propose a similar model for these Fe_2P-type compounds: *the three co-planar Ising-like systems model*, which consists of three Ising-like moments per unit cell, with their Ising axes within the basal plane and rotated by 60^0 with respect to each other.

3.2 Fe_2P-type hexagonal compounds

3.2.1 RAgGe

The RAgGe compounds (R = Y, Sm, Gd - Lu) have been reported by Gibson *et al.* (Gibson, 1996) to crystallize in the hexagonal ZrNiAl-type structure. We were able to grow most of these compounds in single crystalline form, with the exception of YAgGe, SmAgGe and GdAgGe. Attempts to grow the former two compounds out of solution failed to yield any crystals, whereas trying to grow the Gd member of this series, we obtained $Gd_3Ag_1Ge_1$ (Morosan, 2004).

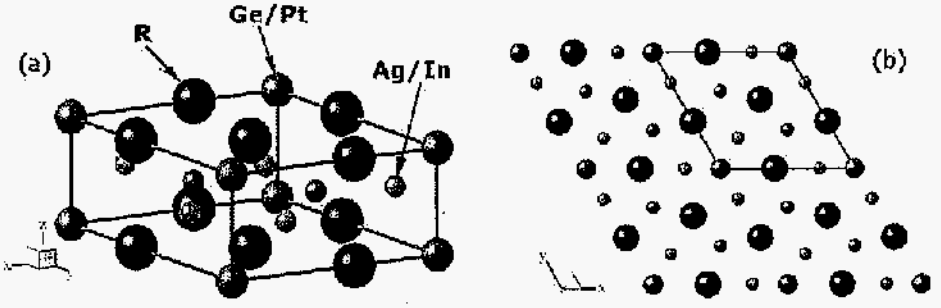

Figure 3.1 (a) Crystal structure of RMX compounds, with R = rare earth, M = Ge, Pt and X = Ag, In; (b) projection along the c-axis, with R-large purple and M-medium green circles, from the z=0 R_3M layers, and M-small green and X-small orange circles from the z=0.5 M_2X_3 layers.

The crystal structure (Fig. 3.1) of the RAgGe compounds can be viewed as alternating R_3Ge and Ag_3Ge_2 layers stacked along the c axis, shown as a c-axis projection in Fig. 3.1b.

The atomic positions are given in Table 3.2 for DyAgGe.

Table 3.2 Atomic positions of DyAgGe (Gibson, 1996)

	Wyckoff site	x	y	z
R	3f	0.5827	0	0
Ge(1)	2d	1/3	2/3	1/2
Ge(2)	1a	0	0	0
Ag	3g	0.2493	0	1/2

In Fig. 3.2, the volume and the dimensions of the unit cell across the series are shown as a function of the R^{3+} ionic radii. Both the a and the c lattice parameters decrease as the series progresses towards heavier rare earths, resulting in the expected lanthanide contraction [Shannon, 1976], indicated by the dotted line on Fig. 3.2a. Throughout the series the a/c ratio is nearly a constant 1.7. YbAgGe falls close to the monotonic decrease of the unit cell parameters, consistent with the Yb ion being essentially trivalent at room temperature in this compound. In Table 3.3 the values of the lattice parameters and the unit cell volume are explicitly given.

Table 3.3 Lattice parameters, the a/c ratio and cell volumes of the RAgGe series of compounds. (Morosan, 2004)

R	a($\AA$)	c($\AA$)	a/c	Vol ($\AA^3$)
Tb	7.13	4.22	1.691	185.75
Dy	7.09	4.20	1.690	182.93
Ho	7.08	4.18	1.693	181.39
Er	7.07	4.17	1.694	180.55
Tm	7.06	4.15	1.702	178.77
Yb	7.06	4.15	1.701	178.92
Lu	7.03	4.13	1.703	176.46

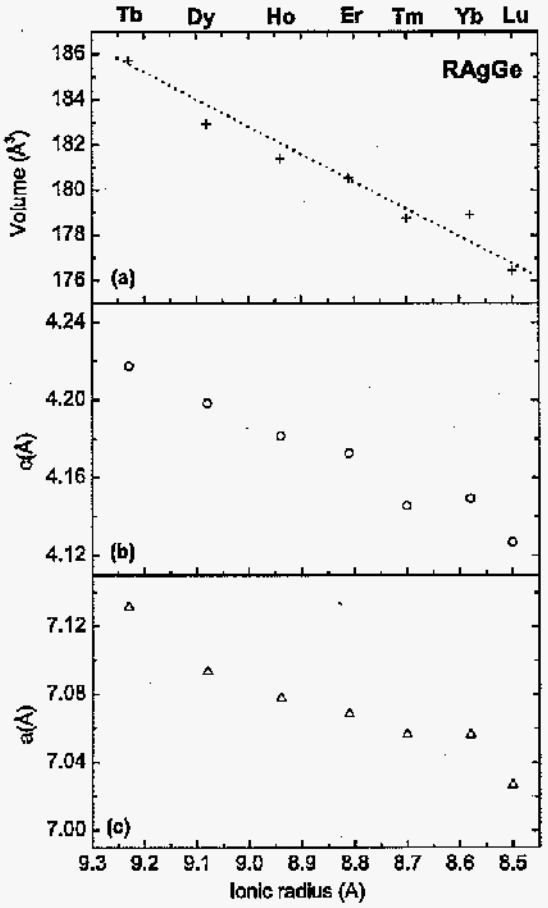

Figure 3.2 Unit cell volumes and lattice parameters for RAgGe, R = Tb - Lu as a function of R^{3+} ionic radius (bottom axis) or rare earth (upper axis).

3.2.2 RPtIn

All members of the RPtIn series have been reported to form with the aforementioned ZrNiAl-type structure (Ferro, 1974; Galadzhun, 2000; Zaremba, 2001), with the exception of EuPtIn. These crystallographic reports were based on measurements on polycrystalline samples. We succeeded in growing stoichiometric single crystals of the R = Y, Gd - Tm, Lu

members of this series using the flux growth method. In the case of Yb, the solution-grown crystals had to be grown from a different initial stoichiometry, and this yielded crystals with a small Pt-deficiency; but single crystals of the stoichiometric YbPtIn system were finally grown using an on-line melt technique, as described in the "Crystal growth" section.

Table 3.4 Atomic positions of TbPtIn (Galadzhun, 2000)

	Wyckoff site	x	y	z
R	3f	0.4070(2)	0	0
Pt(1)	2d	1/3	2/3	1/2
Pt(2)	1a	0	0	0
In	3g	0.7413(2)	0	1/2

Table 3.4 gives the atomic positions of the TbPtIn member of this series (Galadzhun 2000). Fig. 3.3 shows the lattice parameters and the unit cell volumes for the RPtIn compounds. Similar to the case of RAgGe, the unit cell volume of the RPtIn compounds (Fig. 3.3a) generally follows the expected lanthanide contraction (as shown by the dotted line), as does (to a lesser extent) the c lattice parameter (Fig. 3.3b). However an apparent non-monotonic change of the a parameter is noticeable in Fig. 3.3c, and there is also considerable scattering of the a and c values determined from the Rietveld refinement using Rietica software. Consequently the error bars for the lattice parameters and the unit cell volume are also shown.

Table 3.5 Lattice parameters and cell volumes of the flux-grown RPtIn compounds, R = Gd - Lu (Morosan, 2005b) ($^{(*)}$ the on-line grown YbPtIn compound).

R	a($\AA$)	c($\AA$)	Vol ($\AA^3$)
Gd	7.558 ± 0.018	3.922 ± 0.018	194.01 ± 1.809
Tb	7.556 ± 0.016	3.870 ± 0.020	191.33 ± 1.779
Dy	7.550 ± 0.020	3.845 ± 0.025	189.82 ± 2.240
Ho	7.525 ± 0.025	3.825 ± 0.025	187.59 ± 2.472
Er	7.496 ± 0.026	3.806 ± 0.016	185.22 ± 2.068
Tm	7.535 ± 0.015	3.790 ± 0.010	186.37 ± 1.246
Yb	7.535 ± 0.025	3.768 ± 0.012	185.28 ± 1.180
Yb$^{(*)}$	7.548 ± 0.012	3.762 ± 0.010	185.71 ± 1.015
Lu	7.495 ± 0.015	3.760 ± 0.010	182.91 ± 1.231

In addition, the R = Tm and Yb volumes appear to deviate slightly from the monotonic

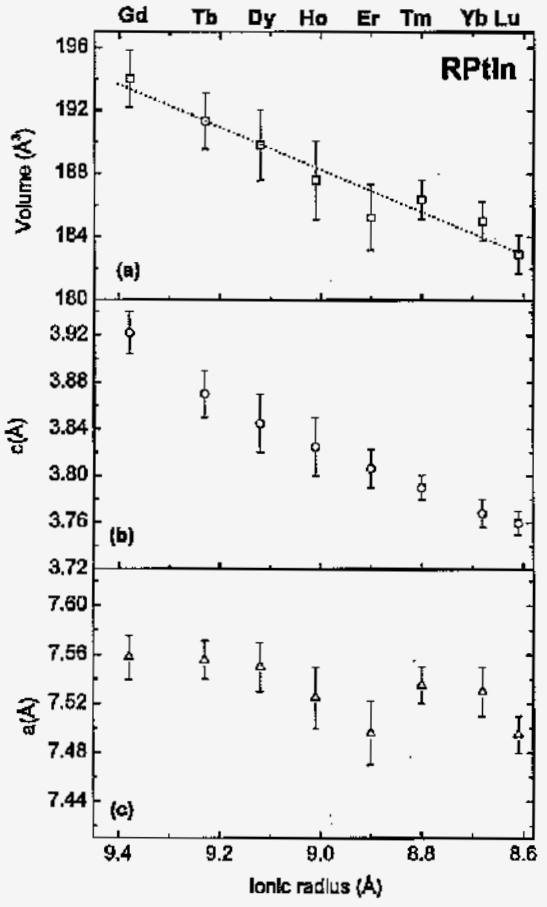

Figure 3.3 Unit cell volumes and lattice parameters for RPtIn, R = Gd - Lu as a function of R^{3+} ionic radius (bottom axis) or rare earth (upper axis).

decrease across the series; whereas this could indicate, at least for R = Yb, a trend toward valence 2+ for the rare earth ions, the magnetic measurements were consistent with the presence of magnetism in the respective compounds, associated with trivalent R ions. Even though a plausible explanation could lie in the site-disorder observed for the flux-grown YbPtIn system, it is invalidated first by the fact that the values shown in Fig. 3.3 with the respective error bars

also encompass the values determined for the ordered YbPtIn compound; secondly, no site-deficiency could be detected for the other compound that shows comparable deviation from the lanthanide contraction, namely the TmPtIn system. The values of the lattice parameters and unit cell volumes are given in Table 3.5, including the ones for the two types of Yb compounds.

CHAPTER 4. Experimental methods

4.1 Crystal growth

Although polycrystalline samples may be used for preliminary characterization of the physical properties of new materials, high-purity single crystals are essential for detailed analysis. In particular, compounds with rare earths in non-cubic point symmetry frequently possess strong anisotropies of the magnetic properties and electronic structure. In a polycrystalline sample, the random orientation of the microscopic grains can average out any such anisotropies. In addition, many measurements require large samples with crystallographically well-ordered, such as neutron or magnetic X-ray diffraction. The quality of single crystal samples is generally superior to polycrystalline samples, since single crystals do not possess grain boundaries. The amount of impurities, which are often present between the grains of polycrystalline materials, are substantially reduced, due the much smaller surface area to volume ratio of single grain crystals. In addition, due to rapid cooling and crystallites growing against each other, it is possible that great amounts of stress and strain are present in polycrystalline materials, and these are typically reduced in well-formed single crystals.

Numerous techniques are presently employed in order to grow single crystal samples, and the utility of each varies greatly. Thorough reviews of many of these methods may be found in Pamplin (1975) and the references therein. Some examples of crystal growth methods include the Bridgeman, Czochralski and zone refining methods, which are essential to the semiconductor industry since they can produce large, very high purity silicon, germanium and gallium arsenide single crystals. Unfortunately, most of these methods require the composition of the melt to be the same or very close to that of the desired product, constraining these methods to the synthesis of congruently (or near-congruently) melting compounds. Furthermore, the

starting components must be heated above the melting temperature of the target compound, which may easily be above the working range of available furnaces and crucibles. Finally, the vapor pressures of the constituent elements may become appreciable at these very high temperatures. For instance, the vapor pressures of some of the rare earth elements, such as samarium, europium and ytterbium, become large at temperatures above 900^0C, leading to chemical reactions with the crucibles as well as a loss of stoichiometry.

One of the most versatile methods which allows for some of the above problems to be avoided is growth from high-temperature solutions. An extensive overview of many of the methods of crystal growth from high-temperature solutions may be found in Elwell and Scheel (1975). The solvent in this high-temperature solution is frequently called a flux, since it produces lower melting temperatures than those of the starting components. At high temperatures, all of the constituent elements are dissolved in the flux. As the temperature of the melt decreases, the solubility of the target compound decreases, forcing the desired compound to precipitate out of the solution. For low enough cooling rates, the growth process occurs via a series of quasi-thermodynamically stable stages, which typically yields crystals relatively free of strains (Fisk, 1989; Canfield, 1992; Canfield 2001).

4.1.1 Growth of ternary compounds from self-flux

Among the key factors to be considered for an initial flux growth are: an appropriate solvent for the desired compound, optimal initial concentrations and minimum temperature for a fully-liquid phase to be reached, as well as the lowest temperatures for which the solvent is still liquid, after the crystal growth has occurred. The last requirement is mandatory in order to be able to isolate the grown crystals out of the flux via centrifugal force: spinning off the flux. Other methods for removing the crystals from the flux would be chemical etch (which often carries the risk of the etchant attacking the crystals) or mechanical removal of the flux.

It is almost always preferable to use as flux for solution growth excess of one or more of the constituent elements of the desired compound. One important reason is that, by introducing no additional elements to the melt, the number of potentially undesired phases that may result

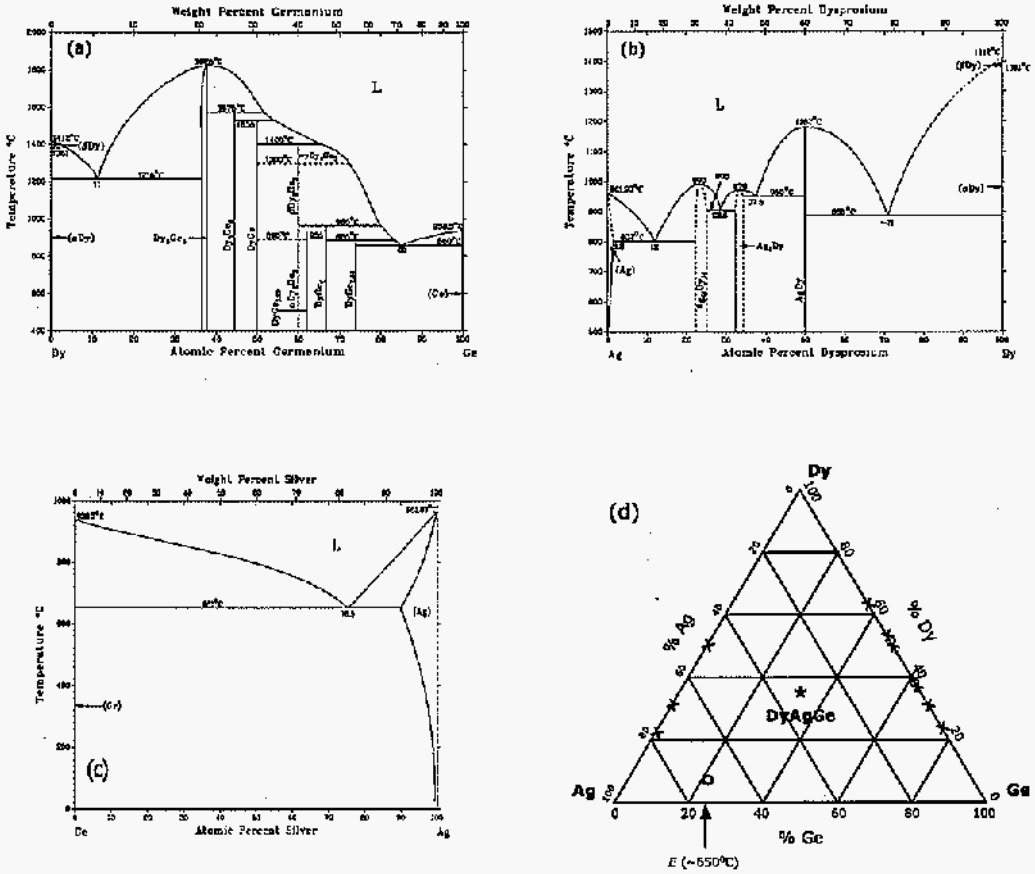

Figure 4.1 Binary phase diagrams of (a) Dy - Ge (Massalski, 1990), (b) Dy - Ag (Gschneidner, 1985) and (c) Ag - Ge (Olesinski, 1988). Note the low eutectic temperature around 75% Ag, and lack of binary compounds on the Ag - Ge binary phase diagram. (d) ternary phase diagram of the Dy-Ag-Ge system. The crosses indicate binary compounds as seen in (a)-(c); the large dot marks the initial composition used for the growth of DyAgGe.

is reduced. However, it is not always practical to employ the self-flux growth method, because of too high melting temperatures, or lack of exposed liquidus-solidus surfaces. A number of elements have been reported to lower the temperature of certain liquid solutions (Canfield, 1992), each of them being a preferred flux when they do not form high-temperature compounds with elements of the target material.

Numerous binary phase diagrams have been experimentally constructed for many elemental pairs, and theoretically proposed for others. They provide an initial map of the composition and temperature space for ternary (or higher) growths, allowing one to estimate the optimal profile for growing a given material. A much smaller number of ternary phase diagrams, and only a limited subset of their isothermal cuts, are currently available. When they do exist, these are also useful tools both for growing binary compounds out of a third elemental flux, or for self-flux ternary solution growths.

In cases where the ternary phase diagram is not available, the three binary phase diagrams, pairing each two of the three elements of the desired compound, are often very useful. Such an example is the growth of DyAgGe out of excess Ag-Ge. The Dy-Ag-Ge ternary phase diagram is not known, but detailed binary phase diagrams (Dy-Ag, Dy-Ge and Ag-Ge) are available (Fig. 4.1a-c). No other ternary compounds with Dy, Ag and Ge are reported to date (or with any other rare earth), but the DyAgGe phase. The lack of ternary phases other the desired one is advantageous for growing this compound (*i.e.*, there are fewer potential second phases). In the Ag-Ge diagram (Fig. 4.1c) there is a broad eutectic with composition $Ag_{0.75}Ge_{0.25}$ at a temperature around 650^0C. This was used as the concentration of the flux for several attempts, as well as a slightly more Ge-rich concentration (around $Ag_{0.60}Ge_{0.40}$). Based on the qualitative (crystal size, morphology, amount of residual flux on the surface) and quantitative (powder x-ray diffraction, resistivity, magnetization) analysis of the resulting crystals, it was concluded that the eutectic concentration was the optimal initial dilution for growing DyAgGe. A solution with initial composition of $Dy_{0.09}(Ag_{0.75}Ge_{0.25})_{0.91}$ was used to obtain well-formed hexagonal rods of DyAgGe.

Fig. 4.1d represents a schematic Dy-Ag-Ge ternary phase diagram, showing the reported

binary compounds (small crosses) and the desired DyAgGe system (black star). The bottom arrow points to the Ag-Ge eutectic concentration, whereas the starting ternary composition which was used for the optimal growth is indicated by the large dot.

4.1.2 Experimental Technique for Flux Growth

In most cases, the starting materials were placed inside a 2 ml or 5 ml alumina crucible, called the "growth crucible" [Fig. 4.2]. Another crucible, called the "catch crucible", is filled two-thirds full with quartz wool and placed inverted on top of the growth crucible. The crucibles were subsequently sealed in a quartz ampoule, under partial argon pressure, which limited the maximum temperature of the growth to 1200^0 C (when quartz starts to soften).

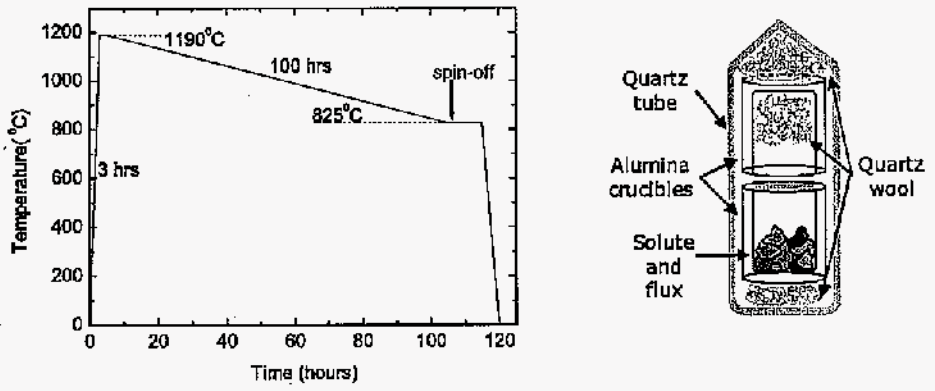

Figure 4.2 (a) Temperature profile for the growth of single crystals of DyAgGe from an Ag-Ge flux. At about 110 hours, the ampoule is removed from the furnace and the remaining flux is decanted from the desired crystals. (b) diagram of the ampoule used for crystal growth (see text).

After allowing the liquid solution to homogenize for a couple of hours at the high temperature, the ampoule is slowly cooled to the desired temperature, at which the flux must be decanted from the growth crucible. This is done effectively by quickly removing the ampoule from the furnace and inserting it inverted into a centrifuge. During the spin, the quartz wool

in the catch crucible acts as a strainer which allows the excess flux to flow to the bottom where it solidifies, and holds any crystals that may have detached from the growth crucible.

Fig. 4.2 also illustrates the growth profile used for growing most of the RAgGe single crystals (R = Dy - Tm, Lu). After initially heating the ampoules to $\sim 1200^0$ C, they were slowly cooled to 850^0 - 825^0 C. After decanting the excess flux, thin hexagonal rods with the c-axis along the axis of the rod were obtained. Two noteworthy modifications to this growth procedure were (i) YbAgGe which was cooled to 750^0 C before decanting, and (ii) TbAgGe for which an initial melt stoichiometry of $Tb_{0.09}(Ag_{0.85}Ge_{0.15})_{0.91}$ was necessary for better quality crystals. A typical hexagonal rod is shown in Fig. 4.3.

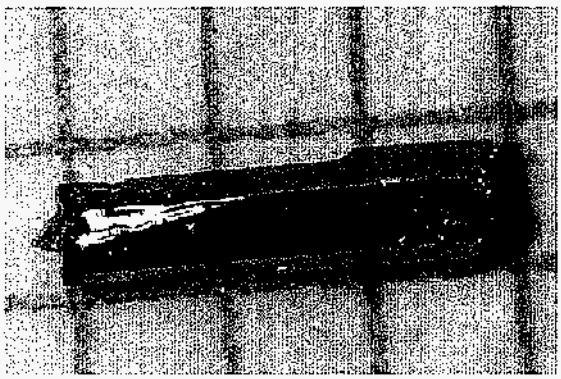

Figure 4.3 Single crystal of YbAgGe, with approximate dimensions $0.4 \times 0.4 \times 3.0\ mm^3$. Hexagonal rod geometry evident (three of the six possible facets are visible here); a few AgGe flux droplets can be seen on the surface of the crystal.

Similar procedures were used for growing most of the RPtIn single crystals (R = Y, Gd - Tm, Lu). Initial concentrations were typically $R_xPt_xIn_{1-2x}$, with $x = 0.05 - 0.10$, making use of the low-melting In as a self-flux. In most cases the ampoules were initially heated up to $\sim 1200^0$ C, and then slowly cooled down to $\sim 800^0$ C, over 50 to 100 hours. Subsequently, the excess liquid solution was decanted, and the resulting hexagonal rods were, if necessary, quickly etched in concentrated HCl to remove residual flux from the surface. Higher decanting

temperatures (*i.e.*, above 1000^0 C) were necessary for R = Y, Gd and Er, whereas in the case of TmPtIn the temperature interval for which best crystals were obtained was lower (between 1100^0 C to 750^0 C). In some cases, the hexagonal rods had hollow channels in the center, sometimes with flux inclusions. We succeeded in optimizing the growth of TbPtIn by using faster cooling rates (*i.e.*, 400^0 C / 50h); this yielded only well-formed, full, hexagonal rods, whereas when slowing down the cooling process hollow crystals were obtained together with full, smaller ones. Slight modifications of the initial concentrations and/or growth profiles for Dy, Ho or Er didn't totally eliminate the formation of hollow rods, but 100 % dense samples could easily be found; however, the cooling rates that gave the best crystals were 400^0 C / 100h for R = Dy and Ho, and 200^0 C / 100h for R = Er.

4.1.3 Growth of $YbPt_{0.98}In$ and YbPtIn compounds

A drastic modification of the above growth procedure needed to be made in order to grow the R = Yb member of the RPtIn series out of liquid solution. The best results were obtained by starting with a $Yb_{0.4}Pt_{0.1}In_{0.5}$ initial composition. Such a large amount of rare earth is likely to react with the alumina crucible at high temperatures, and contaminate or alter the stoichiometry of the melt. Therefore the growth and the catch crucible were replaced in this case by a tantalum ampoule: one end of a Ta tube was sealed with a cap of the same material. After placing the constituent element in the Ta crucible, a Ta strainer (a second Ta cap in which small holes have been drilled) is placed approximately in the middle of the tube. A third Ta cap is welded on the upper end of this ampoule, resulting in the so-called 3-cap Ta crucible (Canfield, 2001). This is then sealed in quartz under partial argon atmosphere, to prevent the oxidation of the Ta tube at high temperatures. The ampoule is heated up to 1190^0 C, and then slow-cooled to 1000^0 C over $\sim$ 100 hours. When the inverted ampoule is placed in the centrifuge, the empty side of the Ta tube acts as the catch crucible, whereas the strainer separates the crystals detached from the growth side from the spun flux.

The resulting crystals had a small Pt-deficiency on one of the two Pt sites in the unit cell, leading to a stoichiometry closest to $YbPt_{0.98}In$ (see Chapter 9 for details).

Another growth procedure, on-line melt, was also used to produce YbPtIn crystals (Trovarelli, 2000). Polycrystalline samples were prepared by placing stoichiometric amounts of Yb, Pt and In in a Ta crucible, which was than sealed under Ar atmosphere. The ampoule was than briefly heated up to 1650^0 C; after allowing the mixture to homogenize for a few minutes, it was quickly cooled to room temperature. Subsequently the Ta ampoule was sealed in a quartz tube, and heated up to 700^0 C; the samples were then annealed at this temperature for 120 hours. Numerous small single crystals of YbPtIn (with the exact 1:1:1 stoichiometry in this case) were visible in the polycrystalline melt, highly intergrown, and mostly embedded in the solidified matrix. However, a few small rods were extracted from the surface of the matrix. These samples were shown to be stoichiometric YbPtIn.

This difference in Pt-occupancy between the flux and on-line grown samples is consistent with YbPtIn having a small width of formation extending towards the Pt-deficient side; given that the initial melt composition is very Pt-poor (*i.e.*, $Yb_{0.4}Pt_{0.1}In_{0.5}$), it would be sensitive to such a small width of formation.

4.2 Measurement methods

4.2.1 Magnetization measurements

Magnetic measurements were performed in a Quantum Design Magnetic Properties Measurement System (MPMS) SQUID magnetometer (T = 1.8 - 350 K, H_{max} = 55 or 70 kG). Since for these measurements, the samples were manually aligned with respect to as-grown facets or edges, it was important to have well-formed, clean single crystals. This required large crystals to be used, whereas the upper limit of the calibrated range of the MPMS instrument (i.e., 1.25 emu) restricted us to using magnetic samples with masses of 20 mg or less. For the non-magnetic compounds, samples with masses up to 100 mg were used to optimize the acquired signal in such low magnetization materials. For magnetic compounds, the use of the largest possible sample masses within the limitations of the measuring instrument also offered the advantage of smaller relative weighing errors; in turn, this minimized the errors of the absolute magnetization values which were often crucial in the interpretation of our data.

Occasionally, residual flux was removed from the surface of the crystals, either mechanically by scraping with a metal scalpel (which was often enough for the RAgGe compounds), or chemically, by etching in acid solution (as was necessary for some RPtIn crystals).

Given the rod-like geometry of both the RAgGe and RPtIn crystals, for $H \parallel [0\ 0\ 1]$ measurements, the samples were mounted between two straws, with the rod axis parallel to the straw axis. For measurements with the field parallel to the hexagonal plane, one facet of the rod was typically glued to a plastic disk; subsequently, the disc was inserted horizontally into the straw, in which case the measurements would be performed for field perpendicular to the as-grown facet. In addition, the sample mount allowed us to measure anisotropic in-plane magnetization, by rotating the disk 90^0 inside the straw, with respect to the (horizontal) axis of the rod. Because of the hexagonal symmetry, this effectively rotated the crystal by 30^0 ($= 90^0$ - 60^0) with respect to the direction of the field. The plastic disks were measured separately, and their (small) contribution was subtracted from the overall signal whenever a disk was used for sample measurements. Typically we refrained from using disks for measurements on non-magnetic samples, in order to avoid additional errors introduced by subtracting their corresponding two small signals.

Additional measurements of the high field DC magnetization of TbAgGe were carried out with a vibrating sample magnetometer in a 180 kG superconducting magnet (National High Magnetic Field Laboratory - Los Alamos Facility), whereas for measurements up to 140 kG performed on a number of samples we used the extraction magnetometer in a Quantum Design Physical Properties Measurement System (PPMS). For the former experiments the samples were glued to a thin quartz rod, similar to the previously described disk and straw mount which was used to align the samples in the latter case; occasionally, a longitudinal hole was drilled through the disk, which allowed us to mount the rods inside, for $H \parallel c$ measurements. This was particularly useful in cases where, in this field orientation, the samples were susceptible to large torques at the highest fields.

Angular dependent magnetization measurements have been performed on the TmAgGe, TbPtIn and $Ho_xY_{1-x}PtIn$ ($x \simeq 0.04$) compounds. For these measurements, the angular

position of the samples was controlled by a specially modified MPMS sample holder which allowed for the rotation of the sample so that either the [001], [100] or [120]-axis stayed perpendicular to the applied magnetic field. In order to avoid torque on the rotator due to the extreme anisotropy of the samples , small mass samples (*i.e.* m = [0.40 ± 0.05] mg in the case of TbPtIn, m = [0.54 ± 0.05] mg for TmAgGe, and m = [2.40 ± 0.05] mg for $Ho_xY_{1-x}PtIn$) were used for the angular dependent measurements. To correct for the larger relative weighing errors that result from such small masses, we used a 13.55 mg TbPtIn sample, a 2.40 mg TmAgGe sample, and a 35.0 mg $Ho_xY_{1-x}PtIn$ sample respectively, to measure *M(H)* curves for field along the primary crystallographic directions; the small-mass rotator data was normalized to the larger-mass data sets for the key directions. Whereas some errors are still introduced by this normalization due to the manual orientation of the large samples, the angular accuracy with which we are able to orient them is probably within 10^0. The various *M(H, θ)* measurements on the smaller samples were than calibrated using the data for the larger mass pieces; this is believed to be very accurate given that the angular uncertainty in the rotator is less than 1^0. There is additional uncertainty introduced by possible misalignment of the small piece with the c-axis exactly perpendicular or perpendicular to the applied field (due to the construction of the sample holder, this misalignment shouldn't be more than 10^0).

4.2.2 Resistivity measurements

The electrical resistance in zero and applied field was measured using a standard AC four-probe technique. These measurements were performed either in the QD PPMS-9 or 14 instrument using the ACT option, or using a Linear Research LR-700 AC resistance bridge (f = 16 Hz, I = 0.3 - 3 mA) in the magnetic field -temperature environment of the QD MPMS system. The He-3 option of the QD PPMS-14 allowed us, when necessary, to extend our transport measurements down to T = 0.4 K, whereas the minimum temperatures reached in all other instruments was close to 2 K, and the maximum used temperature was 300 K. Platinum wires were attached to the samples with Epotek H20E silver epoxy, and cured at 120^0 C for $\sim$ 30 minutes. Typical contact resistances were between 1 and 2 Ω. Since most samples were thin

hexagonal rods, the current was always flowing parallel to the c-axis; we therefore measured transverse ($H \perp i$) magnetoresistance when the field was applied within the basal plane, or longitudinal ($H \parallel i$) for field along the c-axis.

Hall resistivity measurements were performed on single crystals of YbAgGe, TmAgGe, LuAgGe and YbPtIn. The samples were polished down to a plate-like shape, and four Platinum leads were attached with silver epoxy. Except for the case of YbAgGe, the sample geometry also restricted the Hall resistivity measurements only to the field applied within the hexagonal crystallographic plane ($H \parallel ab$). The Hall resistivity ρ_H(H,T) was measured for field perpendicular to both the current and the Hall voltage directions. In order to minimize the inherent (small) misalignment of the voltage contacts, these measurements were taken for two opposite directions of the applied field, H and -H, and the odd component, (ρ_H(H) - ρ_H(-H))/2 was taken as the Hall resistivity.

4.2.3 Specific heat measurements

Specific heat measurements were made using the heat capacity option of the Quantum Design PPMS-9 or 14; as for the transport measurements, specific heat data was often collected for temperatures down to 2 K, but in some cases we used the He-3 option of the QD PPMS-14 system to reach temperatures down to 0.4 K. A relaxation technique was used for the specific heat measurements, in which the sample is briefly heated and then allowed to cool. The thermal response of the sample is then fit over the entire temperature response using a model that accounts for the thermal relaxation of both the sample and the sample platform. The samples were attached to the heat capacity platform with Apiezon N grease. The thermal response of the platform and grease was measured separately for the appropriate field and temperature ranges, to allow for the subtraction of this component from the final measurement. To achieve maximum accuracy within reasonable time constraints, the system was typically allowed to cool for two time constants. Thermal contact with the environment was minimized by evacuating the sample chamber to approximately 0.01 mTorr.

4.2.4 X-ray diffraction measurements

4.2.4.1 Room-temperature powder X-ray diffraction measurements

X-ray diffraction patterns were taken at room temperature on pulverized single crystals to verify whether any impurity phases were present in the samples and to determine/confirm the unit cell dimensions. A conventional tube source was used to obtain the patterns in flat plate geometry using CuKα (1.5406 $\AA$) radiation. Typical measurements consisted of scans with 2 θ between 20^0 and 90^0, data being recorded every 0.02^0. The collected data was subsequently analyzed using the Rietica Rietveld refinement program.

4.2.4.2 Single Crystal X-ray Diffraction

Single crystal X-ray diffraction measurements were performed on flux grown samples of RPtIn, R = Tb, Tm and Yb, and an on-line grown YbPtIn single crystal. Small single crystals (with typical sizes around 2 $\times$ 5 $\times$ 10 μm^3) were extracted from the flux and on-line grown samples. Room-temperature X-ray diffraction data were collected on a STOE IPDSII image plate diffractometer with MoKα radiation, and were recorded by taking 1^0 scans in θ in the full reciprocal sphere. The range of 2 θ extended from 6^0 to 63^0. Numerical absorption corrections for both crystals were based on crystal face indexing, followed by a crystal shape optimization. Structure solution and refinement were done using the SHELXTL program.

CHAPTER 5. Thermodynamic and transport properties of the RAgGe (R = Tb - Lu) single crystals*

5.1 Introduction

Ternary intermetallic compounds R-T-M, with R = rare earth metals, T = transition metals, M = metals of the p block, have raised a lot of interest in the past years, given their structural complexity and their greatly varying physical properties. Studies of the anisotropic properties of such materials, with the R in tetragonal point symmetry, revealed anisotropy (in some cases extreme) in members of the $RAgSb_2$ (Myers, 1999b) and RNi_2Ge_2 (Bud'ko, 1999) series, as well as in the well known quaternary RNi_2B_2C compounds, for R=Tb-Er (Canfield, 1997b; Cho, 1995; Cho, 1996a,b; Canfield, 1998). The strong crystalline electric field (CEF) anisotropy confines the moments either along the c-axis of the tetragonal unit cell (*i.e.*, in $TbNi_2Ge_2$, $ErAgSb_2$, $TmAgSb_2$), or to the basal plane ab (in $ErNi_2Ge_2$, $DyAgSb_2$ and the aforementioned RNi_2B_2C compounds), and metamagnetic transitions occur in the majority of these materials..

In addition to metamagnetism, hybridization of the $4f$ moments occurs in some compounds, making these tetragonal series even more interesting: $YbNi_2B_2C$ (Yatskar, 1996), $CeNi_2Ge_2$ (Bud'ko, 1999; Knopp, 1988), $YbNi_2Ge_2$ (Bud'ko, 1999) are reported to have significant hybridization between the 4f and the conduction electrons.

Having achieved a basic understanding of the physical properties of these tetragonal compounds, in which the R^{3+} ions are positioned in crystallographically unique tetragonal point symmetry sites, we anticipate that materials with different crystal structure would be of further

*after "Thermodynamic and transport properties of RAgGe (R = Tb - Lu) single crystals", E. Morosan, S. L. Bud'ko, P. C. Canfield, M. S. Torikachvili and A. H. Lacerda, J. Magn. Magn. Mater. 277 298 (2004).

interest. Crystals with hexagonal unit cells preserve the axial versus basal plane anisotropy while allowing for three R point symmetries: orthorhombic, trigonal or hexagonal. A representative of the first class of materials (*i.e.*, orthorhombic point symmetry) is the RAgGe series, that crystallizes in the ZrNiAl structure, an ordered variant of the Fe_2P structure.

In this chapter we will present detailed experimental results of magnetization, magneto-transport and specific heat measurements for each compound. We will start with LuAgGe as the non-magnetic member of the series, and then progress from R = Tb through Yb. The experimental section is followed by a brief discussion, where we will emphasize the observed trends in the magnetic properties within the series, as well as a few outstanding questions we are presently trying to address.

5.2 Results and analysis

5.2.1 LuAgGe

LuAgGe has electronic and magnetic properties consistent with a weakly diamagnetic intermetallic compound with no magnetic order.

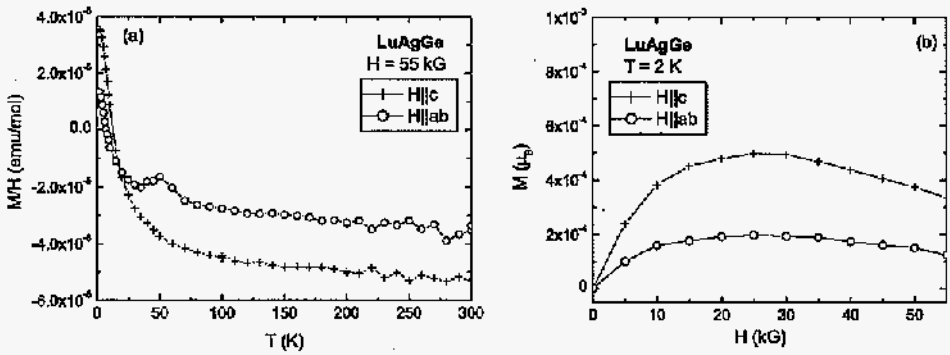

Figure 5.1 (a) Anisotropic temperature-dependent susceptibility and (b) anisotropic magnetization isotherms at T=2K of LuAgGe.

The magnetization as a function of temperature (Fig. 5.1a) is almost constant, with a very small, average, high temperature values around -2.3× 10^{-5} emu/mol ($H \parallel ab$), and -5× 10^{-5} emu/mol ($H \parallel c$) respectively. At low temperatures, an upturn in the susceptibility data occurs, which could be a consequence of some magnetic impurities being present in the original materials (*e.g.*, the tail indicates a magnetic impurity contamination equivalent to 0.2% Gd). Field dependent magnetization curves for the two orientations of the field are shown in Fig. 5.1b; as expected for a non-magnetic compound with some magnetic impurities, the magnetization is a superposition of Brillouin saturation of the impurities with applied field, and a weak diamagnetic signal.

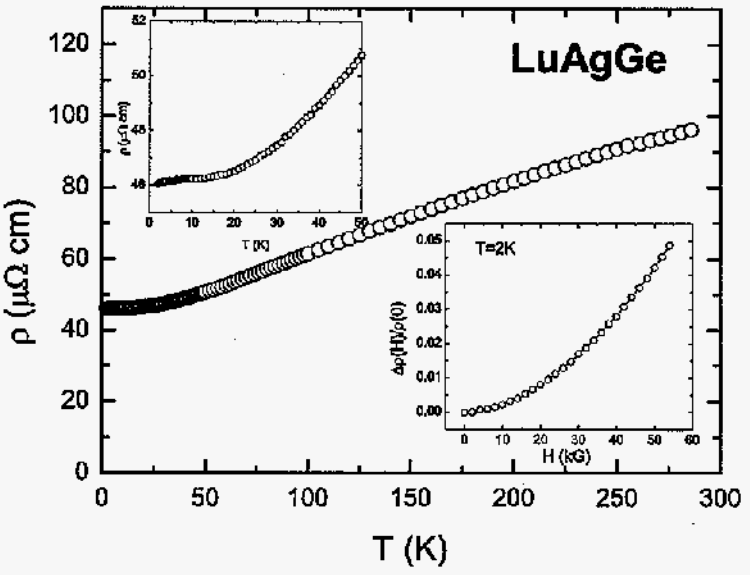

Figure 5.2 Zero-field resistivity and transverse magnetoresistance (lower right inset) of LuAgGe.

The temperature dependent resistivity of LuAgGe (Fig. 5.2) demonstrates the metallic character of this compound. Below ~50K, the impurity scattering becomes dominant, with a relatively large residual resistivity $\rho(1.8K) \approx 45\ \mu\Omega\ cm$, resulting in a relatively poor

RRR of about 2, far smaller than the RRR values found in the rest of the series. The upper inset to Fig. 5.2 shows that there is no clear resistance minimum found in LuAgGe at low temperature. This is important to note given that for the R = Tb - Tm members of the RAgGe series do manifest a minimum in the temperature dependent resistivity for temperatures well above their respective Néel temperatures. The lower inset to Fig. 5.2 presents the transverse magnetoresistance, which varies approximately as H^2, as expected for normal metals.

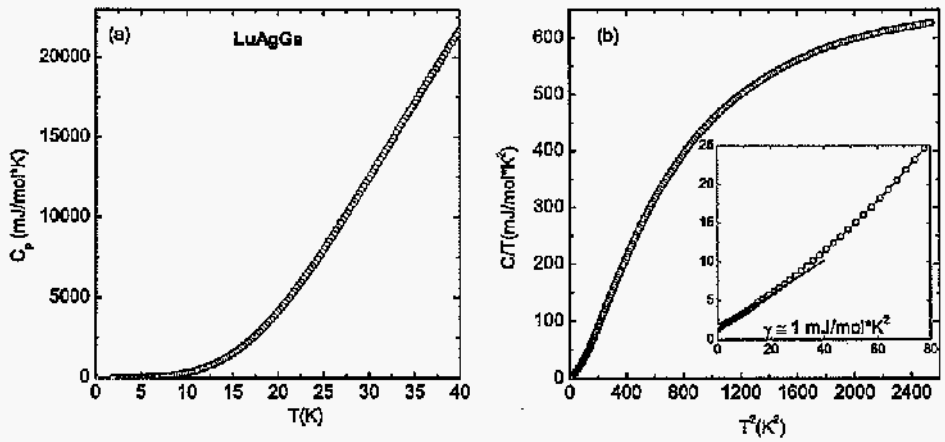

Figure 5.3 (a) Heat capacity of LuAgGe; (b) C_p/T versus T^2 for LuAgGe; insert: low temperature part, line in the inset is a linear fit at low temperatures.

Finally, we have measured the specific heat C_P as a function of temperature (Fig. 5.3a). These data will be used as an estimate of the non-magnetic contribution to the specific heat in all RAgGe, R = Tb - Yb. As calculated from the linear fitting of the low-temperature C_P / $T(T^2)$ data (Fig. 5.3b), the electronic specific heat coefficient for the non-magnetic LuAgGe compound is: $\gamma = (1.37 \pm 0.02)$ mJ / mol*K^2 whereas $\Theta_D \approx 300$ K.

5.2.2 TbAgGe

The anisotropic, inverse susceptibility as a function of temperature for TbAgGe is shown in Fig. 5.4, together with the calculated polycrystalline average. The inset presents the low temperature region of the susceptibility for the applied field $H = 1$ kG parallel and perpendicular to the c-axis. The inverse susceptibility above ~ 50 K is consistent with Curie-Weiss behavior of the magnetization: $\chi(T) = C / (T + \Theta_W)$, where Θ_W is the paramagnetic Weiss temperature. The values of Θ_W for the two orientations of the field, as well as for the polycrystalline average, are listed in Table 5.1 in the discussion section. A linear fitting of the average inverse susceptibility in the paramagnetic state gives a value of the effective moment $\mu_{eff} = 9.7\ \mu_B$, which is close to the theoretical value for Tb^{3+} of $9.72\ \mu_B$.

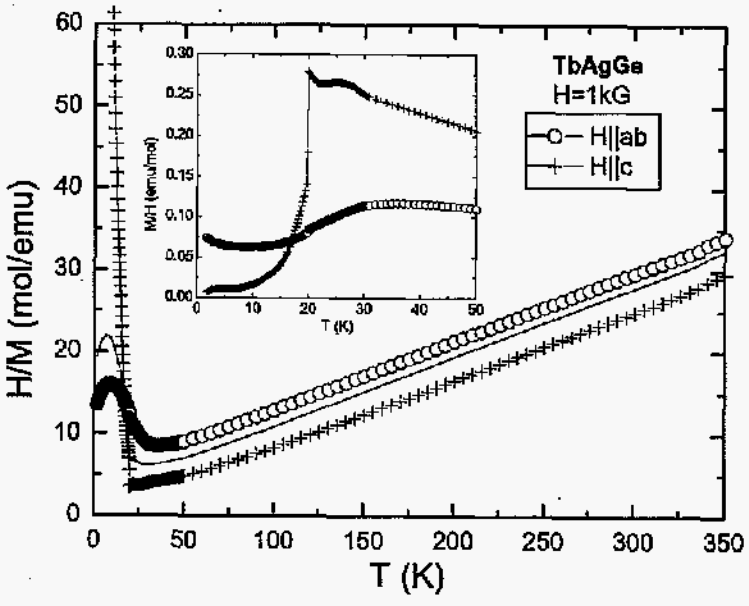

Figure 5.4 Anisotropic inverse susceptibilities of TbAgGe and calculated average (line); inset: low-temperature anisotropic susceptibilities.

The low temperature susceptibility for $H = 1$ kG (shown as an inset in Fig. 5.4) indicates

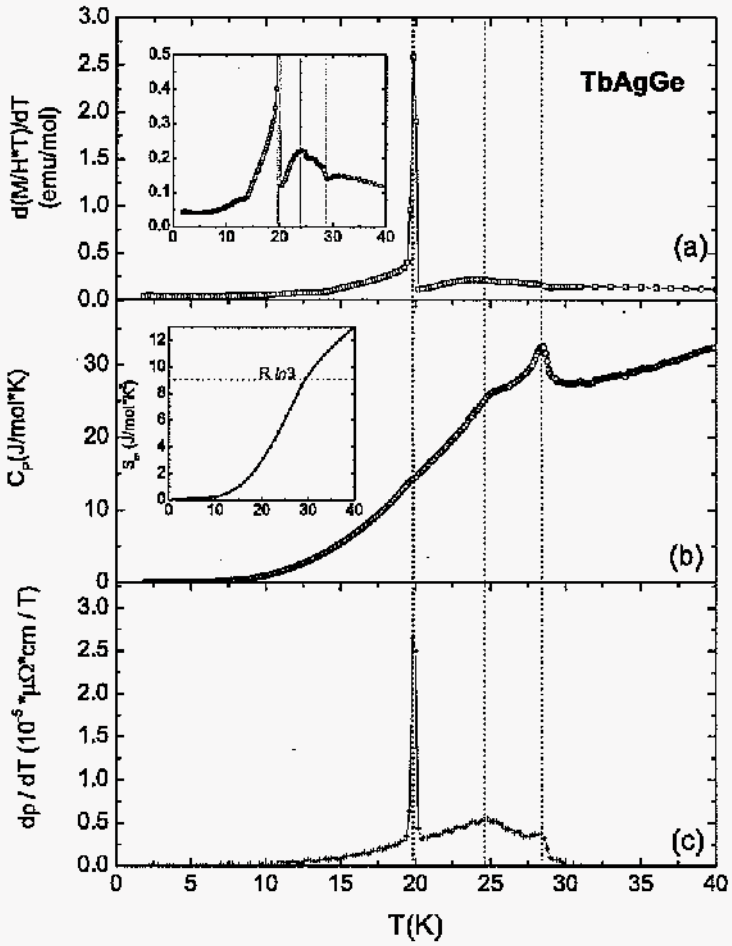

Figure 5.5 (a)Low-temperature $d(\chi T)/dT$ for TbAgGe (inset: enlarged to show lower peaks' position in $d(\chi T)/dT$); (b) specific heat $C_P(T)$ with the magnetic entropy S_m in the inset; (c) low-temperature $d\rho/dT$; dotted lines mark the peak positions as determined from (a).

antiferromagnetic ordering below the Néel temperature $T_N = 28.4$ K. This transition temperature, as well as two others are seen more clearly for $H \parallel c$ and can also be identified in $d(\chi T) / dT$ (around 28.5 K, 24.7 K and 19.8 K respectively) and $d\rho / dT$ (at 28.4 K, 24.6 K and 19.8 K) (Fig. 5.5a and c); in $C_P(T)$ (Fig. 5.5b) only the higher two transitions are visible, around 28.3 K and 24.7 K respectively. Another possible change in slope in $M(T) / H$ occurs around 18 K, but it is obscured in all other measurements, and is therefore unclear if it can be associated with another magnetic transition. However, in the $H_c(T)$ phase diagram for $H \parallel c$ (shown below), we can follow a phase boundary indicative of such a transition.

Specific heat data was also used to estimate the magnetic entropy $S_m(T)$, shown in Fig.5.5b, inset. From these data it can be inferred that the ordered state in TbAgGe is emerging out of triplet ground state, or there are at least a combination of a singlet and a doublet, or three singlet states closely spaced.

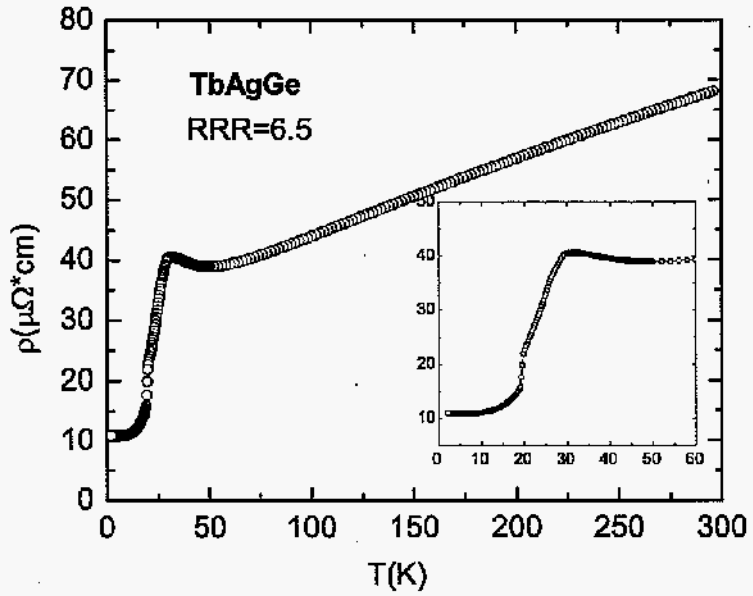

Figure 5.6 Zero-filed resistivity of TbAgGe (inset: enlarged low-temperature part).

At high temperatures, the resistivity measurements (Fig. 5.6) indicate the metallic character of TbAgGe as ρ monotonically decreases with decreasing T. The residual resistivity ratio RRR, calculated as $\rho(300K)$ / $\rho(2K)$ and equal to 6.5, indicates fair crystal quality. The low temperature region of the resistivity measurements features slope changes associated with the magnetic transitions discussed above. On the other hand, there is a clear minimum of the $\rho(T)$ curve around $T \approx 50$ K. This minimum in resistivity occurs far above the Néel temperature (around 2^*T_N), which rules out the possibility of a superzone gap causing this feature, and, as will be seen below, occurs for all other local moment-bearing members of the series. This feature could be explained by magnetic fluctuations or some other, as of yet to be identified, mechanism.

Based on all the measurements performed on single crystals of TbAgGe, we can identify at least three transitions, at T = (28.4 ± 0.1) K, (24.65 ± 0.05) K and (19.8 ± 0.1) K; the lowest two temperatures are very close to those reported in Baran (Baran, 1998) for the polycrystalline samples (from magnetization and neutron diffraction measurements) as the only transitions. We are thus led to believe that the highest (antiferromagnetic) transition temperature, as well as any other possible ordering temperatures, was not detected by the measurements made on polycrystalline samples.

Both resistivity (Fig. 5.7a) and magnetization measurements (Fig.5.7b) as function of applied field provide evidence for a series of metamagnetic transitions in TbAgGe. Initial field dependent magnetization and resistivity measurements up to $H = 70$ kG reveal at least two metamagnetic transitions for critical fields $H_c \approx 20$ kG, and 48 kG respectively, when field is applied along the c-axis. Given that the system seemed to be far below saturation ($M(70kG) = 2.77\ \mu_B$/Tb $\ll 9\mu_B$/Tb), further magnetization measurements were performed for fields up to 180 kG and several other metamagnetic transitions were observed. (It should be noted that there is clear indication of hysteresis as manifested by the difference in $M(H)$ for increasing and decreasing field measurements [inset, Fig. 5.7b]). The value of the magnetization at 180 kG is $M = 7.78\ \mu_B$/Tb, still below the calculated value for $\mu_{sat}(Tb^{3+}) = 9.0\ \mu_B$. This somewhat suppressed value of M could be consistent with more metamagnetic states

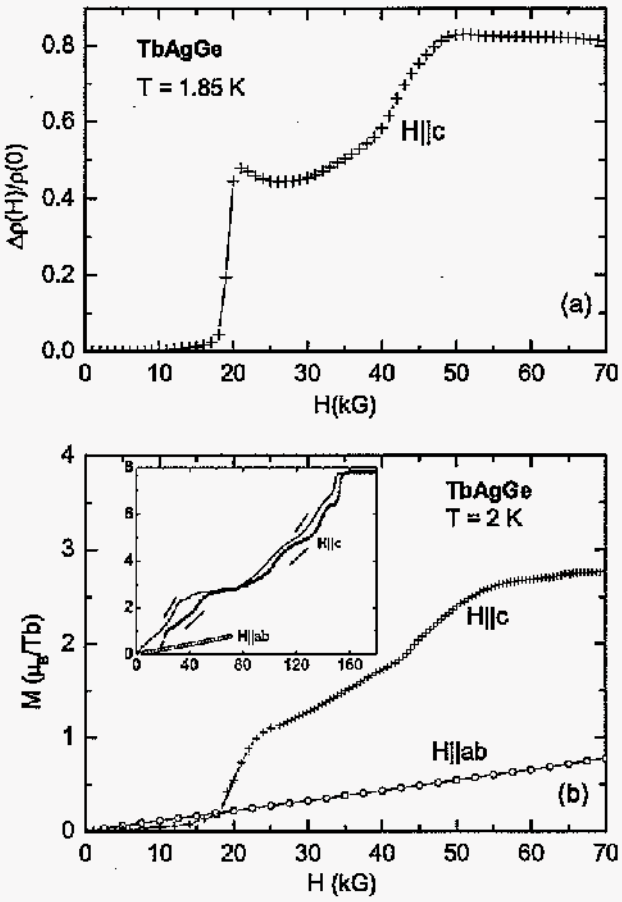

Figure 5.7 (a) Transverse magnetoresistance for TbAgGe; (b) Anisotropic M(H) curves for fields up to 70 kG (inset: axial magnetization up to 180 kG).

beyond 180 kG, or with moments alignment at some angle $\phi \neq 0$ with respect to the c-axis, or may simply be a caliper of the uncertainty in the absolute value of M in this high field measurement.

In order to better determine the number and extent of metamagnetic phases that exist for TbAgGe when $H \parallel c$, more measurements were done (Fig. 5.8a,b), which allowed us to plot a tentative $H_c(T)$ phase diagram shown in Fig. 5.9. Local maxima of $d(\chi T) / dT$ or dM / dH

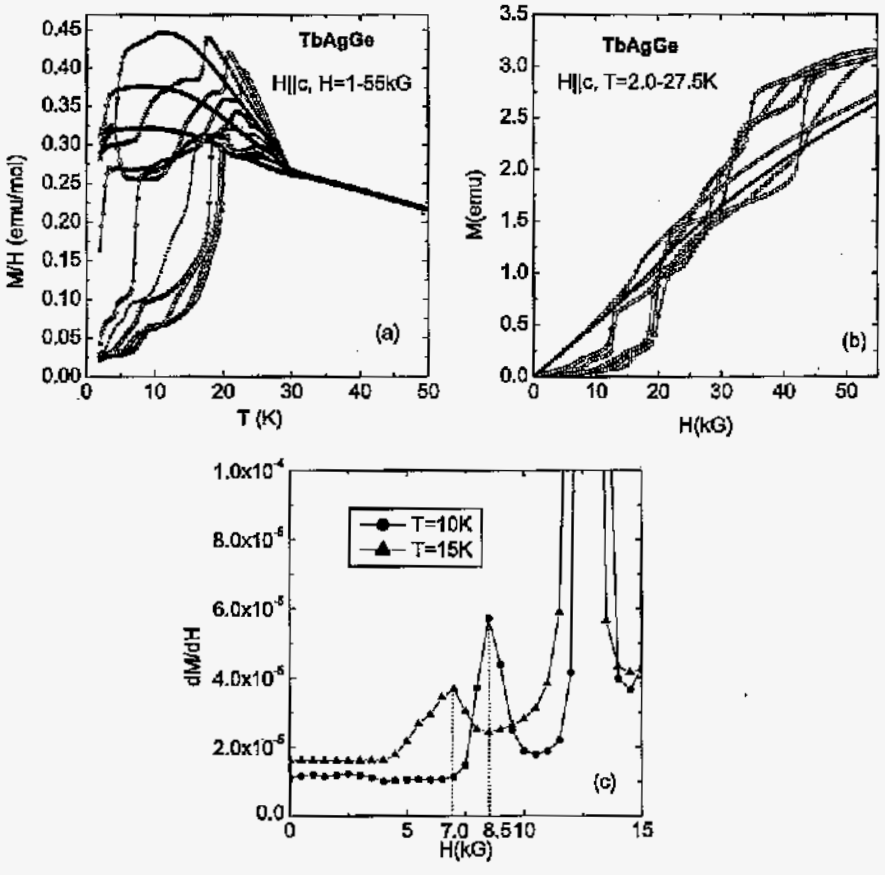

Figure 5.8 $\chi(T)$ curves for various (1, 2.5, 5, 7.5, 10, 12.5, 15, 20, 25, 30, 35, 45, 55 kG) fields (a) and several $M(H)$ (T = 2, 3, 4, 6, 10, 20, 25, 27, 50 K) isotherms (b); (c) - enlarged derivatives of $M(H)$ (for T = 10 K and 15 K) as an example of how the lower line in the phase diagram was obtained.

were used to estimate the H_c and T_c values, as illustrated in Fig. 5.8c. Numerous phases can be observed. Whereas Fig. 5.9 clearly shows the three, $H = 0$, transition temperatures discussed above, it also shows a lower field and temperature phase line existing for finite applied fields. Figure 5.8c illustrates that this lowest phase line is clearly detected in our $M(T, H)$ data. A remaining question associated with this phase diagram is whether this lowest phase

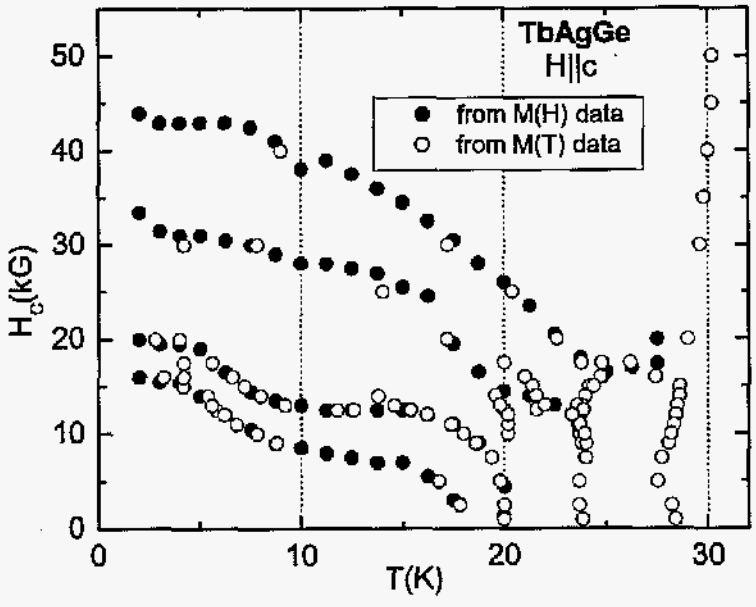

Figure 5.9 $H_c - T$ phase diagram as determined from the magnetization curves in Fig. 5.8.

line intersects the $H = 0$ axis at any finite temperature or flattens out at very low fields such that it intersects $H = 0$ at $T \approx 20$ K, where another transition already exists.

5.2.3 DyAgGe

Although DyAgGe in the paramagnetic state is more isotropic than TbAgGe, with slightly larger susceptibility for $H \parallel c$ than for $H \parallel ab$ (Fig. 5.10), it has an extremely anisotropic ordered state (as seen in Fig. 5.10a inset, for $H = 1$ kG); this low temperature anisotropy is further enhanced for lower (0.1 kG) applied fields (Fig. 5.10b). Two transition temperatures are detected by $d(\chi T) / dT$ (at 14.4 and 12.0 K), $d\rho / dT$ (at 14.4 K, and 12.0 K) and $C_P(T)$ (at 14.6 K and 12.1 K) (Fig. 5.11). These are in agreement with the temperatures determined by earlier measurements on polycrystalline samples (Gibson, 1996; Baran, 1998). There is one more, broader, lower temperature peak in Fig. 5.11a, not visible in any other measurement.

But comparison of $d(\chi\ T)\ /\ dT$ plots for two different applied fields (Fig. 5.11a, $H = 0.1$ kG and $H = 1$ kG) seems to indicate that the low temperature peak is moving down in T rapidly as the applied field increases, whereas the other two are unaffected by the change in H.

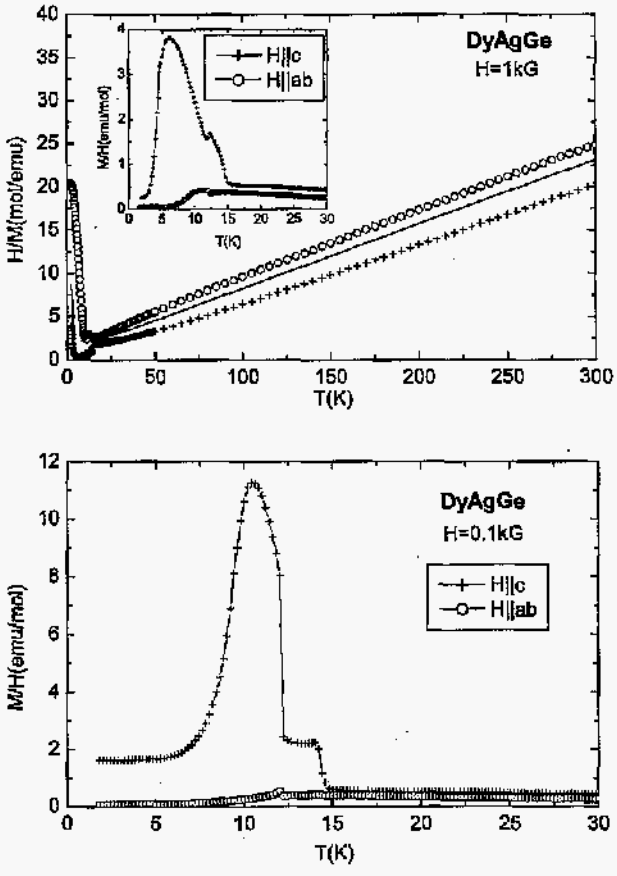

Figure 5.10 (a) Anisotropic inverse susceptibilities of DyAgGe and calculated average (line) at H=1kG; inset: low-temperature anisotropic susceptibilities; (b) low-temperature anisotropic susceptibilities for H=0.1kG.

In order to examine the low temperature state of DyAgGe more carefully 0.1 kG zero-field-cooled-warming (ZFC) and field-cooled warming (FC) data sets were taken and are plotted in Fig. 5.12. These data are consistent with an ordered state below 12.0 K that has a net

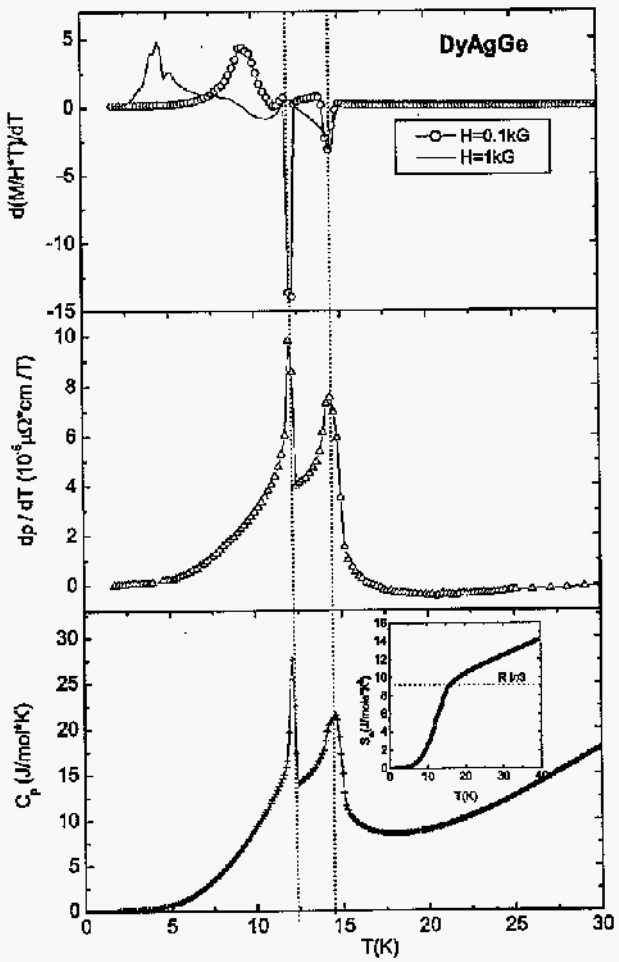

Figure 5.11 (a) Low-temperature $d(\chi T)/dT$ for DyAgGe for H=0.1kG and 1kG; (b) low-temperature $d\rho/dT$; (b) specific heat $C_p(T)$ with the magnetic entropy S_m in the inset; dotted lines mark the peak positions as determined from lowest field data in (a).

ferromagnetic component along the c-axis. The broadness and the field sensitivity of the lowest temperature peak in Fig. 5.11a, as well as the difference between the ZFC and FC data sets shown in Fig. 5.12 are consistent with the rotation of domains in small applied fields. It should also be noted that the magnetization associated with the lowest temperature point of the FC curve shown in Fig. 5.12 corresponds to $M \sim 0.66\ \mu_B$/Dy, the value associated with the low field plateau of the $M(H)$ plot shown in Fig. 5.13. This further supports the idea that below $T \sim 12$ K the magnetically ordered state of DyAgGe has a net ferromagnetic component along the c-axis.

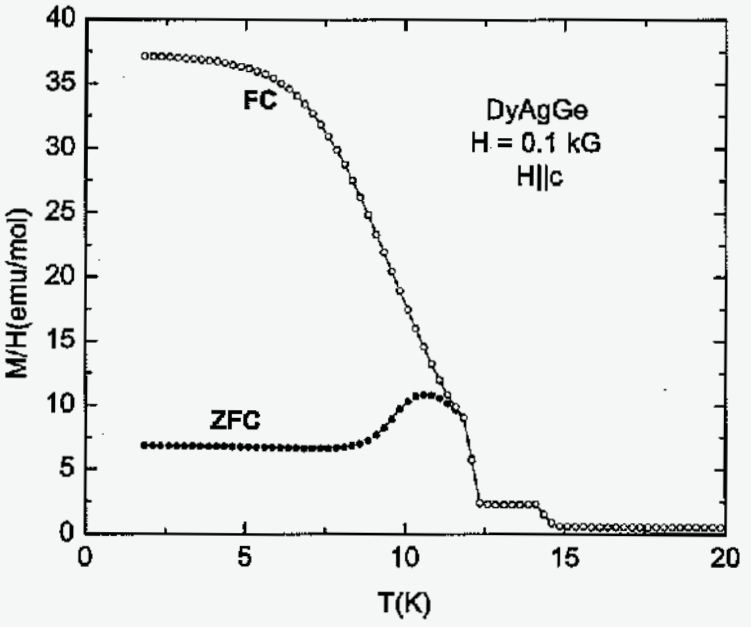

Figure 5.12 ZFC-FC magnetization of DyAgGe, H=0.1kG ($H \| c$).

The linear behavior of the inverse susceptibility above $\sim$ 50 K (Fig. 5.10a) is indicative of Curie-Weiss like susceptibility, the effective magnetic moment determined from the linear region being $\mu_{eff} = 10.3\ \mu_B$ (in good agreement with the theoretical value for Dy^{3+}, which is 10.6 μ_B). Paramagnetic Weiss temperatures Θ_W are listed in Table 5.1.

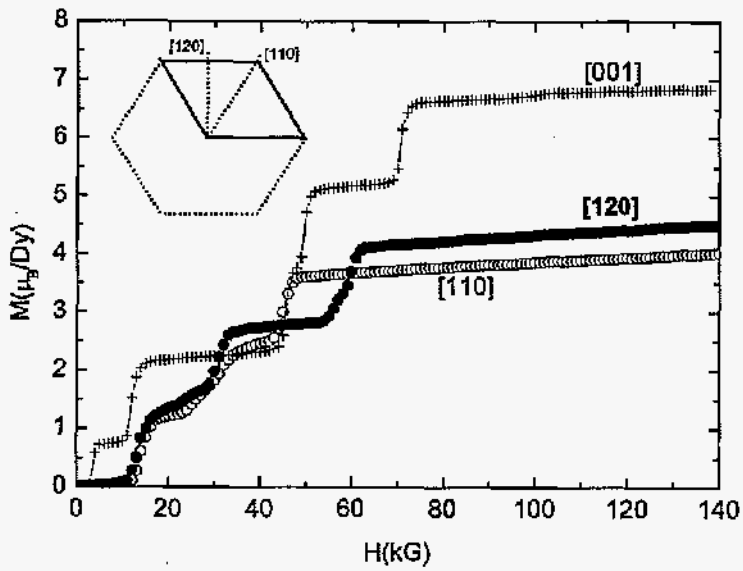

Figure 5.13 Anisotropic magnetization curves shown for three orientations of the applied field.

The resistance of DyAgGe increases linearly with temperature above 50 K (Fig. 5.14a). At low temperatures, the resistivity has a local minimum around 30 K, followed by a sharp drop around the transition temperature; this indicates loss of spin disorder scattering as the system enters the ordered state. The residual resistivity ratio RRR is approximately 5.2.

Field dependent magnetization measurements indicate a complex metamagnetism in DyAgGe, as shown in Fig. 5.13: transitions can be seen in all three orientations of the applied field ($H \parallel [001]$, $H \parallel [120]$ and $H \parallel [010]$), which probably means that, in the saturated state, the magnetic moments are inclined at some angle $0^0 < \varphi < 90^0$ with respect to the c-axis. This could justify the low magnetization values (below the theoretical value $\mu_{sat}(Dy^{3+}) = 10\ \mu_B$) in all three directions even at the highest applied field, as we explain in more detail in the discussion section.

The critical fields for the metamagnetic transitions are $H_c \approx 14$ kG, 31 kG, 45 kG for

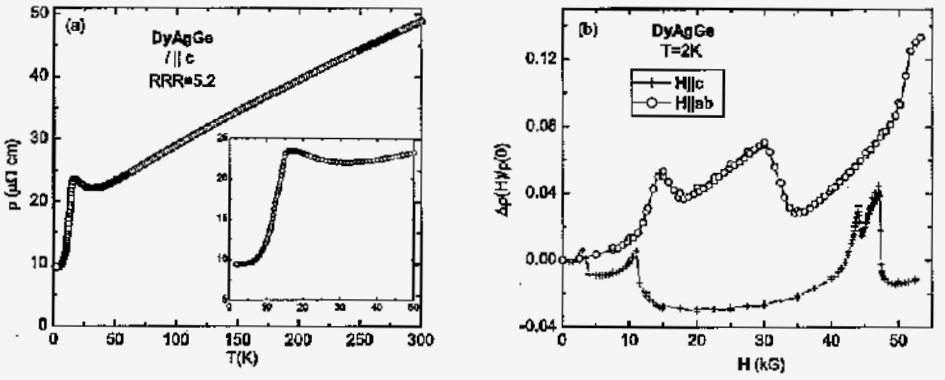

Figure 5.14 (a) Zero-filed resistivity of DyAgGe (inset: enlarged low-temperature part); (b) Anisotropic magnetoresistance at T = 2 K.

$H \parallel$ [120], 13 kG, 31 kG, 60 kG for $H \parallel$ [010], and 3 kG, 12 kG, 46 kG, 50 kG, 71 kG for $H \parallel c$ respectively where it should be noted that for $H \parallel c \sim 3$ kG the transition is thought to be associated with domain rotation (as discussed above). These values can also be seen in the $R(H)$ curves, shown in Fig. 5.14b for $H \parallel c$ and $H \perp c$, except for the ones beyond 55 kG, which was the upper field limit for this magnetoresistance measurement. Once metamagnetism of planar moments is better understood (see discussion section on metamagnetism in TmAgGe below) the study of the angular dependence of metamagnetism in DyAgGe, a system with highly anisotropic but non-planar, non-axial moments, should be interesting and hopefully tractable.

5.2.4 HoAgGe

The susceptibility of HoAgGe in the paramagnetic state is almost isotropic, as can be seen in Fig. 5.15. For temperatures higher than 50 K the susceptibility follows the Curie-Weiss law $\chi(T) = C / (T + \Theta_W)$; the corresponding paramagnetic temperatures Θ_W are given in Table 5.1. From the linear fit of the inverse susceptibility (for the polycrystalline average) we

get an effective moment $\mu_{eff} = 10.0\mu_B$, close to the theoretical value $\mu_{eff}(Ho^{3+}) = 10.6\mu_B$. The compound orders antiferromagnetically below Néel temperature T_N=11.0K, whereas a spin reorientation transition occurs around T=7.4K. Although T_N shows up as a sharp, well-defined peak in all three plots in Fig. 5.16, the lower transition temperature is indicated by broader peaks in $d(\chi\ T)\ /\ dT$ around 7.4K (Fig. 5.16a), and in $d\rho/dT$ around 8.0K (Fig. 5.16c); specific heat plot shown in Fig. 5.16b seems to have an even broader feature close to these temperatures. It should be noted that, as in the case of TbAgGe, the measurements on polycrystalline samples (Baran, 1998) missed a transition (*e.g.*, the lower one for HoAgGe), whereas the reported temperature of the upper transition falls close to our measured value.

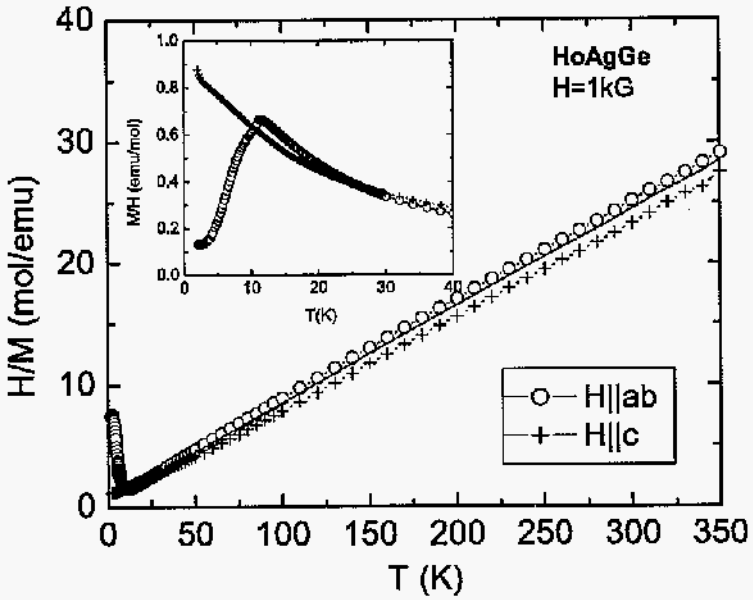

Figure 5.15 Anisotropic inverse susceptibilities of HoAgGe and calculated average (line); inset: low-temperature anisotropic susceptibilities.

The temperature dependent resistivity measurement (Fig. 5.17) demonstrates the metallic character of this compound and the residual resistivity ratio for HoAgGe is RRR=4.0. At a

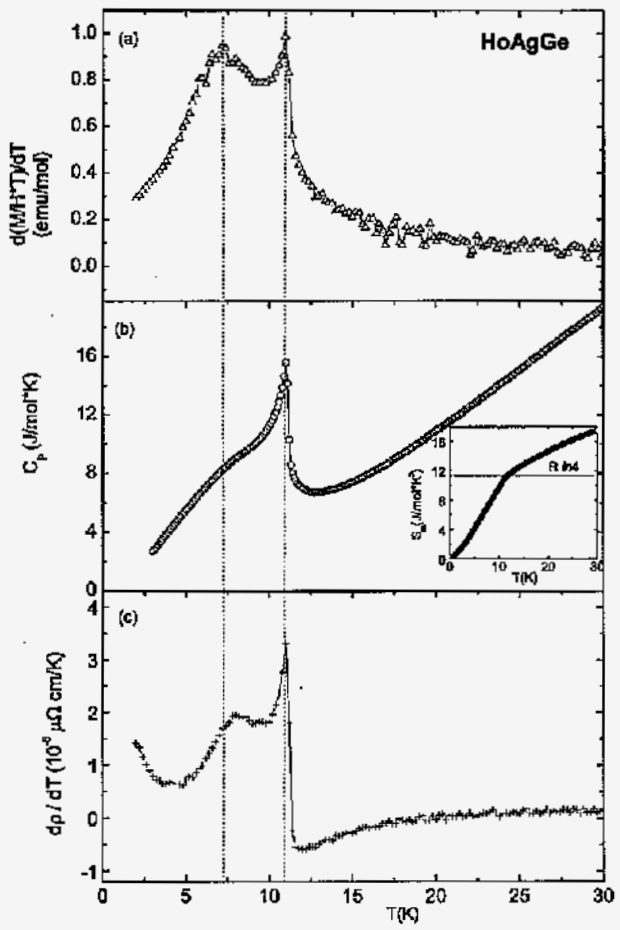

Figure 5.16 (a) Low-temperature $d(\chi T)/dT$ of HoAgGe; (b) Specific heat $C_p(T)$ with the magnetic entropy S_m in the inset; (c) low-temperature $d\rho/dT$; dotted lines mark the peak positions as determined from (a).

temperature of about 19K a broad minimum in $\rho(T)$ is observed, and a drop in resistivity due to the loss of spin disorder scattering in the magnetically ordered phase.

From the specific heat measurements shown in Fig. 5.16b we calculated the magnetic entropy S_m of this compound (shown in the inset); the value of the entropy, $S_m \approx R\ln 4$, at the change in slope that occurs around the ordering temperature suggests that the magnetic

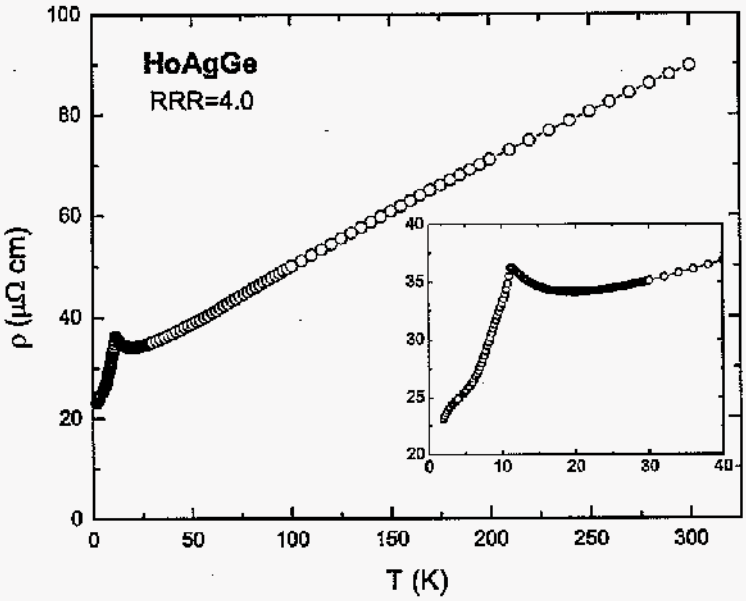

Figure 5.17 Zero-field resistivity of HoAgGe (inset: enlarged low-temperature part).

order in HoAgGe emerges out of state with a degeneracy of 4.

The magnetization curves as a function of applied field (Fig. 5.18a) reveal a series of metamagnetic transitions for H applied in the ab-plane, with critical field values of around 11.0kG, 22.0kG and 35.0kG for $H \parallel [010]$, and 12.0kG, 23.0kG and 28.0kG respectively for $H \parallel [120]$, whereas when H is applied along the c-axis the magnetization curve can either be a broad metamagnetic transition or a continuous spin-flop transition. The theoretical value of the saturated magnetization expected for Ho^{3+} ($\mu_{sat} = 10\mu_B$) is not reached by fields up to 140kG in any of the three orientations; as mentioned before, this can be due to the moments being along an inclined axis with respect to the c-axis of the crystals, or further support the idea of the spin-flop transition, especially given the continuous increase in magnetization as H is being increased. Another possible explanation, which we detail for TmAgGe, is related to

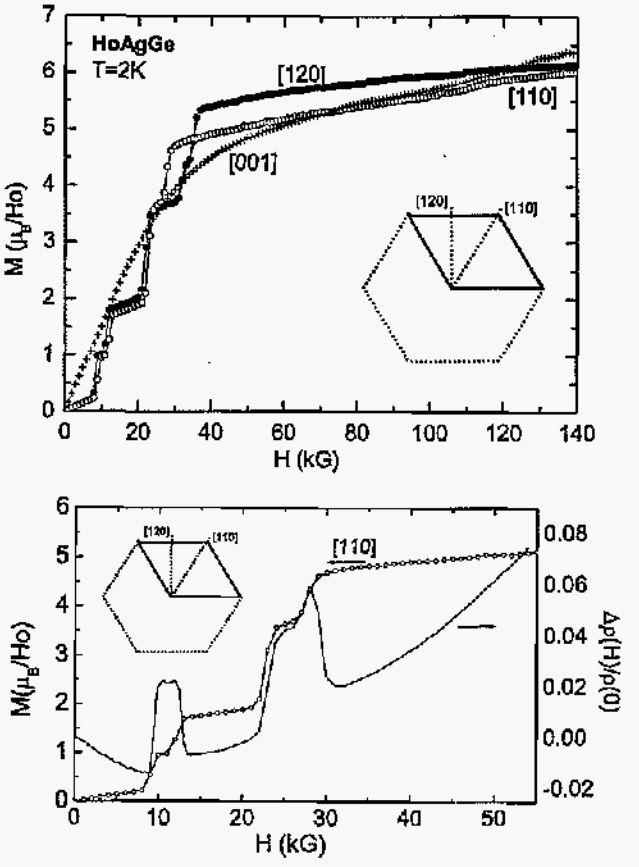

Figure 5.18 (a) Anisotropic magnetization curves in HoAgGe, shown for three orientations of the applied field at T=2K; (b) Transverse magnetoresistance and $M(H)$ for $H\|[120]$ at T=2K.

the crystal structure of these compounds and will be discussed below.

We have also measured magnetoresistance for $H \parallel ab$ (Fig. 5.18b), and it is consistent with the various metamagnetic states seen in $M(H)$. Given the geometry of the crystals, there was more uncertainty in orienting the resistance pieces than the ones for magnetization measurements; consequently, we can infer the approximate orientation of the field in the magnetoresistance measurement by comparison of these data with the $M(H)$ curves for $H \parallel ab$:

since various features in $\Delta\rho(H)/\rho(0)$ occur close to the critical fields in $M([120])$ (Fig. 5.18b), it seems that H was almost parallel to the [120] direction.

5.2.5 ErAgGe

So far in the RAgGe series, we have seen a progression from axial anisotropy in TbAgGe toward $M_{ab} \sim M_c$ for HoAgGe. ErAgGe continues this trend with the local Er moments becoming far more planar in nature (Fig. 5.19). This is analogous to the trend seen in many tetragonal systems (Myers, 1999b; Bud'ko, 1999), in which the change in sign of the B_{20} CEF parameter causes a switch from planar to axial moments between Ho and Er (Wang 1971; Boutron 1973).

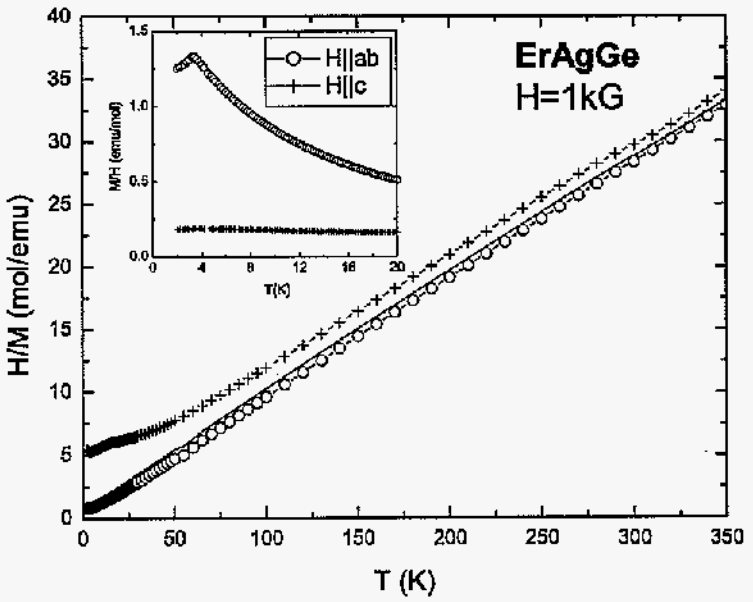

Figure 5.19 Anisotropic inverse susceptibilities of ErAgGe and calculated average (line); inset: low-temperature anisotropic susceptibilities.

The inverse susceptibility of ErAgGe is linear above 75K, with $\mu_{eff} = 9.3\mu_B$, fairly close

to the theoretical value of $9.6\mu_B$ for Er^{3+}. The anisotropic Weiss temperatures Θ_W are given in Table 5.1. For a 1 kG field applied parallel to the *ab*-plane, magnetic ordering is observed below 3 K (inset, Fig. 5.19); a smaller feature seems to indicate the same ordering temperature for field applied parallel to the *c*-axis.

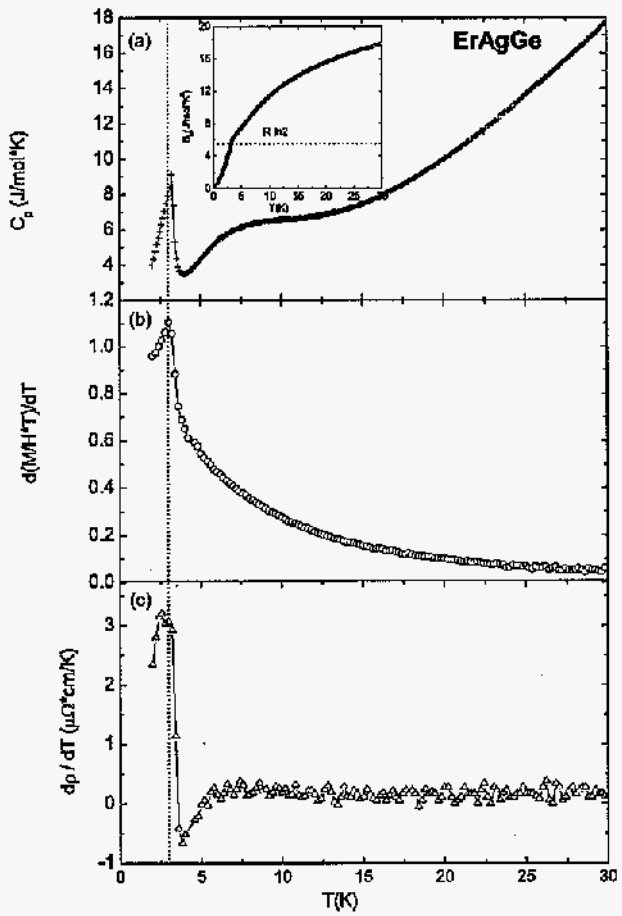

Figure 5.20 (a) Specific heat $C_p(T)$ with the magnetic entropy S_m in the inset; (b) low-temperature $d(\chi T)/dT$ of ErAgGe; (c) low-temperature $d\rho/dT$; dotted line mark the peak position as determined from (b).

The temperature dependent resistivity is consistent with local moment ordering and man-

ifests a local maximum in $d\rho$ / dT at 3 K (Fig. 5.20c). Below the ordering temperature a decrease in resistivity (Fig. 5.21) corresponds to the loss of spin-disorder scattering, as the magnetic moments become antiferromagnetically ordered. The high temperature resistivity is typical of intermetallic compounds, increasing up to $\sim$ 100 $\mu\Omega$ cm at T = 300 K, and leading to a RRR value of $\sim$ 3.0. The increasingly ubiquitous local minimum in the resistivity can still be observed above T_N, centered near $T \sim 6$ K. In Fig. 5.20a the specific heat shows a well-defined peak at $T \approx 3.2$ K, very close to the temperature of the maximum in $d(\chi T)$ / dT (Fig. 5.20b). The inset is a plot of the magnetic entropy of ErAgGe, where the break in slope around $S_m \approx R \ln 2$ indicates that the ground state of this compound is a Kramers doublet.

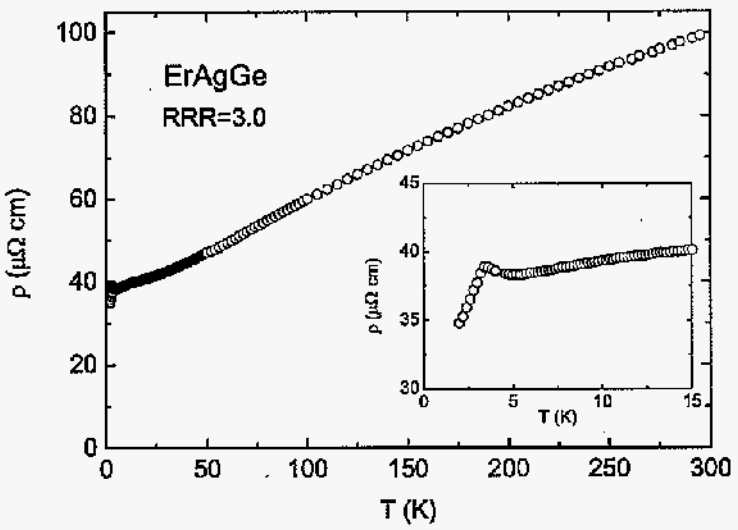

Figure 5.21 Zero-field resistivity of ErAgGe (inset: enlarged low-temperature part).

In the $M(H)$ plots (Fig. 5.22a) we again see clear anisotropy, with the moments somewhat constrained to the basal plane. For field applied along the c direction, magnetization linearly increases with field, up to $H \approx 50$ kG; right before the maximum applied field H = 55 kG, an upturn in the $M(H)$ curve is apparent, possibly indicating a subsequent metamagnetic

transition. When field is applied parallel to the ab-plane, we see a broad, poorly defined metamagnetic transition, as our measurements are being taken at $T = 2$ K, close to T_N of this compound. The magnetoresistance for $H \parallel ab$ (Fig. 5.22b) shows a local maximum around $H = 11$ kG, which further indicates the presence of a metamagnetic transition for this critical field.

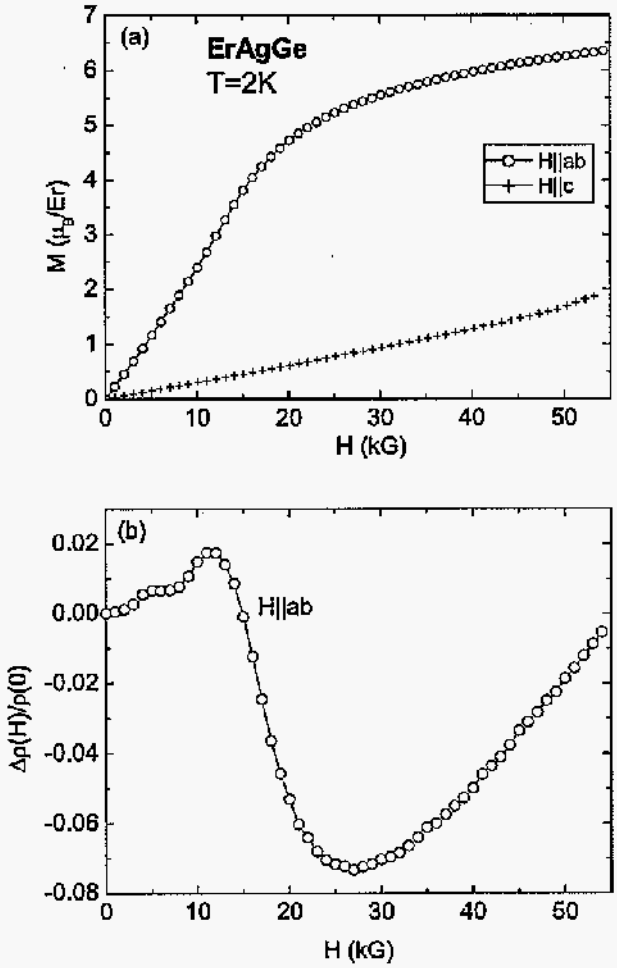

Figure 5.22 (a) Anisotropic field-dependent magnetization for ErAgGe at $T = 2$ K; (b) transverse magnetoresistance at $T = 2$ K.

5.2.6 TmAgGe

Magnetization measurements with field applied perpendicular and parallel to the c-axis (Fig. 5.23) indicate extreme anisotropy in TmAgGe: χ_{ab} / χ_c $\approx$ 30 at T = 5.0 K. This temperature was chosen just above the antiferromagnetic ordering temperature T_N $\approx$ 4.2 K. Above $\sim$ 100 K, inverse susceptibilities are linear with μ_{eff} = 7.9 μ_B, close to the theoretical value of $\mu_{eff}(\mathrm{Tm}^{3+})$ = 7.6 μ_B.

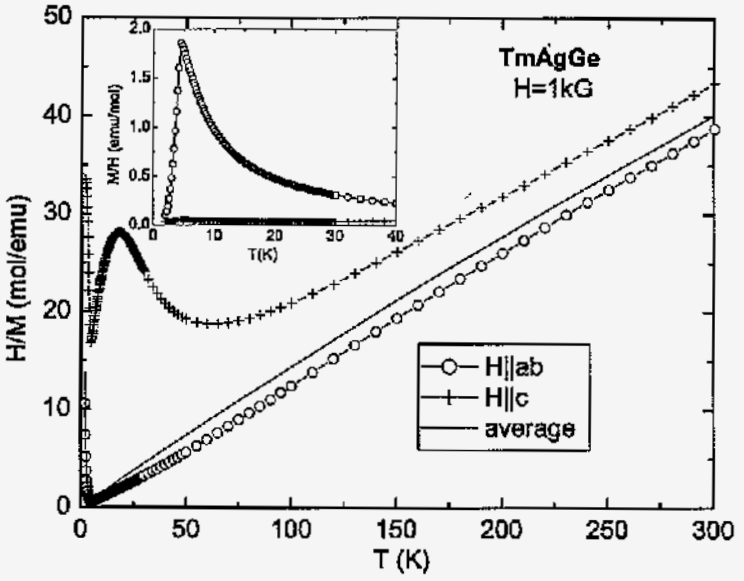

Figure 5.23 Anisotropic inverse susceptibilities of TmAgGe and calculated average (line); inset: low-temperature anisotropic susceptibilities.

Figure 5.24 shows a sharp peak in $C_P(T)$ as well as $d(\chi\ T)$ / dT for 4.2 $\pm$ 0.1 K. The zero-field resistivity data shown in Fig. 5.25, supports the ordering temperature inferred from the thermodynamic data. The plot of $d\rho$ / dT (Fig. 5.24c) has a clear peak between 4.0 and 4.6 K. In the inset of Fig. 5.24a, the calculated magnetic entropy $S_m(T)$ has a break in slope close the transition temperature T_N, for an entropy value of $\sim$ R ln 2, indicative of a

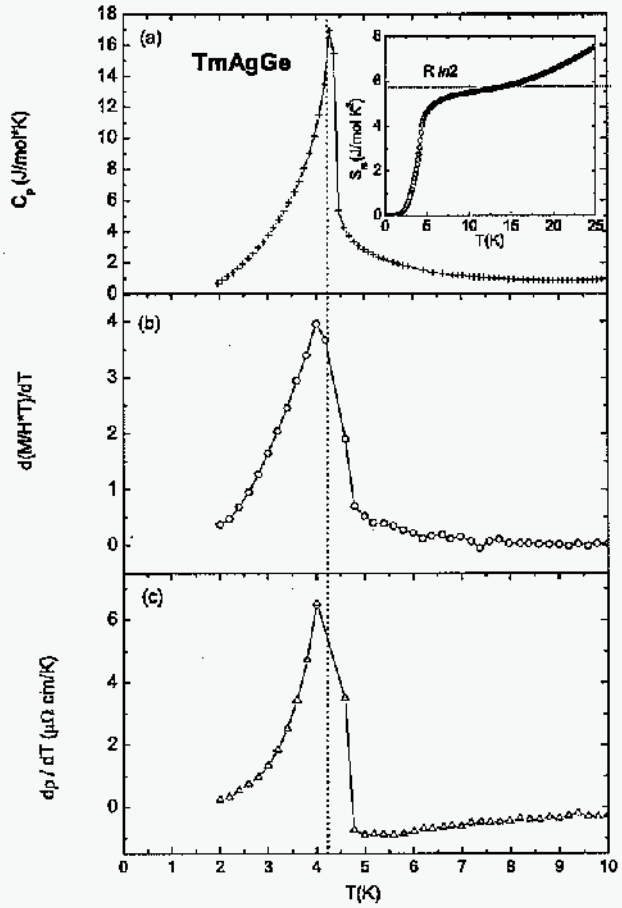

Figure 5.24 (a) Specific heat $C_p(T)$ with the magnetic entropy S_m in the inset; (b) Low-temperature $d(M/H * T)/dT$ for TmAgGe; (c) low-temperature $d\rho/dT$; dotted line marks the peak position as determined from (a).

doublet ground state or two closely spaced singlets. Below T_N, loss of spin disorder scattering is apparent from the sudden drop in resistivity, due to the antiferromagnetic ordering of the Tm^{3+} moments. Above the ordered state, the resistance goes through a broad local minimum around 15 K (far higher than T_N), after which it starts increasing; for temperatures higher than $\sim$ 100 K it becomes approximately linear. The residual resistivity ratio RRR $\approx$ 4.0 reflects

acceptable quality of these crystals.

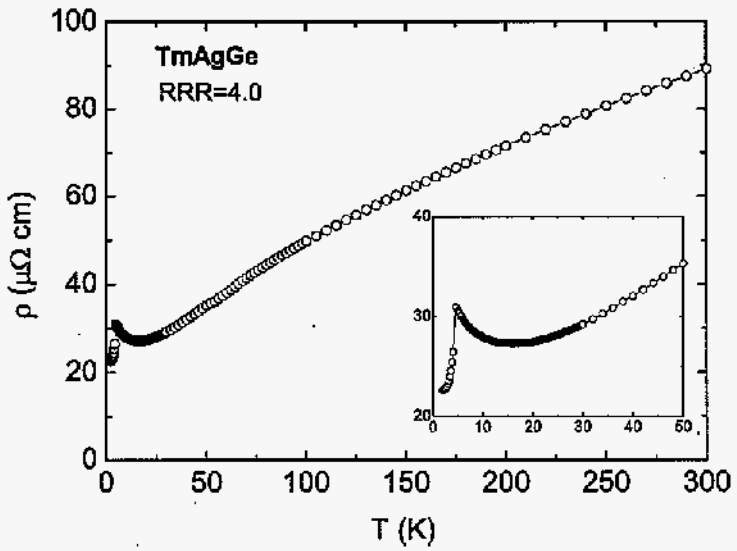

Figure 5.25 Zero-field resistivity of TmAgGe (inset: enlarged low-temperature part).

Clear metamagnetism is seen in the $M(H)$ plot in Fig. 5.26a for in-plane field orientation, as well as in magnetoresistance measurements shown in Fig. 5.26b. Below $H = 70$ kG, the in-plane magnetization curves in Fig. 5.26a show two metamagnetic transitions for $H \parallel [120]$, with critical field values $H_{c1} \approx 4.25$ kG and $H_{c2} \approx 9.25$ kG; for the other orientation, $H \parallel [010]$, they merge into a single transition with a critical field around $H_c \approx 6.0$ kG. A very complex angular dependence of the critical fields, as well as of the locally saturated magnetization values, can thus be anticipated,and this will be presented in detail in Chapter 6.

Similar to the case of HoAgGe, we compare the position of any features revealed by the magnetoresistance measurement in Fig. 5.26b to the critical field values that we get from $M(H \parallel ab)$ curves. Below 10 kG, there is one obvious peak, and another possible change of slope in the plot in Fig. 5.26b; therefore we could probably assume that the field was close to

the [120] direction, for which two metamagnetic transitions can be seen in $M(H)$. However, there is another broad peak in the magnetoresistance that can not be correlated with any feature in magnetization, and which requires further investigation.

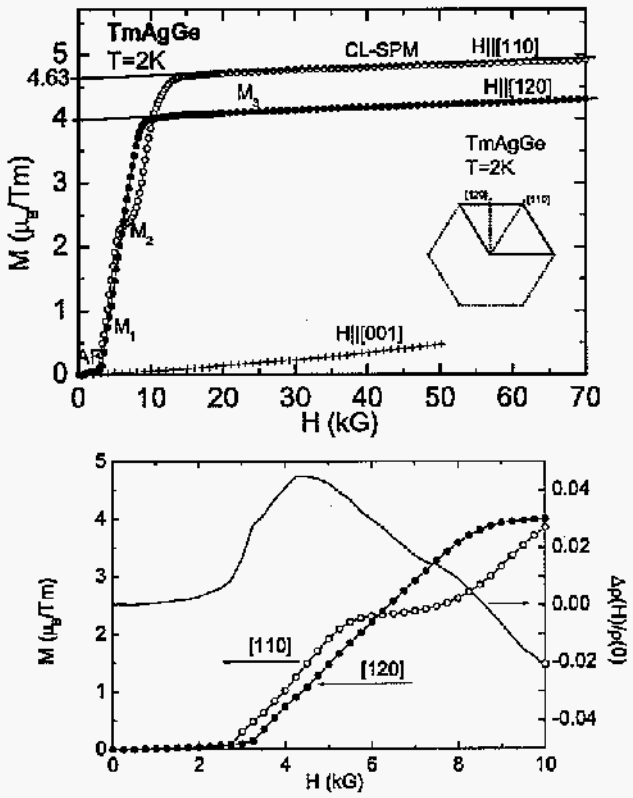

Figure 5.26 (a) Anisotropic magnetization curves in TmAgGe, shown for three orientations of the applied field; (b) Transverse magnetoresistance and $M(H)$ curves for $H \| ab$, at T=2K.

5.2.7 YbAgGe

YbAgGe is a compound with some distinctly different properties compared to all previous members of the series. Fig. 5.27 shows the inverse anisotropic susceptibility in an applied field $H = 1$ kG. It is linear above ~ 20 K, indicating Curie-Weiss behavior at high temperatures with

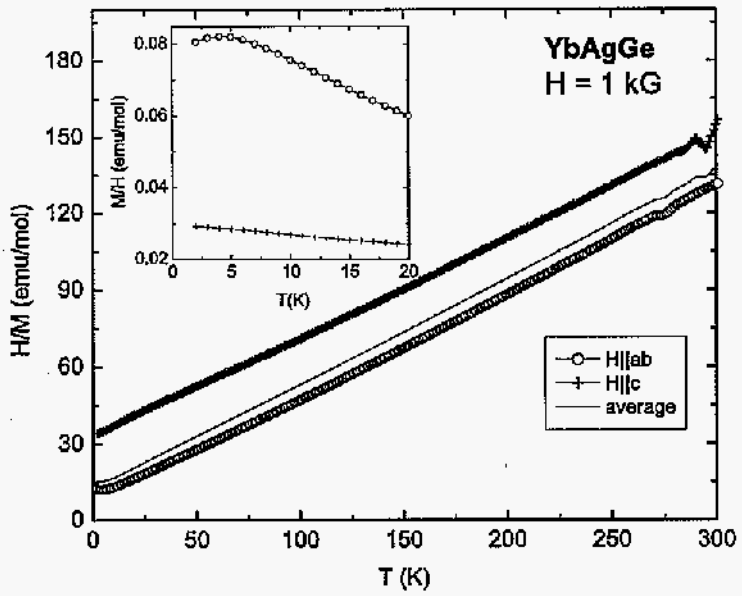

Figure 5.27 Anisotropic inverse susceptibilities of YbAgGe and calculated average (line); inset: low-temperature anisotropic susceptibilities.

an effective moment of $\sim$ 4.4 μ_B/Yb; however, below this temperature, as can be seen in the inset from low temperature susceptibility, there is no sign of magnetic ordering down to 1.85 K. Instead there is an apparent loss of local moment behavior, manifesting itself as a levelling off of the susceptibility. Also, no distinct features appear in the $M(H)$ or magnetoresistance data at $T = 2$ K (Fig. 5.28a,b): for $H \parallel c$ magnetization linearly increases with H up to $H = 140$kG, whereas the in-plane data show that the compound is probably approaching saturation (the fact that the high field magnetization is lower than calculated $\mu_{sat}(Yb^{3+}) = 4.0\,\mu_B$ is possibly a result of the crystal structure and CEF anisotropy of the RAgGe series, see the discussion below); magnetoresistance at this temperature is consistent with what one would expect for anisotropic, paramagnetic metal.

Katoh *et al.* (2004) have already reported the heavy fermion character of YbAgGe based

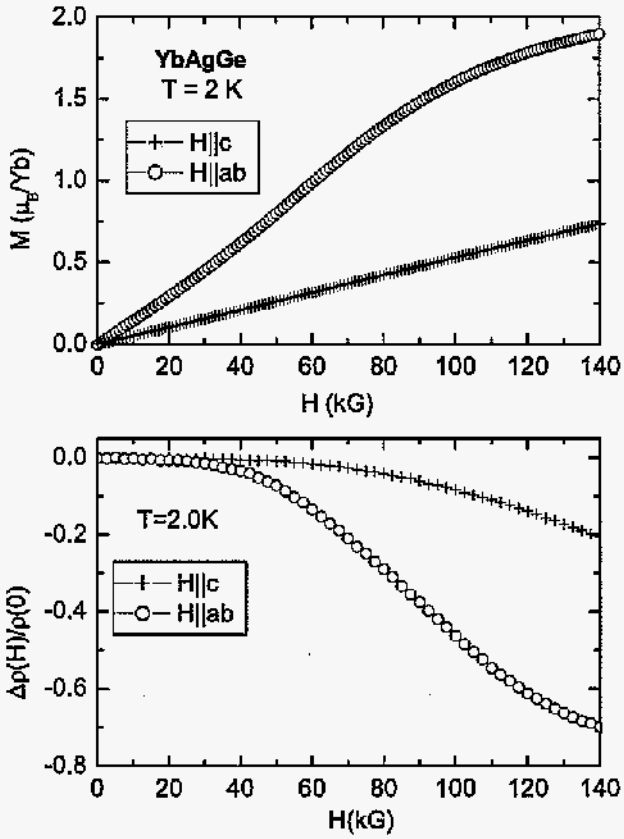

Figure 5.28 (a) Anisotropic field-dependent magnetization and (b) magnetoresistance for YbAgGe at $T = 2$ K.

on zero-field specific heat and resistivity measurements down to 2 K. Although these authors did not go to low enough temperatures to detect the ordering below 1 K, their other data is in good agreement with what we have presented here and elsewhere (Beyermann, 1998).

As can be seen in Fig. 5.29a, no significant change occurred after annealing (600^{0}C for 1 week), and the RRR increase (from 2.8 up to 3.1) was slight. The annealing temperature was limited by the possibility of melting the small amount of residual flux on the sample (note the Ag-Ge eutectic at $\sim 650^0$C). The temperature dependencies of the resistivity, and the specific heat (shown below) were almost identical before and after the heat treatment of the crystals.

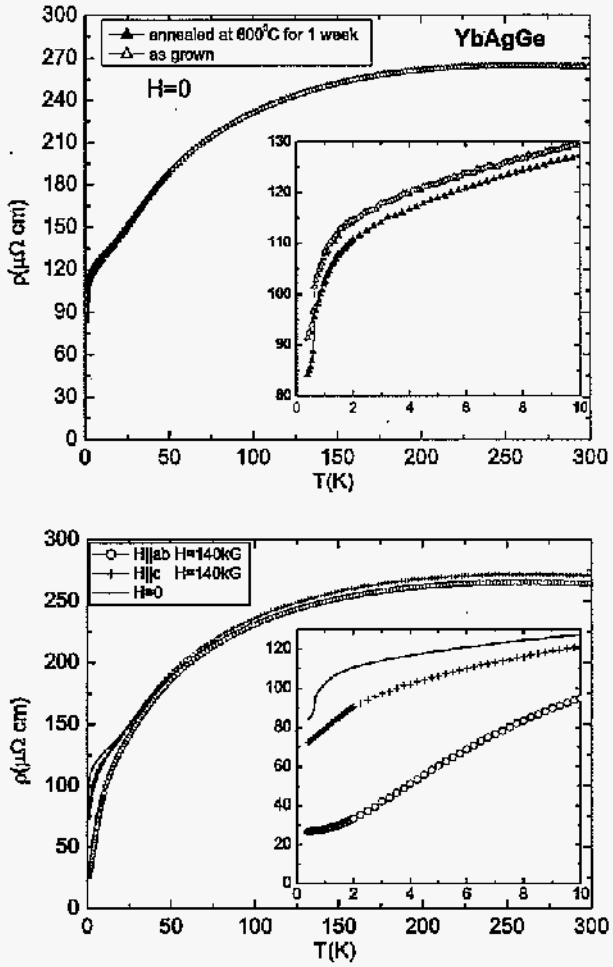

Figure 5.29 (a) Zero-field resistivity of as grown and annealed YbAgGe, (inset: enlarged low-temperature part); (b) anisotropic transverse resistivity for annealed YbAgGe in applied field H=140kG (small symbols) and for $H = 0$ (line).

On the other hand the temperature dependent electrical resistivity can be changed significantly by the application of magnetic field. When large field is applied (Fig. 5.29b), there is an increase in the RRR value: for $H \parallel ab$, the RRR value increases dramatically to RRR $\sim$ 10. This indicates that crystal purity is quite high and apparently the large residual resistivity

ρ_0 for $H = 0$ is due to sensitivity of hybridized Yb state to relatively minor disorder.

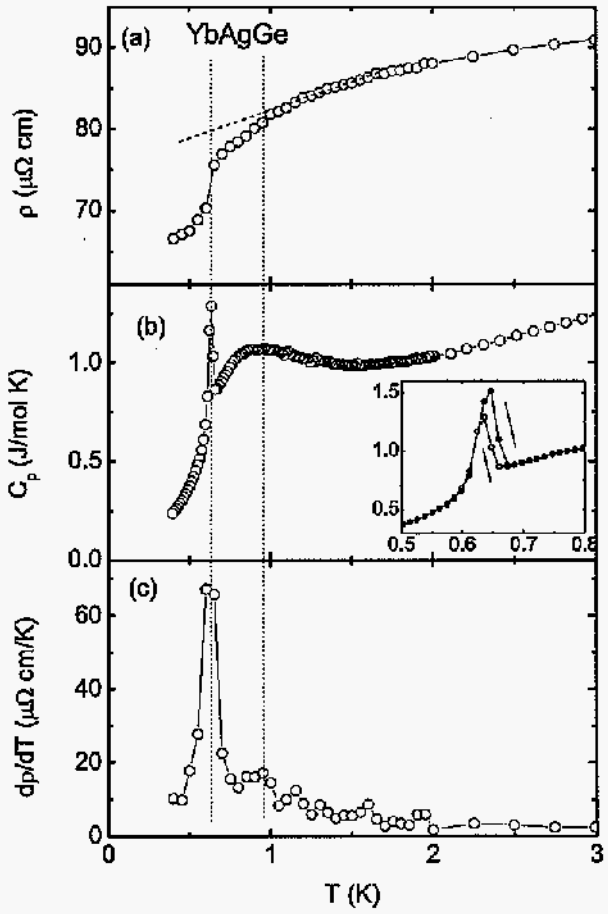

Figure 5.30 Low temperature part of (a) resistivity; (b) specific heat (inset: $C_P(T)$ on warming and cooling); (c) $d\rho/dT$. Lines mark magnetic transitions.

In order to characterize this compound at lower temperatures we have to rely on the resistivity (Figs. 5.29 and 5.30) and specific heat (Figs. 5.30 and 5.31) measurements which were taken down to 0.4 K. (Due to the limitations imposed by our measurement systems magnetization data only go down to 1.85 K.) As the sample is cooled below 1.8 K there are

two features visible in both the resistivity and specific heat. At 1.0 K there is a slight but clear change in slope of the resistivity and there is a relatively broad maximum in the specific heat. At 0.65 K there is an extremely sharp drop in resistivity and as well as a sharp peak in the specific heat. Specific heat data were taken upon heating as well as cooling of the sample (Fig. 5.30b, inset) indicating that if there is any hysteresis associated with the 0.65 K transition it is smaller than the peak width.

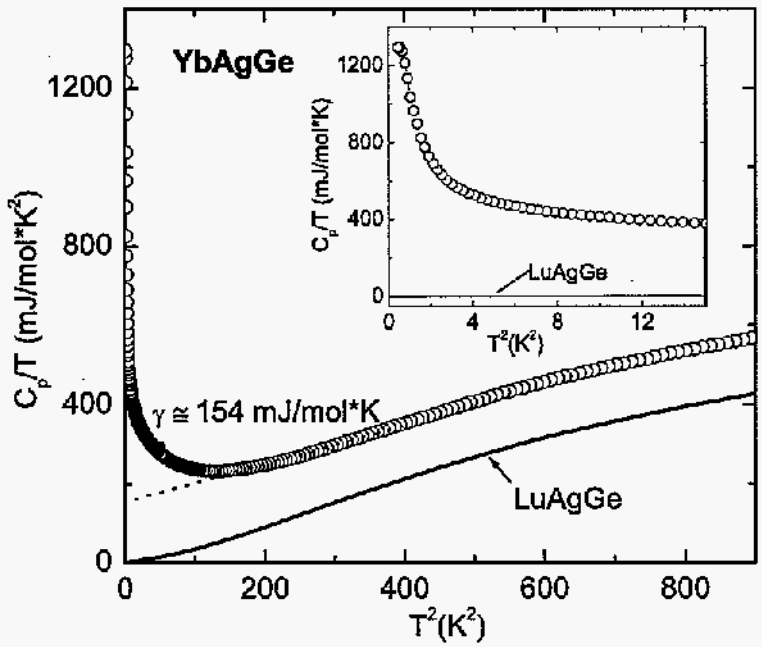

Figure 5.31 $C_p(T^2)/T$ for YbAgGe (open circles) with a high temperatures linear fit (dotted line) giving γ value of $\sim$ 150 mJ/mol K^2; line: $C_P(T^2)/T$ for non-magnetic LuAgGe. Inset: low temperature part.

The calculated magnetic entropy S_m (Fig. 5.32) at $T = 1.0$ K is significantly less than $R \ln 2$. Based on this we can assume that the transition corresponds to small magnetic moment ordering. This is in agreement with the enhanced electronic specific heat coefficient $\gamma \geq 154$ mJ/mol K^2 that we get from extrapolation of the high temperature part of the C_P / T *vs.* T^2

(Fig. 5.31) to $T^2 = 0$.

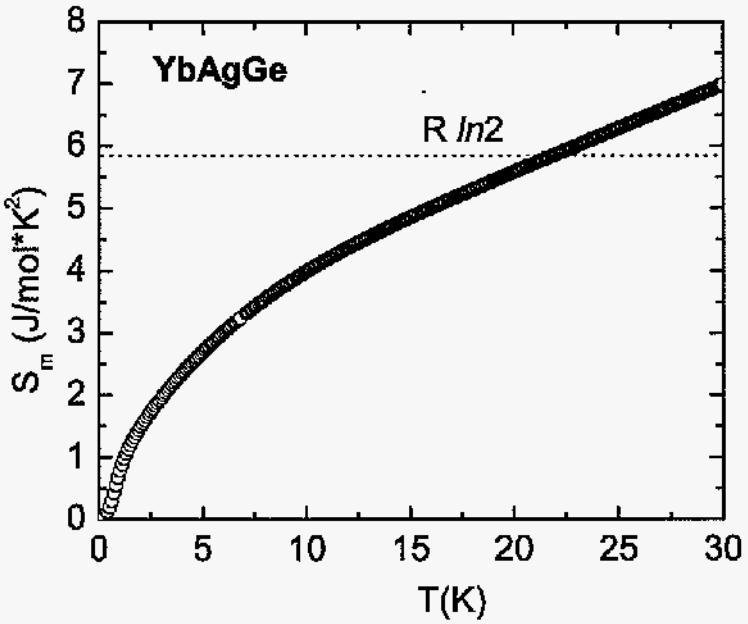

Figure 5.32 Magnetic entropy for YbAgGe. Inset: low temperature part.

Low temperature small magnetic moment ordering is not the only feature indicating that YbAgGe is probably a heavy fermion compound: deviations from the Curie-Weiss behavior in χ_{ave} (for which CEF effects are cancelled to the first order) below $\sim$ 20 K, and quite large Weiss temperature ($\Theta_{ave} \approx -30$ K) suggest that Yb $4f$ levels may be significantly hybridized. If this is true, an estimate of the Kondo temperature is given by $\Theta/10 \leq T_K \leq \Theta$ (Daybell, 1973), *i.e.*, 3 K $\leq T_K \leq$ 30 K. Specific heat data plotted as C_P / T *vs.* T^2 (Fig. 5.31) reveal a distinct enhancement of the electronic specific heat coefficient (compared with the data for LuAgGe on the same plot). This $\gamma \sim 150$ mJ/mol K^2 value, already being significantly enhanced by itself, is apparently a lower limit of γ since a significant upturn in C_P / T *vs.* T^2 is observed below approximately 10 K, similar to that seen in many heavy fermion compounds (Hewson, 1997), including for example $YbNi_2B_2C$ (Yatskar, 1996) and $YbRh_2Si_2$

(Trovarelli, 2000). Keeping in mind that YbAgGe has a low temperature magnetic ordering, and that therefore an ambiguity in the evaluation of low temperature electronic specific heat coefficient is present, Fig. 5.31 suggests that low temperature γ is within the range of $\sim$ 150 mJ/mol K^2 to 1 J/mol K^2. This crude estimate allows us to classify YbAgGe as a new Yb heavy fermion compound, with low temperature reduced moment magnetic ordering, which we already reported in (Beyermann, 1998). Using the single impurity relation (Hewson, 1997), we can estimate the Kondo temperature as $T_K = w_N \pi^3 R / 6 \gamma$, where $w_N = 0.4107$ is the Wilson number and R is the gas constant. Using the aforementioned range of the value of γ, the Kondo temperature can be evaluated as 15 K $< T_K <$ 120 K. Additionally, we can estimate the Wilson ratio, $\mathcal{R} = 4 \chi \pi^2 k_B^2 / 3 \gamma \mu_{eff}^2$ (Hewson, 1997) for YbAgGe using χ and γ determined at $T = 1.8$ K, and the high temperature effective moment μ_{eff}, as $\mathcal{R} \approx 1.8$, which is close to $\mathcal{R} = 2$ expected for heavy fermion compounds, and much higher than $\mathcal{R} = 1$, the Wilson ratio for non-interacting electrons (Hewson, 1997).

Having a Néel temperature, apparently associated with small moment ordering, so close to $T = 0$ K makes YbAgGe an interesting system for the study of the competition between magnetically ordered and correlated ground state. It is anticipated that pressure should be a possible parameter for stabilizing the antiferromagnetic ground state.

5.3 Discussion

Among many properties that we see in the RAgGe series, anisotropy and metamagnetism are particularly interesting, specifically in light of the crystal structure of these compounds: a hexagonal unit cell with a single rare earth site of orthorhombic point symmetry. Across the series, the magnetization is anisotropic, going from axial (in TbAgGe) to extreme planar (in TmAgGe). The magnetic and transport properties throughout the RAgGe series proved to be anisotropic, due primarily to the CEF splitting of the Hunds rule ground state multiplet. In Table 5.1 the Weiss paramagnetic temperatures are given, for the two orientations of the field, as well as for the polycrystalline average. Negative values for Θ_{ave} for all R suggest antiferromagnetic interactions between magnetic moments, although Dy may be an exception,

Table 5.1 Magnetic ordering temperatures, T_m, effective magnetic moments and anisotropic paramagnetic Weiss temperatures Θ_W.

	Tb	Dy	Ho	Er	Tm	Yb
T_m(K)	28.4 ± 0.1, 24.6 ± 0.1, 19.8 ± 0.1	14.5 ± 0.1, 12.15 ± 0.1	11.0 ± 0.2, 7.7 ± 0.1	3.1 ± 0.1	4.15 ± 0.1	0.95 ± 0.05, 0.65 ± 0.05
$\mu_{eff}(\mu_B/\mathrm{R})$	9.7	10.4	10.0	9.3	7.9	4.4
Θ_{ab}(K)	-53.8	-25.5	-10.1	-3.6	7.5	-15.1
Θ_c(K)	1.0	7.4	-1.9	-36.4	-76.3	-83.5
Θ_{ave}(K)	-28.3	-10.5	-7.1	-10.9	-14.4	-30.1

given the presence of the small ferromagnetic component of the magnetization. TbAgGe has an easy axis parallel to c in the paramagnetic state. This is followed by a progression towards a more isotropic case (R = Ho) while having $\Theta_{ab} < \Theta_c$, whereas for R = Er - Yb the easy axis lies in the ab-plane and $\Theta_{ab} > \Theta_c$. The analysis of this anisotropy should allow for the determination of the leading term in the crystal field Hamiltonian, similar to the case of tetragonal systems. But a more complex calculation is needed for our hexagonal compounds, where the R ions are located at sites with *orthorhombic* point symmetry, and this is beyond the scope of this work.

The ordering temperatures in RAgGe (R = Tb - Tm) approximately scale with the de Gennes factor $dG = (g_J - 1)^2 J(J+1)$ (Fig. 5.33), where g_J is the Landé g factor and J is the total angular momentum of the R^{3+} ion Hunds rule ground state. This is consistent with the coupling between the conduction electrons and the local magnetic moments giving rise to the long range magnetic order via the RKKY interaction. However, significant deviations from the linearity may be noticed, suggesting other factors may be involved (*i.e.* strong CEF effects constraining the moments to either the ab plane or the c axis, as seen in the already mentioned tetragonal compounds [Myers, 1999b; Bud'ko, 1999; Noakes, 1982]).

Because the strong CEF splitting confines the magnetic moments to the basal plane in TmAgGe this compound is the simplest candidate in this series for a study of the metamagnetism. Tm^{3+} ions occupy $3g$ Wyckoff sites, with m 2 m (*orthorhombic*) point symmetry, leading to a hexagonal structure with three R ions per unit cell (Fig. 3.1). Consequently,

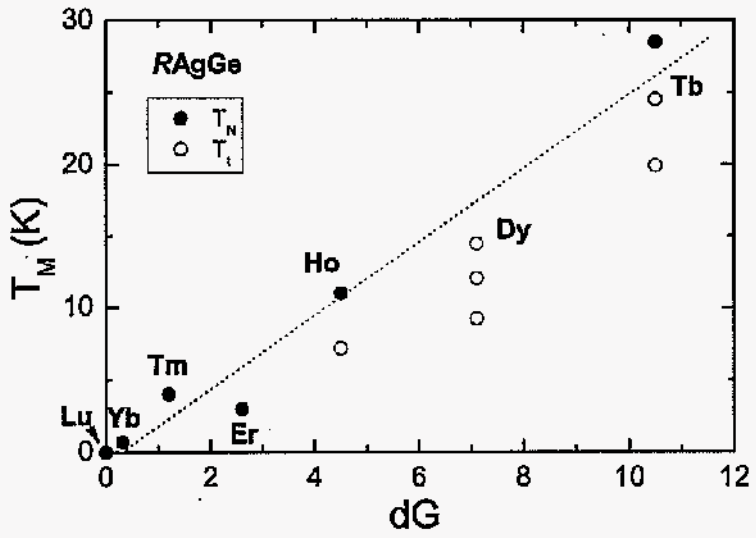

Figure 5.33 Changes of the magnetic ordering temperatures T_m for R=Tb-Lu in the RAgGe series, with the de Gennes scaling parameter dG (the dotted line represents the expected linear dependence).

referring to a single unit cell, we can assume that the magnetic moments of the three R ions behave like Ising systems, rotated by 120^0 with respect to each other in the basal plane. The saturated state is reached when the three magnetic moment vectors add constructively (Fig. 5.34).

As will be presented in detail in Chapter 6, the complex metamagnetism observed in TmAgGe is well described by *the three co-planar Ising-like systems model* (a model in which we assume three Ising systems 120^0 apart in the *ab*-plane of a hexagonal unit cell); furthermore, the same model can be used to describe at least one more compound, isostructural to TmAgGe (*i.e.*, TbPtIn).

If we release the restriction that the three Ising systems be planar, while still imposing that their in-plane projections be 120^0 apart to agree with the symmetry of the crystals, we find this

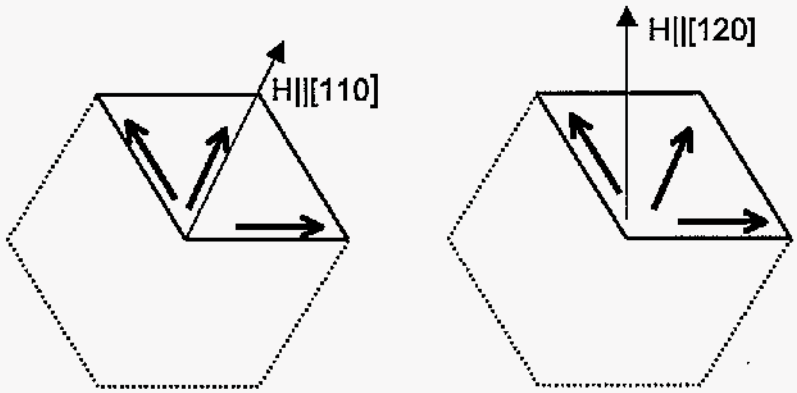

Figure 5.34 Hexagonal unit cell with the magnetic moments (short arrows) in the saturated state of TmAgGe; long arrows indicate the field along the two high-symmetry directions of the crystal.

modified model can describe the case of DyAgGe quite well. From the crystal structure of this compound, and the orthorhombic symmetry of the rare earth sites, we can assume that the three R magnetic moments of the unit cell align themselves along three non-planar equivalent directions. We notice that for H=140kG (Fig. 5.13), the ratio of the magnetizations for the two in-plane orientations (when H is parallel to the two independent high symmetry axes) is:

$$\left.\frac{M(H\|[120])}{M(H\|[010])}\right|_{exp} = \frac{4.02}{4.51} = 0.89$$

This is close to the previously calculated value of for the planar model assumed for TmAgGe. In the case of DyAgGe, given that the three $M(H)$ curves in Fig. 5.13 seem to indicate that the moments are tilted outside the ab-plane, a model similar to that used for TmAgGe, enhanced to 3 dimensions, may be appropriate. Let us assume that the three Dy^{3+} magnetic moments lie on a cone around the c-axis, with the projections in the ab plane 120° apart from each other. These in-plane projections will then behave similarly to the full moments in the case of Tm^{3+},

and thus $M(H\|[010])$ represents $\frac{2}{3}$ of the total ab magnetization M_{ab} (if we assume saturation at H=140kG): $M(H\|[010]) = \frac{2}{3}M_{ab}$. Then $M_{ab} = \frac{3}{2}M(H\|[010]) = \frac{3}{2} * 4.51\mu_B = 6.77\mu_B$. Together with the axial component $M_c(\equiv M(H\|[001])) = 6.85\mu_B$, we can now estimate the total magnetization at H=140kG: $M(140kG) = \sqrt{(6.77\mu_B)^2 + (6.85\mu_B)^2} \approx 9.63\mu_B$, close enough to the calculated value $\mu_{sat}(Dy^{3+}) = 10\mu_B$. We conclude that the model we assumed for the magnetic moments is consistent with the experiment. Moreover, one can estimate the angle φ of the saturated magnetization with respect to the c-axis: from the in-plane magnetization being along the [010] direction, we can conclude that, in the saturated state, the total magnetization vector lies along a $[0kl]$ axis. The angle φ with the c-axis can be calculated as: $\tan\varphi = \frac{M_{ab}}{M_c} = \frac{6.77}{6.85} = 0.99$ and thus $\varphi \approx 45°$.

The lattice parameters of the hexagonal unit cell in DyAgGe are given in Fig. 3.2 to be $a = 7.09\mathring{A}$ and $c = 4.20\mathring{A}$; in the orthogonal system of coordinates that we use in defining the crystalline directions, these correspond to $a' = a = 7.09\mathring{A}$, $b' = a * \frac{\sqrt{3}}{2} = 6.14\mathring{A}$ and $c' = c = 4.20\mathring{A}$. We can now write the direction given by the angle φ in terms of Miller indices h, k and l, where $h = 0$, and k and l are such that

$$\tan\varphi = 0.99 = \frac{kb'}{lc'} = 1.46\frac{k}{l} \Rightarrow \frac{k}{l} = 0.68$$

The closest integer values for k and l are thus 2 and 3 respectively, which means that in DyAgGe the saturated magnetization vector M is parallel to the [023] direction.

HoAgGe resembles DyAgGe in that both these compounds show metamagnetic transitions for both high-symmetry directions in the ab-plane. However attempts to apply the Dy model to Ho failed because the in-plane magnetization is almost isotropic in HoAgGe (Fig. 5.18a).

Another important observation is that in DyAgGe, the last seen metamagnetic transition is followed by an almost constant magnetization (wide plateaus in all three orientations of the field), supportive of the idea of a stable saturated state above $\sim$ 80 kG; in HoAgGe however, magnetization keeps increasing with the applied filed, possibly indicating a continuous spin-flop transition, as already mentioned. If this is true, than with fields around 100 kG this compound is already in a regime of weak CEF, therefore any variant of the previous model is

inappropriate. It is worth noting though that HoAgGe is rather curious given its anisotropy (clear metamagnetism in the two in-plane directions and no clear transition for $H \parallel c$). At some future date it would be interesting to study the angular dependence of metamagnetism in DyAgGe and HoAgGe, to see how the phase diagrams vary as the anisotropy is being relaxed.

Insufficient data on ErAgGe (*i.e.*, two in-plane orientations, higher fields) as well as the low T_N and the single, rather broad feature in $M(H)$ prevent us from checking how the model applies to this compound.

All RAgGe described here seem to be good metals, as shown by the monotonic increase of the resistivity at high temperatures; the residual resistivity ratio RRR ranges from 2.0 to 6.5, and it did not seem to improve considerably by annealing in the case of YbAgGe. However it should be noted that YbAgGe has a RRR of about 10 in a 140 kG applied field, significantly larger than that without field, indicating that a lot of the scattering in this compound is magnetic in origin.

All of the magnetically ordered compounds in this study, except for YbAgGe, have a rather unusual, pronounced minimum in the temperature dependent resistivity above the magnetic transition. It is similar to the $\rho(T)$ behavior recently found in a different family, $RCuAs_2$ (for R = Sm, Gd, Tb, Dy) (Sampathkumaran, 2003). It has to be seen if this type of behavior indeed requires, as suggested by Sampathkumaran (Sampathkumaran, 2003), novel ideas for electrical transport phenomena in the paramagnetic state of relatively simple magnetic metals, but the mere fact that similar, atypical, temperature dependence is observed in resistivity of the members of two unrelated families, $RCuAs_2$ and RAgGe, in the latter case in single crystals, certainly asks for some theoretical input as well as search for other examples.

YbAgGe appears to be a very promising example of a Yb-based intermetallic compound with clear hybridization. Whereas it does not order magnetically within our $M(T)$ measurement range (above 1.85 K), it does have a clear small moment ordering below 1.0 K and also has an enhanced electronic specific heat coefficient value ($\gamma > 150$ mJ/mol*K^2). Based on these data we can conclude that YbAgGe is a heavy fermion, with small moment ordering at very low temperature. Consequently, there is a possibility of approaching a quantum critical

point by experiments under applied magnetic field, variable pressure, or with changing lattice parameters with doping, or with variable concentration of the magnetic moments (i.e. of the Yb^{3+} ions). While in an isotropic case, application of pressure in Yb compounds close to quantum critical point is expected to increase the ordering temperature (Thompson 1994), crystallographically and electronically anisotropic materials like YbAgGe may have non-trivial response to pressure. A detailed investigation of the nature of the ordering in YbAgGe is presented in Chapter 8.

CHAPTER 6. Angular dependent planar metamagnetism in the hexagonal compounds TbPtIn and TmAgGe*

6.1 Introduction

The effects of crystalline electric field (CEF) anisotropy on metamagnetism in intermetallic compounds have been of interest for a long time (Gignoux, 1995; Gignoux, 1997), and numerous studies of *angular dependent* local moment metamagnetism show that simple geometric relationships exist between the critical fields of the metamagnetic phase transitions, and the angle that the applied field makes with the corresponding easy axis. One simple case is that of $TbNi_2Ge_2$ (Bud'ko, 1999), a tetragonal compound with Tb ions in tetragonal point symmetry, where, at low temperatures, the crystalline electric field (CEF) anisotropy confines the local moments along the c ([001]) crystallographic axis (Ising-like system). Consequently, several metamagnetic transitions are observed, with the critical field values H_c having a $1/\cos\theta$ dependence on the angle between the applied field H and the c-axis. A more complex situation is encountered when the magnetic moments are allowed more degrees of freedom , *i.e.*, when the CEF anisotropy constrains them to an easy plane. This is the case in the tetragonal compounds RNi_2B_2C (Cho, 1996b; Canfield, 1997a,b), with R = Tb - Er, and $RAgSb_2$ (Myers, 1999a,b) for R = Dy. The R ions are again in tetragonal point symmetry and the local moments are confined to four equivalent [110] or [100] crystallographic directions; thus the angular dependent magnetization measurements, when the field is applied in the basal plane, reveal the four-fold anisotropy of the longitudinal magnetization that reflects the symmetry of the unit cell. The angular dependencies of the locally saturated magnetizations M_{sat} and the

*after "Angular dependent planar metamagnetism in the hexagonal compounds TbPtIn and TmAgGe", E. Morosan, S. L. Bud'ko and P. C. Canfield, Phys Rev B 71 014445 (2005).

critical fields H_c could be treated by simple analysis, and plausible net distribution of moments could be inferred for each metamagnetic phase (Canfield, 1997b; Myers, 1999a). Kalatsky and Pokrovsky (Kalatsky, 1998) elaborated the four-position clock model, which agrees well with the observed metamagnetism in $HoNi_2B_2C$ and $DyAgSb_2$.

Initially thought to be improbable, angular dependent metamagnetism in extremely planar systems is now an accepted and understandable event in tetragonal compounds; but this has not yet been well studied in hexagonal compounds, and this is the motivation for the present analysis. Recently we reported the presence of metamagnetism in a hexagonal class of materials, *i.e.* the RAgGe compounds, for R = Tb - Tm (Chapter 5). They crystallize in the ZrNiAl-type structure, an ordered variant of the hexagonal Fe_2P family. In this structure, there is a unique rare earth site in the unit cell, with the rare earth ions occupying equivalent 3g positions with orthorhombic point symmetry (Fig. 3.1). The anisotropic susceptibility was found to be axial for TbAgGe and progressed towards extremely planar for TmAgGe. The physical properties of the TmAgGe compound (antiferromagnetic ordering in the ground state, extremely planar anisotropy, metamagnetism when the applied field was perpendicular to the c-axis) are very similar to those of the isostructural TbPtIn system, previously only known in polycrystalline form (Galadzhun, 2000; Watson, 1995), making both compounds good candidates for a study of the angular dependent metamagnetism in hexagonal systems. In both TmAgGe and TbPtIn the R ions occupy the same site, whereas both ligands are different. Having two such systems will allow us to show that the behavior we find is not specific to one compound, but a more general result associated with this structure, or perhaps with the orthorhombic point symmetry in a hexagonal unit cell. As we shall see, the Néel temperature is much higher for TbPtIn (46.0 K) than for TmAgGe (4.2 K), with the former also showing a possible spin reorientation transition at a fairly high temperature (T_m = 27.4 K). This latter transition in TbPtIn was missed by the measurements on polycrystalline samples (Watson 1995), where even the nature of the magnetically ordered state below $\sim$ 50 K was not identified. Thus we can once again emphasize the advantage of analysis on single crystals rather than on polycrystalline samples.

This chapter is organized as follows: first we will present the *M(T,H)* data on TbPtIn, emphasizing the complexity of its ordered state, for field orientations along the two in-plane, high symmetry directions; this will be followed by the M(H,θ) measurements at low temperature, from which the values of the locally saturated magnetizations and critical fields as a function of θ were extracted. Next, we will introduce a model for the net distribution of moments, which we subsequently use to calculate the expected, locally saturated magnetizations M_j and the critical fields (for the transition from state i to state j) $H_{ci,j}$ as functions of θ. This will be followed by a comparison of how the calculated and experimental M_j and $H_{ci,j}$ values vary with the angle between the applied field H and the easy axis for this compound.

Similar measurements performed on TmAgGe will then be shown, leading to the corresponding experimental $M_j(\theta)$ and $H_{ci,j}(\theta)$ phase diagrams, which we will again map onto the appropriate model calculation.

We will also analyze similar $M(H,\theta)$ data of TbPtIn for $T = 20$ K, and use the same model in order to characterize a magnetic phase present only at higher temperatures.

Finally, we will summarize our key results and also indicate how our model can be generalized to a variety of possible point symmetries in tetragonal and hexagonal systems.

6.2 TbPtIn

Fig. 6.1 shows the inverse magnetic susceptibility for TbPtIn, as well as the low-temperature magnetization in the inset. This compound appears to order antiferromagnetically below $T_N = 46.0$ K, with what is probably a spin-reorientation or a commensurate-to-incommensurate transition around $T_m = 27.4$ K, as indicated by the peaks in the $d(M*T/H)/dT$ plot (Fisher 1962) in Fig. 6.2a. In the determination of these temperature values, M/H represents the polycrystalline average susceptibility χ_{ave}, calculated as

$$\chi_{ave} = \frac{1}{3}\,\chi_c + \frac{2}{3}\,\chi_{ab}$$

or, when measurements have been done along all three salient directions,

$$\chi_{ave} = \frac{1}{3}\,(\chi_{[001]} + \chi_{[100]} + \chi_{[120]}).$$

The above temperatures are further confirmed by the $C_p(T)$ and $\rho(T)$ $(i||ab)$ data, also

shown in Fig. 6.2b and c.

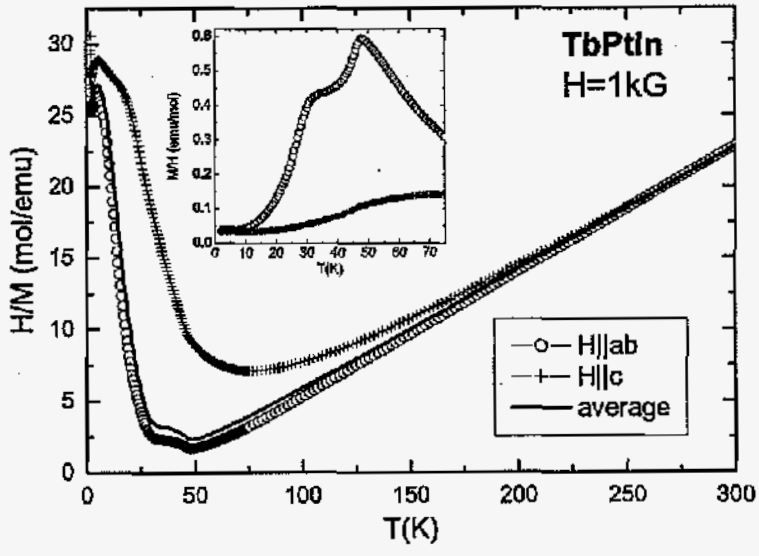

Figure 6.1 Anisotropic inverse susceptibility of TbPtIn (symbols) and the calculated average (line); inset: low-temperature anisotropic susceptibilities.

In the ordered state, as well as in the paramagnetic state up to ~ 100 K, the susceptibility is extremely anisotropic, with the local Tb moments confined to the ab-plane at low temperatures. To check the origin of the anisotropy in the paramagnetic state, single crystals of YPtIn were grown, with a small number of non-magnetic Y^{3+} ions substituted with magnetic Tb^{3+} ions. The extremely anisotropic susceptibility and magnetization of the diluted compound demonstrate that this is single-ion anisotropy associated with the CEF splitting of the Hund's rule ground state J multiplet. From the Curie-Weiss effective moment, as determined from the average inverse susceptibility (Fig. 6.3), the concentration x of the diluted compound $(Tb_xY_{1-x})PtIn$ is $x = 0.024$, whereas the high field magnetization equals $\sim 5.6\ \mu_B/Tb^{3+}$. (If we assume the high field magnetization to be $\sim 6.25\mu_B/Tb^{3+}$, as expected based on the model described below, the resulting concentration will be $x = 0.019$).

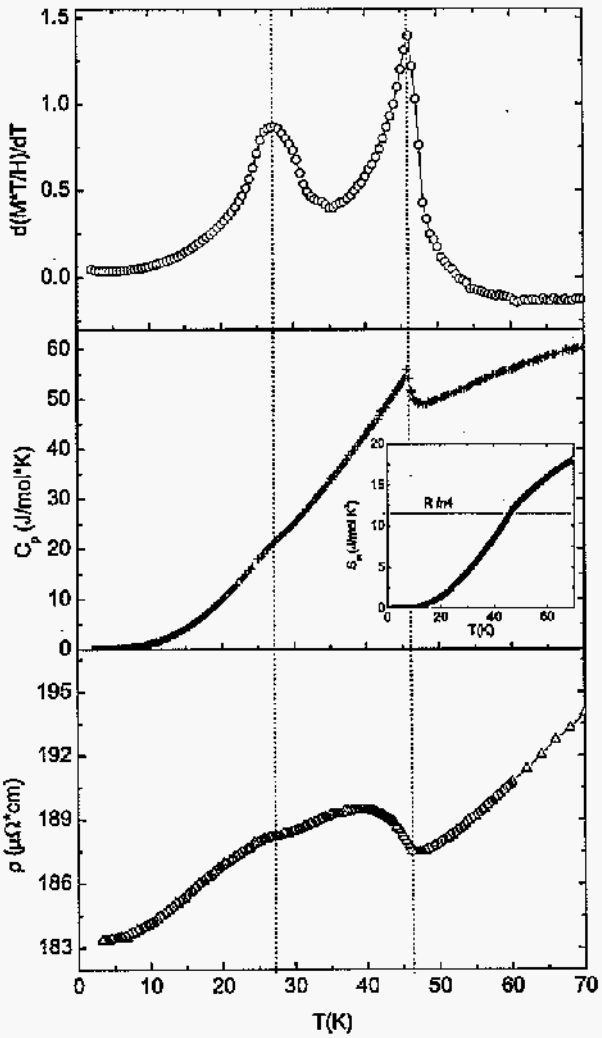

Figure 6.2 (a) Low-temperature $d(\chi_{ave} * T)/dT$, with vertical dotted lines marking the peaks positions; (b) specific heat $C_p(T)$; inset: magnetic entropy $S_m(T)$; (c) low-temperature resistivity $\rho(T)$, for current flowing in the basal plane ($i \parallel ab$).

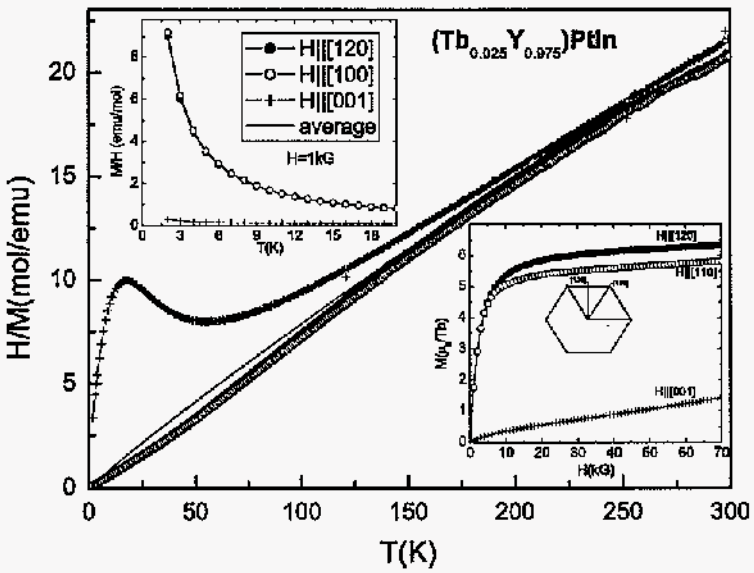

Figure 6.3 Anisotropic inverse susceptibility (symbols) and calculated average (line) for H = 1 kG, for $Tb_xY_{1-x}PtIn$ (x = 0.025); upper inset: low- temperature anisotropic susceptibility; lower inset: field-dependent anisotropic magnetization, for T = 2 K.

For temperatures higher than 150 K, Curie-Weiss behavior of the pure TbPtIn compound can be inferred (Fig. 6.1) from the linear inverse susceptibilities, resulting in anisotropic Weiss temperatures $\Theta_{ab} = 39.0$ K and $\Theta_c = 23.3$ K. The polycrystalline average susceptibility χ_{ave} yielded an effective moment $\mu_{eff} = 9.74\mu_B/\mathrm{Tb}^{3+}$, very close to the theoretical value 9.72 μ_B; the corresponding Weiss temperature is $\Theta_{ave} = 33.3$ K.

The field dependent magnetization measurements shown in Fig. 6.4a not only confirm the in-plane/out-of-plane anisotropy observed in the ordered state, but also indicate anisotropic magnetization within the basal plane. Moreover, several metamagnetic transitions can be seen for the field parallel to the *ab*-plane, for fields up to 140 kG in the $M(H)$ data, and for the magnetoresistance measurements up to 90 kG in Fig. 6.4b. The geometry of the crystals led to more uncertainty in orienting the resistance pieces than the ones for magnetization

measurements; therefore we can infer the approximate orientation of the magnetoresistance sample with respect to the applied field, by comparing the $\Delta\rho(H)/\rho(0)$ data (Fig. 6.4b) with the $M(H)$ curves for $H||ab$ (Fig. 6.4a): since various features in the magnetoresistance measurements occur closer to the critical fields in $M([120])$, we can assume that the field was almost parallel to the [120] direction. (The sharp drop in $\rho(H)$ below ~ 1 kG (Fig. 6.4b) is very likely due to superconductivity of residual In flux on the surface of our resistance bar). For H along the c-axis, the magnetization increases almost linearly with increasing field (Fig. 6.4a), while staying far smaller than M_{ab}.

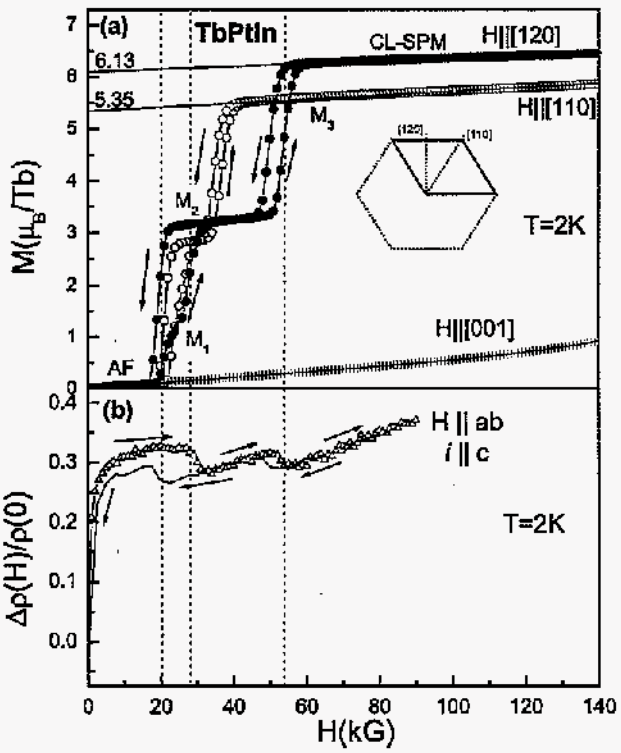

Figure 6.4 (a) Anisotropic field-dependent magnetization (increasing and decreasing field data indicated by arrows) and (b) transverse magnetoresistance, for increasing (symbols) and decreasing (line) field.

At the highest applied field ($H = 140$ kG), the magnetization values for the three shown orientations are $M([110]) = 5.86\,\mu_B$/Tb, $M([120]) = 6.45\,\mu_B$/Tb and $M([001]) = 0.92\,\mu_B$/Tb. Whereas the extreme planar anisotropy of TbPtIn and the anisotropy within the ab-plane recommended this compound for a study of the angular dependent metamagnetism, the fact that the magnetization values were smaller in all three directions than the calculated $\mu_{sat} = 9\mu_B$ for Tb^{3+} ions is somewhat intriguing. One plausible explanation for the low magnetization values would be the existence of more metamagnetic transitions for fields unaccessible with our measurement systems (*i.e.* above 140 kG). Another possibility is that an additional energy scale (such as CEF splitting) exists, that confines the three local moments to three distinct, non-collinear, in-plane orientations. As shall be shown below, we believe the latter to be the more likely scenario.

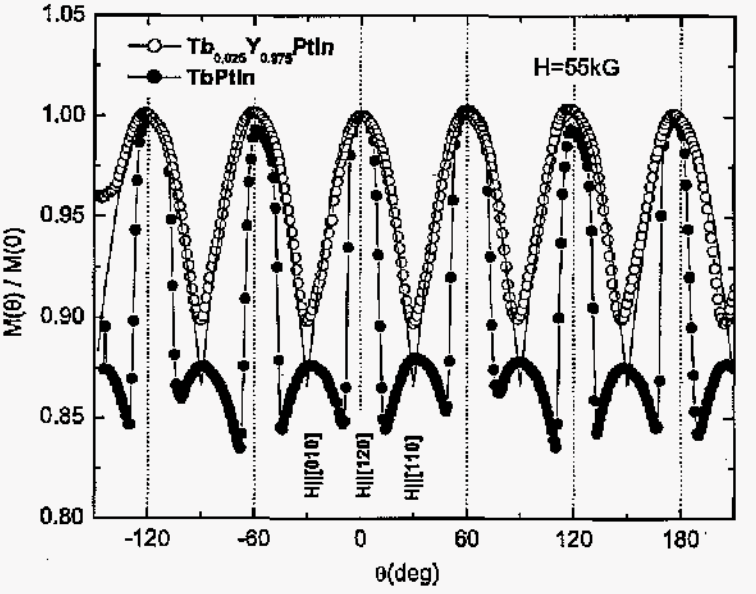

Figure 6.5 M(θ) of TbPtIn (full circles) and $Tb_{0.025}Y_{0.975}$PtIn (open circles) for T = 2 K and H = 55 kG, H⊥c. Solid line represents the calculated $M_{max} * \cos(\theta - n * 60^0)$, n-integer. Note: $\theta = 0^0$ is defined at the [120] direction.

In order to determine the easy axes of the system, we continuously rotated a small piece of the diluted sample $(Tb_xY_{1-x})PtIn$ ($x \approx 0.02$) in an applied field $H = 55$ kG (perpendicular to c); for constant temperature $T = 2$ K, the corresponding magnetization measurement, shown as open symbols in Fig. 6.5, roughly follows a $\cos\theta$ dependence (solid line) around the closest [120]-equivalent directions (*i.e.* $\theta = 60^0 * n$, $n = integer$), where the maxima occur. As we have seen before, the concentration of the diluted sample is $x = (0.0215 \pm 0.0025)$; given this uncertainty, the absolute value of the magnetization $M(\theta)$ in Fig. 6.5 could not be determined, and thus we scaled the data to the maximum value, $M(\theta = 0^0)$. Similar behavior appears in the pure TbPtIn compound (full symbols in Fig. 6.5), where the measured data have also been scaled to their corresponding maximum value at $\theta = 0^0$. We can conclude that the easy axes of the TbPtIn system are the [120] directions. However dramatic departures from the $\cos\theta$ angular dependence can be noticed. The magnetization for TbPtIn, indicative of strong interactions between the local moments, is also consistent with various metamagnetic states crossing the $H = 55$ kG line at different angles. Based on the above data, we will consider the easy axes to be the [120]-equivalent directions, and the angle θ will be measured from the closest easy axis.

In order to get an idea about the various metamagnetic states in this compound, we first explored changes of the critical fields and temperatures for two fixed orientations. The corresponding $M(T)\mid_{H,\theta}$ and $M(H)\mid_{T,\theta}$ measurements shown in Fig. 6.6-6.7 have been used to determine the $H-T$ phase diagrams for the two in-plane high symmetry directions, $H\|[120]$ and $H\|[110]$ respectively.

As illustrated in the insets in these figures, the points in these phase diagrams have been determined from local maxima in $d(M*T)/dT$ (full circles in Fig. 6.8) for fixed fields, and in dM/dH (open circles in Fig. 6.8) for various $M(H)$ isotherms. Even though in Fisher *et al.* (Fisher 1962) the maxima in $d(M*T)/dT$ criterion is described only for antiferromagnetic systems, we apply it here not only for the AF state, but also for high-field states, where the magnetization has a net ferromagnetic component. We are confident that small errors are thus introduced, given the consistency of the critical field and temperature values obtained

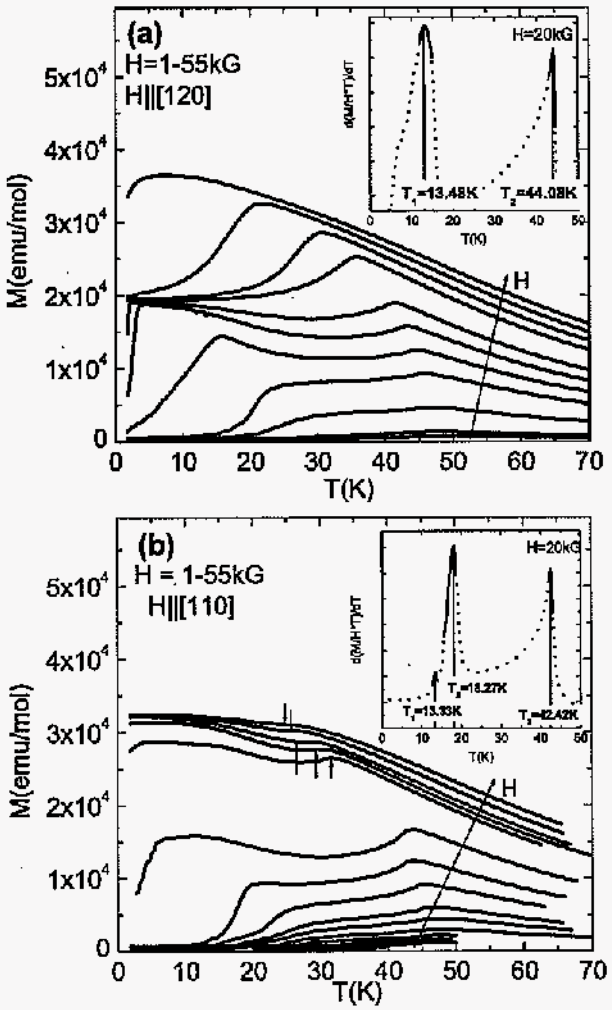

Figure 6.6 M(T) data for various fields for two in-plane orientations of the applied field: (a) H‖[120] for H = 1, 2, 7.5, 15, 20, 25, 30, 40, 45, 50 and 55 kG, and (b) H‖[110] for H = 1, 2.5, 3.5, 5, 7.5, 10, 15, 20, 26, 30, 37.5, 40, 42.5, 45, 50 and 55 kG. Insets show enlarged M(T)*T derivatives (dotted lines) for H = 20 kG, together with the Lorentzian fits of the maxima (solid lines), to exemplify how the points represented by full symbols on the H-T phase diagrams were determined.

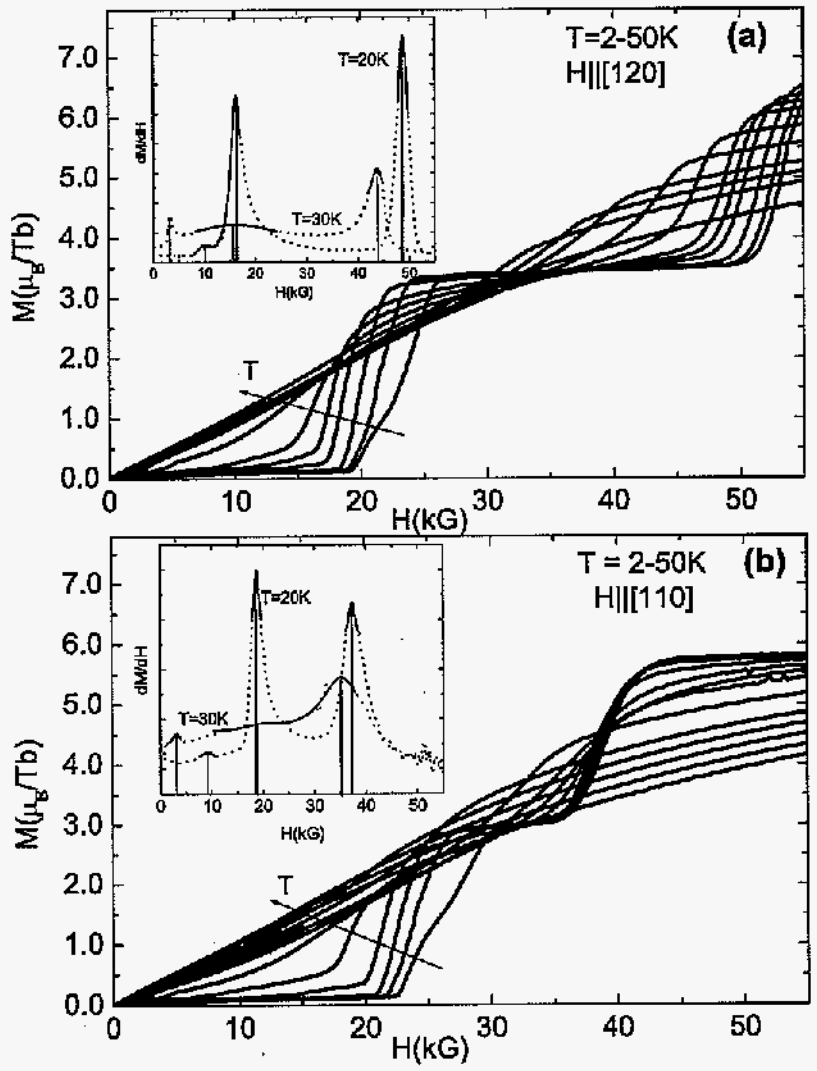

Figure 6.7 M(H) isotherms for two in-plane orientations of the applied field: (a) H||[120] for T = 3, 5, 10, 15, 17.5, 20, 25, 30, 35, 37.5, 40 and 45 K, and (b) H||[110] for T = 2, 5, 10, 15, 20, 25, 30, 35, 40, 42.5, 45 and 47.5 K. Insets show enlarged M(H) derivatives (dotted lines) for T = 20 K and 30 K, for the corresponding field directions, together with the Lorentzian fits of the maxima (solid lines), to exemplify how the points represented by open symbols on the H-T phase diagrams were determined.

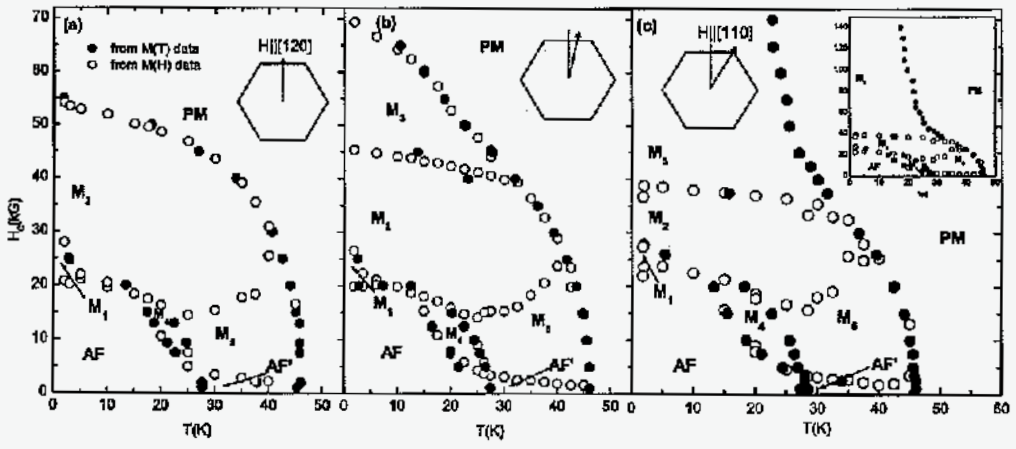

Figure 6.8 H-T phase diagrams for (a) H||[120] and (c) H||[110], as determined from the magnetization data in Fig. 6.6-6.7, with an intermediate field orientation phase diagram (see text) shown in (b).

from both $d(M*T)/dT$ and dM/dH derivatives (full and open symbols respectively in Fig. 6.8). Given that the transition peaks were broad for some field and temperature values, we used Lorentzian fits of the corresponding derivatives (thick lines in Fig. 6.6 and 6.7, insets) to determine the critical values H_c and T_c.

The resulting $H-T$ phase diagrams for H||[120] (Fig. 6.8a) and H||[110] (Fig. 6.8c) are qualitatively similar, at low temperatures and low fields showing the metamagnetic states already seen in the *M(H)* data in Fig. 6.4. For H||[120], Fig. 6.8a shows that the antiferromagnetic ground state persists up to about 20 kG, followed by a small intermediate state M_1 (between $\sim$ 20 kG and 28 kG) and a higher field state M_2 up to $\sim$ 54 kG; as field is being further increased, the paramagnetic PM state is reached, as already indicated in Fig. 6.4a by the horizontal plateaux measured up to 140 kG. (At low temperatures, this is a crystal-field limited saturated paramagnetic CL-SPM state, in which, as discussed below, all moments are assumed to be in their 'up' positions, while still confined by the strong CEF energy to three

distinct, non-collinear directions within the basal plane.) When moving up in temperature at low fields, we find the antiferromagnetic ground state to extend up to $\sim$ 27.4 K, whereas the magnetic ordered state persists up to $\sim$ 46.0 K; both transition temperatures have been already observed (Fig. 6.1 and 3). The M_1 phase exists below $\sim$ 5.0 K, after which, for a limited temperature range (5.0 K $< T <$ 15.0 K), there is a direct transition from the AF to the M_2 state. Between 15.0 K and 27.4 K, or 18.4 kG and 2.0 kG respectively, another intermediate phase, M_4, forms. The inset in Fig. 6.7a represents an example of two isothermal cuts of the [120] phase diagram in Fig. 6.8a: the phase boundaries of the bubble-like phase M_4 are very close in field at constant T, and so the lower peak in the $T = 20.0$ K isothermal derivative dM/dH is poorly defined; the two higher peaks are fairly sharp, similar to the one defining the M_2 to PM transition in the $T = 30.0$ K isotherm. However, as we move down in field along the latter isotherm, one broad peak around 15.4 K may indicate the crossing of another almost horizontal phase boundary (leading into the M_5 state), and thus hard to identify in $d(M*T)/dT$. One more peak at $H_a \simeq 3.4$ kG is indicative of possibly another phase AF' existing below this field, between 28 K and 46.0 K. This is consistent with an antiferromagnetic ordered state below 46.0 K, with an incommensurate-commensurate transition around 28 K which frequently occurs in intermetallic compounds.

For $H||[110]$ (Fig. 6.8c) the $H-T$ phase diagram is fairly similar, with only a few differences: a far less distinct M_1 phase and a lower upper-boundary for the M_2 region. However, the most notable difference is a new high field phase, M_3, whose upper boundary is determined by the points indicated with small arrows in Fig. 6.6b. (As the field is being increased towards 140 kG, this line becomes almost vertical, making it difficult to identify also in $M(H)|_T$ measurements.)

In order to see how the $H-T$ phase diagram evolves from $H||[120]$ to $H||[110]$, we collected comparable $M(T)|_H$ and $M(H)|_T$ data for an intermediate orientation of the applied field (approximately 12^0 from the easy axis [120]). Fig. 6.9a shows these $M(T)$ curves for $H = 1-70$ kG, with the small arrows indicating the highest-T transition at each field value, as determined from the $d(M*T)/dT$ maxima. Thus, the upper-most phase boundary in Fig. 6.8b, representing the phase diagram for this intermediate position, can be followed in field

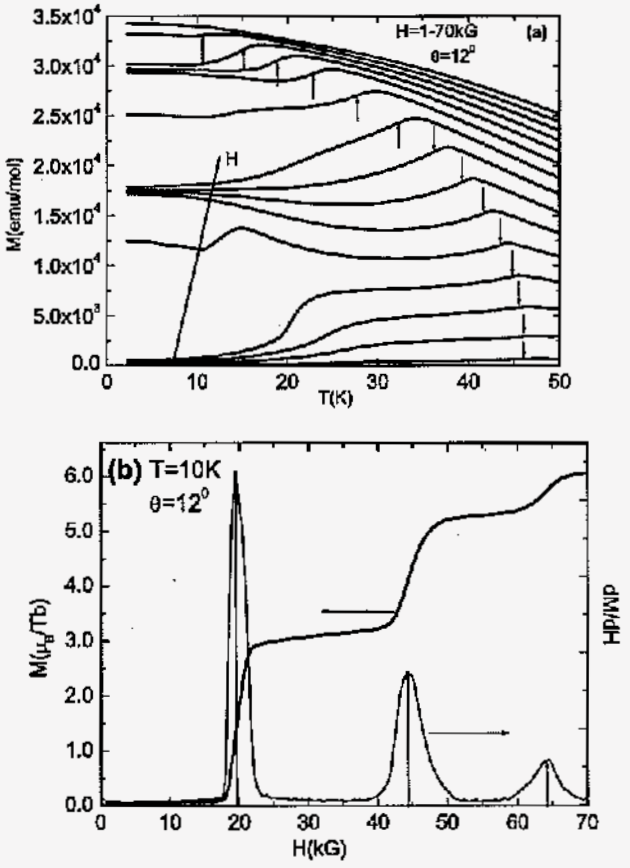

Figure 6.9 (a) M(T) data for various fields: H = 1 kG and 5-70 kG (ΔH = 5 kG) for the intermediate field direction (see text). The small arrows indicate the highest-field transitions at the corresponding temperature. (b) M(H) for T = 10 K, and the corresponding derivative, as an example of how the open symbols on the upper-most phase line in Fig. 6.8b have been determined.

up to $H = 65$ kG (full symbols). For this orientation, we can also identify this line in the $M(H)$ data, and an example is shown in Fig. 6.9b for the $T = 10$ K $M(H)$ isotherm and its dM/dH derivative. Overall, the features common to both Fig. 6.8a and c are also present in Fig. 6.8b; moreover, in going from the [110] to the [120] direction, the M_3 phase is being

compressed, such that in the intermediate position the phase boundary separating it from PM is fully delineated below 70 kG.

Given the clear in-plane anisotropy of the magnetization (Fig. 6.4-6.9), it becomes desirable to systematically determine the angular dependence of the critical fields $H_{ci,j}(\theta)$ and locally saturated magnetizations $M_j(\theta)$ of the $H \perp c$ metamagnetic transitions at $T = 2$ K.

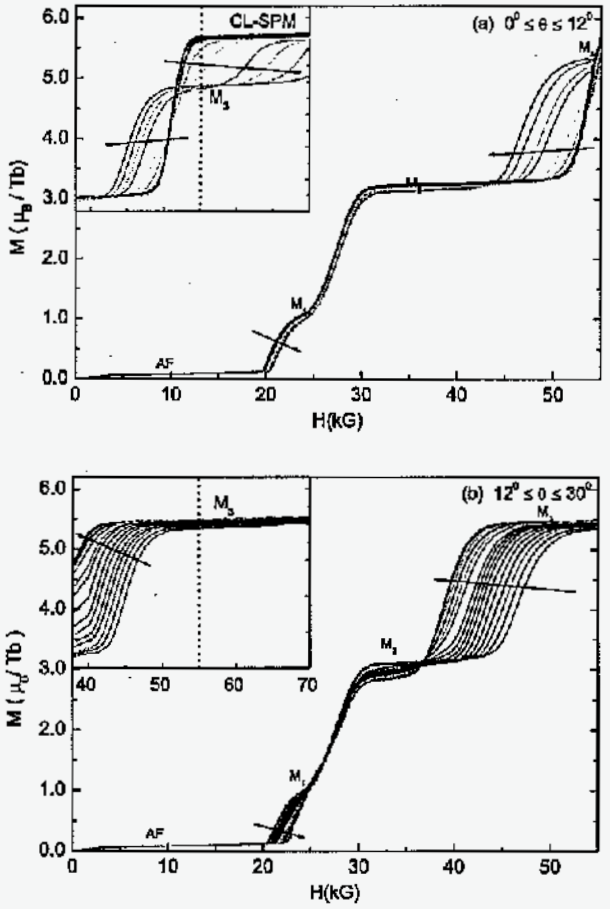

Figure 6.10 M(H) isotherms at T = 2.0 K for (a) $0^0 \leq \theta \leq 12^0$ and (b) $12^0 \leq \theta \leq 30^0$ ($\Delta\theta = 1^0$); inset: enlarged high field, T = 1.85 K (see text) isotherms. Arrows indicate the direction of increasing θ.

Fig. 6.10 shows a series of magnetization isotherms ($T = 2$ K) measured at various angles relative to the easy axis. The critical fields $H_{ci,j}$, for the transition between states i and j, were determined from maxima in dM/dH, as exemplified in Fig. 6.11, and are shown as full symbols in Fig. 6.12a. In most cases, Lorentzian fits of the derivative peaks were used (solid line in Fig. 6.11) to more accurately determine the critical field values. The open symbols in Fig. 6.12 represent reflections of the measured data across the $\theta = 0^0$ direction; whenever the measured points extend beyond the $0^0..30^0$ region, they almost coincide with the calculated reflections, as expected for a symmetry direction.

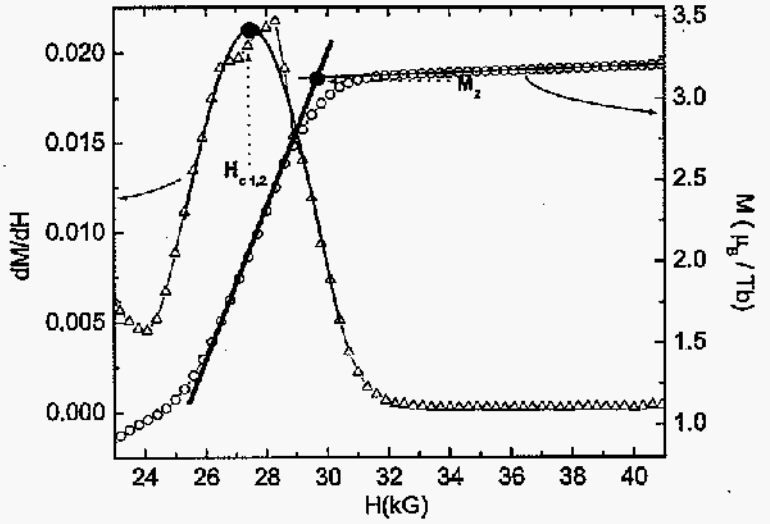

Figure 6.11 Enlarged M(H;$\theta = 12^0$) plot, and the corresponding derivative, illustrating the criteria used in determining the points in Fig. 6.12: large dot on the dM/dH plot indicates the critical field value, determined by the maximum of the Lorentzian fit (solid line) of the peak; straight lines on the M(H) plot are fits to the magnetization plateau (thin), extrapolated down to intersect the maximum-slope line (thick), giving the M_2 value (large dot). Note: the quality of the Lorentzian fit is representative of some of the poorer fits.

For $\theta \leq 12^0$ the antiferromagnetic AF ground state exists for fields up to about 20 kG,

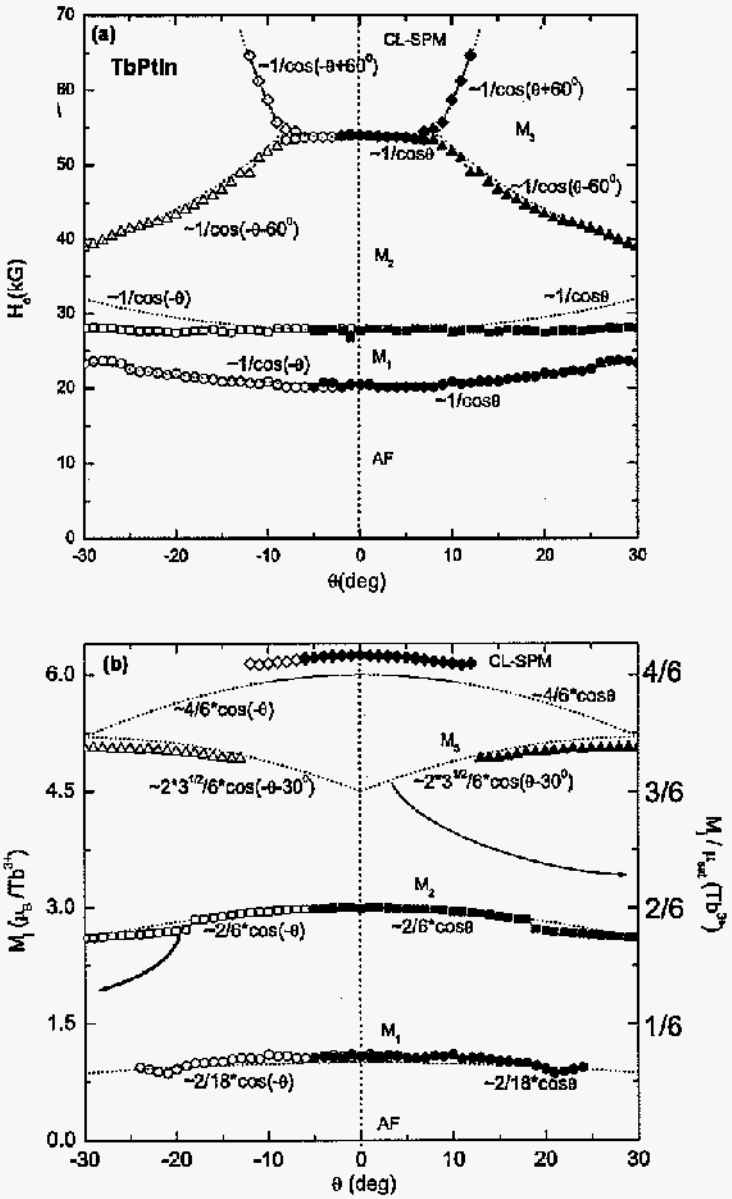

Figure 6.12 (a) Measured critical fields $H_{ci,j}$ and (b) locally saturated magnetizations M_j (full symbols) as a function of angle θ measured from the [120] direction. Open symbols are reflections of the measured data across the $\theta = 0^0$ direction. Also shown are the calculated angular dependencies (dotted lines).

after which two closely spaced metamagnetic transitions occur, with critical fields, at $\theta = 0^0$, $H_{cAF,1} = 20.5$ kG (for the AF to M_1 transition) and $H_{c1,2} = 27.7$ kG (corresponding to the transition from the M_1 to the M_2 state). A third transition from M_2 to $CL-SPM$, around a critical field $H_{c2,CL-SPM} = 53.7$ kG, changes very little with angle up to $\theta \approx 8^0$; for higher angles, another metamagnetic state M_3 forms, being delineated by two distinct critical fields, $H_{c2,3}$ and $H_{c3,CL-SPM}$. As the former decreases with the angle, the latter soon reaches values around the maximum field of 55 kG available in the SQUID magnetometer used for these measurements. In order to follow this latest transition in higher magnetic fields, additional measurements were taken in a different magnetometer, for fields up to 70 kG, and a slightly different temperature ($T = 1.85$ K); these data are shown in the inset in Fig. 6.10a, but by $\theta = 12^0$, $H_{c3,CL-SPM}$ becomes larger than 70 kG, therefore we can only anticipate that this transition still exists for larger angles. (The $H-T$ phase diagrams (Fig. 6.8b and c) seem to indicate that this critical field value increases from $\sim$ 68 kG for $\theta \cong 12^0$, to more than 140 kG at $\theta = 30^0$). Slight differences can be noticed between the data sets taken in the two machines, very likely due to the different temperatures at which they were taken. A linear scaling of the two data sets by a factor of $\sim$ 1.07 was necessary, for both the magnetization values and the critical fields; the scaling of the magnetization values can be explained by an assumption of slightly different angles between the applied field and the rotator axis in each magnetometer, while the field values may have changed with T according to the phase diagrams in Fig. 6.8.

After the scaling of the two data sets, and after additional calibration to the measurements on the large mass 13.55 mg piece, the locally saturated magnetization values were determined. The criterium used for determining the magnetization for each state (M_j), was the onset $M(H)$ value (Fig. 6.11), *i.e.*, the intersection of the linear fit of the M_{j2} magnetization plateau and the highest-slope linear fit of the $M(H)$ curve during the M_{j_1} to M_{j_2} transition. More attention was given to determining the magnetization for the first state (M_1), due to the limited field range over which this state exists. Several criteria tried in this case (onset value, midpoint between transitions, minimum in dM/dH or midpoint on the appropriate linear region on the $M(H)$ curves) resulted in almost identical angular dependencies of M_1; moreover, using any

of the aforementioned criteria, we were still unable to follow this state in the $M(H)$ curves for angles beyond 25^0.

For $\theta > 12^0$, the similar two sets of measurements are shown in Fig. 6.10b. The same criteria were used for the determination of $M_j(\theta)$ and $H_{ci,j}(\theta)$. The two lower metamagnetic transitions can also be seen in this region, while of the higher two, only $H_{c2,3}$ is within our field range; as the angle increases, the first two transitions move closer in field ($H_{cAF,1}$ increases, while $H_{c1,2}$ doesn't vary significantly with θ), such that the M_1 state becomes very narrow, making its determination very difficult. M_2 and M_3 however appear as well defined plateaus, continuously decreasing, and increasing respectively, from the local extremum values seen at $\theta = 0^0$. $H_{c2,3}$ has a minimum of 38.9 kG around $\theta = 30^0$.

The magnetization curves revealed four metamagnetic states, and their angular dependence is presented in Fig. 6.12b: M_1, M_2 and M_{CL-SPM}, which have local maxima at $\theta = 0^0$ around 1.08 μ_B/Tb, 3.00 μ_B/Tb, and 6.25 μ_B/Tb respectively, and M_3 which exists only beyond $\theta = 8^0$ and has a maximum of 5.06 μ_B/Tb at $\theta = 30^0$. Similar to the $H_{ci,j}$ in Fig. 6.12a, the open symbols in Fig. 6.12b represent reflections of the measured data across the $\theta = 0^0$ (easy axis) direction.

The dotted lines in Fig. 6.12a and b are fits to $H_{ci,j}(\theta)$ and $M_j(\theta)$ respectively, as calculated based on the model that will be discussed below. Their angular dependencies are described by $1 \,/\, cos(\theta \pm \varphi_j)$, and $cos(\theta \pm \varphi_j)$ respectively, with $\varphi_j = 0^0$, 30^0 or 60^0. These values are integer or half-integer multiples of $360^0 \,/\, n$, where $n = 6$ in our hexagonal system. Considering the six-fold symmetry of the this compound, these simple geometrical relationships render TbPtIn as very similar to RNi_2B_2C (Canfield, 1997a,b) or $DyAgSb_2$ (Myers, 1999a), tetragonal compounds where the analogues φ_j values were 0^0, 45^0 or 90^0 (integer or half-integer multiples of $360^0 \,/\, n$, where $n = 4$).

As seen earlier in the cases of the tetragonal compounds $HoNi_2B_2C$ (Canfield, 1997b) or $DyAgSb_2$ (Myers, 1999a), simple angular dependencies of the critical fields, as well as of the locally saturated magnetizations exist in the hexagonal compound TbPtIn; this will be further confirmed by similar geometrical relationships that appear to exist in TmAgGe.

6.3 Data analysis

The field and temperature dependent magnetization measurements on TbPtIn (Fig. 6.1 and 6.4) have shown that this compound is extremely anisotropic, with the magnetic moments confined to the hexagonal basal plane. Moreover, when the direction of the applied field is varied within the basal plane, six fold anisotropy of the saturated magnetization is revealed in both TbPtIn and its dilution $(Tb_xY_{1-x})PtIn$ (Fig. 6.5). Consequently, detailed magnetization measurements with $H \perp c$ were performed, allowing us to quantitatively describe the angular dependencies of the critical fields $H_{ci,j}$ and locally saturated magnetizations M_j (Fig. 6.12). By analogy to the four-position clock model (Canfield, 1997b; Myers, 1999a; Kalatsky, 1998) for tetragonal systems, we are now proposing a simple model for the net distribution of moments in the hexagonal compound TbPtIn: three co-planar Ising-like systems, 60^0 apart in the basal plane. Such a hypothesis was first suggested by the high field magnetization values observed in the pure compound TbPtIn, as well as in the highly diluted $(Tb_xY_{1-x})PtIn$. As the maximum measured magnetization for TbPtIn was around 6 μ_B/Tb^{3+} (far smaller than the calculated 9 μ_B value), it is reasonable to assume the existence of more metamagnetic transitions beyond our maximum applied field $H = 140$ kG. However, in the highly diluted compound, where, within our field and temperature ranges, we are only probing the paramagnetic state, the magnetization also reaches only ~ 6 μ_B/Tb^{3+} at the highest H. This is consistent with the $M = 6$ μ_B/Tb^{3+} corresponding to a crystal-field limited saturated paramagnetic (CL-SPM) state. Consequently we chose our model based on three Ising-systems such that it described the hexagonal symmetry of the compound having three magnetic ions in orthorhombic point symmetry, with the above value corresponding to saturation (in the limit of high CEF energy). In order to verify this hypothesis, the expected angular dependencies of possible moment configurations resulting from such a model will be compared with our measurements. Furthermore, we will use our experimental results to refine the model, by considering multiples of the three Ising-like systems, resulting in more complex angular dependencies of the calculated magnetization and critical field values.

In the $P\bar{6}2m$ space group, TbPtIn assumes a hexagonal crystal structure, with 3 Tb^{3+}

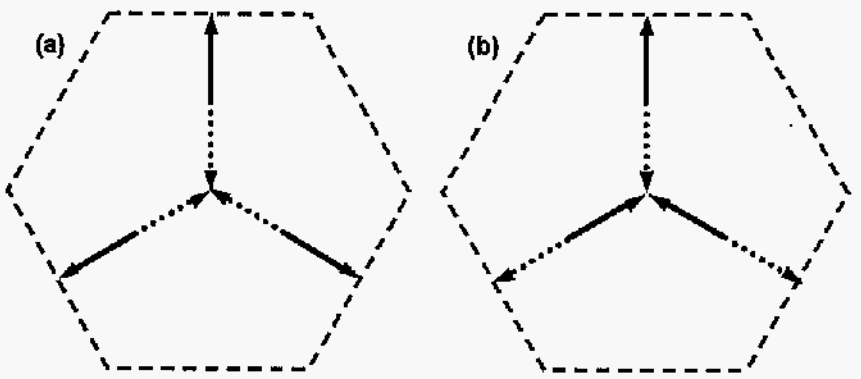

Figure 6.13 Schematic representation of the three co-planar Ising-like systems model with three distinct R in the unit cell, sitting in unique orthorhombic sites) in (a) the antiferromagnetic and (b) the CL-SPM state. Solid arrows: "up" and dotted arrows: "down" orientations of the magnetic moments along the easy axes.

ions at equivalent 3g (orthorhombic) sites. The fact that a strong CEF anisotropy confines the local moments to the basal plane calls for a two dimensional model, greatly simplifying the analysis. (A schematic description of an equivalent three-dimensional model has been introduced for DyAgGe (Morosan, 2004)). Having three equivalent magnetic moments in orthorhombic point symmetry, one possible way to achieve the overall hexagonal symmetry is by restricting the moments to three of the six-fold symmetry axes, 60^0 apart, while allowing for both the 'up' (solid arrows) and 'down' (dotted arrows) positions for a given direction (Fig. 6.13). Any specific Tb-site would, at low temperatures, behave like an Ising system, with each third of the sites having parallel Ising directions. Thus, each metamagnetic state of

TbPtIn can be described by a multiple S of three Ising-like systems along three [120] equivalent directions (the easy axes for this system). We will use $\nwarrow$, $\uparrow$ and $\nearrow$ symbols, to denote the orientation of the three moments in their 'up' positions, and $\searrow$, $\downarrow$ and $\swarrow$ symbols respectively, for the corresponding 'down' positions. The order of the arrows is not meaningful for our model; only the number of arrows for each orientation is significant for the net distribution of moments. Moreover, we describe each metamagnetic state with the minimum-S value moment configuration consistent with the experimental data. However, higher S values are possible for most of the states, and information about the wave vectors (*e.g.* from scattering experiments) would be required to determine unique S values.

Since in our experiments we only measure the projection of the magnetic moment along the field direction, the angular dependence of the magnetization M_j per moment of an arbitrary 3 S-moments configuration is

$M_j(\theta)/\mu_{sat}(\mathrm{Tb}^{3+}) = \frac{1}{3*S}\,[\,\sum_{i=1}^{S} m_i{*}\cos(\theta{-}60^0){+}\sum_{i=1}^{S} m_i{*}\cos\theta + \sum_{i=1}^{S} m_i{*}\cos(\theta{+}60^0)\,]$

where θ is a continuous variable representing the angle between the applied field and the closest easy axis ($-30^0 \leq \theta \leq 30^0$), and the three sums give the magnetization value due to each of the three directions of the Ising-like systems; the m_i parameters equal $\pm$ 1, depending on whether a certain moment is in the 'up' (+ 1) or 'down' (− 1) position for the respective direction. We restrict our model description to the $0^0 \leq \theta \leq 30^0$ angular region, which, by symmetry across the $\theta = 0^0$ direction, also describes the $-30^0 \leq \theta \leq 0^0$ region.

For $S = 1$, our model corresponds to one set of three such Ising-like systems. We assume that in high applied fields, the three magnetic moments occupy the three allowed easy axes closest to the direction of the field; as the field is lowered, the metamagnetic transitions occur such that the measured magnetization is being decreased with H. In this hypothesis, there are three distinct moment configurations for the system: ($\nwarrow\uparrow\nearrow$) for the CL-SPM state, ($\searrow\uparrow\nearrow$) for intermediate field values, and ($\searrow\uparrow\swarrow$) for the AF ground state. The above formula yields the following angular dependencies of the resulting longitudinal (measured) magnetizations: $2/3 * \cos\theta$, $2/3 * \cos(\theta - 60^0)$ and 0 respectively, represented by open circles in Fig. 6.14.

Fig. 6.12b shows that such a model only describes the CL-SPM state:

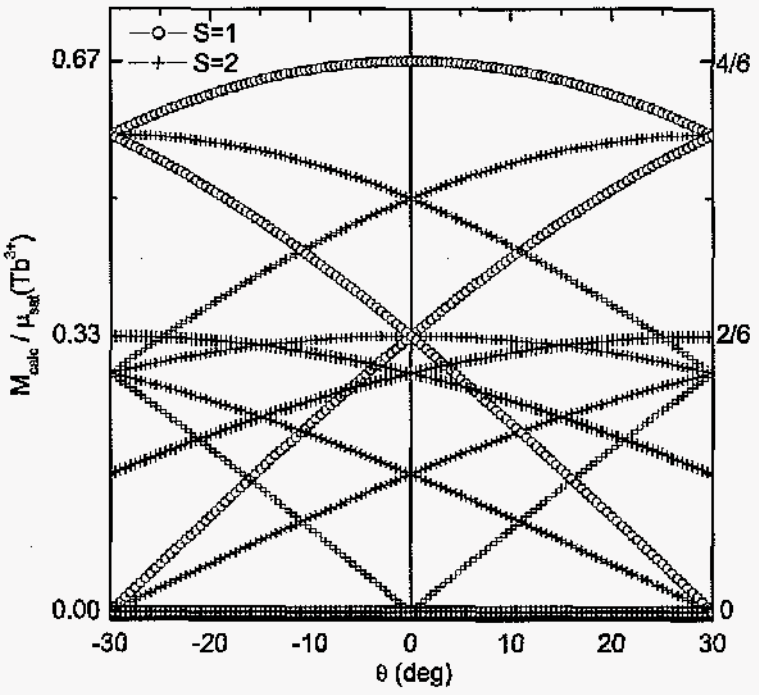

Figure 6.14 Calculated magnetizations as a function of θ, based on the *three coplanar Ising model*: open circles - S = 1 and crosses- S = 2 (see text for details).

$M_{CL-SPM}(\theta)/\mu_{sat}(\mathrm{Tb}^{3+}) = 2/3 * \cos\theta$

and the AF ground state $M_{AF}/\mu_{sat}(\mathrm{Tb}^{3+}) = 0$ of TbPtIn; according to the proposed model, the local moment configurations from which the above angular dependencies follow are (↖↑↗) and (↘↑↙) respectively. It is worth noting that the CL-SPM magnetization value, calculated based on the above moment configuration, is 6 μ_B, smaller than the measured 6.25 μ_B. One possible explanation is that with increasing field, the system is slowly approaching the CEF splitting energy. This is also consistent with the increasing plateaus in the high field magnetization data in Fig. 6.4a; however, the extrapolation of these plateaus down to $H = 0$ results in smaller values for the [120] direction (6.13 μ_B) and the [110] direction (5.35 μ_B), closer to

the calculated values (6.0 μ_B and $\sqrt{3}/2 * 6\ \mu_B\ =\ 5.2\ \mu_B$ respectively).

To characterize all the other observed metamagnetic states, larger S-values are needed, *i.e.*, the local moment configurations are described by an integer multiple $S\ >\ 1$ of sets of three Ising-like systems. Fig. 6.14 (crosses) also shows all possible angular dependencies of the magnetizations resulting from such a generalized model when $S\ =\ 2$. By comparison with the experimental data, it appears from Fig. 6.12b that two more metamagnetic states can now be described with $S\ =\ 2$:

$M_3(\theta)/\mu_{sat}(\mathrm{Tb}^{3+})\ =\ 2\sqrt{3}/6 * \cos(\theta - 30^0)$ (moment configuration (↖↖↑↑↙↗)),

and

$M_2(\theta)/\mu_{sat}(\mathrm{Tb}^{3+})\ =\ 2/6 * \cos\theta$ (moment configuration (↘↖↑↑↙↗)) .

There is still one more metamagnetic state, M_1, which cannot be described within the $S\ =\ 2$ model; however, for most of the angular range, its magnetization has an angular dependence consistent with: $M_1(\theta)/\mu_{sat}(\mathrm{Tb}^{3+})\ =\ 2/18 * \cos\theta$. The $\cos\theta$ dependence (*i.e.* cos is an even function) requires that the moment configuration be symmetric with respect to the $\theta\ =\ 0^0$ direction. The simplest possibility is (↖↑↗), for which the magnetization varies as $2/3 * \cos\theta$; to this, a number of sets of three moments needs to be added, with zero net magnetization (*e.g.* multiples of (↘↑↙) or (↘↖↑↓↙↗)), to get a resulting magnetization amplitude of 2/18. Consequently a minimum $S\ =\ 6$ configuration (↘↘↘↘↘↖↑↑↑↑↑↙↙↙↙↙↗) or (↘↘↘↖↖↖↓↓↑↑↑↑↙↙↙↗↗↗) yields the desired calculated magnetization $2/18 * \cos\theta$.

Assuming the above net distributions of moments for the observed metamagnetic states, one can derive the expected angular dependencies of the critical fields. Comparison between the data in Fig. 6.12a and these calculated $H_{ci,j}(\theta)$ values will further confirm or refute the net distributions of moments proposed above.

Since the energy associated with a magnetic moment $\overrightarrow{M}$ in an applied field $\overrightarrow{H}$ is $\overrightarrow{M} \cdot \overrightarrow{H}$ (Myers, 1999a), the corresponding energy difference ΔE_{ji} between metamagnetic states $\overrightarrow{M_i}$ and $\overrightarrow{M_j}$ is:

$\Delta E_{ji}\ =\ \overrightarrow{M_j} \cdot \overrightarrow{H} - \overrightarrow{M_i} \cdot \overrightarrow{H}$

If there is a critical energy $E_c = \Delta E_{ji}$ to be exceeded for a metamagnetic transition between

states i and j to occur, than the critical field value is given by:

$H_{ci,j} = \frac{E_a}{M_j - M_i}$,

where M_j and M_i are the measured (projections along the field) respective magnetizations. The numerator in the above expression is angle and field independent, and the angular dependence of $H_{ci,j}$ follows only from the denominator. In other words,

$H_{ci,j} \sim \frac{1}{M_j - M_i}$.

Consequently, the expected critical field values, shown as dotted lines in Fig. 6.12a, are:

$H_{cAF,1}(\theta) \sim 1/\cos\theta$,

$H_{c1,2}(\theta) \sim 1/\cos\theta$,

$H_{c2,3}(\theta) \sim 1/\cos(\theta - 60^0)$,

$H_{c3,CL-SPM}(\theta) \sim 1/\cos(\theta + 60^0)$

and $H_{c2,CL-SPM}(\theta) \sim 1/\cos\theta$.

The reflections across the $\theta = 0^0$ direction result from the above formulas, when substituting θ with $-\theta$; moreover, since *cos* is an even function, this is equivalent to a change in sign only for the φ in the above expressions written as $1/\cos(\theta - \varphi)$.

As described above and similar to the analogous study in the tetragonal compound $HoNi_2B_2C$ (Canfield, 1997b), in most cases we used maxima in dM/dH, and not the on-set criterion, to determine the critical field values, because the magnetizations during the transition were not always linear; however, comparison with the calculated critical fields based on the above model is still appropriate, given that only small departures from linearity were encountered, mostly close to the bordering states (M_i and M_j). (The non-linear change of the magnetization with increasing field indicates that other factors (*i.e.* the demagnetization factor of the sample (Suzuki, 2002), coexistence of more than two phases, non-linear superposition of the various states) may be responsible for the broadening of the transition).

Comparison of the measured critical fields and locally saturated magnetizations (Fig. 6.12a,b full and open symbols) with the calculated values as described above (Fig. 6.12a,b dotted lines) confirms, in most cases, the assumed local distribution of moments. However, the first metamagnetic state M_1 follows well the calculated $2/18 * \mu_{sat}(Tb^{3+}) * \cos(\theta)$ dependence

up to $\theta \approx 25^0$, after which it is difficult to determine it with reasonable accuracy. Despite the fact that both $H_{cAF,1}$ and $H_{c1,2}$ should depend on this magnetization value, the former follows the expected angular dependence fairly well, whereas the latter falls under the calculated $1/\cos\theta$ curve. Even though at this point we don't have a rigorous calculation to support our assumption, we anticipate that the proximity of the two lowest transitions requires a calculation with more than two coexisting phases, which may render a better fit of the observed experimental data in this region. On the other hand, the $H_{c2,3}$ and $H_{c3,CL-SPM}$ critical fields, which have the most evident angular dependence, are well fitted by the calculated functions based on the present model. It is thus reasonable to assume that, whereas possibilities for refining the model exist, in the simple form that we present here it describes our system fairly well.

The polar plot in Fig. 6.15 helps in understanding how the hexagonal crystal structure of this compound is reflected in the angular dependence of the metamagnetic phase transitions: similar to the polar phase diagrams for tetragonal compounds $HoNi_2B_2C$ (Kalatsky, 1998) or $DyAgSb_2$ (Myers, 1999a), when we plot $H_c * \sin\theta$ vs. $H_c * \cos\theta$, the phase boundaries become straight lines, with slopes equal to either $\pm\, 1/\sqrt{3}$ or ∞. These slopes correspond to directions either parallel or perpendicular to the high symmetry axes (*i.e.* [110] or [120]) in the hexagonal structure, just as within the four position clock model the corresponding phase lines were either parallel or perpendicular to the tetragonal high symmetry axes ([110] or [010]). As described in Myers *et al.* (Myers, 1999a), the equations of these straight lines in polar coordinates can be used to verify the transitions already discussed: if we substitute the above slope values in the general formula

$$R(\theta) \;=\; a/(\sin\theta - b * \cos\theta),$$

for a line with slope b, we get:

$$H_c(\theta) \;\sim\; 1/\cos\theta \text{ for } b \;=\; \infty$$

$$H_c(\theta) \;\sim\; 1/\cos(\theta - 60^0) \text{ for } b \;=\; -1/\sqrt{3}, \text{ or}$$

$$H_c(\theta) \;\sim\; 1/\cos(\theta + 60^0) \text{ for } b \;=\; 1/\sqrt{3},$$

which are consistent with the angular dependencies of the transitions determined above.

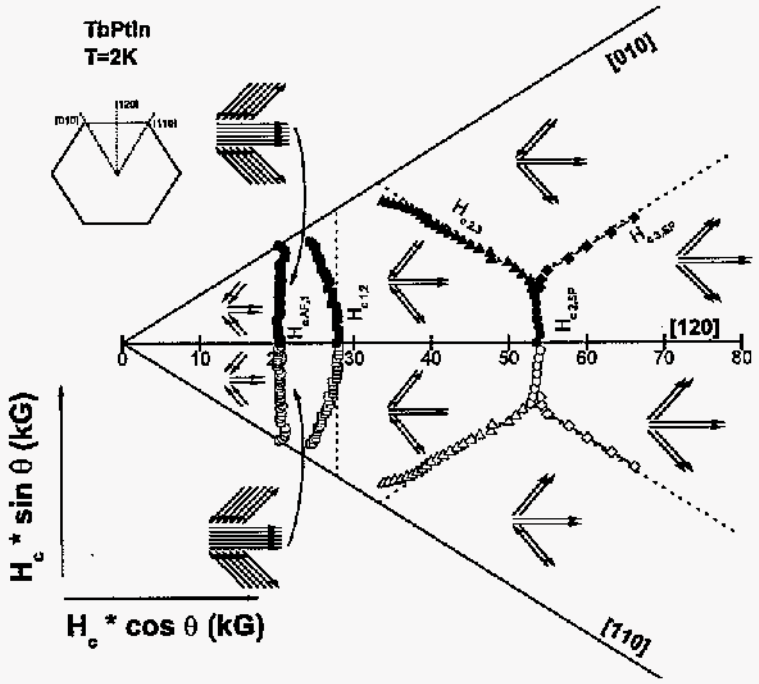

Figure 6.15 Polar plot of the critical fields $H_{ci,j}$, with one possible moment configuration shown for each observed metamagnetic state; open symbols represent reflections of the measured data -full symbols- across the $\theta = 0^0$ direction (see text).

For the most part, the experimental points fall onto the calculated straight lines, as expected. Some deviations from the straight lines can be noticed, with the most evident one for $H_{c1,2}$, for which we already emphasized the necessity of a more complex model. In a similar manner (even though only for fewer angles), $H_{c2,3}$ curves under the calculated straight line as we move away from the [120] easy axis, while some even smaller deviations from lincarity are apparent in $H_{cAF,1}$; this may indicate that special attention needs to be paid in determining the angular dependence of the critical fields, when rotating from the proximity of one easy axis to another.

6.4 TmAgGe

We already reported the basic magnetic properties of TmAgGe (Morosan 2004), which strongly resemble those of TbPtIn: the magnetic susceptibility is extremely anisotropic (Fig. 5.23), indicating antiferromagnetic order below $T_N = 4.2$ K. The local magnetic moments are confined by the strong CEF anisotropy to the basal plane, both below and above T_N. This can also be seen in the field dependent magnetization measurements, shown in Fig. 5.26a, where in-plane anisotropy of the ordered state is also apparent. Similar to the case of TbPtIn, several metamagnetic transitions exist for both $H||[110]$ and $H||[120]$; these result in magnetization values of 4.92 μ_B and 4.30 μ_B respectively, at $H = 70$ kG, far below $\mu_{sat}(Tm^{3+}) = 7.0\ \mu_B$, whereas for the c direction, the magnetization is linear and much smaller up to the maximum applied field. The ratio of the two in-plane magnetizations is $\frac{M([120])}{M([110])} = 0.87$, close to the $\cos 30^0$ value expected within the model described before for TbPtIn for the CL-SPM state. However, the two absolute values are larger than the corresponding ones, calculated from the above model: $M([110]) = 4.67\mu_B$ and $M([120]) = 4.00\ \mu_B$, but the extrapolation of the high-field plateaus down to $H = 0$ (solid lines in Fig. 5.26a) yields magnetizations very close to these calculated values. As in the case of TbPtIn, the slight increase of the magnetization plateaus after the supposed saturation may be caused by the slow approach of the CEF splitting energy.

In calculating the above expected magnetization values, we assumed the easy axes to be along the [110]-equivalent directions, based on the directions where maximum magnetization values at $H = 70$ kG were achieved (Fig. 5.26a). This is consistent with the angular dependent magnetization measurement for $H = 70$ kG shown in Fig. 6.16, where angle θ was measured from the [110] direction; thus the six-fold symmetric magnetization has maxima occurring for the [110]-equivalent directions (*i.e.* for $\theta = n * 60^0$, where n is an integer). Consequently, for TmAgGe the angle θ will be measured from the closest [110] easy axis. The comparison of TmAgGe and TbPtIn indicates that, even though the easy axes in the two compounds correspond to the two different sets of six-fold symmetry directions, as we shall see, their physical properties are very similar.

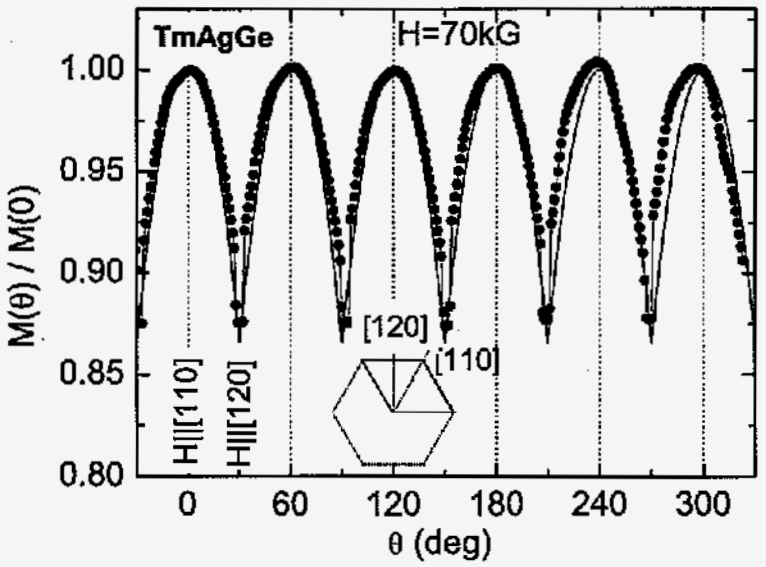

Figure 6.16 M(θ) of TmAgGe (full symbols) at T = 2 K and H = 70 kG, H⊥c. Solid line: calculated magnetization $M_{max} * \cos(\theta - n * 60^0)$, n-integer. Note: $\theta = 0^0$ is defined at the [110] direction.

Around each easy axis, these magnetization measurements follow the $\cos\theta$ angular dependence (the solid line in Fig. 6.16), as expected within our proposed model. Some differences between the the experimental data (filled circles in Fig. 6.16) and the magnetization could be caused by small misalignment of the sample (rendering slightly asymmetric measured peaks), or by the strong interactions between the local moments. Similar to TbPtIn, this also indicates that different metamagnetic states cross $H = 70$ kG at different angles.

From the $M(T)\,|_{H,\theta}$ (Fig. 6.17) and $M(H)\,|_{T,\theta}$ (Fig. 6.18) measurements, detailed $H-T$ phase diagrams for this compound can be determined. They are shown in Fig. 6.19a,c, for field along the [110] or $\theta = 0^0$, and [120] or $\theta = 30^0$ directions respectively, with an intermediate-position $\theta \approx 24^0$ phase diagram in Fig. 6.19b. In the same manner used for TbPtIn, the points in these phase diagrams have been obtained from maxima in either $d(M*T/H)/dT$ for

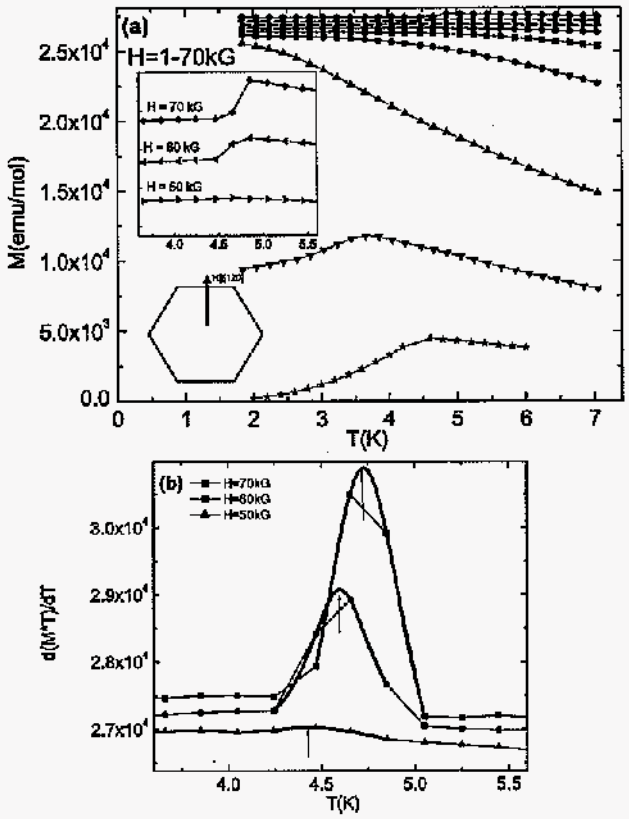

Figure 6.17 (a) M(T) data for H = 1, 5 kG and 10 - 70 kG (ΔH = 10 kG) for H||[120], with enlarged high-field data in the inset; (b) M*T derivatives for H = 50, 60 and 70 kG, together with the Lorentzian fits of the maxima (solid lines), illustrating how the vertical line in Fig.22c was determined for high applied fields.

constant field (full symbols) or in dM/dH for fixed temperatures (open symbols).

For $H||[110]$ (Fig. 6.19a), at low temperatures the antiferromagnetic, AF, ground state exists for $H \leq 3.1$ kG, followed by a small intermediate phase M_1 (up to $\sim$ 4.4 kG) and a larger state M_2 above. This latest phase extends up to 8.9 kG, after which, at low temperatures, the system reaches the crystal field-limited saturated paramagnetic, CL-SPM, state. As temperature is increased, the M_1 phase disappears around 2.5 K , and a direct

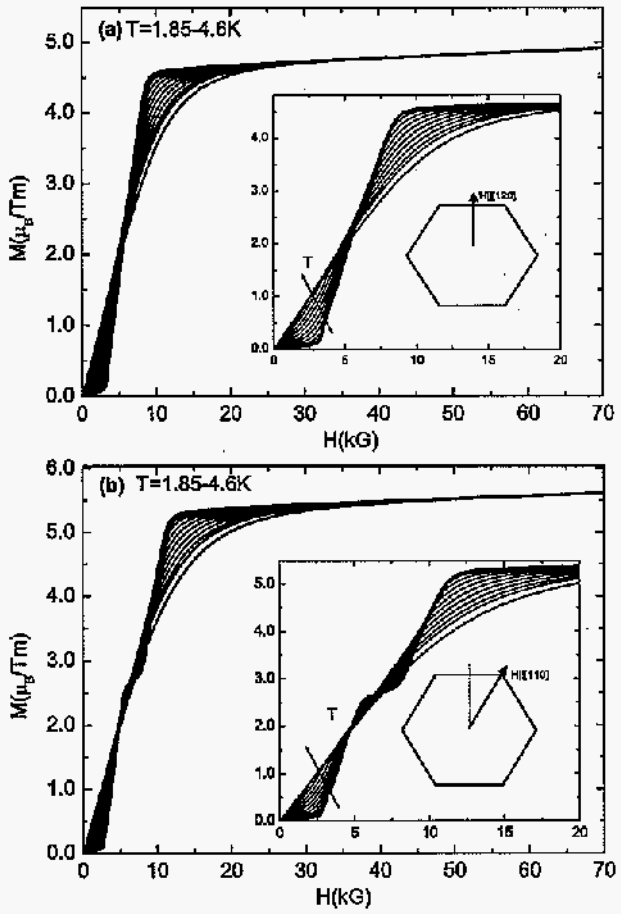

Figure 6.18 M(H) isotherms for T = 1.85, 2 − 4 K (ΔT = 0.25 K), 4.2 and 4.6 K for (a) H‖[120] and (b) H‖[110]; insets show the enlarged data around the metamagnetic transitions. (Arrows indicate direction of increasing T.)

transition from the AF to the M_2 state occurs at a decreasing critical field value. The upper phase boundary (for the M_2 to the PM state transition) also falls down in field as T increases, such that at very low fields only one transition is observed close to T_N = 4.2 K.

As we rotate away from the easy axis, the low-field phase diagram changes very little, with a small enhancement of the critical field values towards low temperatures. As field is being

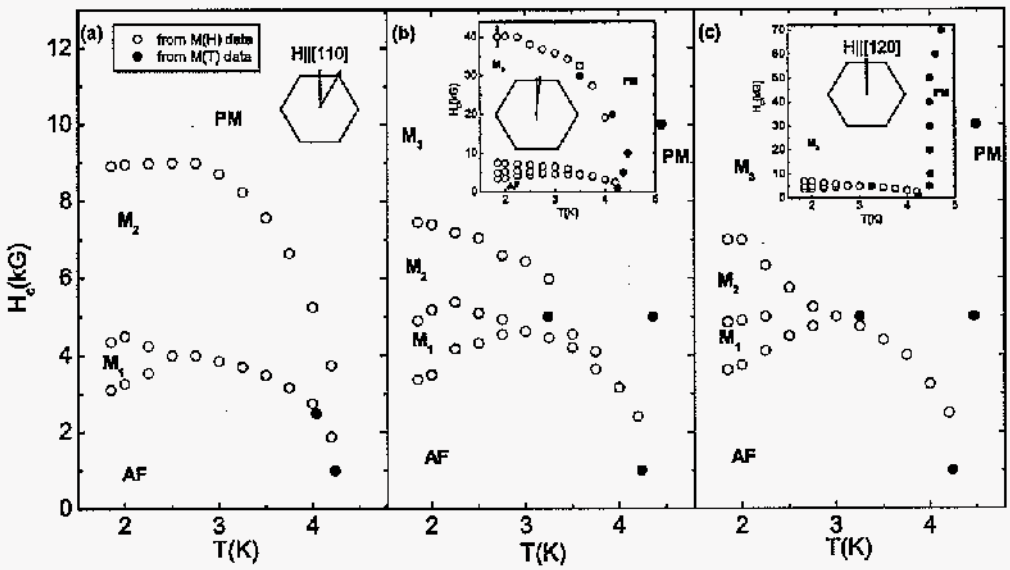

Figure 6.19 H-T phase diagrams for TmAgGe, with (a) H$\|$[110] and (c) H$\|$[120], as determined from magnetization data in Fig.20-21; (b) intermediate-position phase diagram (see text); the error bar shown in inset of (b) represents the range of values for the high-field line, as determined from Fig. 6.20.

increased, M_2 is getting smaller as a new distinct phase M_3 forms. Its upper bordering line appears to have a strong angular dependence, as can be seen in Fig. 6.19b and c, similar to the upper-most phase boundary seen in TbPtIn : for $H\|$[120] (Fig. 6.19c), this phase boundary is an almost vertical line at $T \approx 4.5$K, up to our maximum applied field $H = 70$ kG. As a consequence, the corresponding points on this line have been determined from $d(M*T/H)/dT$ data, as shown in Fig. 6.17c for high fields, and could not be identified in the field-dependent derivatives. At low temperatures, the $H_{cAF,1}$ and $H_{c1,2}$ values (3.62 kG and 4.86 kG respectively) are very close to the corresponding ones in the [110] direction, whereas the M_2 to M_3 transition occurs around 7.0 kG. These three phase lines merge around $T = 3.0$ K, such that for higher temperatures a single transition occurs at decreasing fields. This line

appears to intersect the $H = 0$ axis around $T_N = 4.2$ K.

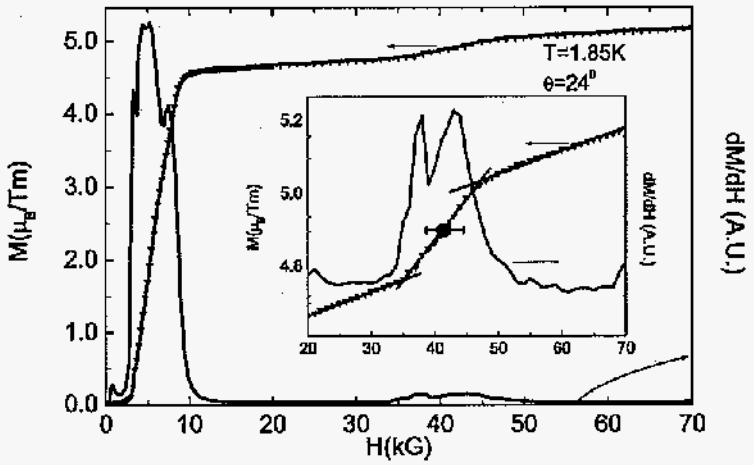

Figure 6.20 M(H) for T = 1.85 K (symbols), and the corresponding derivative (line). The inset shows an enlargement around the high field transition, to exemplify the two criteria used for determining this critical field (see text). Note: the error bar shown in the inset (determined from the position of the peaks in the derivative) gives a caliper of the uncertainty in determining this critical field value.

The intermediate-orientation phase diagram presented in Fig. 6.19b allowed us to observe the upper-most phase line moving down in field at low temperatures, such that for $\theta \approx 24^0$, it intersects the $T = 0$ axis close to 40.1 kG. In this orientation, this phase boundary can be identified in the M(H) derivative, as shown in Fig. 6.19 for $T = 1.85$ K. However, the high field peak in dM/dH is poorly defined, making the determination of the corresponding critical field value more difficult. For a more precise estimate, another criterium was used together with the derivative maxima, as illustrated in the inset in Fig. 6.19: the mid-point (large dot) on the highest-slope linear fit (solid line) of the magnetization data around the transition. Also shown is the error bar for this critical field value, as determined from the two criteria used here.

The fact that this line is now apparent in both $M(T)$ and $M(H)$ data is further confirmation that this phase boundary exists, whereas at lower fields, the only noticeable difference from the $H||[120]$ direction is the persistence of the M_2 state up to higher (*i.e.* $\sim$ 3.5 K) temperatures.

A number of similarities between TbPtIn and TmAgGe have already been established: same crystal structure, antiferromagnetic ground state, extremely anisotropic magnetization, in-plane anisotropy and metamagnetism leading to crystal field-limited saturated magnetizations smaller than the calculated single ion μ_{sat} values. As a consequence, we proceed to study the angular dependence of the planar metamagnetism in TmAgGe, and subsequently apply the model developed for TbPtIn to the case of this compound.

When we fix the temperature at $T = 2$ K, the angular dependence of the metamagnetic transitions can be studied based on the $M(H)$ isotherms shown in Fig. 6.21. The critical fields and the locally saturated magnetization values (full symbols in Fig. 6.22) have been determined as maxima in dM/dH, and from on-set values respectively (see the TbPtIn section). An exception was made for M_{CL-SPM} above 10^0, and the criterion used for determining this state is described below. Moreover, because of the proximity of the first two transitions, the M_1 state is poorly defined; no precise saturated magnetization data could be extracted for this state, but the phase diagrams in Fig. 6.19, as well as the angular dependent critical fields in Fig. 6.22a, are consistent with the existence of this phase. As before, the open symbols in Fig. 6.22 represent reflections of the measured data across the $\theta = 0^0$ direction. The TmAgGe measurements allowed us to determine the critical field and locally saturated magnetization values for the full angular range ($-30^0 \leq \theta \leq 30^0$); the resulting somewhat asymmetric data (most obvious in the case of the M_2 data) maybe due to a small sample misalignment. The experimental data (full symbols) together with the reflections (open symbols) in Fig. 6.22 give the caliper of the error bars for these measurements.

For $\theta \leq 10^0$, two closely spaced metamagnetic transitions can be seen in Fig. 6.22a, with critical fields $H_{cAF,1} = 3.0$ kG and $H_{c1,2} = 4.37$ kG respectively at $\theta = 0^0$, followed by a third transition $H_{c2,CL-SPM}$ at $\sim$ 9.37 kG. It should be noted that these $H_{ci,j}$ values are slightly different from the corresponding ones (3.10 kG, 4.36 kG and 8.92 kG respectively at

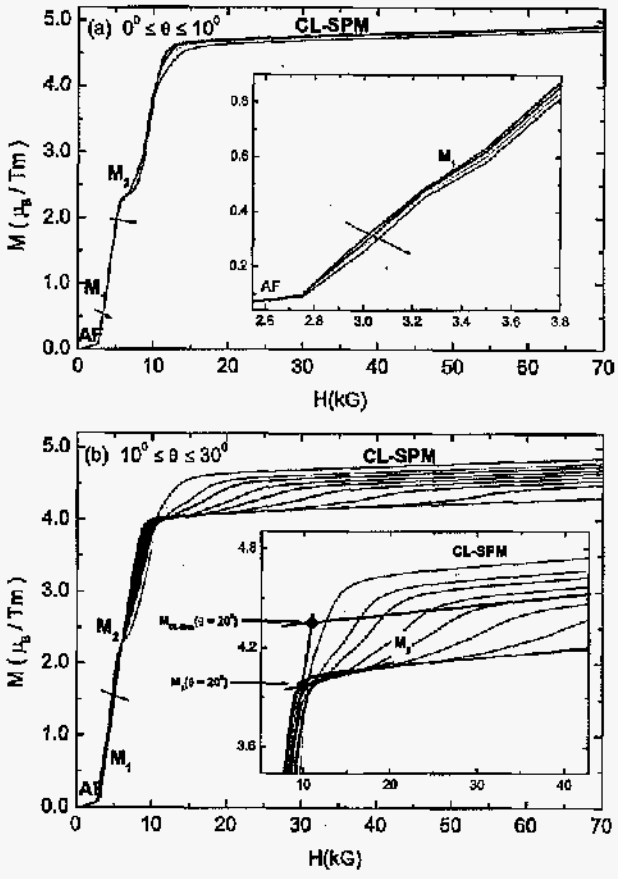

Figure 6.21 M(H) isotherms ($T = 2.0$ K) for (a) $0^0 \leq \theta \leq 10^0$, $\Delta\theta = 2^0$ (enlarged M_1 state shown in the inset) and (b) $10^0 \leq \theta \leq 30^0$, $\Delta\theta = 2^0$; inset in (b) shows the extrapolation of the two higher metamagnetic states down to lower fields, such that the intersection with the maximum-slope line gives the magnetization values M_3 and M_{CL-SPM}- solid dots (see text). Arrows indicate increasing θ.

$T = 2.0$ K, $\theta = 0^0$) in the $H-T$ phase diagrams (Fig. 6.19a), as they have been determined from two distinct measurements. Thus small errors in the angular position ($\pm 1^0$) may convert into small errors in the critical field values ($\leq 3\%$).

Somewhat larger differences between the two data sets are observed for $\theta \geq 10^0$, specifically

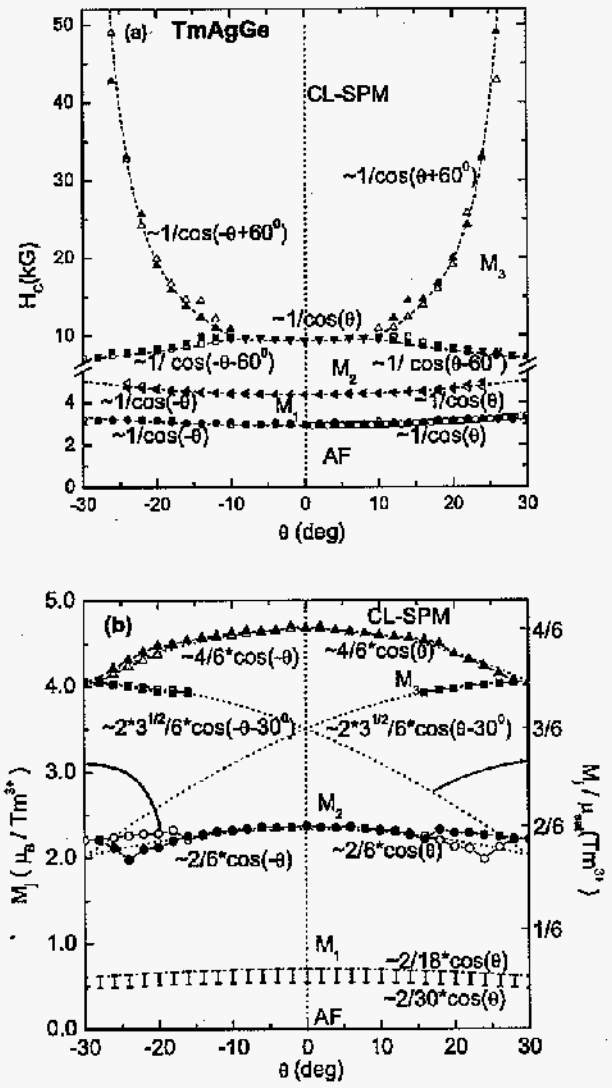

Figure 6.22 (a) Measured critical fields $H_{ci,j}$ and (b) locally saturated magnetizations M_j (full symbols), as a function of angle θ measured from the easy axis. Open symbols are reflections across the $\theta = 0^0$ direction (see text). Also shown are the calculated angular dependencies of $H_{ci,j}$ and M_j (dotted lines). The error bars shown in the low part of (b) give the range of values that we can infer for M_1 from the data shown in Fig. 6.21.

for $H_{c3,CL-SPM}$, which varies more rapidly with the angle than any other critical field. In this angular region, the two lower transitions occur at almost the same critical fields as below 10^0, whereas the critical field for the third one slowly decreases with angle, as a fourth transition appears and rapidly moves up in field. Consequently, the M_1 metamagnetic state changes little with the angle, whereas the M_2 state narrows down as the bordering critical fields move closer to each other. The fourth transition being very broad makes the determination of the M_3 state fairly difficult. Also, with $H_{c3,CL-SPM}$ broadening out and rapidly moving towards our field limit (*i.e.* 70 kG), it was difficult to get a meaningful linear fit of the $M(H)$ curves during the M_3 to $CL-SPM$ transition; instead we used the intersection of the maximum slope line corresponding to the M_2 to M_3 transition, and the best linear fit of the highest magnetization state, to determine M_{CL-SPM} for $\theta \geq 10^0$ (Fig. 6.21b, inset).

The best fits to the experimentally measured angular dependent data are shown in Fig. 6.22 as dotted lines. We will use these fits to infer the net distribution of moments as multiples S of three Ising-like systems, similar to the case of TbPtIn. As mentioned before, we infer that the M_1 state should exist based on the angular dependent critical fields in Fig. 6.22a, and the $T = 2.0$ K metamagnetic phases revealed by the phase diagrams in Fig. 6.19. Consequently, in Fig. 6.22b we are only showing the expected angular dependence of such a phase, by analogy with the TbPtIn case: $M_1^{calc}/\mu_{sat}(\mathrm{Tm}^{3+}) = 2/18{*}cos\theta$, which appears to be the upper limit of these magnetization values, as indicated by the error bars shown in Fig. 6.22b. As already seen for TbPtIn, the moment configuration that would result in such a M_1 magnetization is a $S = 6$ state: (↘↘↘↘↘↖↑↑↑↑↑↙↙↙↙↙↗) or (↘↘↘↖↖↖↓↓↑↑↑↑↙↙↙↗↗↗). $M_2(\theta)$ has a maximum value at $\theta = 0^0$ equal to 2.37 μ_B/Tm^{3+}, close to $2/6 * \mu_{sat}(Tm^{3+}) = 2/6 * 7\mu_B/\mathrm{Tm}^{3+}$, and a $\cos\theta$ angular dependence. This suggests that a possible net distribution of moments for this state, realized with a minimum $S = 2$, could be (↘↖↑↑↙↗). If one local moment is flipped from its ↙ position to ↗ in the previous state, the resulting state could be described by the (↘↖↑↑↗↗) configuration, whose magnetization varies as $2\sqrt{3}/6 * \mu_{sat}(\mathrm{Tm}^{3+}) * \cos(\theta - 30^0)$; this fits well the measured M_3 data, indicating that the previously assumed local moment distribution may be appropriate for this metamagnetic state.

When all the magnetic moments are in their 'up' positions, the CL-SPM (↖↖↑↑↗↗) state is achieved, and the corresponding angular dependence is $4/6 * \mu_{sat}(\mathrm{Tm}^{3+}) * \cos\theta$. This best describes the last observed metamagnetic state, which has a maximum of $4.68\mu_B/\mathrm{Tm}^{3+}$ around $\theta = 0^0$, very close to $4/6 * \mu_{sat}(\mathrm{Tm}^{3+}) = 4/6 * 7\mu_B/\mathrm{Tm}^{3+}$. (As before, the order of the arrows used to describe the net distribution of moments has no physical meaning).

According to the calculation given in the case of TbPtIn, for TmAgGe one would also expect the critical fields to vary with the angle θ as

$H_{ci,j} \sim \frac{1}{M_j - M_i}$.

Using the net distributions of moments assumed above to best describe the locally saturated magnetization states, we expect the following angular dependencies of the critical fields:

$H_{cAF,1}(\theta) \sim 1/\cos\theta$,

$H_{c1,2}(\theta) \sim 1/\cos\theta$

$H_{c2,3}(\theta) \sim 1/\cos(\theta - 60^0)$,

$H_{c3,CL-SPM} \sim 1/\cos(\theta + 60^0)$

and $H_{c2,CL-SPM}(\theta) \sim 1/\cos\theta$.

The experimental data (full symbols in Fig. 6.22a) are in good agreement with these calculated critical fields, with $H_{c2,CL-SPM}(\theta)$ present only for $\theta \leq 10^0$, while the $H_{c2,3}$ and $H_{c3,CL-SPM}$ exist only for $\theta \geq 10^0$. This is consistent with the presence of the M_3 state for angles larger than 10^0, even though experimentally we were only able to accurately determine it for $\theta \geq 16^0$. (The bordering transitions of this state are very close in field when θ is close to 10^0, which made the determination of M_3 in this angular region difficult). It is worth pointing out the excellent fit of the measured $H_{c3,CL-SPM}$ data with the calculated angular dependency, this transition showing the most dramatic change with the angle θ.

Apart from the absolute values of the critical fields and the locally saturated magnetizations, the $H_c(\theta)$ and $M_{sat}(\theta)$ phase diagrams for TmAgGe (Fig. 6.22) are identical to the TbPtIn analogues in Fig. 6.12: to the same number of critical fields with identical angular dependencies correspond identical metamagnetic values (scaled to the saturated moment of the respective R^{3+} ion), which also vary similarly with the angle. This is consistent with our

model being indeed a general description of the Fe_2P-type systems, or even more generally, of hexagonal systems with the R in orthorhombic point symmetry.

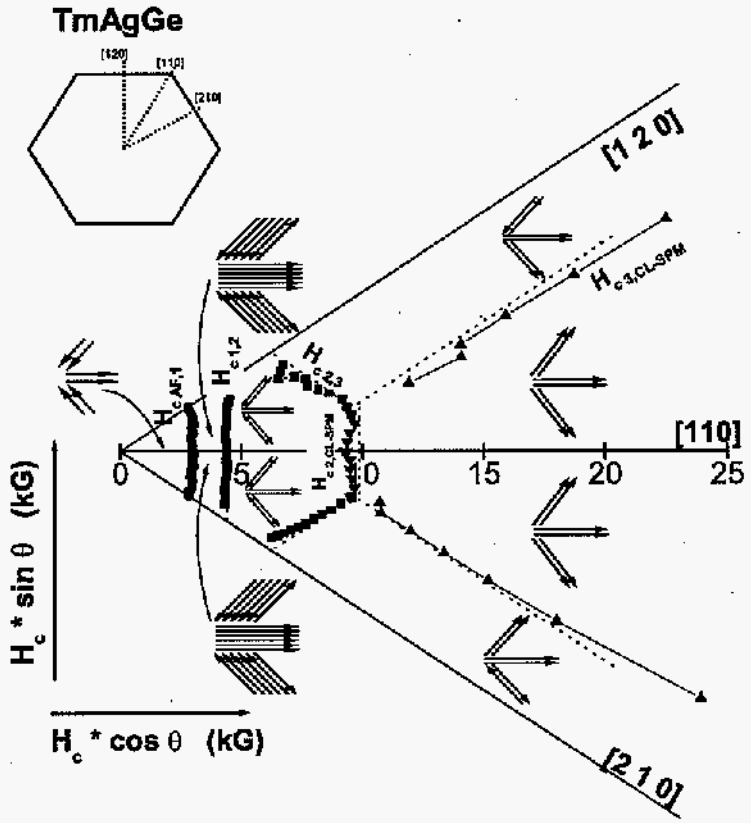

Figure 6.23 Polar plot of the critical fields H_c, with one of the possible moment configurations shown for each observed metamagnetic state.

When the $H_c(\theta)$ phase diagram for TmAgGe is converted into a polar plot (Fig. 6.23), similar to that for TbPtIn, we again notice that the phase boundaries are straight lines, with $\pm 1/\sqrt{3}$ or ∞ slopes. From the equations of these straight lines, we can once more confirm the transitions determined before:

$H_c(\theta) \sim 1/\cos\theta$ for $b = \infty$

$H_c(\theta) \sim 1/\cos(\theta - 60^0)$ for $b = -1/\sqrt{3}$, or

$H_c(\theta) \sim 1/\cos(\theta + 60^0)$ for $b = 1/\sqrt{3}$.

As already noted, in the case of TmAgGe, we were able to determine the critical fields from experimental data for $\theta = -30^0 .. 30^0$, as seen in the phase diagrams in Fig. 6.22a, as well as in Fig. 6.23. Slight differences between the expected straight lines in Fig. 6.23 and measured critical fields can be noticed for $H_{c2,3}$ for angles close to $\pm 30^0$, or for $H_{c3,CL-SPM}$ also for large angles; besides being a consequence of small misorientation of the sample, this may indicate, similar to the TbPtIn case, that a more complex model needs to be used to describe the regions around the 'hard' in-plane direction.

6.5 Angular dependent metamagnetism at $T = 20$ K in TbPtIn

Whereas TmAgGe has fairly simple $H-T$ phase diagrams, with all metamagnetic phases present at low temperatures, the TbPtIn phase diagrams are somewhat more complex, manifesting an additional intermediate-temperature phase, M_4 (Fig. 6.8). In order to perform a similar angular dependent study of this metamagnetic state, a set of $M(H)|_\theta$ data was taken at $T = 20$ K. Assuming that all existing transitions have been identified and are shown in Fig. 6.8 (at least below 20 K), at this temperature the $M(H)$ curves should intersect the same magnetic phases as in the low temperature case, with the exception of M_1; instead, the measurements at $T = 20$ K intersect the bubble-like phase M_4, as seen in the three different orientations phase diagrams in Fig. 6.8.

Fig. 6.24 shows the $M(H)$ isotherms at $T = 20$ K for various angles θ. The $M_j(\theta)$ and $H_{ci,j}(\theta)$ phase diagrams have been determined as described before for TbPtIn or TmAgGe for $T = 2$ K, and are shown in Fig. 6.25. It should be noted that, due to the enhanced temperature, all transitions are broadened, and the locally saturated magnetization plateaus are no longer horizontal. Both of these facts make the analysis of these data somewhat harder and more ambiguous.

For $\theta \leq 12^0$ (Fig. 6.25a), the lowest transition changes very little with angle, having

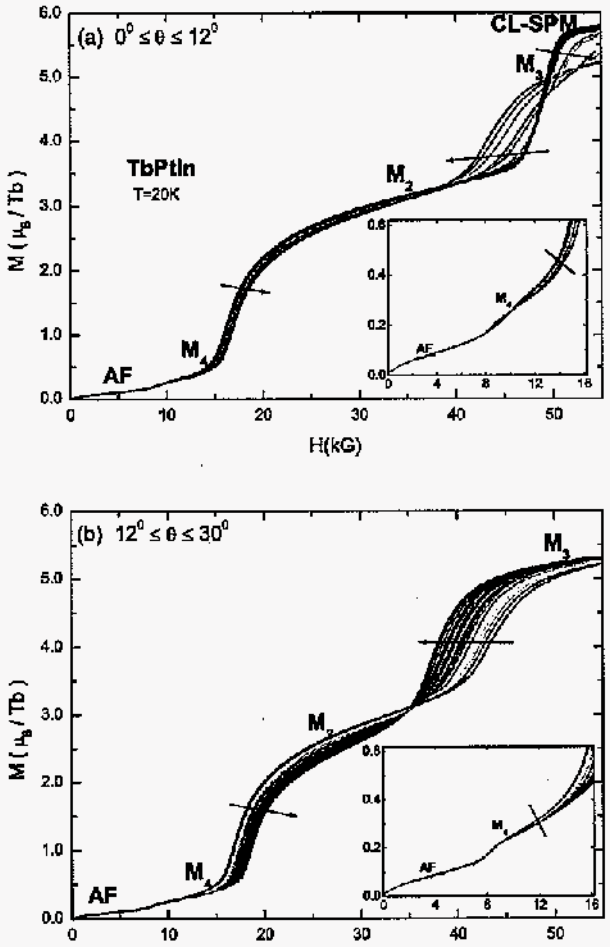

Figure 6.24 M(H) isotherms at $T = 20$ K for (a) $0^0 \leq \theta \leq 12^0$ and (b) $12^0 \leq \theta \leq 30^0$ ($\Delta\theta = 1^0$); inset: enlarged M_4 state. Arrows indicate the direction of increasing θ.

a critical field value $H_{cAF,4} \approx 8$ kG. As field is being increased, two more transitions can be observed for angles lower than 8^0, with local minima of the critical fields, at $\theta = 0^0$, of $H_{c4,2} = 16.2$ kG and $H_{c2,CL-SPM} = 48.7$ kG respectively. For larger angles, the highest transition splits into two different ones, $H_{c2,3}$, with decreasing values as we rotate away from

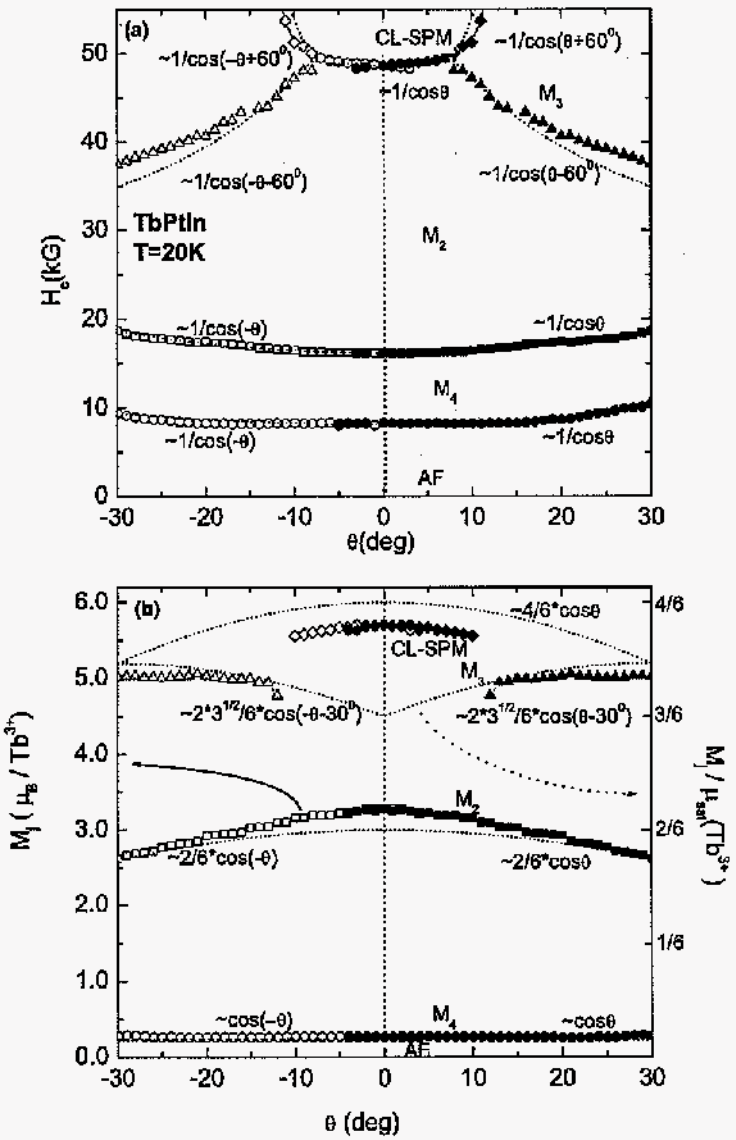

Figure 6.25 (a) Measured critical fields $H_{ci,j}$ and (b) locally saturated magnetizations M_j (full symbols), as a function of angle θ, for $T = 20$ K. Open symbols are reflections across the $\theta = 0^0$ direction. Also shown are the calculated angular dependencies of $H_{ci,j}$ and M_j (dotted lines).

the easy axis, and $H_{c3,CL-SPM}$, which rapidly increases above our field limit (*i.e.* 55 kG) around $\theta = 12^0$. It should be noted that we are still referring to the high-field state at $T = 20$ K as the crystal field-limited saturated paramagnetic CL-SPM state, even though it is possible that cross-over to the paramagnetic PM state has occurred between 2 K and 20 K at high H. (This would be a plausible explanation for the measured magnetization values for this high field state being, as seen below, lower than the calculated values.)

The locally saturated magnetization of the M_4 state is equal to $\sim 0.25\ \mu_B$/Tb at $\theta = 0^0$ and doesn't appear to change much with the angle. According to the $H-T$ phase diagrams in Fig. 6.8, all higher metamagnetic states are identical at low ($T = 2$ K) temperature and at $T = 20$ K; consequently, they seem to have similar angular dependencies (Fig. 6.25b): M_2 and M_{CL-SPM} have local maxima around $3.3\mu_B$/Tb and $5.7\mu_B$/Tb respectively, at $\theta = 0^0$, and slowly decrease with increasing angle in this region. Beyond $\sim 8^0$, a third metamagnetic state should exist, defined by the $H_{c2,3}$ and $H_{c3,CL-SPM}$ critical fields; however, it is difficult to identify it in this angular region, given the broadness of the bordering transitions and the $H_{c3,CL-SPM}$ proximity to our field limit.

As we move further away from the easy axis (*i.e.* $\theta > 12^0$, Fig. 6.25b), the lower two metamagnetic states can again be observed, whereas the CL-SPM state may still exist for fields larger than 55 kG (also apparent from the $H-T$ phase diagram in Fig. 6.8b). Also, we can now see the third state M_3 slowly increasing with angle θ, similar to the low temperature case.

The $T = 20$ K phase diagrams (Fig. 6.25) are very similar to their low temperature analogues (Fig. 6.12), except for the M_4 state, and some evident differences between the experimental data and the model calculations (dotted lines). It was rather difficult to determine the angular dependencies of M_4 and M_2, therefore we had to infer the possible theoretical fits in a more indirect way: as we already mentioned, the state described by M_2 at $T = 20$ K should be the same as the corresponding one at low temperature, since they characterize the same metamagnetic phase. Therefore we expect it to vary with the angle like $2/6 * \mu_{sat}(\mathrm{Tb}^{3+}) * \cos\theta$ (Fig. 6.12b). For large angles, this is consistent with the measured data in Fig. 6.25b, whereas significant deviations can be noticed closer to $\theta = 0^0$. The lower magnetization state M_1 has

much smaller values than any of the states characterized at $T = 2$ K, therefore we cannot fit it accurately with a calculated angular dependence; however, $H_{c4,2}$ can be fitted with 16.2 kG $*1/\cos\theta$ and should relate to M_4 through

$H_{c4,2}(\theta) \sim 1/[M_2(\theta) - M_4(\theta)]$

or

$1/\cos\theta \sim 1/[\ 2/6 * \mu_{sat}(\mathrm{Tb}^{3+}) * \cos\theta - M_4(\theta)]$.

Thus $M_4(\theta)$ should vary like $M_{sat,4} * \cos\theta$, with a locally saturated magnetization $M_{sat,4} \approx 0.25 * \mu_{sat}(\mathrm{Tb}^{3+})$, but, as already mentioned, it is difficult to determine it with reasonable accuracy. However, the corresponding local moment configuration should be similar to the low temperature one, in order to get the *cosθ* dependence, except that the number S of three Ising-like systems which would yield the appropriate $M_{sat,4}$ value is uncertain.

All other locally saturated magnetizations and critical fields can be best fitted with the same angular dependencies as for the low temperature case:

$M_3(\theta) = 2\sqrt{3}/6 * \mu_{sat}(\mathrm{Tb}^{3+}) * \cos(\theta - 30^0)$,

$M_{CL-SPM}(\theta) = 4/6 * \mu_{sat}(\mathrm{Tb}^{3+}) * \cos\theta$,

and

$H_{cAF,4} \sim 1/\cos\theta$,

$H_{c2,3} \sim 1/\cos(\theta - 60^0)$,

$H_{c2,CL-SPM} \sim 1/\cos\theta$,

$H_{c3,CL-SPM} \sim 1/\cos(\theta + 60^0)$.

Apart from the already mentioned differences between the measured data and the calculated curves, small departures from the corresponding theoretical angular dependencies can be noticed for $M_3(\theta)$ and $H_{c2,3}$; a more significant difference appears for the saturated magnetization state $M_{CL-SPM}(\theta)$, which seems to have the expected angular dependence, but with smaller values than the calculated ones. This may be a high-temperature effect (*i.e.* cross-over from low-T CL-SPM state to high-T paramagnetic PM state), or it may be one more indication that a more refined model is needed.

A polar plot analogues to the low temperature case (Fig. 6.26) shows that at $T = 20$ K,

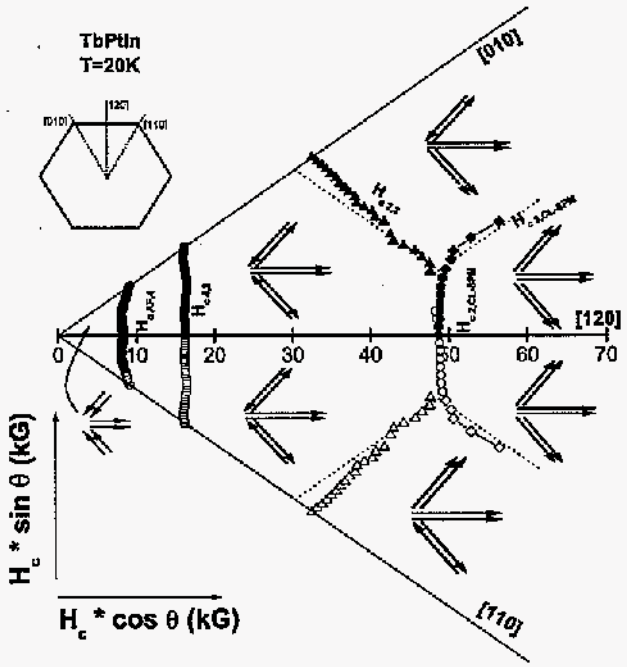

Figure 6.26 Polar plot of the critical fields $H_{ci,j}$, with one possible moment configuration shown for each observed metamagnetic state (except for M_1, where the moment configuration is uncertain-see text); open symbols represent reflections of the measured data-full symbols- across the $\theta = 0^0$ direction.

the critical fields are still well described by straight lines, but with more pronounced differences between experiment and the theoretical calculations. We attribute these to the thermal broadening at this temperature, but, as already seen in the low temperature case, a requirement for a more complex model cannot be excluded.

6.6 Summary

Motivated by the extensive work done on highly anisotropic local moment systems with tetragonal unit cells and unique rare earth sites of tetragonal point symmetry, we have performed detailed studies on two highly anisotropic, local moment, hexagonal compounds: TbPtIn

and TmAgGe. Whereas both of these compounds are ternary members of the Fe_2P class of materials, they have different ligands. In addition, whereas both of these compounds manifest extreme planar anisotropy, they have different easy axes: [120] for TbPtIn and [110] for TmAgGe. Even with these differences we have found that these two compounds have very similar $H-T$ as well as $H-\theta$ phase diagrams.

TbPtIn and TmAgGe have a single rare earth site with orthorhombic point symmetry (with three rare earth sites per unit cell) and both compounds have high field saturated moments well below the single ion values. These two observations, combined with our experience with the four position clock model that was developed for the tetragonal compounds with rare earths in tetragonal symmetry, lead us to propose a similar model for these Fe_2P-type compounds: a triple coplanar Ising model, which consists of three Ising-like moments per unit cell, with their Ising axes within the basal plane and rotated by 60^0 with respect to each other. This model preserves the six-fold symmetry at high fields and also explains why the saturated moments are significantly lower than the free ion values. By analyzing the magnitudes and angular dependencies of the critical metamagnetic fields, as well as the locally saturated magnetizations within the framework of this model, we can infer the net distribution of moments along the six possible moment orientations. However, field-dependent neutron diffraction or magnetic x-ray measurements are needed to test these hypothetical net distributions of moments and to obtain the propagation vectors for each magnetically ordered state. (Some preliminary experiments on TbPtIn are already reported (Garlea, 2004), confirming the two low-field ordering temperatures that we observed in the magnetization measurements. Moreover, the neutron data are consistent with our inferred direction of the moments.)

The successful extension of the four state clock model to the current triple coplanar Ising-like model implies that a wider set of local moment compounds with planar anisotropy can be understood in a similarly simple manner. Clearly tetragonal unit cell compounds with the rare earth in orthorhombic point symmetry could be expected to behave in a manner similar to TbPtIn and TmAgGe, *i.e.* to form a class of double coplanar Ising model materials. In a similar manner, hexagonal unit cell compounds with the rare earth in hexagonal point symmetry could

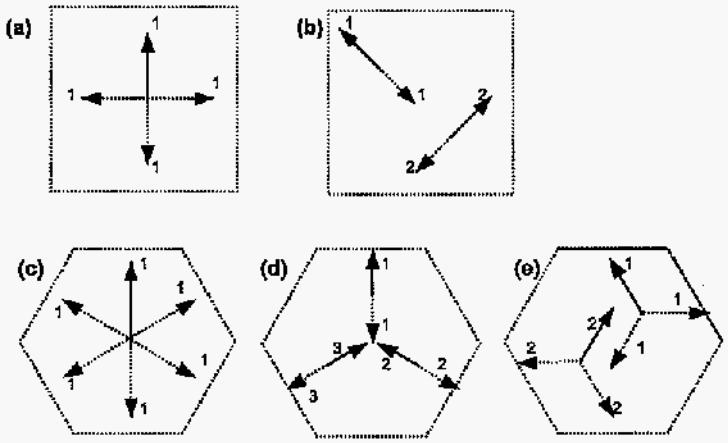

Figure 6.27 Plausible models for extremely anisotropic, planar compounds (see text) with (a-b) tetragonal and (c-e) hexagonal unit cells. The numbers are used to identify the different magnetic moments in the unit cell. (a) *Four position clock model* describing tetragonal systems with one R in tetragonal point symmetry; (b) *Double coplanar Ising-like model*: for orthorhombic point symmetry in tetragonal unit cell, two magnetic moments would be necessary (Ising-like systems, 90^0 away from each other in the basal plane). (c) *Six position clock model*: one magnetic moment with six possible orientations (arrows along six high symmetry orientations in the basal plane); (d) *Triple coplanar Ising-like model*: three R ions in unique orthorhombic point symmetry are needed in a hexagonal compound (three Ising-like systems, 60^0 away from each other in the basal plane); (e) A *double coplanar three position clock model* can describe hexagonal systems with two magnetic moments in unique trigonal point symmetry position, with three possible orientations (120^0 away from each other in the basal plane) for each. In all cases, the corresponding CL-SPM states (described in text) are represented by full arrows (applied field is assumed to be vertically up.

be expected to behave in a manner similar to $HoNi_2B_2C$ (Canfield, 1997b) or $DyAgSb_2$ (Myers, 1999a), *i.e.*, to form a class of six position clock model materials. Hexagonal unit cell materials may offer one other, potentially new class of materials: highly planar anisotropic compounds with the rare earth in trigonal point symmetry. In this case we anticipate a double coplanar three position clock model. Such compounds would have two magnetic sites, each with three possible positions 120^0 apart. Fig. 6.27 gives schematic representations of all expected five models described above.

CHAPTER 7. Magnetic ordering and effects of crystal electric field anisotropy in the hexagonal compounds RPtIn, R = Y, Gd - Lu*

7.1 Introduction

The RPtIn compounds (R = Y, La-Sm, Gd-Lu) have been reported to crystallize in the ZrNiAl hexagonal structure (Ferro, 1973; Zaremba, 2001; Galadzhun, 2000), space group $P\bar{6}2m$, with the rare earth in orthorhombic point symmetry, whereas the R = Eu member of this series forms in an orthorhombic TiNiSi-type structure (Pöttgen, 1996; Müllmann, 1998) (space group *Pnma*). Magnetic and transport measurements on some of these materials revealed a variety of physical properties across the series: CePtIn (Fujita, 1988; Kurisu, 1999; Yamaguchi, 1990; Satoh, 1990) and YbPtIn (Trovarelli, 2000; Kaczorowski, 2000; Yoshii, 2004) appear to be dense Kondo systems, with the electronic specific heat coefficient γ larger than 500 mJ/mol K^2, and 430 mJ/mol K^2 respectively; no magnetic order was observed in the former compound down to 60 mK (Satoh, 1990), whereas the latter appears to order antiferromagnetically below 3.4 K (Trovarelli, 2000). In TbPtIn (Watson 1995) the antiferromagnetic nature of the magnetic order below 50 K was indirectly suggested by the metamagnetic transitions observed in the M(H) data below this temperature. Watson *et al.* (Watson 1995) have also reported that the R = Gd and Dy members of this series have ferromagnetic ground states, with T_C = 89 K, and 38 K respectively, with reduced values of both the effective and the saturated moments of these two compounds. Whereas for the Dy system, the disagreement with the respective theoretical values could be attributed to crystal electric field CEF effects, it was unclear what was causing it in GdPtIn. CEF effects are also apparent in the magnetization measurements

*after "Magnetic ordering and effects of crystal electric field anisotropy in the hexagonal compounds RPtIn, R = Y, Gd - Lu", E. Morosan, S. L. Bud'ko and P. C. Canfield, Phys. Rev. B (2005).

on PrPtIn down to T = 1.7 K, which, together with the resistivity data (Zaremba, 2001) suggest a possible ferromagnetic transition at lower temperatures. Similar data on SmPtIn are indicative of ferromagnetic ordering in this compound below $T_C = 25$ K.

We recently presented detailed magnetization and transport measurements on single crystals of TbPtIn (Morosan 2005), and these data are discussed in detail in Chapter 6: anisotropic low-field susceptibility and specific heat measurements confirm the antiferromagnetic ground state, with $T_N = 46$ K, slightly different than the previously reported value (Watson 1995); below the ordering temperature, complex metamagnetism is revealed by magnetization measurements with applied field in the basal plane. Whereas from the high-temperature inverse susceptibility we obtained an effective moment $\mu_{eff} = 9.74\ \mu_B/Tb^{3+}$, close to the theoretical value 9.72 μ_B, the high-field magnetization data yielded values only up to $\sim 6\ \mu_B/Tb^{3+}$, much smaller than the theoretical saturated moment of 9 μ_B. In order to explain the reduced magnetization values, as well as the angular dependence of the metamagnetic properties, we proposed a *three co-planar Ising-like systems model*, which took into account the orthorhombic point symmetry of the rare earth ions in the hexagonal unit cell of the RPtIn compounds (Morosan 2005). Within such a model, for applied magnetic fields far smaller than the CEF splitting energy, for TbPtIn one expects a crystal field limited saturated paramagnetic CL-SPM state equal to 6 μ_B.

In view of these existing magnetization and transport data, the magnetic ordering in the heavy rare earth members of the RPtIn series was somewhat intriguing: whereas for GdPtIn and DyPtIn, ferromagnetic ground states were reported, the intermediate R = Tb member appears to order antiferromagnetically, which is a rather unusual discontinuity for a magnetically ordering local moment series.

In the present work we are trying to address this problem, and also extend the characterization of the physical properties to all the heavy RPtIn systems (*i.e.*, for R = Y, Gd - Lu). Having been able to grow single crystals for all of these compounds, we have the possibility of determining the effect of the CEF anisotropy on their magnetic properties, more so than in the previous studies on polycrystalline samples. As we shall see, the hexagonal crystal structure

of these compounds, with three R ions in the unit cell occupying unique orthorhombic point symmetry sites, is of crucial importance in explaining the moment configurations and magnetic ordering in the RPtIn materials described here.

In presenting our data, we will start with the non-magnetic members of the RPtIn series, R = Y and Lu; then we will continue with the magnetic ones (R = Gd - Tm), characterizing each of the compounds by temperature- and field-dependent magnetization, as well as zero-field specific heat measurements. A brief description of the previously reported (Trovarelli, 2000; Kaczorowski, 2000; Yoshii, 2004) heavy fermion compound YbPtIn is also included, our measurements being performed, as with all the other R compounds, on solution-grown single crystals.

Next we will briefly present the model for the magnetic moment configuration, characterizing the extremely planar TbPtIn compound (which is described in detail in Chapter 6); a more generalized version of this model, extended to three dimensions, will then be used to describe the magnetism in the other magnetic RPtIn compounds except YbPtIn.

7.2 Results

We are characterizing each compound by anisotropic magnetization and specific heat measurements, starting with the non-magnetic YPtIn and LuPtIn members of the series. Next the magnetic RPtIn will be introduced, for R = Gd to Tm. For each, we will emphasize the nature of the ordered state together with the ordering temperatures, as well as the high field, anisotropic magnetization data, as these provide key values in our discussion and analysis following the data presentation. Lastly, similar data on YbPtIn is presented, with a note that a more detailed analysis of the heavy fermion character of this compound is the subject of Chapter 9.

7.2.1 YPtIn and LuPtIn

The anisotropic susceptibilities of the two members of the RPtIn series with non-magnetic R ion (R = Y and Lu) are very small and basically temperature-independent.

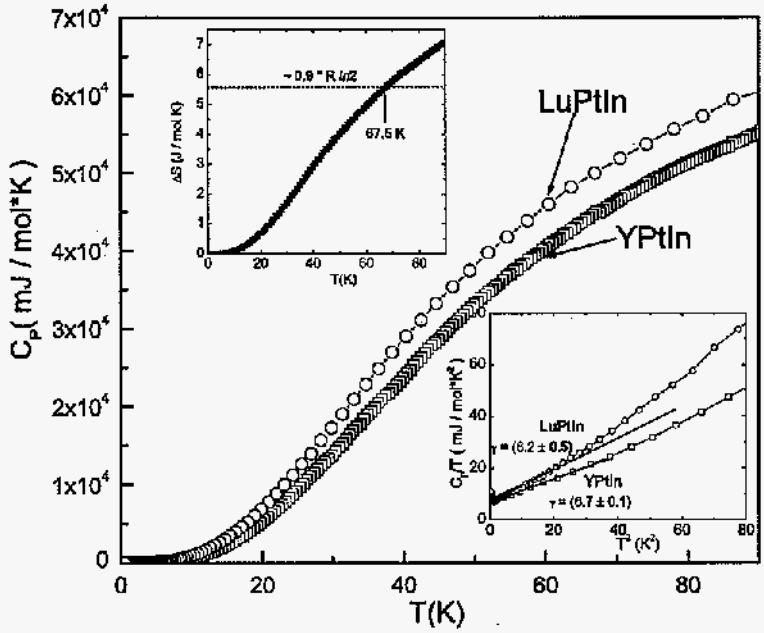

Figure 7.1 Specific heat for YPtIn and LuPtIn, with low-temperature C_P / T vs. T^2 shown in lower inset (linear fits of the low-T data give γ in units of mJ / mol * K^2); upper inset: entropy difference ΔS (see text).

However, the dominant terms in the susceptibility data seem quite different for the two compounds, as the average high-temperature values are positive in the case of YPtIn (around $(6.6 \pm 0.7) \times 10^{-5}$ emu/mol for $H \parallel ab$, and $(4.6 \pm 1.1) \times 10^{-5}$ emu/mol for $H \parallel c$), and negative for LuPtIn (around $(-3.8 \pm 0.2) \times 10^{-4}$ emu/mol for $H \parallel ab$, and $(-4.5 \pm 0.3) \times 10^{-4}$ emu/mol for $H \parallel c$). (The core diamagnetic susceptibilities of Y and Lu (-12 $\times$ 10^{-5} emu/mol, and -17 $\times$ 10^{-5} emu/mol respectively) are far too small to fully account for the above susceptibility valucs in YPtIn and LuPtIn compounds.) The field-dependent magnetization values for both compounds are extremely small, as expected for non-magnetic R compounds.

Heat capacity measurements in zero applied field were performed for the two systems, for $2 \leq T \leq 90$ K. As seen in Fig. 7.1, they have similar temperature dependencies; the higher

molecular weight for LuPtIn (and consequently the expected lower Debye temperature) could explain the values of the specific heat data being larger for this compound than for YPtIn. However, this does not account for the big entropy difference for these two systems (upper inset). This estimated entropy difference has a fairly large value $\Delta S \approx 0.9 * R \ln 2$ around 67 K, which, as we shall see, is the magnetic ordering temperature for GdPtIn. (The entropy difference is still considerably large when the measured specific heat data are scaled by their molecular weights, according to the Debye model.) Consequently, no meaningful magnetic specific heat estimates can be made for the magnetic RPtIn compounds using either the R = Y or Lu compounds as the non-magnetic analogues.

7.2.2 RPtIn, R = Gd - Tm

7.2.2.1 GdPtIn

The anisotropic H / M data for GdPtIn, together with the polycrystalline average, are shown in Fig. 7.2. The inset presents the low-temperature M / H data for low applied field (H = 100 G), measured on warming up after either zero-field cooling ZFC (symbols) or field cooling FC (solid lines) of the sample. The paramagnetic susceptibility shows Curie-Weiss behavior $\chi(T) = C/(T + \Theta_W)$ above $\sim$ 100 K. Θ_W represents the Weiss temperature, which can be determined from the linear fit of the high-temperature inverse susceptibility, and the values corresponding to the two orientations of the field, as well as the one for the polycrystalline average, are listed in Table 1. The inverse susceptibility data appear slightly anisotropic, contrary to the expected isotropic paramagnetic state for a Gd compound. This is possibly caused by the dominant anisotropic interaction in a pure S-state (*i.e.*, L = 0) compound (Jensen, 1991), also consistent with the different anisotropic Weiss temperatures for this Gd system (see Table 1). The effective moment value determined from the linear region in the inverse average susceptibility is $\mu_{eff} = 7.62\ \mu_B$, comparable to the theoretical value of 7.94 μ_B for the Gd^{3+} ions.

The field dependent magnetization data (Fig. 7.3) appears to indicate ferromagnetic ordering along the c-axis. Measurements performed for both increasing and decreasing applied

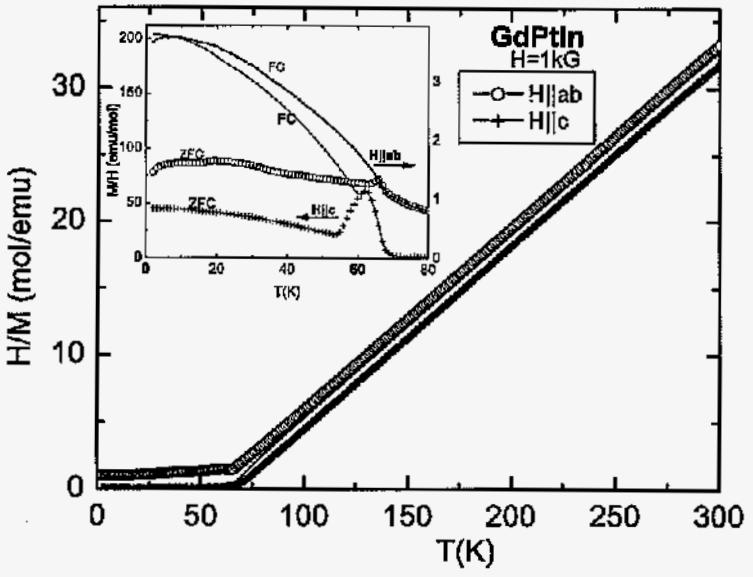

Figure 7.2 Anisotropic H / M data of GdPtIn and calculated average (line) at H = 1 kG, with the anisotropic ZFC - FC low-temperature M / H data for H = 0.1 kG shown in the inset.

field reveal hysteresis loops for both H parallel and perpendicular to the c-axis. At $H \approx 50$ kG, the magnetization saturates in both directions around the expected 7 μ_B/ Gd^{3+} value. As the increase of the axial magnetization with field (*i.e.*, for $H \parallel c$) is much faster than for $H \perp c$, we are led to believe that the ferromagnetic exchange interaction favors moments' alignment along the c-axis.

There is significant difference between the ZFC and the FC data in the ordered state for both $H \parallel ab$ and $H \parallel c$, with $\chi_c > \chi_{ab}$ in the low-temperature paramagnetic state (inset Fig. 7.2). This is consistent with the magnetic moments ordering ferromagnetically along the c-axis below the irreversibility temperature $T_{irr} = 63.8 \pm 1.9$ K, as it has already been reported on polycrystalline samples by Watson *et al.* (Watson 1995). The irreversibility temperature for $H \parallel ab$ is slightly different ($\sim$ 65.2 K). Specific heat data is needed to determine the magnetic ordering temperature, and using an on-set criterion (Fig. 7.4), the

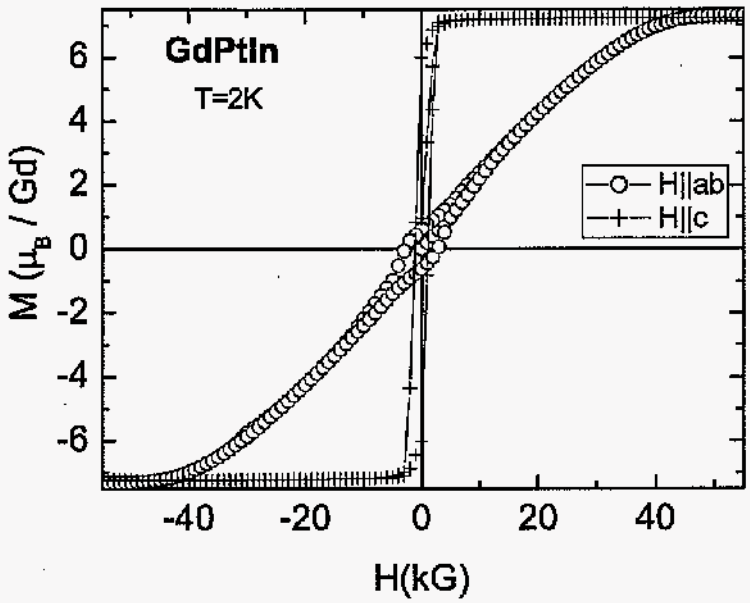

Figure 7.3 Anisotropic field-dependent magnetization loops for GdPtIn, at T = 2 K.

Curie temperature was determined to be $T_C = 67.5 \pm 0.5$ K, larger than the anisotropic T_{irr} values. In turn, this value is significantly lower than the previously reported ordering temperature for the polycrystalline samples (Watson 1995). We believe that the discrepancies in the ordering temperature estimates are due to the different criteria used for determining T_C, as well as to the different types of samples used in the measurements, with the single crystal data possibly being more accurate.

7.2.2.2 TbPtIn

We have already looked in detail at the magnetic and transport properties of TbPtIn (Chapter 6): in contrast to the neighboring R = Gd member of the series, TbPtIn has an antiferromagnetic ground state below $T_N = 46.0$ K, with an extremely anisotropic, planar susceptibility even in the paramagnetic state (Fig. 6.1). At higher temperatures, the inverse

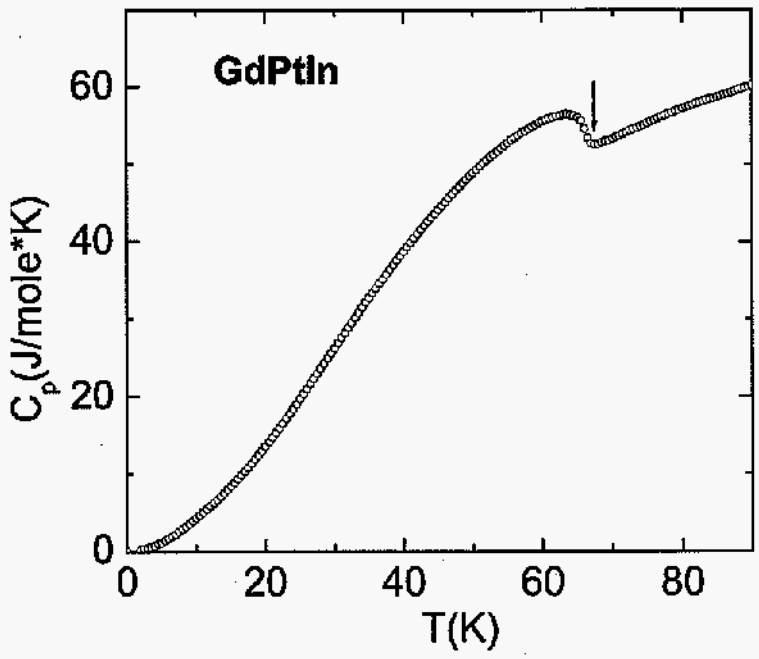

Figure 7.4 Specific heat $C_P(T)$ of GdPtIn; small arrow indicates T_C determined from on-set (see text).

average susceptibility becomes linear, indicating Curie-Weiss like behavior. Extrapolation of the polycrystalline linear fit down to low temperatures yields an effective moment value $\mu_{eff} = 9.74\ \mu_B$, in good agreement with the theoretical value 9.72 μ_B for Tb^{3+} ions. The anisotropic Weiss temperatures were also determined, and the corresponding values are given in Table 1. Another phase transition is apparent around $T_m = 27.4$ K, possibly associated with a spin reorientation. This phase transition was obscured in the measurements on polycrystalline samples (Watson 1995), whereas the T_N value that we determined based on measurements on single crystals is fairly close to the previously reported one.

As already seen by Morosan *et al.* (Morosan, 2005a), the TbPtIn specific heat shown in Fig. 6.2b confirms the Néel temperature and the lower temperature transition at T_m (marked by the vertical dotted lines). These transition temperatures are also consistent with those

revealed by the $d(M_{ave}/H * T)/dT$ (Fig. 6.2a) and $\rho(T)$ data (Fig. 6.2c), as expected for antiferromagnetic compounds (Fisher, 1962).

Anisotropic field-dependent measurements at $T = 2$ K (Fig. 6.4) reveal the presence of several metamagnetic transitions for field applied perpendicular to the hexagonal c-axis, whereas for field along the c-axis an almost linear increase of the magnetization with field is observed up to $\sim$ 140 kG. As emphasized by Morosan *et al.* (Morosan 2005), apart from the extreme in-plane/out-of-plane anisotropy, there is also a complex angular dependence of the observed metamagnetism for $H \perp c$. The full and open circles in Fig. 6.4a represent the measurements corresponding to the two high symmetry in-plane directions of the applied field (*i.e.*, the [120] and [110] directions respectively), for increasing and decreasing fields. The high-field magnetization values reach 6.45 μ_B / Tb^{3+} and 5.86 μ_B/ Tb^{3+} for the two in-plane directions, and, within the *three coplanar Ising-like model* (Morosan, 2005a), correspond to the crystal field limited saturated paramagnetic CL-SPM state. Also consistent with this model in the low energy limit is the low value of the axial component of the magnetization $M([001]) = 0.92\ \mu_B$ / Tb^{3+}. However, a slow increase of the high-field magnetization plateaus is apparent for $H \perp c$; this, as well as the slow increase of M_c with the applied field, may be due to the fact that the system is approaching the CEF splitting energy scale. Extrapolation of the high-field magnetization data (solid lines in Fig. 6.4a) down to $H = 0$ leads to smaller values (*i.e.*, 6.13 μ_B, 5.86 μ_B and 0 for $M([120])$, $M([110])$, and $M([001])$ respectively), even closer to the theoretical ones (Morosan, 2005a).

7.2.2.3 DyPtIn

So far we have seen that GdPtIn has a ferromagnetic ground state, with $\chi_c > \chi_{ab}$ in the low-temperature paramagnetic state, whereas TbPtIn orders antiferromagnetically and is extremely planar, even for a limited temperature range above T_N.

As we move towards the heavier R members of the series, DyPtIn resembles more the R = Gd compound rather than the neighboring R = Tb one: from the anisotropic H / M data data shown in Fig. 7.5, it appears that DyPtIn has a linear inverse average susceptibility, from

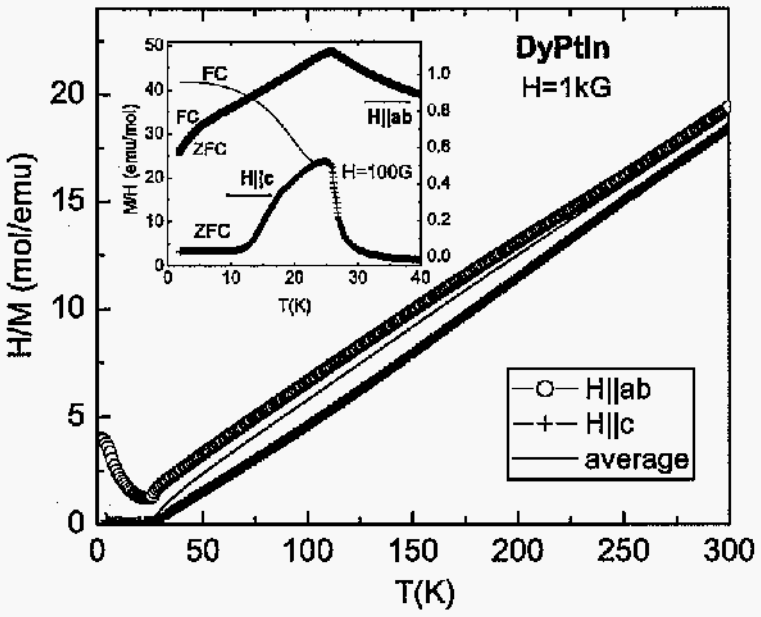

Figure 7.5 Anisotropic H / M data for DyPtIn and the calculated average (line) at H = 1 kG; inset: ZFC-FC low-temperature anisotropic M / H data for H = 0.1 kG.

which an effective moment $\mu_{eff} = 10.7\,\mu_B$ can be determined, consistent with the theoretical value of 10.6 μ_B. The anisotropic inverse susceptibilities can also be used to determine the Weiss temperatures, listed in Table.1 for both orientations of the field, as well as for the polycrystalline average. Below $\sim$ 30 K, DyPtIn orders magnetically (the Curie temperature T_C will be determined from the specific heat data, shown below). The ordered-state M / H data indicates a possible net ferromagnetic component along the c-axis. Moreover, ZFC and FC data for $H = 100$ G (inset, Fig. 7.5) further confirm this hypothesis, given the irreversibility of the χ_c data below $\sim$ 25 K, and no visible irreversibility for the χ_{ab} data.

As previously seen for GdPtIn, a rather broad peak in the specific heat data (Fig. 7.6) indicates the magnetic ordering of the DyPtIn. Using the on-set criterion, the Curie temperature is determined to be $T_C = (26.5 \pm 0.5)$ K, indicated by the small vertical arrow. The

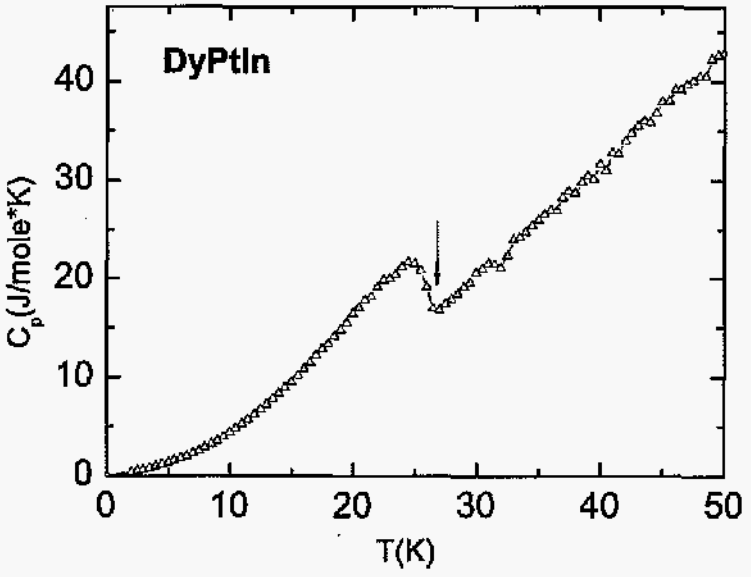

Figure 7.6 Specific heat $C_P(T)$ of DyPtIn; small arrow indicates T_C determined from on-set (see text).

substantial difference between our estimates and those of Watson et al. (Watson, 1995) for the ordering temperature, which appears to persist for all RPtIn members (R = Gd - Dy) described so far, could be a consequence of the two sets of data having been collected on single crystal or polycrystalline samples, respectively. However, for the ferromagnetic compounds, different criteria used for determining the ordering temperature may also be causing the aforementioned differences.

The field-dependent magnetization loops ($-$ 55 kG $\leq$ H $\leq$ 55 kG) are shown in Fig. 7.7, for both $H \parallel c$ and $H \perp c$. For the applied field along the c-axis (crosses), a small hysteresis can be observed, whereas the magnetization rapidly increases towards a saturated-like value around $\sim$ 6.88 μ_B / Dy^{3+}. This is consistent with a ferromagnetic component of the magnetization along the c-axis, which is well below the expected 10 μ_B saturated value for Dy^{3+} ions. For $H \perp c$, a metamagnetic transition occurs around $\sim$ 37 kG, leading to

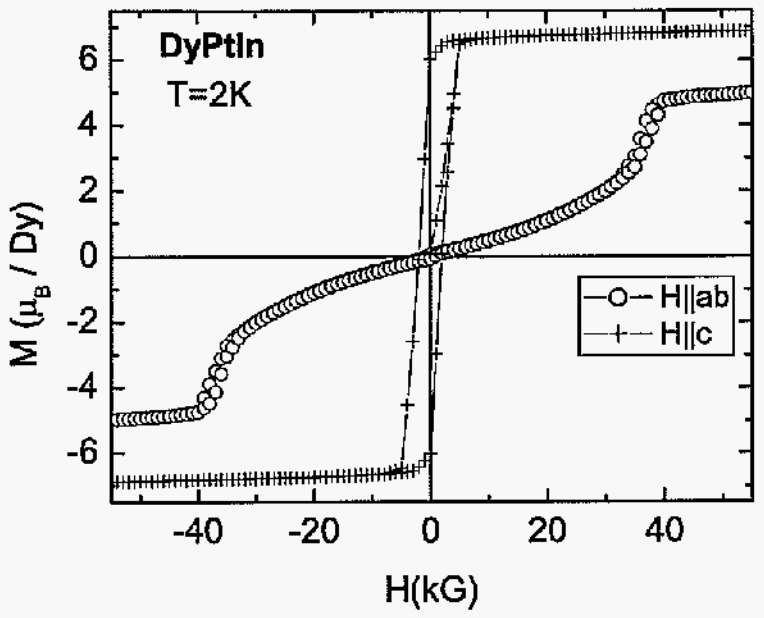

Figure 7.7 Anisotropic field-dependent magnetization loops for DyPtIn, at T = 2 K.

a state with the magnetization value around 4.98 μ_B, even smaller than the axial component. As we shall see for the rest of the local-moment members of the series (R = Ho, Er, Tm), the measured values of the magnetization at the highest applied field are far smaller than the theoretical saturated values for the respective ions, for both $H \parallel c$ and $H \perp c$. Starting from the two-dimensional model already developed for TbPtIn (Morosan, 2005a), we will attempt to generalize it to three dimensions such as to explain the nature of the ordered state across the whole RPtIn series (R = Gd - Tm).

7.2.2.4 HoPtIn

HoPtIn has similar physical properties to GdPtIn and DyPtIn, and appears to conform to some general characteristics of the RPtIn series, with the Tb member as an apparent exception: axial ferromagnetic component of the ordered state magnetization, less than the theoretical

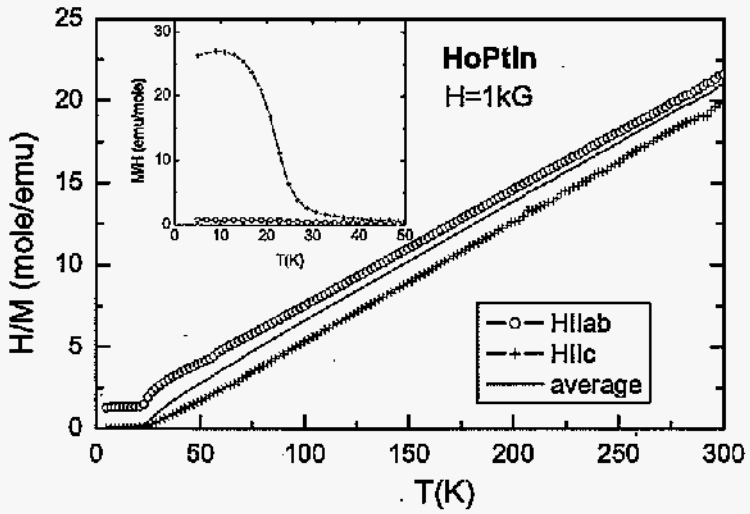

Figure 7.8 Anisotropic H / M data for HoPtIn and the calculated average (line) at H = 1 kG; inset: low-temperature anisotropic M / H data.

saturated values above $\sim$ 50 kG for both the axial and the planar magnetizations.

As can be seen in Fig. 7.8, the anisotropic inverse susceptibilities are linear at high temperatures; from the polycrystalline average, we get an effective moment of 10.5 μ_B, close to the theoretical value $\mu_{eff}(Ho^{3+}) = 10.6\ \mu_B$. The presence of the ferromagnetic component of the ordered state is evidenced by the anisotropic M / H data featuring a large, broad peak at low temperatures for $H \parallel c$ (inset Fig. 7.8), with $\chi_c > \chi_{ab}$ in the low-temperature paramagnetic state. In the specific heat data (Fig. 7.9), magnetic ordering is apparent below $T_C = 23.5 \pm 0.5$ K, as indicated by the small arrow.

The idea of a ferromagnetic component of the magnetization is further confirmed by the field dependent data in Fig. 7.10, where for the field applied in the c direction (crosses), the magnetization rapidly increases with H. The maximum value reached within our field limits is $\sim$ 7.81 μ_B, less than the calculated saturated moment for Ho^{3+} ions. As the magnetic field is applied parallel to the basal plane, the resulting magnetization curve is consistent with either

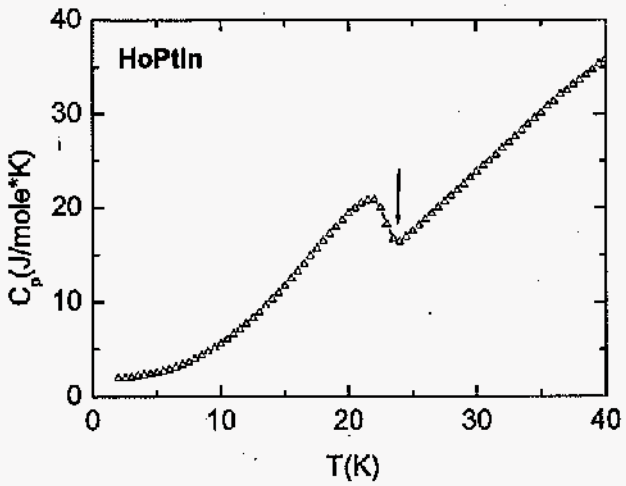

Figure 7.9 Specific heat $C_P(T)$ of HoPtIn; small arrow indicates T_C determined from on-set (see text).

a broad metamagnetic transition or with a continuous spin-flop transition. Around $H = 55$ kG, the in-plane component of the magnetization is 4.3 μ_B, even smaller than the axial one and less than half of $\mu_{sat}(Ho^{3+})$.

7.2.2.5 ErPtIn

As TbPtIn appears to be an exception, the R = Er member of the RPtIn series follows the already observed trends for the other heavy R compounds. The H / M average data seen in Fig. 7.11a is linear towards high temperatures, indicative of Curie-Weiss behavior of magnetization. However, crossing of the planar and axial inverse susceptibilities occurs around 150 K, possibly a result of strong crystal field effects at high temperatures in this compound.

Similar crossing of the anisotropic inverse susceptibilities was also observed for the R = Er member of the RNi_2B_2C series (Cho 1995). The effective moment value extracted from the high-T linear region of the inverse average susceptibility is $\mu_{eff} = 10.1$ μ_B, close the theoretical 9.6 μ_B value (within the accuracy of our data and fit).

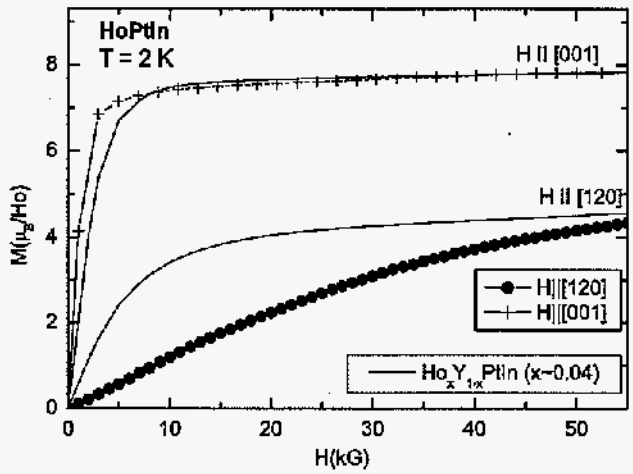

Figure 7.10 Anisotropic field-dependent magnetization curves for HoPtIn (symbols), and $Ho_xY_{1-x}PtIn$, x $\sim$ 0.04 (lines), at T = 2 K.

The low temperature anisotropic H / M data shown in the inset is consistent with ferromagnetic ground state, with $\chi_c > \chi_{ab}$ in the low-T paramagnetic state. The Curie temperature, as determined from the specific heat data in Fig. 7.11b, is $T_C = 8.5 \pm 0.5$ K, as the small arrow indicates.

From the field-dependent measurements in Fig. 7.12 we also infer that the magnetization has a ferromagnetic component along the c-axis, as the corresponding data (crosses) rapidly increase with field. Above $\sim$ 10 kG, the axial magnetization has an almost constant value around 7.50 μ_B, whereas the theoretical saturated moment for Er^{3+} ions is 9 μ_B. When $H \perp c$ (open circles), the magnetization data is almost linear in field, with a weak hint of un upward curvature around 20 kG, possibly indicating a metamagnetic transition. Towards 50 kG, the magnetization almost levels off around a 2.77 μ_B value, much lower than the expected saturated moment.

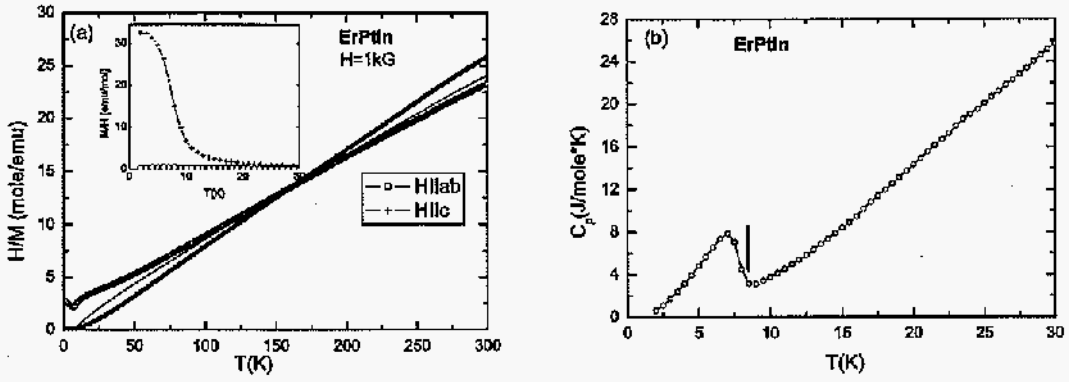

Figure 7.11 (a) Anisotropic H / M data for ErPtIn and the calculated average (line) at H = 1 kG; inset: low-temperature anisotropic M / H data; (b) Specific heat $C_P(T)$ of ErPtIn; small arrow indicates T_C determined from on-set (see text).

7.2.2.6 TmPtIn

Having an antiferromagnetic ground state and a planar magnetization component larger than the axial one, TbPtIn differs from the rest of the RPtIn compounds mentioned so far, whereas below we show that it resembles the R = Tm member of this series.

The high temperature inverse susceptibility of TmPtIn (Fig. 7.13) is linear, yielding an effective magnetic moment around 7.7 μ_B, close to the theoretical value calculated for Tm^{3+} ions, $\mu_{eff} = 7.6\ \mu_B$. However, unlike the aforementioned members of the series (except Tb), below $\sim$ 4 K this compound appears to order antiferromagnetically, as suggested by the low-temperature susceptibility data in the inset. Sharp peaks in the susceptibility data around T_N are typically indicative of antiferromagnetic ordered state, as is the case with the $H \parallel c$ data (crosses) shown in the inset in Fig. 7.13. The similar peak for the in-plane susceptibility (open circles) is somewhat broader, possibly due to spin fluctuations or CEF effects, which result in reduced susceptibility values around the ordering temperature.

A peak in the specific heat (Fig. 7.14a) suggests that the magnetic order occurs at $T_N = 3.0 \pm 0.5$ K, and, as expected for antiferromagnetic compounds (Fisher 1962), is consistent with the $d(M_{ave}/H * T)/dT$ data in Fig. 7.14b.

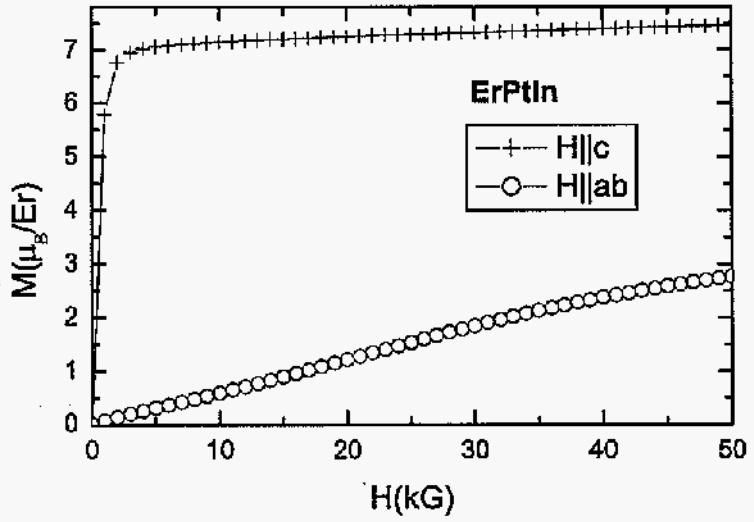

Figure 7.12 Anisotropic field-dependent magnetization curves for ErPtIn, at T = 2 K.

The $T = 2$ K magnetization isotherms (Fig. 7.15) indicate one (for $H \parallel c$) or more (for $H \parallel ab$) metamagnetic transitions. Following these fairly broad transitions (due to the high temperature, compared to T_N, for which these data were taken), the magnetization curves seem to approach some horizontal plateaus around 2.26 μ_B for the field along the c-axis, and 4.42 μ_B for the field within the ab-plane respectively. As for the other RPtIn (except for R = Gd), both these values are much smaller than the calculated effective moment of 7 μ_B for the Tm^{3+} ions.

7.2.3 YbPtIn

YbPtIn stands out from the rest of the RPtIn compounds through a number of distinctly different properties. Fig. 7.16a shows the inverse anisotropic susceptibilities (symbols), together with the calculated polycrystalline average (solid line). The latter data is linear above $\sim$ 50 K, despite a pronounced departure from linearity of the axial inverse H / M data

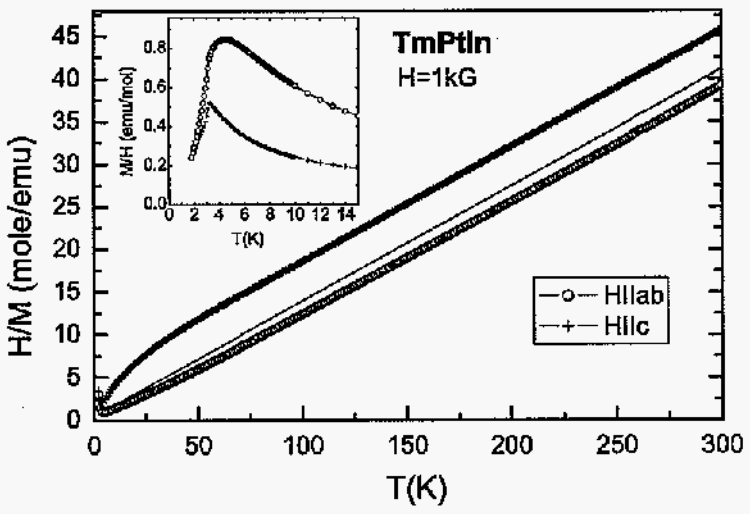

Figure 7.13 Anisotropic H / M data for TmPtIn and the calculated average (line) at H = 1 kG; inset: low-temperature anisotropic M / H data.

(crosses) below $\sim$ 200 K, probably due to CEF effects. From the fit of the linear part of the average H / M data, an effective moment of 4.3 μ_B/ Yb^{3+} can be determined, close to the theoretical 4.5 μ_B/ value. For lower temperatures, no distinguishable features associated with magnetic order are visible in the M / H data data down to 1.8 K (inset, Fig. 7.16a), for field values of 0.1 and 20 kG. This observations are consistent with the susceptibility data reported by Kaczorowski *et al.* (Kaczorowski 2000). However, the specific heat data (Fig. 7.16b) shows a sharp peak around 2.1 K, and the feature associated with this transition could have been missed in the M / H measurements because of the limited temperature range below the transition.

Trovarelli *et al.* (Trovarelli 2000) presented magnetization measurements that, for low applied fields (H = 0.1 kG), suggest antiferromagnetic ordering below T_N = 3.4 K, a value that is different from the possible transition temperature indicated by our measurements. In trying to understand the possible cause of such differences, single crystal x-ray measurements

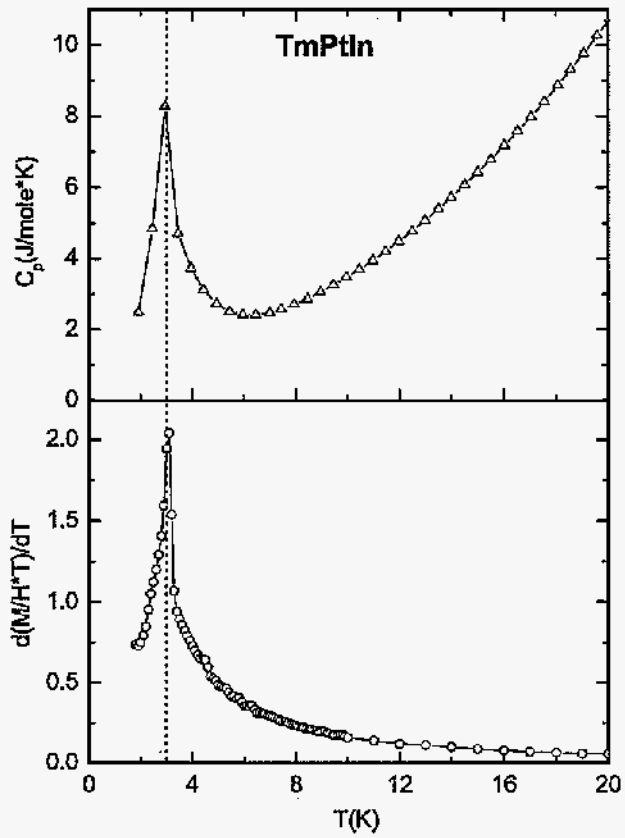

Figure 7.14 (a) C_P(T) and (b) low-temperature $d(M_{ave}/H * T)/dT$ for TmPtIn; dotted line marks the peak position, corresponding to T_N.

were performed. They indicate that our flux-grown YbPtIn single crystals have a partial (*i.e.*, $\sim$ 94 %) occupancy for one of the two Pt sites in the unit cell, such that the stoichiometry of these crystals is closest to $YbPt_{0.98}In$. This is not entirely surprising, given the different flux growth process (a low Pt-concentration used in the initial $Yb_{0.4}Pt_{0.1}In_{0.5}$ solution). Consequently the R = Yb compound is excluded from the following discussion. A more complete analysis of the thermodynamic and transport properties of this material is the subject of Chapter ??.

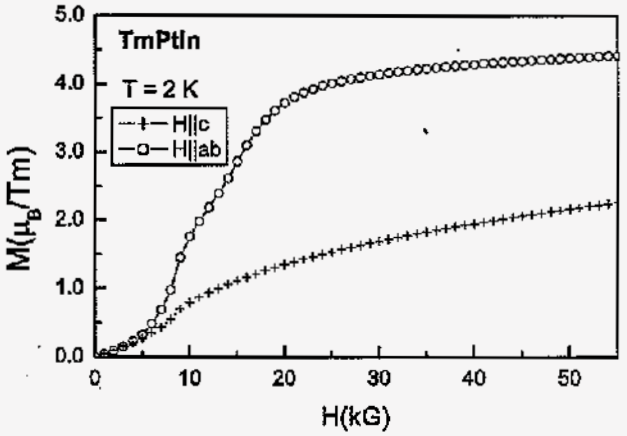

Figure 7.15 Anisotropic field-dependent magnetization curves for TmPtIn, at T = 2 K.

7.3 Data analysis

The magnetic RPtIn compounds that we investigate here appear to order magnetically below $\sim$ 70 K. As can be seen in Fig. 7.17, their ordering temperatures T_{ord} (also given in Table 7.1) scale fairly well with the de Gennes factor $dG = (g_J - 1)^2 J (J + 1)$, where g_J is the Landé g-factor, and J is the total angular momentum of the R^{3+} ion Hund's rule ground state. Whereas this suggests that the RKKY interaction between the conduction electrons and the local magnetic moments gives rise to the long-range magnetic order, slight departures from linearity, similar to those seen for other rare earth-series (Myers, 1999b; Bud'ko, 1999; Morosan, 2004), are due to the extremely simplified assumptions associated with the de Gennes scaling. The scaling is apparently unaffected by the curious switching from ferromagnetic to antiferromagnetic ordering across the RPtIn series, which appears to be correlated with a change in the anisotropy, such that, in the low-T paramagnetic state, $\chi_c > \chi_{ab}$ for the ferromagnetic compounds, and $\chi_{ab} > \chi_c$ for the antiferromagnetic ones. At first, this may seem inconsistent with de Gennes scaling, which would indicate similar ordering mechanisms

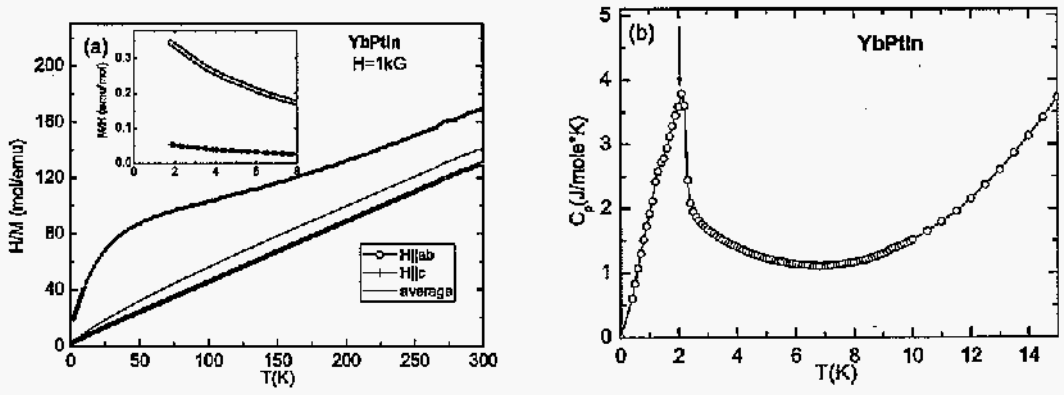

Figure 7.16 (a) Anisotropic H / M data for YbPtIn and the calculated average (line) at H = 1 kG; inset: low-temperature anisotropic M / H data; (b) Specific heat $C_P(T)$ of YbPtIn; small arrow indicates T_m.

for all RPtIn compounds, R = Gd - Tm. As we shall see, we believe that, because of their Fe_2P-type hexagonal structure, with three R ions sitting at orthorhombic point symmetry sites, strong CEF effects constrain the local magnetic moments in R = Tb - Tm to equivalent non-collinear easy-axes. This results in (i) anisotropic paramagnetic magnetization, and (ii) crystal field limited saturated paramagnetic CL-SPM states with magnetization values well below the corresponding free ion saturated moments.

We have already modelled the effects of strong crystal electric fields on the Fe_2P-type crystal structure, for the case of the extremely planar R = Tb member of the RPtIn series and the similar R = Tm member of the RAgGe series, using the *three co-planar Ising-like systems model* (Morosan 2005): having three rare earths in orthorhombic point symmetry, the hexagonal symmetry of the unit cell was achieved by constraining the local moments to three equivalent co-planar directions, 60^0 away from each other. In allowing both the "up" and "down" positions (*i.e.*, Ising-like) for each of the three magnetic moments, the antiferromagnetic ground state was, in the simplest case, realized by a ($\searrow\uparrow\swarrow$) moment configuration (Fig. 6.13a); upon increasing the applied magnetic field within the basal plane, a number of metamagnetic states occurred, showing simple dependencies of the critical fields H_c and the

Table 7.1 Magnetic ordering temperatures, T_{ord}, effective magnetic moments and anisotropic paramagnetic Weiss temperatures Θ_W.

	Gd	Tb	Dy	Ho	Er	Tm	Yb
T_{ord}(K)	67.5 ± 0.5	46.0 ± 0.5 27.4 ± 0.5	26.5 ± 0.5	23.5 ± 0.5	8.5 ± 0.5	3.0 ± 0.5	2.1 ± 0.2
$\mu_{eff}(\mu_B)$	7.6	9.7	10.7	10.5	10.1	7.7	4.3
Θ_{ab}(K)	-57.2 ± 1.5	-38.1 ± 1.4	-2.2 ± 5.2	7.5 ± 0.2	14.5 ± 10.8	-7.8 ± 2.2	8.2 ± 0.9
Θ_c(K)	-67.9 ± 0.5	-29.2 ± 3.1	-29.0 ± 0.4	-27.8 ± 0.3	-9.6 ± 1.9	36.9 ± 0.5	135.9 ± 4.0
Θ_{ave}(K)	-61.6 ± 0.8	-34.7 ± 4.6	-9.1 ± 0.8	-7.7 ± 1.0	13.2 ± 3.3	2.5 ± 0.5	32.5 ± 2.8

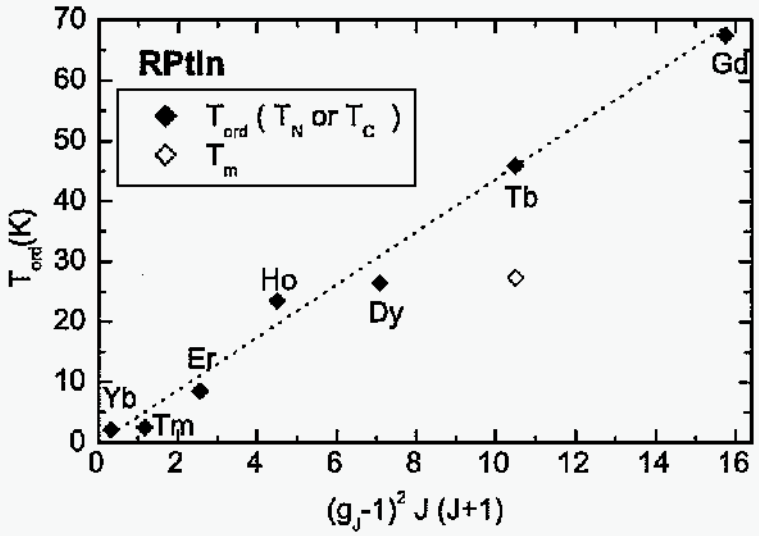

Figure 7.17 Changes of the magnetic ordering temperatures T_{ord} for RPtIn (R = Gd - Tm) with the deGennes scaling factor dG (the dotted line represents the expected linear dependence). Open symbol (for R = Tb) represents the low temperature transition from the higher-T to lower-T antiferromagnetic state.

locally saturated magnetizations M_{sat} on the angle θ between the direction of the field and the easy axis (see Fig.13 and related discussion by Morosan *et al.* (Morosan, 2005a)). When all the moments are in their "up" positions (↖↑↗), a crystal field limited saturated paramagnetic CL-SPM state is reached (Fig. 6.13b); the expected magnetization value is

$$1/3 * \mu_{sat}(\mathrm{Tb}^{3+}) * (1 + 2 * \cos 60^0) \; = \; 2/3 * \mu_{sat}(\mathrm{Tb}^{3+}) \text{ or } 2/3 * 9 \; \mu_B \; = \; 6 \; \mu_B,$$

consistent with the easy-axis measured data (full circles) shown in Fig. 6.4a.

We thus see that the aforementioned *three co-planar Ising-like systems model* explains how the measured magnetization values can be much smaller than the theoretical saturated value of 9 μ_B for the Tb^{3+} ions.

By contrast, the GdPtIn doesn't exhibit such reduced values of the magnetization for high applied fields (Fig. 7.3), given that the Gd^{3+} ions are in a symmetric $^8S_{7/2}$ state, and thus the

CEF effects are minimal: for $H \parallel c$ (crosses), the magnetization rapidly increases, reaching $\mu_{sat}(Gd^{3+}) = 7\,\mu_B$ for $H \geq 10$ kG. This is typical of a ferromagnetic magnetization for field applied along the direction of the moments (easy axis). Furthermore, the $H \perp c$ data (open circles) represent classical hard axis data, and are consistent with axial ferromagnetic ordering in this compound, as the saturated state is also reached, however at a slower rate (*i.e.*, for $H \geq 40$ kG).

For the other neighboring TbPtIn compound, the DyPtIn magnetization resembles the similar data for GdPtIn, even though the presence of CEF effects in the former system results in reduced magnetization values at our maximum applied field: as can be seen in Fig. 7.7, the $H \parallel c$ magnetization (crosses) rapidly increases with field, as expected for a ferromagnet with moments along c, but at $H = 55$ kG its value is only ~ 0.7 of the theoretical saturated moment of 10 μ_B. For field applied within the basal plane (open circles), only 0.5 of the saturated moment is reached following a metamagnetic transition around 35 kG. Whereas more metamagnetic transitions beyond our maximum field of 55 kG could account for the small magnetization values in this compound, such a hypothesis does not address one more peculiarity already apparent for the RPtIn series: even though the R = Gd and Dy compounds are ferromagnetic, and the R = Tb one is antiferromagnetic, their ordering temperatures scale well with the de Gennes factor, as we showed in Fig. 7.17. Furthermore, the R = Ho and Er compounds also display ferromagnetic components of the ordered state magnetization, whereas TmPtIn is antiferromagnetic, and yet the dc Gennes scaling still holds for all heavy RPtIn compounds (Fig. 7.17). The question arises whether a generalized hypothesis exists, which could account for the magnetic ordering in all RPtIn systems (R = Gd - Tm), or whether TbPtIn and TmPtIn should be regarded as exceptions from the ferromagnetic axial ordering across the series. We will try to address this question in Chapter 6, after presenting a detailed study of the metamagnetism observed in the two extremely planar compounds, for which the *three co-planar Ising-like systems model* has been introduced (Morosan 2005).

In what follows we will present one plausible model for the magnetic ordering in the local moment RPtIn compounds, a generalized version of the two-dimensional *three Ising-like sys-*

tems model, which addresses the above points. We first proposed such a model for DyAgGe (Morosan, 2004), an isostructural compound to RPtIn, for which a ferromagnetic component of the magnetization was also apparent along the c-axis.

In the *three co-planar Ising-like systems model* in Chapter 6, we assume that the magnetic moments are allowed to three orientations (along any three of the six equivalent six-fold symmetry axes within the basal plane), with two positions ("up" and "down") per orientation. This results in a set of three two-fold degenerate easy-axes, 60^0 away from each other, the degeneracy being a direct consequence of the requirement that the Ising-like systems be co-planar: the "up" position for a given easy-axis is indistinguishable from the "down" position for the equivalent direction $3 * 60^0 = 180^0$ away.

If we release the restriction that the moments be co-planar, while still imposing that their *in-plane* projections be 60^0 away from each other to preserve the hexagonal symmetry of the crystals, this degeneracy is lifted, and the moments are not necessarily Ising-like systems any more. The three-dimensional model described above can be directly derived from the planar one, as follows: we consider that Fig. 6.13 represents the *in-plane* projection of the magnetic moments' configuration, to which non-zero axial components of the moments are added. The possible resulting moment configurations can be obtained using any combination of "up" (thin solid arrows) or "down" (thin dotted arrows) planar and axial components of the magnetic moments, as shown in Fig. 7.18. Given the orthorhombic point symmetry of the magnetic moments' sites, this yields two possible co-planar orientations for each magnetic moment, with the corresponding "up" and "down" positions for each. The thick solid arrows in Fig. 7.18 represent the full magnetic moments, which are parallel to three non-planar, equivalent directions (*i.e.*, easy axes), inclined at an angle α from the c-axis. This configuration corresponds to the crystal field limited saturated paramagnetic CL-SPM state, where all *in-plane* and axial components of the magnetic moments are in their respective "up" positions.

It is worth noting that, by analogy with the two-dimensional model, there are two sets of easy axes: the [1 2 l]-equivalent axes, where l is the c-axis Miller index, for which the corresponding *in-plane* model exactly describes TbPtIn, or the [1 1 l]-equivalent directions,

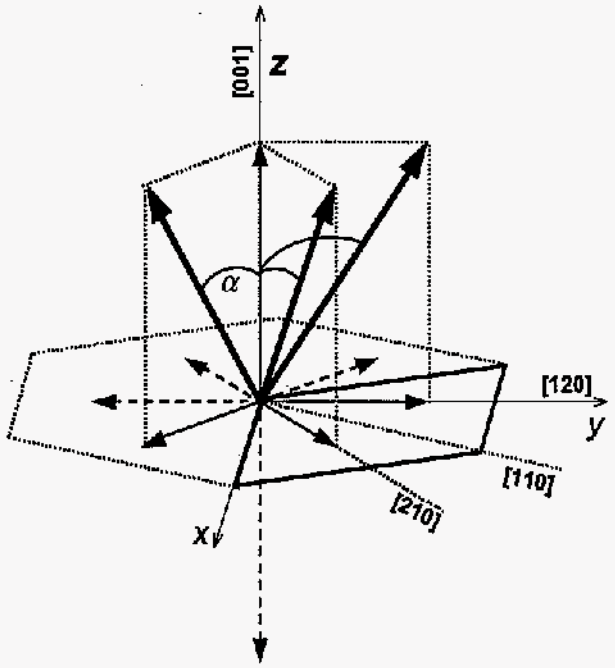

Figure 7.18 The three-dimensional model for three magnetic moments at unique orthorhombic point symmetry sites: thin arrows (solid - "up" and dotted - "down") represent the non-zero components of the magnetic moments along the [001] or the easy in-plane directions (as shown, the [120] - equivalent directions). Thick arrows: full magnetic moments in the CL-SPM state.

with a two-dimensional analogous example being TmAgGe (also described in detail by Morosan *et al.* (Morosan, 2005a)). In our present model and data analysis, we are assuming the first scenario, in which the easy axes are the [1 2 *l*]-equivalent directions, which project in the *ab*-plane onto the [1 2 0] directions. Consequently we will refer to the (1 2 0) planes as the "easy" planes and the [1 2 0] directions as "easy" *in-plane* axes, whereas the (1 1 0) planes and the [1 1 0]-axes will be called in this case "hard" planes and "hard" *in-plane* axes respectively. When the [1 1 *l*] directions are the easy axes, the same description is still valid, with the "easy" and "hard" planes and *in-plane* directions interchanged from the previous case.

We have thus introduced a model generalized from the *three co-planar Ising-like systems model*, which takes into account the CEF effects on hexagonal compounds with orthorhombic point symmetry of the rare earths. For each compound, the strength of the CEF effects will be reflected by the value of the angle α between the easy-axes and the c-axis. At low temperatures, another energy scale is introduced by the applied magnetic field, and the model described above is only valid for fields much smaller than the CEF energy. In this limit, for the highest applied fields, a CL-SPM state is reached, for which the anisotropic magnetization values are smaller than the theoretical saturated moments μ_{sat} for the respective R ions.

For a fixed angle α, there are six possible easy-axes (or three pairs of co-planar easy axes), each with the corresponding "up" and "down" positions. As in the case of the two-dimensional model, multiples S of three moments may be required to characterize the moment configuration for a given applied field. The orientation of the applied field will determine the magnetic moments to align along the three easy axes closest to the direction of the field, whereas its magnitude will determine the number of "up" and "down" moments along those three easy axes.

The CL-SPM state is reached when all three magnetic moments are in their "up" positions along three adjacent easy axes closest to the field direction (or, equivalently, when all *in-plane* and axial components of the magnetic moments are in their "up" positions). This state is illustrated in Fig. 7.18, for the magnetic field applied off the c-axis. (If H is parallel to the c-axis, all six "up" positions of the magnetic moments are equally probable, and only when rotating the field away from c the three easy axes closest to the applied field direction are uniquely determined).

Experimentally we can only measure the projection of the magnetic moments along the field direction, with the resulting magnetization per magnetic moment given by

$$M = \frac{1}{3} [\vec{M}_1 + \vec{M}_2 + \vec{M}_3] \cdot \frac{\vec{H}}{H}.$$

Moreover, we were able to measure the angular dependent magnetization for the magnetic field applied within the horizontal ab-plane and the high-symmetry vertical planes (*i.e.*, "easy" or "hard" planes). Such data can be used to probe the validity of our model, by comparison with

the theoretical calculation of the expected angular dependent "easy" and "hard" magnctization values.

For a fixed angle α, and for field making an angle θ with the c-axis, the magnetization values $M^e(\theta)$ and $M^h(\theta)$ in the CL-SPM state are, as calculated in detail in Appendix ??:

$M^e_{CL-SPM}/\mu_{sat}(\mathrm{R}^{3+}) = \frac{2}{3} * \sin\alpha * \sin\theta + \cos\alpha * \cos\theta$

and

$M^h_{CL-SPM}/\mu_{sat}(\mathrm{R}^{3+}) = \frac{\sqrt{3}}{3} * \sin\alpha * \sin\theta + \cos\alpha * \cos\theta,$

where θ is the angle between the applied magnetic field and the c-axis, and the indexes "e" and "h" denote, respectively, the "easy"- and "hard"-plane components of the magnetization. As already mentioned, we assume the "easy" and "hard" axes to be the [1 2 0] and the [1 1 0] directions, respectively. In what follows, our analysis refers only to the CL-SPM state, therefore the subscript denoting the respective state has been dropped for clarity.

From these calculations, the expected magnetization components (in units of $\mu_{sat}(\mathrm{R}^{3+})$) for field parallel or perpendicular to the c-axis are:

$M([001]) = M^e(\theta = 0^0) = M^h(\theta = 0^0) = \cos\alpha \leq 1,$

$M([120]) = M^e(\theta = 90^0) = \frac{2}{3}\sin\alpha < 1$

and

$M([110]) = M^h(\theta = 90^0) = \frac{\sqrt{3}}{3}\sin\alpha < 1.$

Moreover, local maxima for the M^e and M^h curves are reached for $\theta_{max} = \arctan(\frac{2}{3}\tan\alpha)$, and $\arctan(\frac{\sqrt{3}}{3}\tan\alpha)$ respectively, with the corresponding magnetization values equal to

$\sqrt{\cos^2\alpha + (\frac{2}{3})^2\sin^2\alpha} = \sqrt{1 - \frac{5}{9}\sin^2\alpha} < 1,$

and $\sqrt{\cos^2\alpha + (\frac{\sqrt{3}}{3})^2\sin^2\alpha} = \sqrt{1 - \frac{6}{9}\sin^2\alpha} < 1.$

As can be seen from the above calculations, one should expect the measured magnetization values to be smaller than the theoretical saturated moment $\mu_{sat}(\mathrm{R}^{3+})$, regardless of the direction of the applied field. The only exception is the axial magnetization $M([001])$ for $\alpha = 0^0$ (moments parallel to the c-axis), when the expected value is exactly $\mu_{sat}(\mathrm{R}^{3+})$. These observations lend support to the idea that the three-dimensional model considered above could describe the RPtIn compounds, since for all R = Tb - Tm we have indeed observed reduced

values of the high-field anisotropic magnetizations. On the other hand, it appears that the fully saturated magnetization measured for GdPtIn could be described by the above model for $\alpha = 0^0$, but the absence of CEF effects restricts the applicability of our model to this compound.

In the case of TbPtIn the magnetization measurements revealed extreme planar anisotropy of this compound (Fig. 6.1 and 6.4a). Within our three-dimensional model, this is consistent with the angle α being equal to 90^0, when the magnetic moments become co-planar. In this case, the calculated magnetization values become (in units of $\mu_{sat}(\mathrm{Tb}^{3+})$)

$M([001]) = \cos 90^0 = 0,$

$M([120]) = \frac{2}{3} \sin 90^0 = \frac{2}{3}$

and

$M([110]) = \frac{\sqrt{3}}{3} \sin 90^0 = \frac{\sqrt{3}}{3}.$

These values show that when $\alpha = 90^0$, our model indeed reduces to the *three co-planar Ising-like systems model* (Morosan 2005).

When $0^0 \leq \alpha < 90^0$, our model yields axial magnetization values larger than 0, and this is observed for all RPtIn, R = Tb - Tm. Therefore we can verify the applicability of our model to these systems by estimating the angle α, and comparing the measured and calculated magnetization values in the CL-SPM state as follows:

For all RPtIn compounds, the in-plane magnetization measurements were performed for field along the [1 2 0] direction. Since it is not readily apparent whether this represents the "easy" or "hard" in-plane direction, one way to estimate the angle α is from the M([0 0 1]) data:

$M([0\ 0\ 1]) \ / \ \mu_{sat}(\mathrm{R}^{3+}) = \cos\alpha.$

Therefore $\alpha = \arccos(M([0\ 0\ 1]) \ / \mu_{sat}(\mathrm{R}^{3+}))$. These values are listed in Table 2, together with the measured magnetization values M([0 0 1] at $H = 55$ kG, which were used in the above formula. For this value of the angle α, the "easy" and "hard" in-plane magnetization components should be, as described above,

$M^e \ / \ \mu_{sat}(\mathrm{R}^{3+}) = \frac{2}{3} \sin\alpha$

and

M^h / $\mu_{sat}(R^{3+})$ = $\frac{\sqrt{3}}{3}$ $\sin\alpha$.

However, slight misalignments of the samples can occur for $H \parallel c$, which may result in significant errors in our determination of angle α. In order to minimize these errors, another way to determine α is from the ratio of the two anisotropic measured magnetizations:

$M([1\ 2\ 0])$ / $M([0\ 0\ 1])$ = 2/3 * $\sin\alpha$ / $\cos\alpha$ if the [1 2 0] direction is the easy axis, or $M([1\ 2\ 0])$ / $M([0\ 0\ 1])$ = $\sqrt{3}/3$ * $\sin\alpha$ / $\cos\alpha$ if the [1 2 0] direction is the hard axis. The measured M([1 2 0]) values which were used for these calculations are listed in Table 2.

Thus the angle α is either

arctan(3 / 2 * $M([1\ 2\ 0])$ / $M([0\ 0\ 1])$) or arctan(3 / $\sqrt{3}$ * $M([1\ 2\ 0])$ / $M([0\ 0\ 1])$), and these estimated values are also listed in Table 2 as α^e and α^h.

As can be observed from the angle values listed in Table 2, together with the error bars resulting from the two different calculations, the angle α ranges from 89^0 for TbPtIn, to $\sim 32^0$ for ErPtIn. Our three-dimensional model seems to be consistent with the experimental data for all RPtIn, R = Tb - Tm.

In order to further explore the validity of the above model, angular dependent magnetization measurements were performed for a $Ho_xY_{1-x}PtIn$ system ($x \approx 0.04$), for the applied field continuously rotated within the (0 0 1) or the (1 2 0) plane. The above R = Ho system was preferred because the $M(H)$ curves in Fig. 7.10 are consistent with CL-SPM saturated state at H = 55 kG for both $H \parallel c$ and $H \perp c$, whereas the system with low concentration of magnetic ions was chosen for this measurement in order to check the validity of our model in the single-ion limit. Moreover, the anisotropic field dependent data for the diluted sample (lines, Fig. 7.10) show almost horizontal plateaus for fields higher than $\sim$ 30 kG, with magnetization values close to the corresponding ones for the pure HoPtIn (symbols). The angle α for $Ho_xY_{1-x}PtIn$, calculated using $M([0\ 0\ 1])\ |_{55\ kG}$ = 7.41 μ_B/ Ho, is 42.1^0, close to the corresponding value for the pure compound.

The magnetization measured for field applied within the basal plane (*i.e.*, the (0 0 1) plane) reveals the six-fold anisotropic data, with the ratio $M([1\ 1\ 0])$ / $M([1\ 2\ 0])$ close to

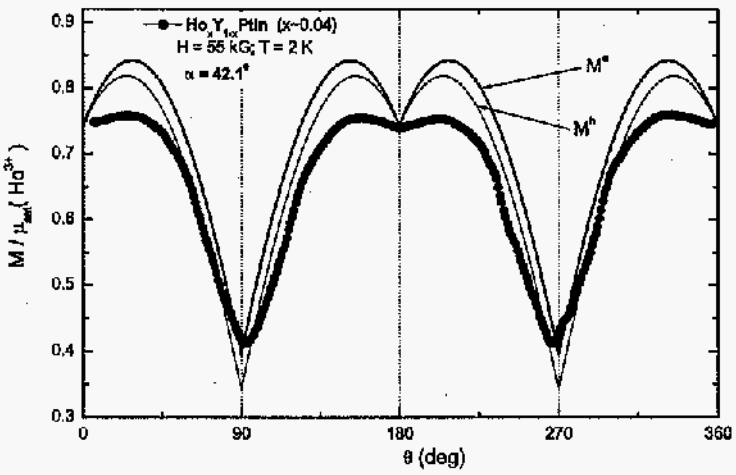

Figure 7.19 Angular dependent magnetization for $Ho_xY_{1-x}PtIn$ (x $\sim$ 0.04) (full circles) at H = 55 kG and T = 2 K. The solid lines represent the "easy" and "hard" plane calculated magnetizations as a function of θ (see text), for fixed angle α.

$cos\ 30^0 \simeq 0.9$, as expected based on the proposed model. The angular dependent magnetization at $H = 55$ kG is shown in Fig. 7.19 (full circles) for $H \parallel (1\ 2\ 0)$. Also shown as solid lines are the calculated $M^e(\theta)$ and $M^h(\theta)$, for fixed $\alpha = 42.1^0$ determined above. As can be seen, the measured data qualitatively reproduces the features expected based on the above model (*i.e.*, two-fold symmetry with respect to both the *c*-axis and the *ab*-plane, local minima corresponding to $H \parallel [001]$ or $\theta = n * 180^0$, n-integer, and maxima at some intermediate angle). More detailed models which would characterize the RPtIn may exist, and determining all of them is beyond the scope of this paper. However, if we restrict our discussion to the three-dimensional model described before, we see that significant departures from both calculated $M^e(\theta)$ and $M^h(\theta)$ curves can still be observed, despite the apparent qualitative agreement between calculations and measured data. This may mean that either a totaly different model needs to be considered, or that the aforementioned model needs further refinement in order to describe at least the HoPtIn, and perhaps the rest of the RPtIn com-

pounds. Furthermore, additional experiments (*i.e.*, neutron diffraction) are required to help identify the most appropriate model for the magnetization of the RPtIn compounds.

7.4 Conclusions

Single crystals of the RPtIn compounds (R = Gd - Lu) have been grown using the self-flux technique, and have been characterized by anisotropic temperature- and field-dependent magnetization and zero-field specific heat measurements. A small Pt-deficiency in the YbPtIn is apparent from single crystal X-ray data, whereas all the other heavy R members of the series are believed to form stoichiometrically. Because of this difference in composition, we leave the characterization of the YbPtIn system to a separate study, presented in Chapter ??.

The magnetic RPtIn compounds order magnetically above 2 K, with the ordering temperatures (given in Table 7.1) scaling well with the deGennes dG factor (Fig. 7.17). This is consistent with the coupling between the conduction electrons and the local magnetic moments giving rise to the long-range magnetic order via RKKY exchange interaction. However, the R = Tb and Tm members of the series have antiferromagnetic ground states, whereas in the ordered state, the magnetization of all the other compounds has at least a ferromagnetic component along the c-axis. These discontinuous changes from antiferromagnetic to ferromagnetic state across the series seems to also be associated with a change of low-temperature anisotropy of the paramagnetic state, such that $\chi_{ab} > \chi_c$ for TbPtIn and TmPtIn, and $\chi_{ab} < \chi_c$ for the rest of the magnetic RPtIn.

The magnetization of the TbPtIn compound is extremely anisotropic, with the magnetic moments confined to the ab-plane. Below the antiferromagnetic ordering temperature $T_N = 46.0$ K, a second magnetic phase transition is apparent around 27 K. At low temperature, in-plane magnetization data reveals complex metamagnetism, and this has been studied in detail, and described using the *three co-planar Ising-like systems model* by Morosan *et al.* (Morosan, 2005a).

Having understood the complex angular dependent metamagnetism in the planar TbPtIn compound, we attempted to generalize the *three co-planar Ising-like systems model* to three

dimensions, such as to characterize the magnetically ordered state in the other RPtIn compounds: instead of assuming the moments to be confined to equivalent co-planar directions, 60^0 away from each other, they could be restricted to equivalent directions within vertical planes rotated by 60^0 around the c-axis. This is equivalent with sets of six non-planar easy axes, each at an angle α from the c-axis, with "up" and "down" orientations for each directions. When the applied field is oriented at a non-zero angle from the c-axis, the three magnetic moments will align along the three easy axes closest to the direction of the field. (This implies that at high enough fields, all three moments will be in the "up" positions of three adjacent easy axes, corresponding to the CL-SPM moment configuration.)

The angle α between the easy axes and the c direction is dependent, in each compound, on the crystalline electric field CEF energy. Simple geometrical relations allow us to calculated the expected components of the CL-SPM magnetization along the c-axis, as well as for the "easy" and "hard" in-plane orientations of the field. Assuming that for $H = 55$ kG (in most cases the maximum available field for our measurements), the RPtIn systems indeed reach the CL-SPM state at low temperatures, we can determine the fixed value for the angle α for each compound, and compare the high-field measured magnetization values with the calculated ones.

As can be seen from Table 7.2, all RPtIn (R = Tb - Tm) are well described by this model, with α values between 89^0 for R = Tb, and $\sim 32^0$ for R = Er. However, such a model does not fully account for the angular dependence of the magnetization, at least in the case of $Ho_xY_{1-x}PtIn$: this is qualitatively reproduced by the model calculations, with considerable differences between the measured and theoretical magnetization values for the whole angular range. Whereas reasonable misorientation of the rotation sample cannot account for these differences, we are led to believe that it is necessary to refine the over-simplified model described here, and also that additional measurements may help clarify the magnetic structure in these RPtIn compounds.

Table 7.2 Anisotropic magnetization values measured at $H = 55$ kG, and the angles α determined as described in the text.

	Tb	Dy	Ho	Er	Tm
$M^{exp}([0\ 0\ 1])/\mu_{sat}(R^{3+})$	0.03	0.69	0.78	0.83	0.33
$\alpha^{(a)}$	88^0	46.5^0	38.6^0	34.0^0	71.0^0
$M^{exp}([1\ 2\ 0])/\mu_{sat}(R^{3+})$	0.68; $0.62^{(b)}$	0.50	0.42	0.28	0.63
α^c; α^h	90^0; 90^0	47.4^0; 51.3^0	39.7^0; 43.8^0	29.1^0; 32.7^0	71.0^0; 73.4^0
α	$89.0^0 \pm 1.0^0$	$48.9^0 \pm 2.4^0$	$40.6^0 \pm 2.0^0$	$31.6^0 \pm 2.5^0$	$72.2^0 \pm 1.2^0$

7.5 Appendix

In a cartesian coordinate system as shown in Fig. 7.18, the three magnetization vectors in the CL-SPM state can be written as

$\vec{M}_1 = \mu_{sat}(\mathrm{R}^{3+})\ (0,\ \sin\alpha,\ \cos\alpha),$

$\vec{M}_2 = \mu_{sat}(\mathrm{R}^{3+})\ (\sin\alpha * \cos 30^0, \sin\alpha * \sin 30^0, \cos\alpha)$

and

$\vec{M}_3 = \mu_{sat}(\mathrm{R}^{3+})\ (\sin\alpha * \cos 30^0, -\sin\alpha * \sin 30^0, \cos\alpha),$

whereas, in general, the applied field vector can be written as

$\vec{H} = (H_x,\ H_y,\ H_z).$

Thus the general expression for the CL-SPM magnetization M becomes

$$M = \tfrac{1}{3}\,[(0 + \sin\alpha * \cos 30^0 + \sin\alpha * \cos 30^0) * \tfrac{H_x}{H} + (\sin\alpha + \sin\alpha * \sin 30^0 - \sin\alpha * \sin 30^0) * \tfrac{H_y}{H} + (\cos\alpha + \cos\alpha + \cos\alpha) * \tfrac{H_z}{H}]$$

or

$$M = \tfrac{\sqrt{3}}{3}\ \sin\alpha\ * \tfrac{H_x}{H} + \tfrac{1}{3}\ \sin\alpha * \tfrac{H_y}{H} + \cos\alpha * \tfrac{H_z}{H}.$$

Experimentally, we are able to measure the angular dependence of the magnetization within the "easy" and "hard" planes. If the magnetic field is continuously rotated within the "easy" plane ((2 1 0) in Fig. 7.18) than, in cartesian coordinates, the vector $\vec{H}$ becomes

$\vec{H} = H\ (\cos 30^0 * \sin\theta,\ \sin 30^0 * \sin\theta,\ \cos\theta),$

where θ is a continuous variable representing the angle between the applied field and the c-axis.

In this case, the angular dependent magnetization becomes

$$M^e/\mu_{sat}(\mathrm{R}^{3+}) = \tfrac{\sqrt{3}}{3}\ \sin\alpha * \tfrac{\sqrt{3}}{2}\ \sin\theta + \tfrac{1}{3}\ \sin\alpha * \tfrac{1}{2}\ \sin\theta + \cos\alpha * \cos\theta =$$
$$= \tfrac{2}{3} * \sin\alpha * \sin\theta + \cos\alpha * \cos\theta,$$

where the index "e" refers to the "easy" plane component.

Similarly, if the magnetic field is rotated within the "hard" (1 1 0) plane, the vector $\vec{H}$ can be written as

$\vec{H} = H\ (\cos 60^0 * \sin\theta,\ \sin 60^0 * \sin\theta,\ \cos\theta))$

and the corresponding angular dependent magnetization is

$$M^h/\mu_{sat}(\mathrm{R}^{3+}) = \tfrac{\sqrt{3}}{3}\ \sin\alpha * \tfrac{1}{2}\ \sin\theta + \tfrac{1}{3}\ \sin\alpha * \tfrac{\sqrt{3}}{2}\ \sin\theta + \cos\alpha * \cos\theta =$$

$$= \frac{\sqrt{3}}{3} * \sin\alpha * \sin\theta + \cos\alpha * \cos\theta.$$

The index "h" is used to indicate the "hard" plane component of this magnetization.

Both calculated $M^e(\theta)$ and $M^h(\theta)$ are shown in Fig. 7.19 (solid lines) for fixed $\alpha = 42.1^0$, as calculated for the $Ho_xY_{1-x}PtIn$ system (see text). As expected, the two-fold symmetry with respect to the c-axis ($\theta = 2n * 90^0$, n-integer) and the ab-plane ($\theta = (2n+1) * 90^0$, n-integer) is revealed by both the calculated angular dependent magnetizations.

CHAPTER 8. Field induced Quantum Critical Point in YbAgGe

8.1 Magnetic field induced non-Fermi-liquid behavior in YbAgGe single crystals*

8.1.1 Introduction

YbAgGe is the penultimate member of the hexagonal RAgGe series (Morosan, 2004) and was recently identified (Morosan, 2004; Beyermann, 1998; Canfield, 2003; Katoh, 2004) as a new Yb-based heavy fermion compound. Magnetization measurements on YbAgGe down to 1.8 K (Morosan 2004) show moderate anisotropy (at low temperatures $\chi_{ab}/\chi_c \approx 3$) and a loss of local moment character below $\sim$ 20 K (Fig.8.1) (also see Fig. 33 and related discussion in Morosan 2004). The in-plane $M(H)$ at $T = 2$ K shows a trend toward saturation whereas $H \parallel c$ field-dependent magnetization continues to be virtually linear below 140 kG (Fig. 8.1, inset). Initial thermodynamic and transport measurements down to 0.4 K (Beyermann, 1998; Canfield, 2003; Morosan, 2004) reveal two magnetic transitions, a higher one at $\approx$ 1 K, and a lower one, with very sharp features in $\rho(T)$ and $C_p(T)$, at $\approx$ 0.65 K (Fig. 5.30). Given that the magnetic entropy inferred from the Fig. 5.30 is only $\sim$ 5% of $R\ln 2$ at 1 K and only reaches $R\ln 2$ by $\sim$25 K it seems likely that these transitions are associated with a small moment ordering. Based on these measurements the compound was anticipated to be close to the quantum critical point. The linear component of $C_p(T)$, γ, is $\sim$150 mJ/mol K^2 between 12 K and 20 K. $C_p(T)/T$ rises up to $\sim$1200 mJ/mol K^2 for $T \sim 1$ K but given the presence of the magnetic transitions below 1 K, it is difficult to unambiguously evaluate the electronic specific heat. Grossly speaking, 150 mJ/mol K^2 $< \gamma <$ 1 J/mol K^2 leading to an estimate 10

*after "Magnetic field induced non-Fermi-liquid behavior in YbAgGe single crystals", S. L. Bud'ko, E. Morosan and P. C. Canfield, Phys. Rev. B 69 014415 (2005).

K $< T_K <$ 100 K for the Kondo temperature, T_K.

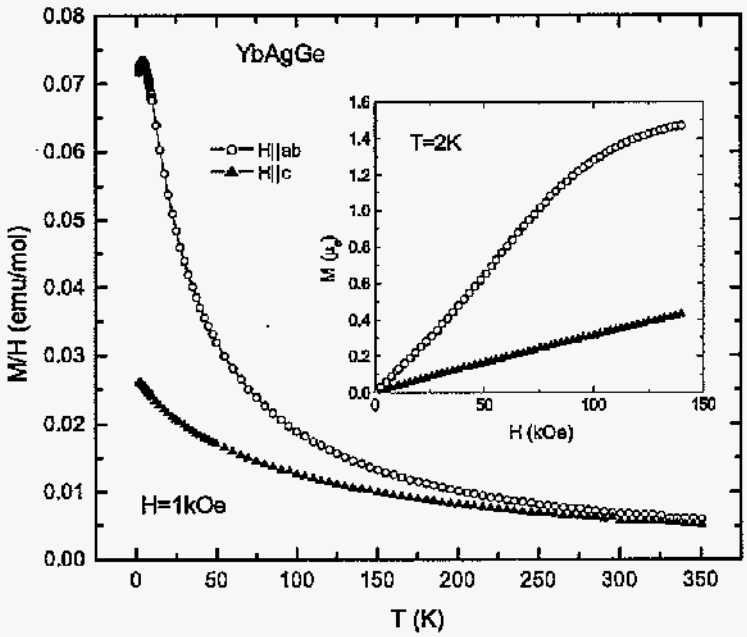

Figure 8.1 Anisotropic temperature-dependent DC susceptibility and (inset) field-dependent magnetization of YbAgGe.

Since the number of the Yb-based heavy fermion compounds is relatively small (Stewart, 1984; Fisk, 1992; Hewson, 1997) any new member of the family attracts attention (Fisk, 1992; Thompson, 1994). As an up to date example, $YbRh_2Si_2$, a heavy fermion antiferromagnet (Trovarelli, 2000), became a subject of intensive, rewarding exploration (Gegenwart, 2002; Ishida, 2002; Custers, 2003). The case of YbAgGe appears to have the potential of being somewhat similar to $YbRh_2Si_2$: the relatively high value of γ and the proximity of the magnetic ordering temperature to $T = 0$ suggest that YbAgGe is close to a quantum critical point (QCP) and make it a good candidate for a study of the delicate balance and competition between magnetically ordered and strongly correlated ground states under the influence of a number of parameters such as pressure, chemical substitution and/or magnetic field.

In this work we report the magnetic-field-induced evolution of the ground state of YbAgGe as seen in anisotropic resistivity and specific heat measurements up to 140 kG. We show that on increase of the applied magnetic field the progression from small moment magnetic order to QCP with the evidence of non-Fermi-liquid (NFL) behavior and, in higher fields, to low temperature Fermi-liquid (FL) state is observed.

8.1.2 Results

8.1.2.1 $H \parallel (ab)$

The low temperature part of the temperature dependent resistivity measured in various constant magnetic fields applied in the (ab) plane is shown in Fig. 8.2(a). There are several features that apparently require detailed examination. Multiple transitions in zero field is a feature that is common throughout the RAgGe series (Morosan, 2004) and in the case of YbAgGe in zero field in addition to the sharp transition at approximately 0.64 K another, albeit less pronounced feature is apparent at $\sim$ 1 K. Whereas the 0.64 K transition seems to be pushed below the base temperature of our measurements by a 20 kG field, the other feature shifts down in temperature more gradually and is seen up to 40 kG. For applied field between 60 and 90 kG (Fig. 8.2(c)) low temperature $\rho(T)$ functional dependence is linear down to our base temperature, with the upward curvature in $\rho(T)$ starting to occur below $\sim$ 0.8 K in 100 kG field. In higher applied fields ($H \geq 100kG$) (Fig. 8.2(d)) low temperature resistivity follows $\rho(T) = \rho_0 + AT^2$ (Fermi-liquid-like) functional behavior with the range of its occurrence (for each curve the upper limit is marked with arrow in Fig. 8.2(d)) increasing with the increase of applied field and the coefficient A decreasing.

Field dependent resistivity data taken at constant temperatures between 0.4 K and 5.0 K are shown in Fig. 8.3(a). At $T = 0.4$ K two fairly sharp features, at $\sim$ 13 kG and $\sim$ 40 kG are seen in the $\rho(H)$ data. The lower field feature may be identified as a signature of a metamagnetic transition between two different magnetically ordered phases. This feature vanishes as the temperature increased to $T > 0.65$ K (Fig. 8.3(b)). The second, more smoothed, higher field feature, may be to a transition from a magnetically ordered state to a saturated

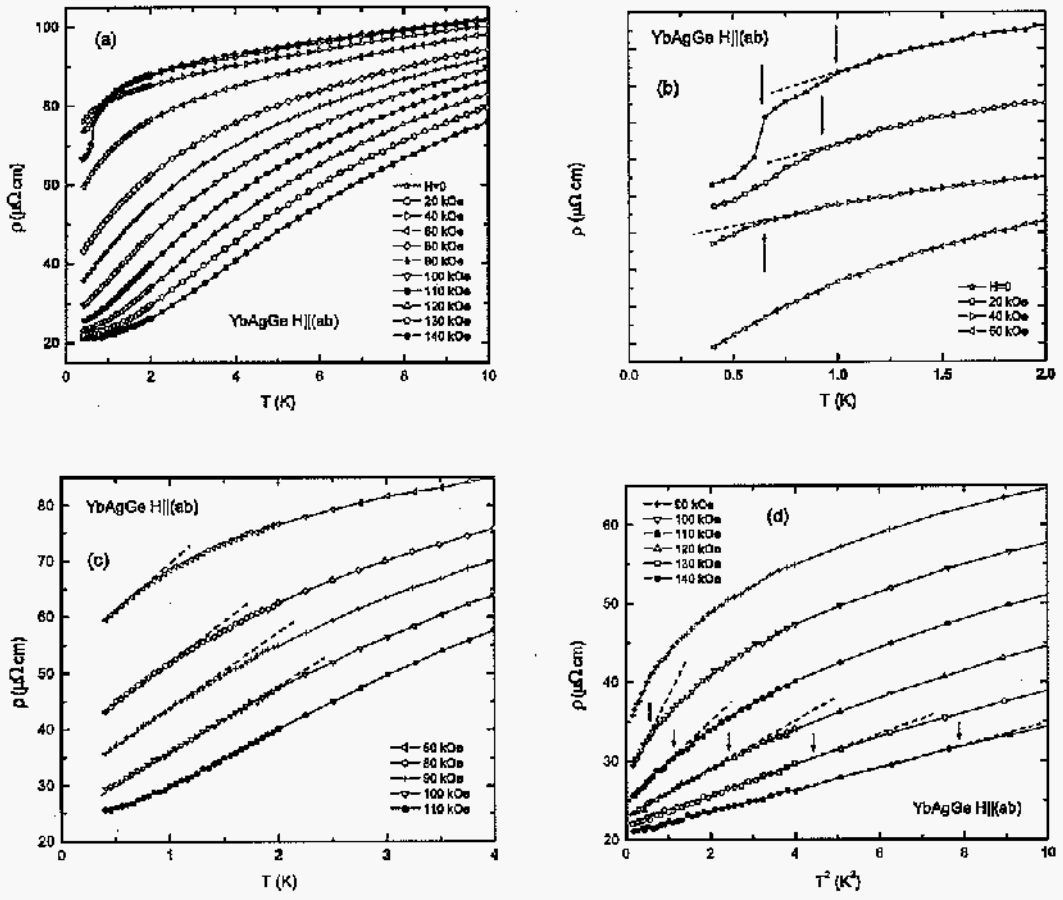

Figure 8.2 (a)Low temperature part of $\rho(T)$ curves for YbAgGe taken at different applied fields $H \parallel (ab)$; (b)$\rho(T)$ for $H = 0$, 20, 40 and 60 kG below 2 K (curves are shifted along y axis by 15, 5, -2.5 and 0 $\mu\Omega$ cm respectively for clarity), arrows indicate possible magnetic ordering transitions; (c)$\rho(T)$ for $H = 60$, 80, 90, 100 and 110 kG below 4 K, dashed lines are guides for the eye emphasizing regions of linear $\rho(T)$; (d)resistivity at $H =$ 90, 100, 110, 120, 130 and 140 kG below $\sim$ 3 K as a function of T^2, dashed lines bring attention to the regions where $\rho(T) = \rho_0 + AT^2$, arrows indicate temperatures at which deviations from T^2 behavior occur.

paramagnetic state. If the critical field for this transition is inferred from the maximum in $\rho(H)$, this transition can be discerned up to 0.8-0.9 K (Fig. 8.3(b)), consistent with it being associated with the $\sim$ 1 K transition seen in the $H = 0$ $\rho(T)$ and $C_p(T)$ data (Fig. 5.30). At higher temperatures (Fig. 8.3(a)) this feature broadens and resembles a crossover rather than a transition. For 2 K $< T <$ 5 K $\rho(H)$ looks like a generic magnetoresistance of a paramagnetic metal (Yosida, 1957). The large black dots in Fig. 8.3(b) show the evolution of the two aforementioned features.

The low temperature heat capacity of YbAgGe is shown for several values of applied magnetic field in Fig. 8.4(a). The lower temperature, sharp peak is seen only for $H = 0$, having been suppressed below the base temperature by an applied field of 20 kG. The higher temperature maximum seen just below 1 K (for $H = 0$) shifts down with the increase of the applied field and drops below 0.4 K for $H \geq 60kG$. The field dependence of this feature is consistent with that of the higher temperature feature in resistivity discussed above giving further evidence that YbAgGe has two closely-spaced magnetic transitions. The same data plotted as C_p/T textitvs T^2 (Fig. 8.4(b)) allow for the tracking of the variation of the electronic specific heat coefficient γ in applied field (for $H \geq 60$ kG, when the magnetic order is suppressed). The values at $T^2 = 0.35$ K^2 (a value chosen to avoid the upturn in lowest temperature, highest field $C_p/T(T^2)$ data possibly associated with the nuclear Schottky contribution) give a reasonable approximation of $\gamma(H)$. A more than four-fold decrease of γ is observed from 60 kG to 140 kG.

The magnetic contribution to the YbAgGe specific specific heat (defined as $C_{magn} = C_p(YbAgGe) - C_p(LuAgGe)$) is shown in Fig. 8.4(c) in C_{magn}/T textitvs $\lg T$ coordinates. (It should be noted that $C_p(T)$ of LuAgGe was measured at $H = 0$ and 140 kG and found to be insensitive to the applied field in this temperature range.) For intermediate values of applied field there is a region of the logarithmic divergency seen in the specific heat data $C_{magn}/T \propto -\ln T$. The largest range of the logarithmic behavior (more than an order of magnitude in temperature, from below 1 K to above 10 K) is observed for $H = 80$ kG. These data can be described as $C_{magn}/T = \gamma\prime_0 \ln(T_0/T)$ with $\gamma\prime_0 \approx 144$ mJ/mol K^2 and $T_0 \approx 41$ K. These

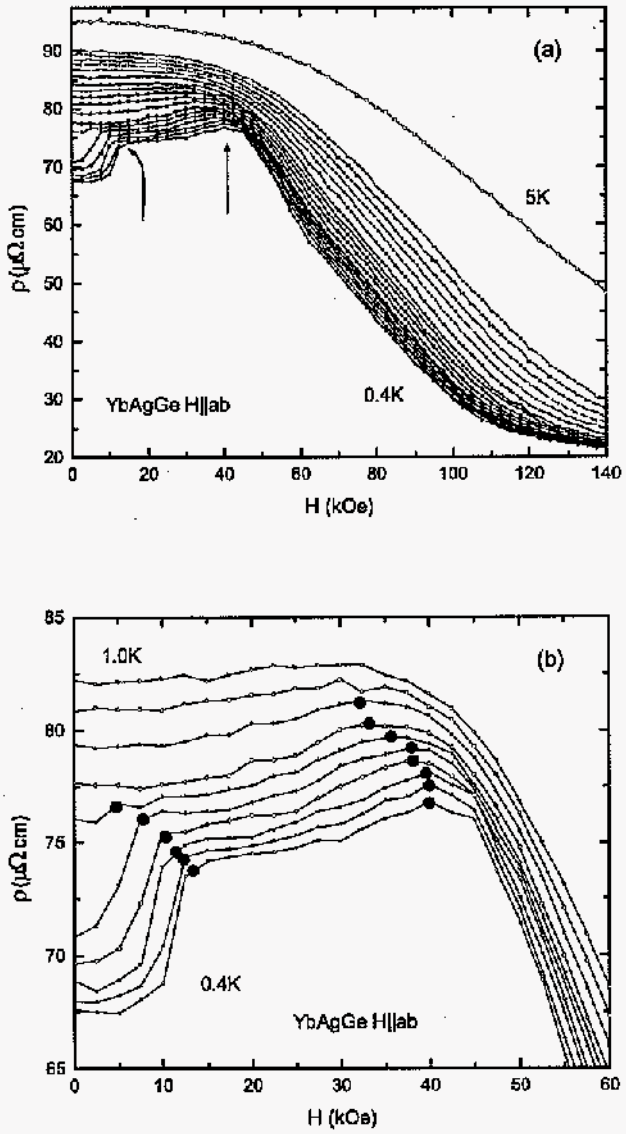

Figure 8.3 (a)$\rho(H)$ ($H \parallel (ab)$) isotherms for YbAgGe taken every 0.05 K between 0.4 K and 0.7 K, every 0.1 K between 0.7 K and 1.2 K, every 0.2 K between 1.2 K and 2.0 K and at 2.3 K, 2.5 K and 5.0 K, arrows point to the transitions discussed in the text; (b)enlarged low field - low temperature (0-60 kG, 0.4-1.0 K) part of the panel (a), black dots mark transitions on the respective curves.

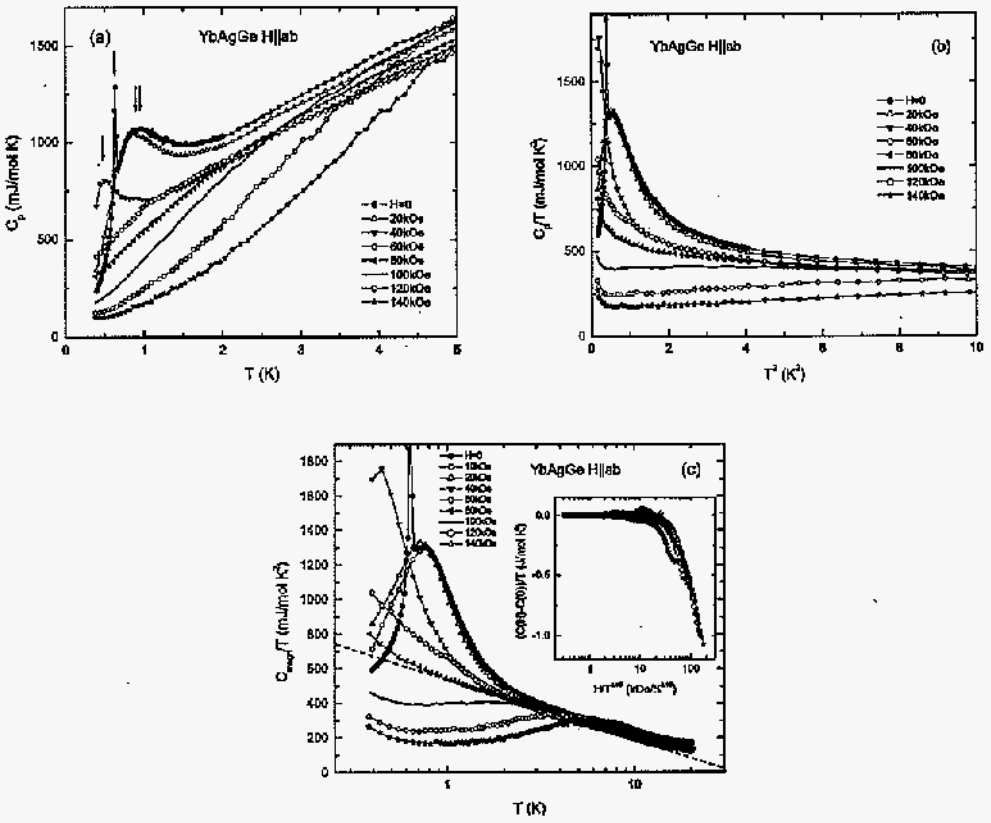

Figure 8.4 (a)Low temperature part of the heat capacity curves for YbAgGe taken at different applied fields $H \parallel (ab)$, arrows indicate peaks associated with magnetic ordering; (b)low temperature part of C_p *vs* T^2 curves; (c)*semi-log* plot of the magnetic part ($C_{magn} = C_p(YbAgGe) - C_p(LuAgGe)$) of the heat capacity, C_{magn}/T *vs* T, for different applied magnetic fields, dashed line is a guide to the eye, it delineates linear region of the $H =$ 80 kG curve; inset: *semi-log* plot of $(C(H) - C(H=0))/T$ *vs* $H/T^{1.15}$ ($T \geq 0.8$ K), note approximate scaling of the data for $H \geq 60$ kG.

parameters are of the same order of magnitude as those reported for $YbRh_2Si_2$ (Trovarelli, 2000). In higher fields Fermi-liquid-like behavior apparently recovers, in agreement with the resistivity data.

The crossover function $(C(H) - C(H = 0))/T$ *vs* H/T^{β} ($\beta = 1.15$) (one of the expressions considered in the scaling analysis at a QCP) is shown in the inset to Fig. 8.4(c). Data for $H \geq 60$ kG collapse onto one universal curve. Such scaling behavior (Tsvelik ,1993) with β between 1.05 and 1.6 was observed for a number of materials that demonstrate NFL properties (Trovarelli, 2000; Andraka, 1991; Lenkewitz, 1997; Heuser, 1998; KGrner, 2000) and may be considered as further corroboration of the proximity of YbAgGe to a QCP.

8.1.2.2 $H \parallel c$

YbAgGe manifests an easy plane anisotropy in both its low-field and high-field magnetization (Fig. 8.1). This is a trend that evolves across the RAgGe series (Morosan 2004), textite.g. in TmAgGe the local moments are extremely anisotropic being confined to the basal plane. Not surprisingly this anisotropy manifests itself in the low-temperature $\rho(H,T)$ and $C_p(H,T)$ data. The variation of the temperature dependent resistivity for $H \parallel c$ (Fig. 8.5(a)) is comparable to that for $H \parallel (ab)$. As for the in-plane orientation of the field, the two transitions seen for $H = 0$ move to lower temperatures with application of magnetic field, albeit the effect of field is weaker, so that the lower temperature transition is still being detected as a break in slope for $H = 20$ kG whereas the higher temperature transition persists up to 80 kG (Fig. 8.5(b)). The field range for which linear, low temperature resistivity can be seen is smaller and is shifted to higher fields (Fig. 8.5(c)), whereas the $\rho - \rho_0 \propto T$ behavior can be recognized for $H = 100$ kG and 120 kG, and a slight upward curvature above 0.4 K is already seen at $H = 130$ kG. The low temperature resistivity can be characterized by $\rho(T) = \rho_0 + AT^2$ (Fig. 8.5(d)) and this curvature can be viewed as a signature of a FL behavior. The range of T^2 behavior increases and the value of A decreases with an increase of applied field. The field-dependent resistivity for this orientation of the magnetic field (Fig. 8.6(a)) is similar to the set of $\rho(H)$ isotherms for $H \parallel (ab)$ except for the weaker field dependence of the observed transitions (Fig.

8.6(b)).

The low temperature part of the heat capacity measured for $H \parallel c$ up to 140 kG is shown in Fig. 8.7(a). Upper magnetic ordering transition temperature decreases with increase of applied field and can be followed up to 60 kG. Electronic contribution to the specific heat for fields where the ordering transition is suppressed can be estimated from the Fig. 8.7(b). For this orientation the largest range of the logarithmic behavior $C_{magn}/T \propto -\ln T$ is observed for $H = 140$ kG (Fig. 8.7(c)) and these data can be expressed as $C_{magn}/T = \gamma_0 \ln(T_0/T)$ with $\gamma_0 \approx 143$ mJ/mol K^2 and $T_0 \approx 44$ K, the values of γ_0 and T_0 being, within the accuracy of the data and the fit, the same as for $H \parallel (ab)$. Scaling behavior of the specific heat data plotted as $(C(H) - C(H=0))/T$ *vs.* H/T^β (the value of the exponent $\beta = 1.15$ is the same as for $H \parallel (ab)$) is observed for $H \geq 100$ kG (Fig. 8.7(c), inset).

8.1.3 Summary and Discussion

For both sets of data ($H \parallel (ab)$ and $H \parallel c$), at high enough applied fields, long range magnetic order is suppressed, and the electronic contribution to the specific heat can be estimated, whereas the low temperature resistivity shows $\Delta\rho \propto AT^2$ FL-like behavior. The values of γ were estimated at $T^2 = 0.35$ K^2 ($T \approx 0.6$ K) and decrease with the increasing magnetic field (Fig. 8.8(a)) in a manner similar to what was observed in $YbRh_2Si_2$ (Gegenwart, 2002) and other materials. Although the data set is sparse, it is worth noting that an approximately 50-55 kG shift down of the data for $H \parallel c$ (Fig. 8.8(a)) brings it into rough agreement with the $H \parallel (ab)$ data and so that the two sets form a universal curve. The T^2 coefficient of FL-like resistivity, A, also decreases with an increase of applied field (Fig. 8.8(b)). The shift required to have the A data for the two H orientations on the same curve is 30-25 kG. The field dependence of the Kadowaki-Woods ratio, A/γ^2 (Kadowaki, 1986) is presented in Fig. 8.8(c). Many of the γ and A values were reckoned for the same magnetic field. In some cases when additional values of A were available a straightforward interpolation of $\gamma(T)$ was used. Although more data points may be required to clarify these trends, several features are seen in the Fig. 8.8: the obtained values of A/γ^2 are of the same order of magnitude, but

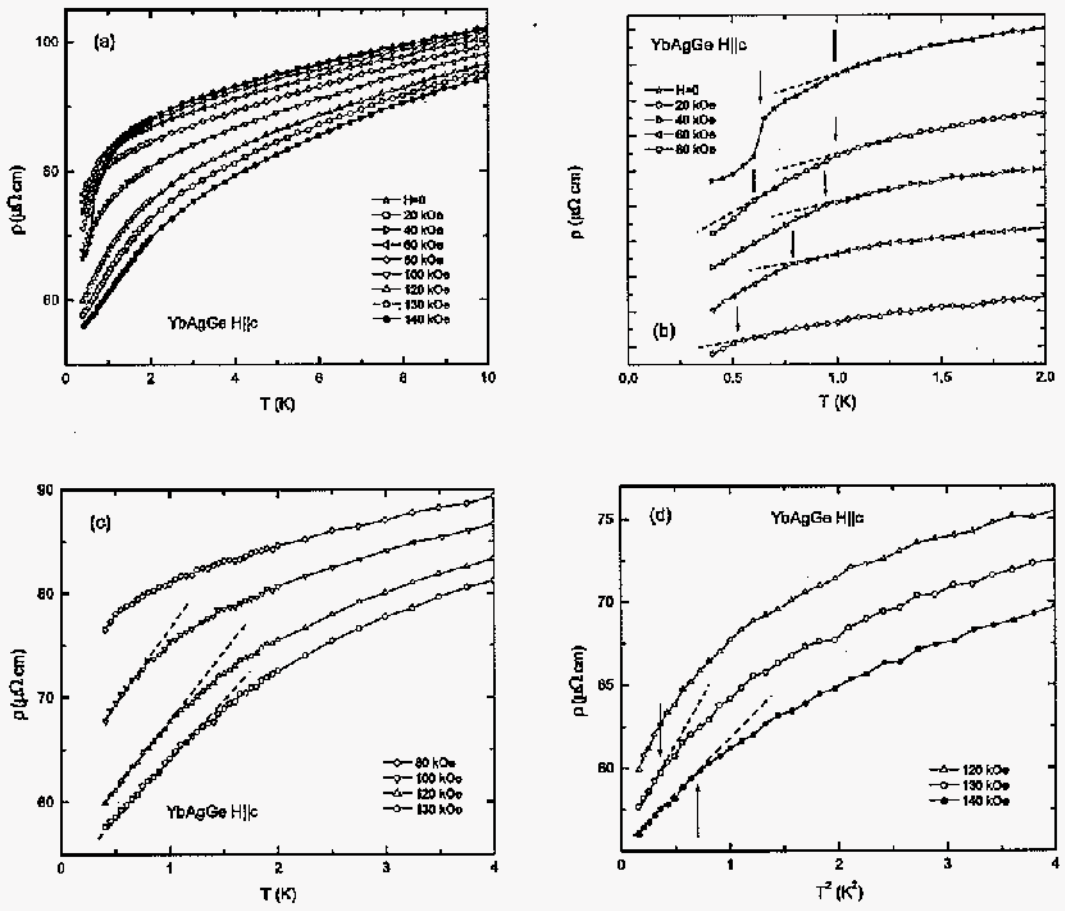

Figure 8.5 (a)Low temperature part of $\rho(T)$ curves for YbAgGe taken at different applied fields $H \parallel c$; (b)$\rho(T)$ for $H = 0$, 20, 40, 60 and 80 kG below 2 K (curves are shifted along y axis by 22, 10, 2.5, -5 and -12.5 $\mu\Omega$ cm respectively for clarity), arrows indicate magnetic ordering transitions; (c)$\rho(T)$ for $H = 80$, 100, 120 and 130 kG below 4 K, dashed lines are guides for the eye emphasizing regions of linear $\rho(T)$; (d)resistivity at $H = 120$, 130 and 140 kG below ~ 3 K as a function of T^2, dashed lines bring attention to the regions where $\rho(T) = \rho_0 + AT^2$, arrows indicate temperatures at which deviations from T^2 behavior occur.

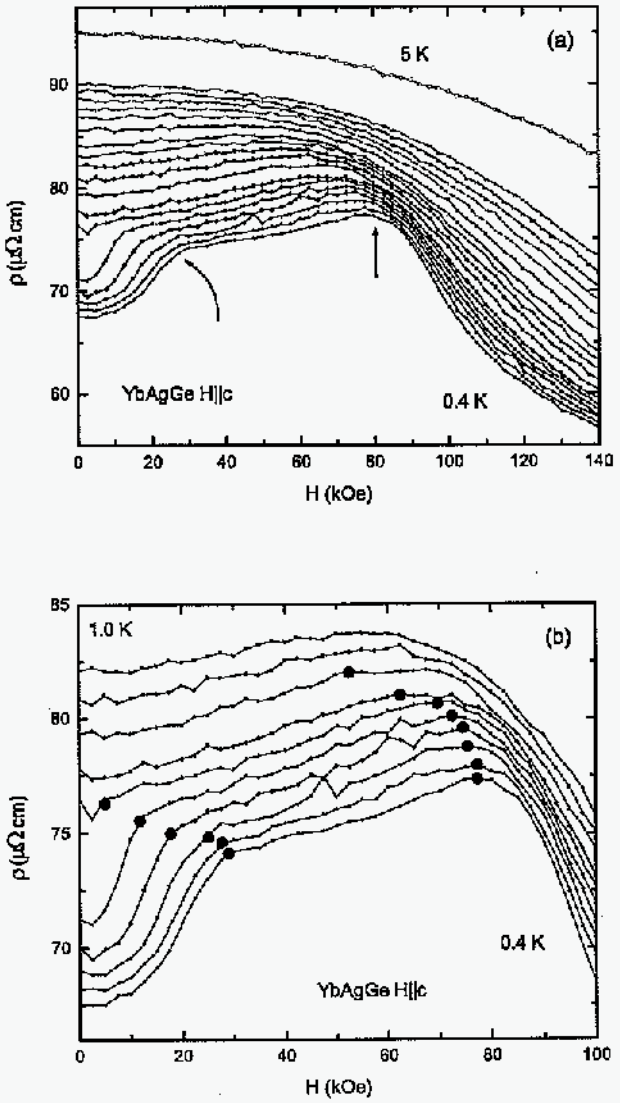

Figure 8.6 (a)$\rho(H)$ ($H \parallel c$) isotherms for YbAgGe taken every 0.05 K between 0.4 K and 0.7 K, every 0.1 K between 0.8 K and 1.2 K, every 0.2 K between 1.4 K and 2.0 K and at 2.3 K, 2.5 K and 5.0 K, arrows point to the transitions discussed in the text; (b)enlarged low field - low temperature (0-100 kG, 0.4-1.0 K) part of the panel (a), black dots mark transitions on the respective curves.

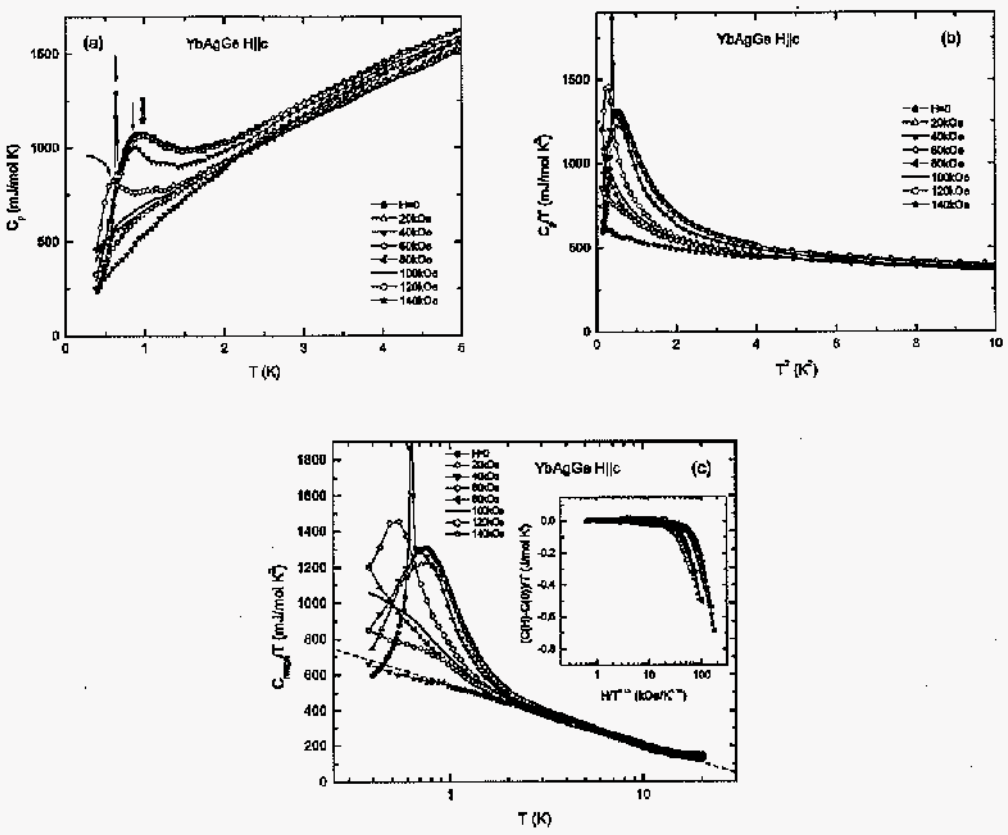

Figure 8.7 (a)Low temperature part of the heat capacity curves for YbAgGe taken at different applied fields $H \parallel c$, arrows indicate peaks associated with magnetic ordering; (b)low temperature part of C_p *vs* T^2 curves; (c)*semi-log* plot of the magnetic part ($C_{magn} = C_p(YbAgGe) - C_p(LuAgGe)$) of the heat capacity, C_{magn}/T *vs* T, for different applied magnetic fields, dashed line is a guide to the eye, it delineates linear region of the $H =$ 140 kG curve; inset: *semi-log* plot of $(C(H) - C(H = 0))/T$ *vs* $H/T^{1.15}$ ($T \geq 0.8$ K), note approximate scaling of the data for $H \geq 100$ kG.

several times higher than $\sim 1\times10^{-5}$ $\mu\Omega$ cm/(mJ/mol K)^2 obtained in (Kadowaki, 1986) and corroborated by the larger set of data in (Continentino, 1994; Tsujii 2003); for $H \parallel (ab)$ the Kadowaki-Woods ratio decreases with an increase of the field (not enough data is available for $H \parallel c$). Though magnetotransport measurements down to lower temperatures will allow for the estimate of A in a wider temperature range and may refine our A/γ^2 data, both of the features seen in Fig. 8.8(c) were observed in $YbRh_2Si_2$ (Custers, 2003) and apparently are common for materials where NFL behavior can be induced by magnetic field. In addition, a larger value of the Kadowaki-Woods ratio is anticipated theoretically in the close vicinity of a magnetic instability (Takimoto, 1996), in agreement with our experimental data, whereas constant (*i.e.* field-independent in our case) Kadowaki-Woods ratio is expected only in the local critical regime (Continentino, 2001).

Finally, based on the thermodynamic and transport data down to $\sim$ 0.4 K and up to 140 kG, we can construct tentative $T-H$ phase diagrams for the two orientations of the applied magnetic field (Fig. 8.9). Both phase diagrams are very similar. Initially increasing magnetic field drives first the lower and then the higher magnetic transitions to zero. With further increase in field signatures of the NFL behavior appear in the temperature dependent resistivity ($\Delta\rho \propto T$) and heat capacity ($C_{magn}/T \propto -\ln T$) and at our highest applied field values FL-like low temperature resistivity ($\Delta\rho \propto T^2$) (*i.e.* the coherence line (Continentino, 2001; Continentino, 1989) on the $T-H$ phase diagram) is observed. Although the current lack of data below $\sim$ 0.4 K impairs our ability to fully delineate the critical field that corresponds to $T = 0$ QCP, a rather crude assessment of the data (Fig. 8.9) suggests $H_c^{ab} \approx$ 45-70 kG, $H_c^c \approx$ 80-110 kG.

8.1.4 Conclusions

We presented results that allow for the classification of YbAgGe as a new heavy fermion material with magnetic field induced NFL behavior (critical fields are $H_c^{ab} \approx$ 45-70 kG, $H_c^c \approx$ 80-110 kG). Although its critical fields are somewhat higher than found for the extensively studied $YbRh_2Si_2$, they are still within the range accessible by many groups. It should be

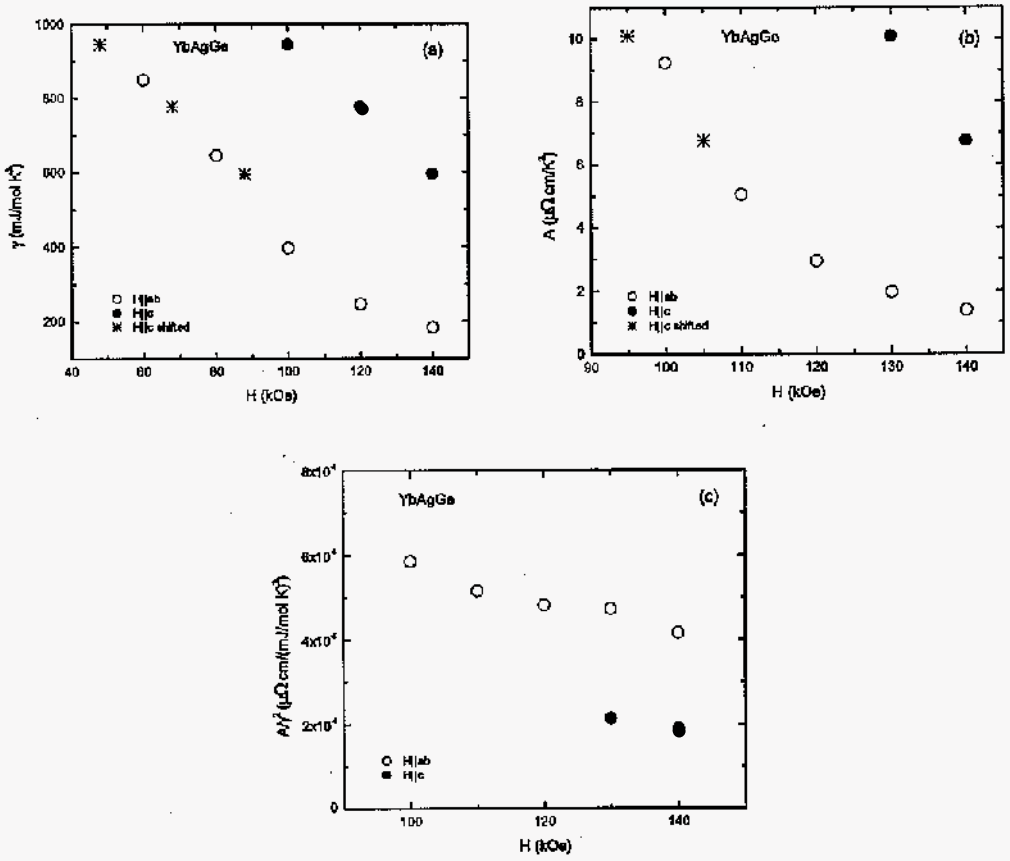

Figure 8.8 The anisotropic field dependence of (a)the electronic specific heat coefficient γ; (b)the resistivity coefficient A and (c)the Kadowaki-Woods ratio A/γ^2. In figures (a) and (b) shifted data for $H \parallel c$ are shown as $*$ (see text). The shift for figure (a) is -52 kG and for figure (b) -35 kG.

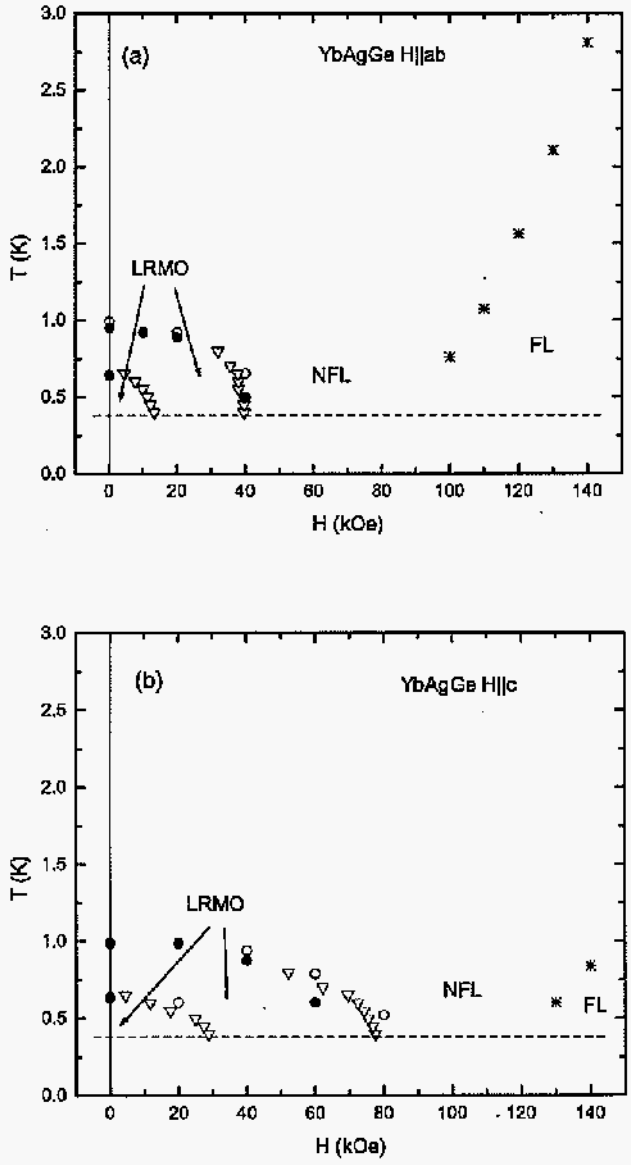

Figure 8.9 Tentative $T - H$ phase diagram for (a)$H \parallel (ab)$; (b)$H \parallel c$. Long range magnetic order (LRMO), NFL and FL regions are marked on the phase diagram. Symbols: Filled circles - from $C_p \mid_H$ measurements, open circles - from $\rho(T) \mid_H$, open triangles - from $\rho(H) \mid_T$, asterisks - temperatures below which $\Delta\rho \propto AT^2$ in $\rho(T) \mid_H$ data (coherence temperature, T_{coh}). Dashed line - low temperature limit of our measurements, vertical line marks $H = 0$.

mentioned that only very few *stoichiometric* compounds are known to demonstrate this type of behavior, making YbAgGe an important and interesting addition to the family of strongly correlated materials. Results of this work can serve as a road map for further studies, delineating further experimental courses: macroscopic (magnetization) and microscopic (neutron diffraction, μSR, Mocssbauer spectroscopy) measurements at low temperatures and in applied field are desirable to clarify the nature of the magnetically ordered states in YbAgGe and their evolution in field; lower temperature ($T < 0.4$ K), detailed thermodynamic and transport measurements in the vicinity of the field-induced QCP would be very helpful for the understanding of the physics of field induced NFL behavior and as a point of comparison with a number of existing theories (Stewart, 2001; Coleman, 2001; Pogorelov, 2003; Continentino, 2003) and with other materials with similar behavior. In addition, as is often the case for materials close to QCP, pressure and doping study may have a great potential in fine tuning of the ground state properties of YbAgGe.

8.2 Anisotropic Hall effect in single-crystal heavy fermion YbAgGe*

8.2.1 Introduction

Based on low temperature resistivity and heat capacity measurements in applied magnetic fields YbAgGe was recently classified as a new heavy fermion material with long range, possibly small moment, magnetic order below 1 K (Morosan, 2004; Budko, 2004; Katoh, 2004; Umeo, 2004) that shows magnetic field induced non-Fermi-liquid (NFL) behavior (Budko, 2004). The critical field required to drive YbAgGe to the field-induced quantum critical point (QCP) is anisotropic ($H_c^{ab} \approx 45$ kG, $H_c^c \approx 80$ kG) and conveniently accessible by many experimental groups (Budko, 2004). YbAgGe is one of the *rarae aves* of intermetallics (apparently only second, after the extensively studied $YbRh_2Si_2$ [Trovarelli, 2000; Gegenwart, 2002; Ishida, 2002; Custers, 2003]) a *stoichiometric*, Yb - based, heavy fermion (HF) that shows magnetic field induced NFL behavior and as such is suitable to serve as a testing ground for experimental

*after "Anisotropic Hall effect in single-crystal heavy fermion YbAgGe", S. L. Bud'ko, E. Morosan and P. C. Canfield, Phys. Rev. B **71** 054408 (2005).

and theoretical constructions relevant for QCP physics. Among the surfeit of detailed descriptions developed for a material near the antiferromagnetic QCP we will refer to the outcomes (Coleman 2001) of two more general, competing, pictures: in one viewpoint the QCP is a spin density wave (SDW) instability (Overhauser, 1959) of the Fermi surface; within the second picture that originates in the description of heavy fermions as a Kondo lattice of local moments (Doniach, 1977a; Doniach, 1977b), heavy electrons are composite bound states formed between local moments and conduction electrons and the QCP is associated with the breakdown of this composite nature. It was suggested (Coleman 2001) that Hall effect measurements can help distinguish which of these two mechanisms may be relevant for a particular material near a QCP. In the SDW scenario the Hall coefficient is expected to vary continuously through the quantum phase transition, whereas in the composite HF scenario the Hall coefficient is anticipated to change discontinuously at the QCP. Perhaps more importantly, in both scenarios a clear and sharp change in the field dependent Hall effect (for the field-induced QCP) is anticipated to occur at low temperatures, near the critical field value.

Although Hall effect measurements appear to be a very attractive method of gaining insight into the nature of the QCP, one has to keep in mind that an understanding of the different contributions to the measured Hall coefficient, in particular in magnetic or strongly correlated materials, is almost inevitably difficult and potentially evasive (Hurd, 1972; Paschen, 2003). Therefore measurements on samples well characterized by other techniques (Morosan, 2004; Budko, 2004) as well as comparison with non-magnetic as well as non-HF members of the same series can be beneficial. In this work we present temperature- and field- dependent Hall effect measurements on YbAgGe single crystals. The non-magnetic member of the same RAgGe (R = rare earth) series, LuAgGe, and the magnetic, essentially non-hybridizing, TmAgGe were used for "common sense" checks, or calipers, of the YbAgGe measurements.

8.2.2 Results and Discussion

8.2.2.1 LuAgGe and TmAgGe

The field-dependent Hall resistivity for LuAgGe for $H \| ab$ is shown in the upper inset to Fig. 8.10(a) for several temperatures. ρ_H is only slightly non-linear in field over the whole temperature range. This minor non-linearity causes some difference in the ρ_H/H *vs.* T data obtained in different applied fields (Fig. 8.10(a)). The Hall coefficient, $R_H = \rho_H/H$, is measured to be negative. The overall temperature dependence is monotonic, slow and featureless with approximately a factor of two increase in the absolute value of ρ_H/H from room temperature to low temperatures. This temperature-dependency of the Hall coefficient of the non-magnetic material possibly reflects some details of its electronic structure (for example, comparable factor of 2 changes in R_H were recently observed in $LaTIn_5$, T = Rh, Ir, Co, [Hundley, 2004]).

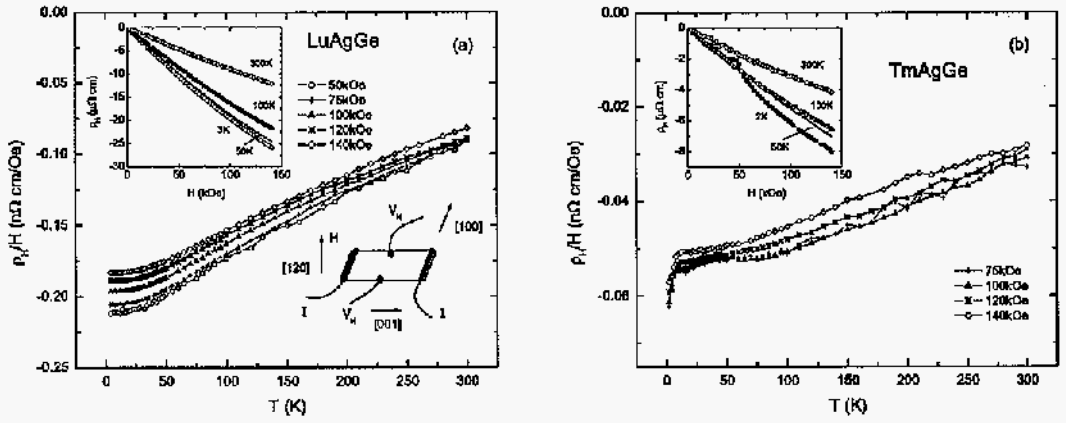

Figure 8.10 (a) Temperature-dependent Hall coefficient, ρ_H/H, of LuAgGe measured in different applied fields ($H \| ab$). Upper inset: field-dependent Hall resistivity of LuAgGe measured at different temperatures. Lower inset: the sample, current and applied field geometry used during the measurements. (b) Similar data for TmAgGe.

Overall the temperature- and field-dependence of the Hall coefficient for TmAgGe (Fig.

8.10(b)) is similar to that of LuAgGe with two main differences: (i)the long range order and metamagnetism of TmAgGe (Morosan 2004) is reflected in Hall measurements as a low temperature decrease in $R_H(T)$ and as anomalies in $\rho_H(H)$ for $T = 2$ K that are consistent with the fields of the metamagnetic transitions; (ii)the absolute values of the $R(H)$ data for TmAgGe are a factor of 3-4 smaller than for LuAgGe.

8.2.2.2 YbAgGe, $H \| ab$

The temperature dependent Hall coefficient and the DC susceptibility data for YbAgGe with the same orientation of the magnetic field with respect to the crystallographic axis are shown in Fig. 8.11. The susceptibility, M/H, is field-independent above 50 K (*i.e.* $M(H)$ is linear below 140 kG in this temperature range) and is similar to the data reported in (Morosan, 2004; Budko, 2004). The Hall coefficient, R_H, is field-independent above approximately 25 K. The temperature dependencies of the susceptibility and the Hall coefficient at high temperatures closely resemble each other. At low temperatures a field-dependent maximum in R_H (see inset to Fig. 8.11) is observed. Qualitatively the temperature dependence of the Hall coefficient is consistent with the picture presented in (Coleman, 1985; Hadzic-Leroux, 1986; Fert, 1987; Lapierre, 1987) (see also (Hurd 1972; Chien 1980) for a comprehensive review). Within this picture the temperature dependence of the Hall coefficient in heavy fermion materials is a result of two contributions: a residual Hall coefficient, $R_H^{res} = \rho_H^{res}/H$, and a Hall coefficient due to the intrinsic skew scattering, $R_H^s = \rho_H^s/H$. The residual Hall coefficient is ascribed to a combination of the ordinary Hall effect and residual skew scattering by defects and impurities and, to the first approximation, is considered to be temperature-independent, although, realistically, both the ordinary Hall effect and the residual skew scattering may have weak temperature dependence.

The temperature-dependent, intrinsic skew scattering contribution (R_H^s) at high temperatures ($T \gg T_K$, where T_K is the Kondo temperature) increases as the temperature is lowered in a manner that is mainly due to the increasing magnetic susceptibility. At lower temperatures R_H^s passes through a crossover regime, then has a peak at a temperature on the order

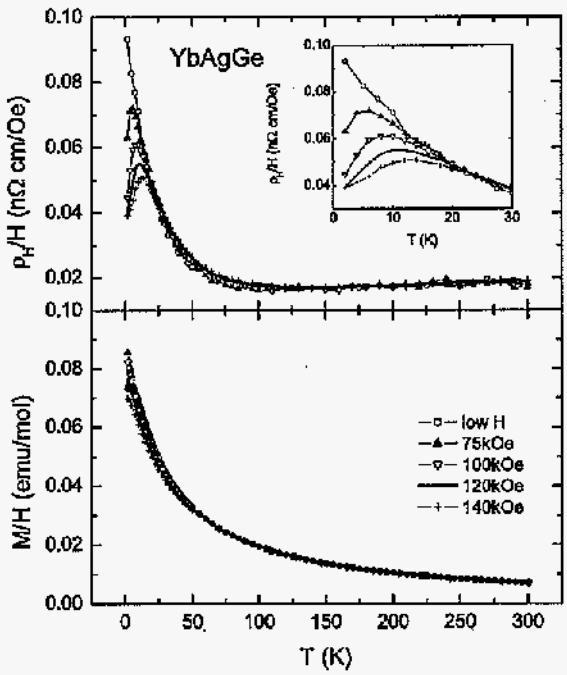

Figure 8.11 Upper panel: temperature-dependent Hall coefficient, ρ_H/H, of YbAgGe measured in different applied fields ($H \| ab$). Inset: enlarged, low temperature part of the data. Lower panel: DC susceptibility of YbAgGe (H along [120] direction). The "low H" label in the legend refers to the low field Hall resistivity (see Experimental section) and for susceptibility measured in $H = 1$ kG.

of the coherence temperature, T_{coh}, and finally, on further cooling rapidly decreases (in the coherent regime of skew scattering by fluctuations) to zero (*i.e.* R_H ultimately levels off to the $\sim R_H^{res}$ value at very low temperatures (Hadzic-Leroux, 1986; Fert, 1987; Lapierre, 1987). In the high temperature ($T \gg T_K$) limit we can (very roughly, within an order of magnitude) separate these two contributions to the observed temperature-dependent Hall coefficient using a phenomenological expression $R_H(T) = R_H^{res} + R_s \times \chi(T)$ (O'Handley, 1980) with the temperature-dependent skew scattering contribution written as $R_H^s(T) = R_s \times \chi(T)$ where $\chi(T) = C/(T - \Theta)$, C is the Curie constant, and Θ is the Weiss temperature. Using $\Theta_{ab} =$

-15.1 K from (Morosan 2004) we can plot $R_H(T) \times (T - \Theta)$ *vs.* $(T - \Theta)$ (Fig. 8.12) and from the linear part of the curve we can estimate $R_H^{res} \approx 0.02$ nΩ cm/Oe and $R_s \approx$ -0.17 nΩ cm/Oe.

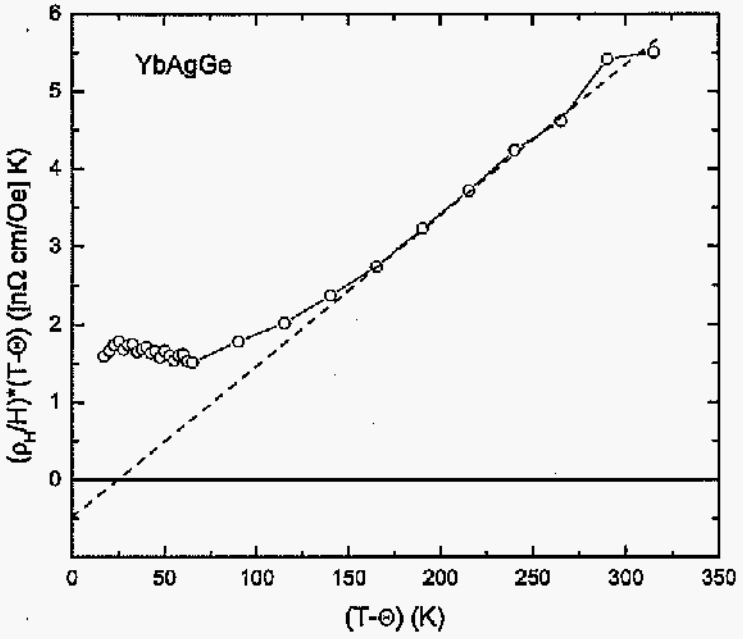

Figure 8.12 Temperature-dependent low field Hall coefficient ($H \| ab$) plotted as $(\rho_H/H) \times (T - \Theta)$ *vs.* $(T - \Theta)$.

It seems peculiar that our estimate of R_H^{res} for YbAgGe differs noticeably from the Hall coefficient measurements for LuAgGe and TmAgGe (see Fig. 8.10). Regarding this discrepancy it should be mentioned that besides possible experimental (mainly geometrical) errors these three materials may have different residual skew scattering and, additionally, as indicated by the preliminary results of band structure calculations (Samolyuk, 2004), the density of states at the Fermi level can be considerably different for all three compounds under consideration. Although the magnetic susceptibility, $\chi(T)$ of TmAgGe above the Néel temperature has a clear Curie - Weiss behavior (Morosan 2004), in contrast to the case of YbAgGe, the temperature dependence of the Hall coefficient for TmAgGe (Fig. 8.10(b)) does not have a similar functional

form. The reason for this difference is apparently the very small skew scattering contribution ($R_s \ll R_H^{res}$) to the Hall coefficient in TmAgGe. Similarly small couplings of local moment magnetism with the Hall effect has been seen in other rare earth intermetallics, *e.g.* RNi_2B_2C (R = rare earth) borocarbides (Fisher, 1995; Mandal, 1997; Narozhnyi, 1999).

In order to further explore the low temperature behavior of the Hall coefficient, measurements down to 0.4 K were performed. The results (on a semi -*log* scale) are shown in Fig. 8.13. The data taken in applied fields of 75 kG and higher show the expected levelling off of the $R_H(T)$ as $T \to 0$. It is noteworthy that the measured value of $R_H(T \to 0)$ is close to the aforementioned estimate of the residual Hall coefficient. This agreement suggests that at the lowest temperatures the Hall coefficient is dominated by R_H^{res} and, barring the residual skew scattering contribution, can probe the concentration of the electronic carriers.

Whereas the higher field values of the Hall coefficient vary smoothly with temperature (Fig. 8.13), the low field data, below $T \approx 3$ K, show large variations. Although the signal to noise ratio in the low field measurements is inherently lower, these variations appear to be above the noise level (Fig. 8.13, inset) and the peaks slightly above 0.6 K and 1.0 K are understood as the signatures of the magnetic transitions in YbAgGe (Morosan, 2004; Budko, 2004; Umeo, 2004) that are suppressed (in this orientation) when a 75 kG, or higher, magnetic field is applied.

To further study the field-induced QCP in YbAgGe, field dependent Hall resistance measurements were performed at different temperatures (Fig. 8.14). Although the theoretical constructions are usually formulated in terms of the Hall *coefficient*, not Hall *resistivity*, in the case of YbAgGe the magnetic field itself is a control parameter for the QCP that makes the proper definition of the Hall coefficient ambiguous. We will continue presenting our data as Hall resistivity, since it is a quantity unambiguously extracted from the measurements, and leave the discussion on the suitable definition of the Hall coefficient for the Appendix.

For temperatures at and above ~10 K, the $\rho_H(H)$ behavior is monotonic and, at higher temperatures, eventually linear (Fig. 8.14(b)). This type of behavior has been observed in a number of different materials in the paramagnetic state (Hurd, 1972). The low temperature evolution of the $\rho_H(H)$ behavior is more curious (Fig. 8.14(a)) and ought to be compared

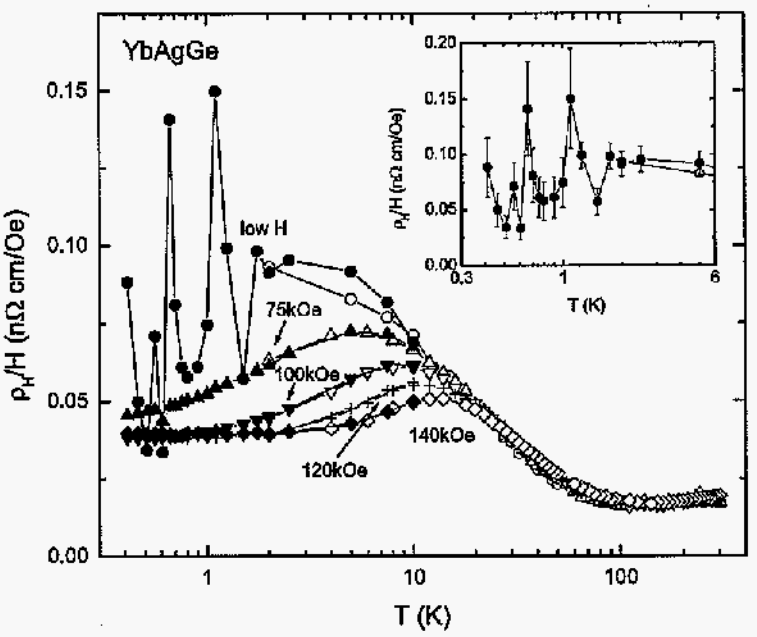

Figure 8.13 Temperature-dependent Hall coefficient of YbAgGe ($H\|ab$) measured in different applied fields down to 0.4 K. Open symbols - He-4 measurements (2-300 K), filled symbols - measurements using He-3 option (0.4-10 K). Inset: enlarged low temperature part of the low field data with the estimated error bars.

with the phase diagram obtained for YbAgGe ($H\|ab$) in (Budko, 2004) (an augmented version of which is shown in Fig. 8.9 below). The lines in Fig. 8.14(a) roughly connect the points according to the phase lines in (Budko, 2004) (see also Fig. 8.9 below). It can be seen that the lower $H-T$ magnetically ordered phase line possibly has (despite the scattering of the points) correspondent features in $\rho_H(H)$, and the coherence line in (Budko, 2004) (and Fig. 8.9) roughly corresponds to the beginning of the high field linear behavior in $\rho_H(H)$. On the other hand, the higher $H-T$ magnetically ordered phase line cannot unambiguously be associated with any feature in $\rho_H(H)$ curves.

The most interesting feature shown in Fig. 8.14(a) though is the presence of the pronounced

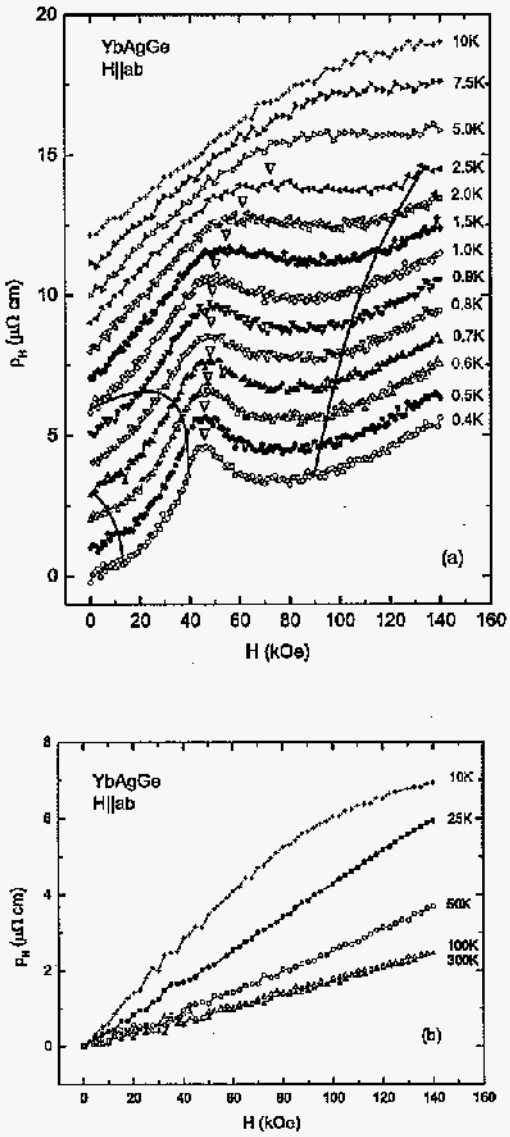

Figure 8.14 Field-dependent Hall resistivity of YbAgGe ($H||ab$) measured at different temperatures: (a)low temperature data: the curves, except for $T = 0.4$ K, are shifted by $1\mu\Omega$ cm increments for clarity; the lines represent the phase lines from the phase diagram in Fig. 10(a) of the Ref. 2; the triangles mark the position of the local maximum in $\rho_H(H)$; (b)intermediate and high temperature data. Note: $T = 10$ K data is shown in both plots for reference and is un-shifted in (b).

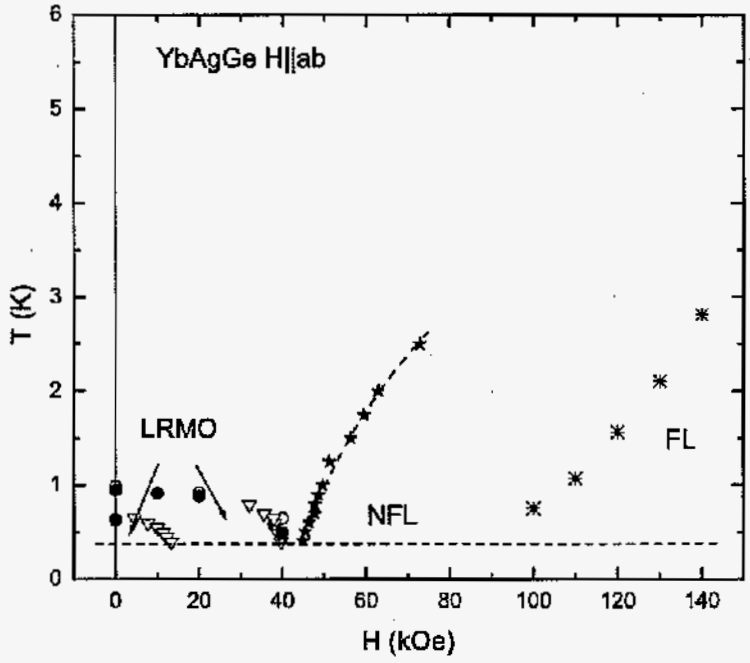

Figure 8.15 Revised tentative $T-H$ phase diagram for $H \parallel ab$. Long range magnetic order (LRMO) and the coherence temperature lines marked on the phase diagram are taken from Ref. 2. Filled stars and corresponding dashed line as a guide to the eye are defined from the maximum in the $\rho_H(H)$ curves.

peak, or local maximum, in $\rho_H(H)$ that occurs at ≈ 45 kG for the $T = 0.4$ K curve and can be followed up to temperatures above long range magnetic order transition temperatures. For $T =$ 2.5 K a broad, local maximum in ρ_H, centered at $H \approx 100$ kG can just barely be discerned. As temperature is reduced this feature sharpens and moves down in field. For $T = 1$ K the local maximum in ρ_H is clearly located at $H \approx 50$ kG and by $T = 0.4$ K ρ_H has sharpened almost to the point of becoming discontinuous with $H_{max} \approx 45$ kG. The temperature dependence of H_{max} is shown in Fig. 8.15 clearly demonstrating that as $T \rightarrow 0$, $H_{max} \rightarrow H_{crit}$ for the QCP. Independent of any theory these data clearly show that (i) ρ_H is an extremely sensitive

method of determining H_{crit} of QCP, (ii) H_{max} has a clear temperature dependence, and (iii) the QCP influences ρ_H up to $T \leq 2.5$ K, a temperature significantly higher than the $H = 0$ antiferromagnetic ordering temperature.

The new phase line (shown as stars in Fig. 8.15) associated with ρ_H maximum is distinct from the lines inferred from $C_p(T, H)$ and $\rho(T, H)$ data (Budko, 2004). As $T \to 0$ this line approaches H_{crit}, but for finite T it is well separated from the coherence line that was determined by the onset of T^2 resistivity behavior. This new H_{max} line rather clearly locates H_{crit} at ~ 45 kG, the field at which the long range antiferromagnetic order appears to be suppressed.

8.2.2.3 YbAgGe, $H \| c$

Since the response of YbAgGe to an applied magnetic field is anisotropic (Morosan, 2004; Budko, 2004; Katoh, 2004; Umeo, 2004), it is apposite to repeat the Hall measurements for the magnetic field applied parallel to the crystallographic c-axis. The temperature-dependent Hall coefficient taken in different applied fields is presented in Fig. 8.16 (the low-field data were obtained as described above). The $R_H(T)$ behavior for $H \| c$ is qualitatively similar to that for $H \| ab$ with a broad maximum being shifted to ~ 30 K (as compared to ~ 10 K for $H \| ab$) and being less sensitive to the applied field.

The low temperature, field-dependent Hall resistivity for $H \| c$ is shown in Fig. 8.17. In many aspects the overall behavior is similar to that for $H \| ab$: there are no apparent features associated with the phase lines derived from magnetoresistance and specific heat measurements (Budko, 2004) (shown as lines in Fig. 8.17), however there is the presence of a pronounced minimum in $\rho_H(H)$ that occurs at ≈ 98 kG for the $T = 0.4$ K curve and can be followed up to the temperatures well above the zero-applied-field magnetic transition temperatures. For $T = 2$ K a broad, local minimum in ρ_H, centered at $H \approx 128$ kG can still be recognized and at $T = 2.5$ K a local minima occurs just at the edge of our field range. As temperature is reduced this feature sharpens and moves down in field. The temperature dependence of H_{min} is shown in Fig. 8.18 clearly demonstrating that, similar to the $H \| ab$ case, as $T \to 0$, $H_{min} \to H_{crit}$ for the QCP. The $\rho_H(H)$ behavior for this orientation is more complex, and

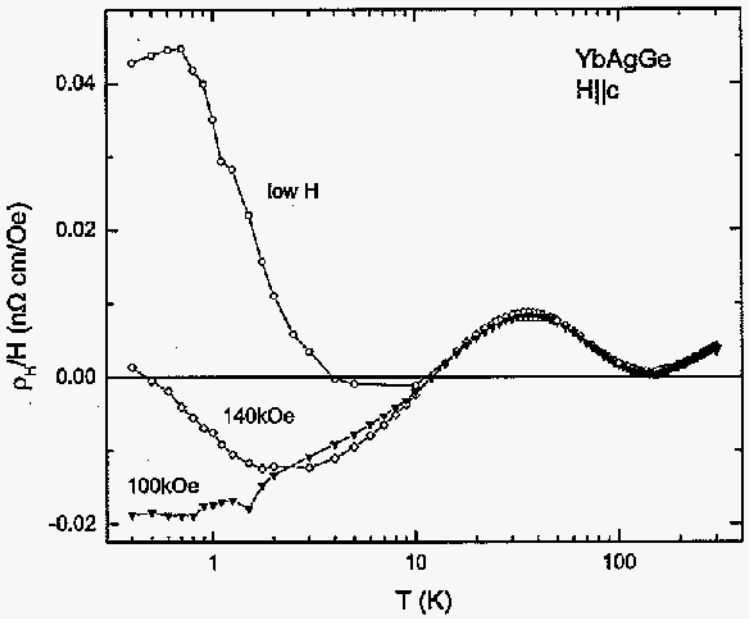

Figure 8.16 Temperature-dependent Hall coefficient of YbAgGe ($H\|c$) measured in different applied fields down to 0.4 K.

there is an additional, broad maximum in lower fields ($H \approx 50$ kG at 0.4 K) that fades out with increasing temperature. This highly non-monotonic in field behavior is the origin of the dissimilarities in the low temperature $R_H(T)$ data (Fig. 8.16) taken in different applied fields.

The high field minimum in $\rho_H(H)$ (Fig. 8.17) defines a new phase line (shown as stars in Fig. 8.18) which is clearly different from the lines inferred from $C_p(T,H)$ and $\rho(T,H)$ data (Budko, 2004). As $T \to 0$ this line approaches H_{crit}, but for finite T it is well separated from the coherence line that was determined by the onset of T^2 resistivity behavior. For this orientation of the applied field this new H_{min} line rather clearly locates H_{crit} at ~ 100 kG, the field at which the long range antiferromagnetic order appears to be suppressed.

It should be noted that the new lines in the $H-T$ phase diagrams were established from different types of extrema in $\rho_H(H)$, *maximum* for $H\|ab$ and *minimum* for $H\|c$. We neither

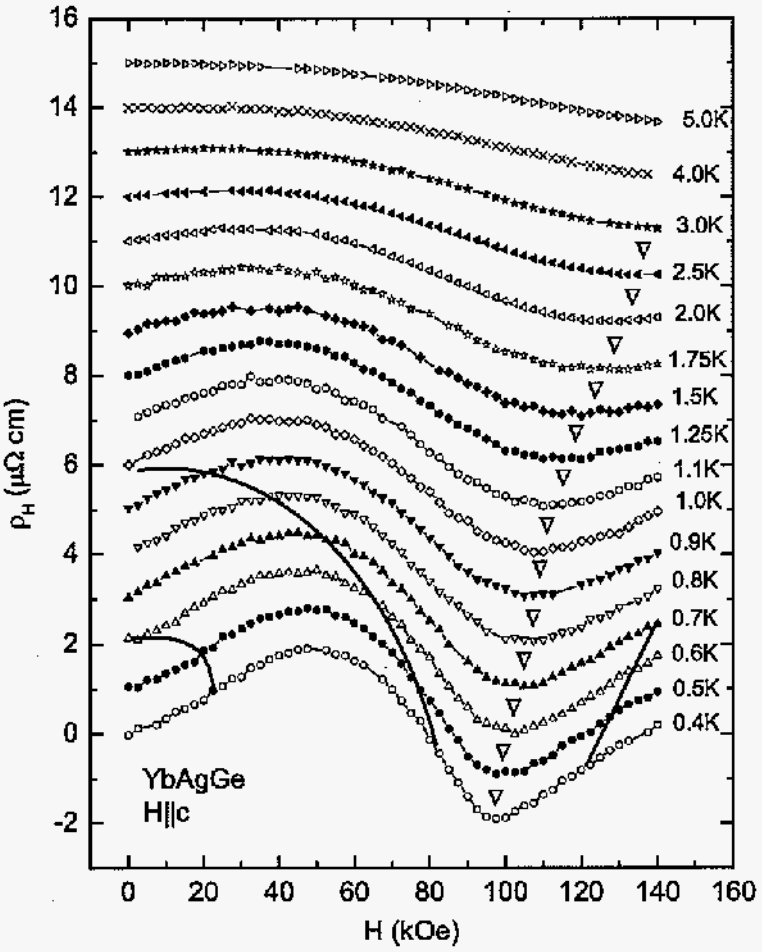

Figure 8.17 Low temperature field-dependent Hall resistivity of YbAgGe ($H \| c$); the curves, except for $T = 0.4$ K, are shifted by $1\mu\Omega$ cm increments for clarity; the lines represent the phase lines from the phase diagram in Fig. 10(b) of the Ref. 2; the triangles mark the position of the peak in $\rho_H(H)$.

consider this difference as a reason for particular discomfort nor do we necessarily view it as a potential clue to deeper understanding of the nature of the field-induced QCP in this material. The preliminary band structure calculations (Samolyuk, 2004) on LuAgGe, the non-magnetic

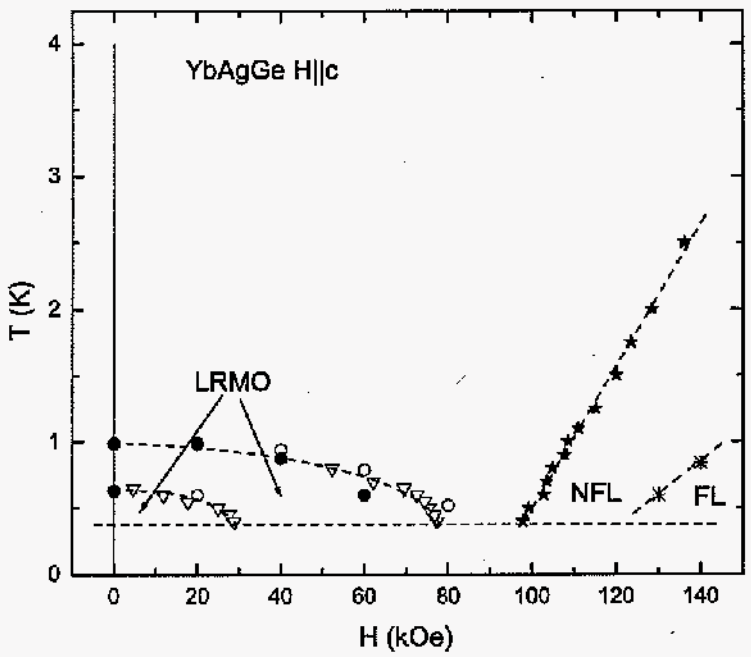

Figure 8.18 Revised tentative $T - H$ phase diagram for $H \parallel c$. Long range magnetic order (LRMO) and the coherence temperature lines marked on the phase diagram are taken from Ref. 2. Filled stars are defined from the minimum in the $\rho_{II}(H)$ curves. Dashed lines are guides to the eye.

analogue of the title compound, suggest that the members of the RAgGe series have a complex Fermi surface consisting of multiple sheets. In such a case a change in the Fermi surface may possibly have different signatures in the Hall measurements with different field orientation. In addition, existing QCP models appear not to be at the level of considering different shapes and topologies of the Fermi surfaces.

Whereas these new, H_{max}/H_{min} lines on the $H - T$ phase diagrams (Figs. 8.15 and 8.18) appear to be closely related with the QCP their detailed nature and temperature dependencies will require further experimental and theoretical attention.

8.2.3 Summary

The temperature- and field-dependent Hall resistivity have been measured for YbAgGe single crystals with $H\|ab$ and $H\|c$ orientation of the applied magnetic field. The temperature dependent Hall coefficient of YbAgGe behaves similarly to other heavy fermion materials. Low temperature, field-dependent measurements reveal a local maximum ($H\|ab$) or minimum ($H\|c$) in $\rho_H(H)$ for $T \leq 2.5$ K that occurs at a value that approaches $H_{crit} \approx 45$ kG ($H\|ab$) and $H_{crit} \approx 90$ kG ($H\|c$) as $T \to 0$. These data indicate that (i) the Hall resistivity is indeed a useful measurement for the study of QCP physics and (ii) the influence of the QCP extends to temperatures significantly higher than the $H = 0$ antiferromagnetic ordering temperature.

8.2.4 Appendix

Coleman *et al.* (Coleman 2001) suggest that $R_H(P)$ data (where P is a control parameter, *i.e.* H in our case) can be used to distinguish between two possible QCP scenarios: diffraction off of a critical spin density wave or a breakdown of the composite nature of the heavy electron, with the former manifesting a change of slope at P_{crit} and the latter manifesting a divergence in the slope of $R_H(P)$ at P_{crit}. Since in our case the magnetic field is itself the control parameter, it in not clear if $R_H = \rho_H/H$, $R_H = d\rho_H/dH$ or just simply ρ_H should be used for comparison with the theory. $R_H(H)$ curves determined by two aforementioned ways are presented in Fig. 8.19 ($H\|ab$) and Fig. 8.20 ($H\|c$). For both definitions and both orientations the evolution of a clear feature in $R_H(H)$ (defined as a local extremum for ρ_H/H and as a mid-point between two different field-dependent regimes for $d\rho_H/dH$) replicates (albeit with slight H-shift) the behavior of the Hall resistivity (Figs. 8.14(a), 8.17). Given that the new phase line in Figs. 8.9a and b is fairly insensitive to the data analysis we feel that the use of $\rho_H(H)$ data is currently the least ambiguous data set to analyze. On the other hand, if the form of the anomaly near H_{crit} is to be analyzed in detail it will be vital to have a more detailed theoretical treatment of magneto-transport in field-induced QCP materials.

It is tempting to say that for the case of applied field as a control parameter the quantity $d\rho_H(H)/dH$ (rather than $\rho_H(H)/H$) serves the role of the low-field Hall coefficient and should

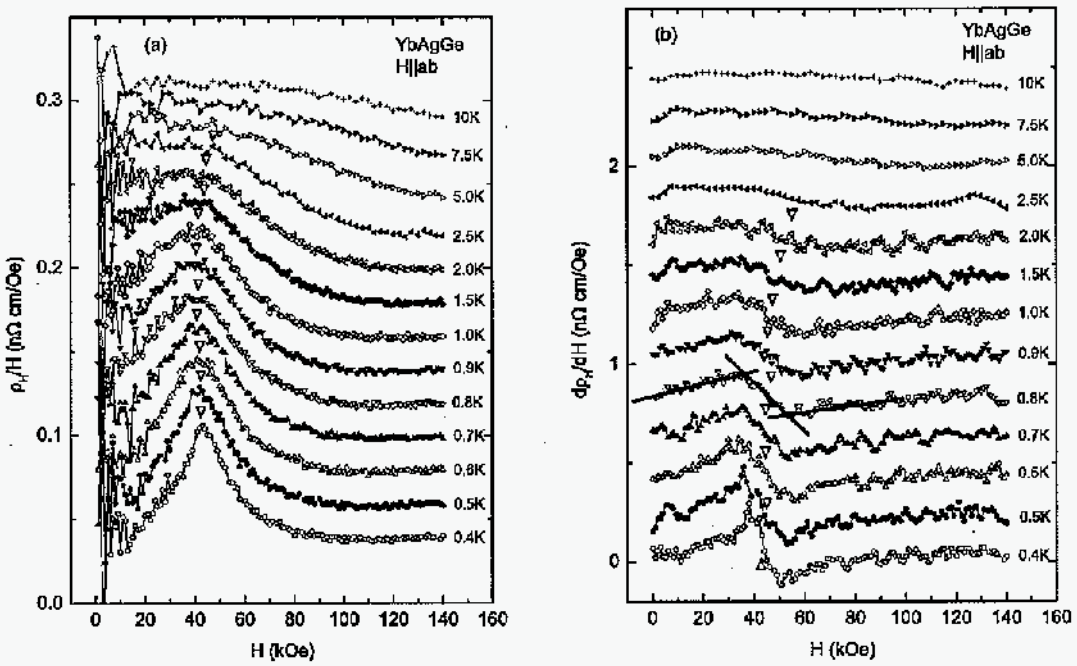

Figure 8.19 Field-dependent Hall coefficient of YbAgGe ($H\|ab$), defined as (a) $R_H = \rho_H/H$ and (b) $R_H = d\rho_H/dH$, measured at different temperatures. The curves, except for $T = 0.4$ K, are shifted by (a) 0.02 nΩ cm and (b) 0.2 nΩ cm increments for clarity; the triangles mark the position of the feature in $R_H(H)$: a local maximum in ρ_H/H and a mid-point of the transition between two different field-dependent regimes (see *e.g.* 0.8 K curve)in $d\rho_H/dH$. Curves in the (b) panel were obtained by differentiation of the 5-adjacent-points-smoothed $\rho_H(H)$ data. Small downturn at $H \geq 130$ kG in some $d\rho_H/dH$ curves (panel (b)) is most likely an artifact of using digital smoothing and differentiation.

be compared with the prediction of the models. If this point of view is accepted, then for $H\|ab$ the shape and evolution of the $d\rho_H(H)/dH$ curves (Fig. 8.19(b)) suggest that possibly the composite fermion model of the QCP is more relevant to the case of YbAgGe, although for $H\|c$ the shape and evolution of the $d\rho_H(H)/dH$ curves (Fig. 8.20(b)) are at variance with the simple theoretical views. The lack of the $T < 0.4$ K data and an absence of more detailed, realistic-Fermi-surface-tailored, model do not allow us to choose the physical picture of the

field-induced QCP in YbAgGe unambiguously.

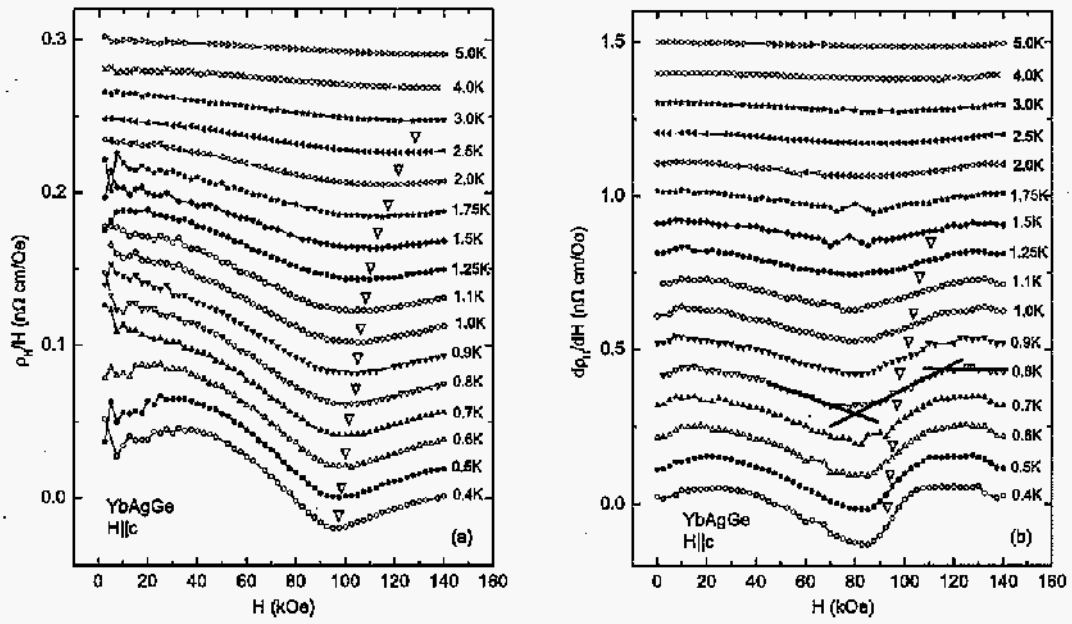

Figure 8.20 Field-dependent Hall coefficient of YbAgGe ($H \| c$), defined as (a) $R_H = \rho_H/H$ and (b) $R_H = d\rho_H/dH$, measured at different temperatures. The curves, except for $T = 0.4$ K, are shifted by (a) 0.02 nΩ cm and (b) 0.1 nΩ cm increments for clarity; the triangles mark the position of the feature in $R_H(H)$: a local minimum in ρ_H/H and a mid-point of the transition between two different field-dependent regimes (see *e.g.* 0.8 K curve)in $d\rho_H/dH$. Curves in the (b) panel were obtained by differentiation of the 5-adjacent-points-smoothed $\rho_H(H)$ data. Small downturn at $H \geq 130$ kG in some $d\rho_H/dH$ curves (panel (b)) is most likely an artifact of using digital smoothing and differentiation.

CHAPTER 9. Magnetic field-induced quantum critical point in YbPtIn and $YbPt_{0.98}In$ single crystals*

9.1 Introduction

In recent years, stoichiometric Yb-based heavy fermion compounds have raised a lot of interest, particularly due to the limited number of such systems known to date. YbPtIn is one of the few examples of such heavy fermion systems (Trovarelli, 2000a; Kaczorowski, 2000; Yoshii, 2004), as indicated by measurements performed on single crystal samples extracted from on-line melts of the polycrystalline material. Based on the existing data (Trovarelli, 2000a; Kaczorowski, 2000), YbPtIn has a relatively low magnetic ordering temperature ($T_{ord} \sim 3$ K) and an enhanced electronic specific heat coefficient ($\gamma > 400$ mJ/mol K^2), whereas the magnetic entropy at T_{ord} amounts to only about 60% of the $R \ln 2$ value expected for a doublet ground state. In light of these observations, this system appears to be qualitatively similar to the other recently studied Yb-based heavy fermion antiferromagnets, $YbRh_2Si_2$ (Trovarelli, 2000b; Gegenwart, 2002; Ishida, 2002; Paschen, 2003; Paschen, 2004), and YbAgGe (Beyermann, 1998; Katoh, 2004; Morosan, 2004; Bud'ko, 2004; Bud'ko, 2005), the latter compound isostructural to YbPtIn. In $YbRh_2Si_2$, magnetic order occurring at very low temperature (below 70 mK) (Trovarelli, 2000b) was associated with a low entropy release (less than 0.45 $* R \ln 2$) at T $\sim$ 10 K. For the YbAgGe (Morosan, 2004; Bud'ko, 2004) compound, the temperature associated with the magnetically ordered state, whereas still fairly low ($\sim$ 1.0 K), is enhanced compared to that of $YbRh_2Si_2$; also, the magnetic entropy at the ordering temperature is larger than in $YbRh_2Si_2$, but still less than 10% of $R \ln 2$. Thus these two

*after "Magnetic field-induced quantum critical point in YbPtIn and $YbPt_{0.98}In$ single crystals", E. Morosan, S. L. Bud'ko, Y. A. Mozharivskyj and P. C. Canfield, submitted to Phys Rev B (June, 2005).

compounds can be regarded as systems with small moment ordering. Having an even higher ordering temperature and magnetic entropy at T_{ord}, YbPtIn seemed a good candidate to further study a progression from small moment to reduced moment ordering, in stoichiometric Yb-based heavy fermion compounds, with field-induced quantum critical point.

In contrast to a classical phase transition at finite temperatures, driven by temperature as a control parameter with thermal fluctuations, a quantum phase transition is driven by a control parameter C other than temperature (*e.g.*, C = pressure, doping or magnetic field) at T = 0, with quantum mechanical fluctuations. Such a control parameter tunes the system from a magnetically ordered state towards a disordered state, at zero temperature, crossing a quantum critical point. Due to the hybridization of the 4f electrons and the conduction electrons in heavy fermion HF systems, which can be modified by any one of the aforementioned C control parameters, the HF compounds are very suitable to study quantum critical behavior. Moreover, close to the critical value C_{crit} which drives the ordering temperature close to zero, pronounced deviations from the Fermi liquid-like FL behavior can occur. This has been observed in a large number of HF systems where C = doping or pressure, and only a few doped systems have been field-tuned through a QCP (Stewart, 2001). To date, $YbRh_2Si_2$ (Trovarelli, 2000b; Gegenwart, 2002; Ishida, 2002; Paschen, 2003; Paschen, 2003) and YbAgGe (Beyermann, 1998; Katoh, 2004; Morosan, 2004; Bud'ko, 2004; Bud'ko, 2005) are the only stoichiometric Yb-based HF compounds in which a field-induced quantum critical point QCP has been observed. The heavy fermion character of the YbPtIn system has already been reported (Trovarelli, 2000a; Kaczorowski, 2000); in this paper we will discuss the existence of a field-induced QCP in YbPtIn which has not been yet studied, and which renders it very similar to the other two stoichiometric, Yb-based heavy fermions.

In Chapter 7 we presented anisotropic low-field susceptibility measurements, as well as specific heat data in zero applied field, on solution-grown single crystals of the RPtIn series, including YbPtIn. No features indicative of magnetic order could be identified in our magnetization measurements on single crystals of the R = Yb compound, down to T $\sim$ 2 K. However, a well-defined peak at T = 2.1 K in the zero-field specific heat data suggests that this compound

orders magnetically below 2.1 K, just above the low temperature limit of our magnetization measurements. As we will present in this paper, detailed transport and thermodynamic measurements down to 0.4 K not only confirm the magnetic ordering in this compound below 2.1 K, but also suggest that another phase transition might exist in this system around 1 K.

However, our measurements were in part inconsistent with all previous reports on YbPtIn single crystals: whereas Kaczorowski *et al.* (Kaczorowski, 2000) have also presented magnetization data showing no features associated with magnetic ordering above 1.7 K, in their specific heat measurements three anomalies can be observed (at 3.1, 2.3, and 1.2 K), all at slightly different temperatures than in our data. Furthermore, the low-field susceptibility data presented by Trovarelli *et al.* (2000a) are consistent with an ordering temperature around 3.4 K, also confirmed by their resistivity and specific heat measurements.

In order to address these apparent discrepancies between our data on solution grown single crystals and the two previous reports on on-line grown single crystals (Trovarelli, 2000a; Kaczorowski, 2000), we reproduced the growth as described by Trovarelli *et al.* (2000a). The anisotropic specific heat and transport measurements on our single crystals extracted from the melt confirmed the existence of magnetic phase transitions at 3.4 K and 1.4 K, as observed previously.

In this chapter we will try to examine the differences between solution and on-line grown single crystals, given that a small Pt-deficiency occurred in the former types of crystals, leading to a stoichiometry closest to $YbPt_{0.98}In$; no disorder could be detected in the on-line grown crystals. Also, given that heavy fermion compounds with small moment ordering can be driven to a quantum critical point QCP by disorder or applied field, we will study the evolution of both $YbPt_{0.98}In$ and YbPtIn towards a field-induced QCP. Detailed anisotropic measurements of specific heat and resistivity on the two types of crystals, for fields up to 140 kG and temperatures down to 0.4 K, will be used for the comparison between the two types of crystals. Additional Hall effect measurements were performed on the solution grown single crystals for the same temperature and field ranges, allowing us to further explore the effects of the QCP in this compound.

Following the results of single crystal x-ray diffraction, we will compare the low field data for the two types of compounds, pointing out the similarities, as well as the significant differences in their physical properties. Next we will present the higher field data for both types of crystals, for $H \parallel ab$ and $H \parallel c$. This will allow us to follow, in both systems, the progression from reduced magnetic moment order to the quantum critical point QCP, as driven by the application of increasing magnetic field. Also, we will extend the zero-field comparison between the two YbPtIn systems to their field- dependent properties, and will try to identify common features as well as possible effects of the site deficiency.

9.2 Results

9.2.1 Crystal structure

For both solution and on-line grown crystals, the crystal structure was confirmed by powder x-ray diffraction, with no detectable impurity peaks. However, additional single crystal x-ray measurements were performed on the two types of YbPtIn compounds. Crystals with dimensions $\sim 2 \times 7 \times 11\ \mu m^3$ and $\sim 2 \times 6 \times 13\ \mu m^3$ were extracted from the flux and on-line grown samples respectively. Room-temperature X-ray diffraction data were collected on a STOE IPDSII image plate diffractometer with Mo Kα radiation, and were recorded by taking 1^0 scans in θ in the full reciprocal sphere. The range of $2\ \theta$ extended from 6^0 to 63^0. Numerical absorption corrections for both crystals were based on crystal face indexing, followed by a crystal shape optimization. Structure solution and refinement were done using the SHELXTL program. The crystallographic and structural data are summarized in Tables 9.1 - 9.2.

A high temperature factor was observed for Pt(1) of the flux-grown crystal during final stages of the refinement, which is usually indicative of possible atomic deficiencies, symmetry reduction or superstructure formation. No superstructure reflections were observed, and symmetry reduction did not resolve the issue. However, relaxing Pt(1) site occupancy resulted in a statistically significant deficiency (0.06(1), Table 9.1), and led to improvements in the Pt(1) temperature factor and overall residual R value. We also tested for possible deficiencies on

Table 9.1 Atomic coordinates and equivalent isotropic displacement parameters ($\AA^2$) for the flux-grown YbPtIn system. U(eq) is defined as one third of the trace of the orthogonal U^{ij} tensor. Space group $P\,\bar{6}\,2\,m$, a = 7.5568(8) $\AA$, c = 3.7658(3) $\AA$, R = 0.0273, R_ω = 0.0598.

	Occupancy	x	y	z	U(eq)
Yb	1.00	0.5940(1)	0	0	0.0088(3)
Pt(1)	0.94(1)	0	0	0	0.0099(5)
Pt(2)	1.00	1/3	2/3	1/2	0.0075(3)
In	1.00	0.2604(2)	0	1/2	0.0093(4)

the other atomic sites in this crystal, but refined occupancies for Yb (1.00(6)), Pt(2) (1.00(6)) and In (1.02(2)) did not suggest presence of atomic deficiencies. Thus the composition of the flux-grown crystal can be written as $YbPt_{0.98}In$, noting that the $Pt_{0.98}$ value reflects the Pt stoichiometry of the whole unit cell, not just of the Pt(1) site. In contrast to the flux-grown sample, the Pt(1) temperature factor of the on-line grown crystal had a reasonable value. Relaxing the Pt(1) occupancy yielded only a slight and statistically insignificant deficiency of 0.014(9) (Table 9.2). Occupancy refinement for other atomic sites showed no deviations from unity. Although small deficiencies on the Pt(1) site could not be excluded, the YbPtIn formula is a good presentation of the composition of the on-line crystal in terms of sensitivity of our X-ray diffraction experiments. This difference in the stoichiometry of the solution and on-line grown samples is consistent with YbPtIn having a small width of formation extending towards the Pt-deficient side; given that the initial melt composition is very Pt-poor (*i.e.*, $Yb_{0.4}Pt_{0.1}In_{0.5}$), it is expected to be sensitive to such a small width of formation.

A closer look at the atoms' positions given in Tables 9.1-9.2 suggests that two compounds might be mirror images of each other; whereas racemic twinning could not be excluded for

Table 9.2 Atomic coordinates and equivalent isotropic displacement parameters ($Å^2$) for the on-line-grown YbPtIn system. U(eq) is defined as one third of the trace of the orthogonal U^{ij} tensor. Space group $P\,\overline{6}\,2\,m$, a = 7.5486(12) Å, c = 3.7617(7) Å, R = 0.0217, R_ω = 0.0453.

	Occupancy	x	y	z	U(eq)
Yb	1.00	0.4052(1)	0	0	0.0076(2)
Pt(1)	0.986(9)	0	0	0	0.0082(4)
Pt(2)	1.00	1/3	2/3	1/2	0.0071(2)
In	1.00	0.7378(2)	0	1/2	0.0071(2)

either the solution or the on-line grown compounds, no evidence of the existence of both "left" and "right" structures in each system could be found.

The lattice parameters and unit cell volume for the solution-grown, $YbPt_{0.98}In$ crystals were $a = (7.55 \pm 0.01)$ Å, $c = (3.76 \pm 0.01)$ Å and $Vol = (186.28 \pm 0.51)$ $Å^3$. The analogous unit cell dimensions on the on-line grown crystals were slightly smaller: $a = (7.54 \pm 0.01)$ Å, $c = (3.75 \pm 0.01)$ Å and $Vol = (185.61 \pm 0.11)$ $Å^3$.

9.2.2 Low magnetic field comparison

Anisotropic magnetization measurements are presented in Fig.9.1 for both the $YbPt_{0.98}In$ (full symbols) and the YbPtIn (open symbols) compounds. As can be observed in Fig.9.1a, the paramagnetic susceptibility indicates moderate anisotropy for both systems (with $\chi_{ab}/\chi_c \sim 6$ at the lowest temperature), and no clear sign of magnetic ordering down to $T = 1.8$ K. The anisotropic M(H) isotherms show a continuous increase of the magnetization, with a trend towards saturation above 40 kG (Fig.9.1b) for H applied within the ab-plane; the axial magnetization remains linear and significantly smaller than M_{ab} up to our maximum field available

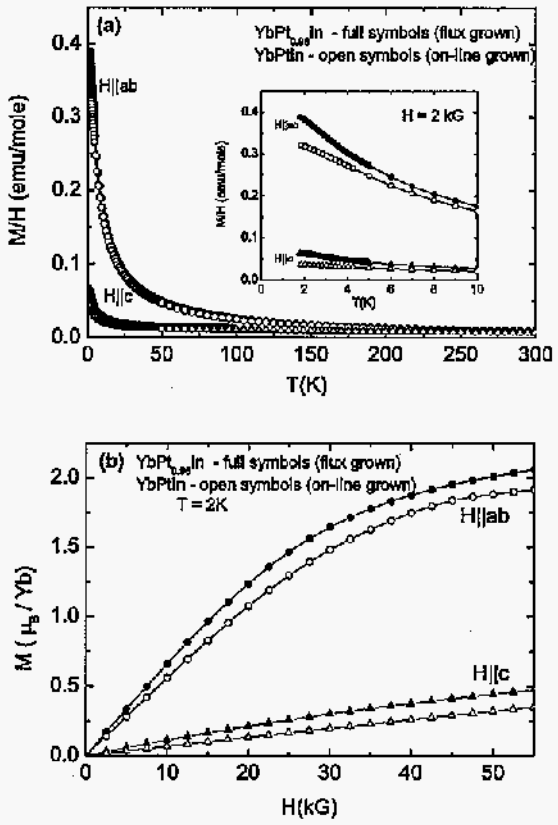

Figure 9.1 (a) Anisotropic susceptibilities for H = 2 kG (with the low-temperature part enlarged in the inset) and (b) field-dependent magnetization at T = 2 K for YbPtIn (open symbols) and $YbPt_{0.98}In$ (full symbols).

for these measurements (55 kG). Whereas qualitatively there is an overall similarity between the corresponding data of the two compounds, the absolute values of both susceptibility and field-dependent magnetization are slightly larger for $YbPt_{0.98}In$ than for YbPtIn. We believe the $\sim$ 10 to 20% difference to be too large to have been caused by weighing errors alone, and thus we conclude that it may reflect the different Kondo temperatures and exchange coupling due to the change of stoichiometry in the two compounds.

The zero-field specific heat and resistivity data shown in Fig.9.2 are consistent with mag-

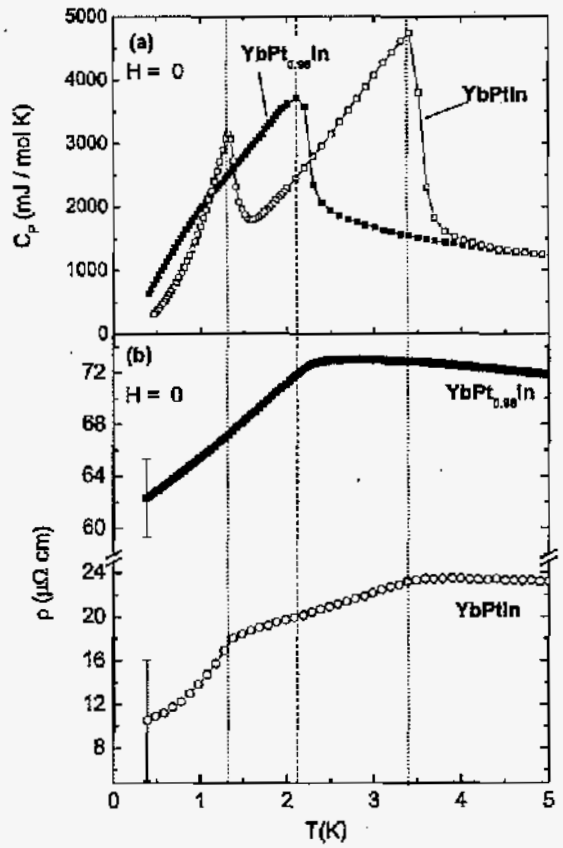

Figure 9.2 (a) Low-temperature specific heat and (b) resistivity data for H = 0, for YbPtIn (open symbols) and $YbPt_{0.98}In$ (full symbols), with the resistivity error bars shown for the lowest temperature (T = 0.4 K); the transition temperatures are indicated by two dotted lines (for YbPtIn) and one dashed line (for $YbPt_{0.98}In$).

netic ordering in both compounds, however at different temperatures: two well defined peaks at T $\approx$ 3.4 K and 1.4 K are visible in the YbPtIn $C_P(T)$ data (open symbols, Fig.9.2a), whereas only one peak can be distinguished, around 2 K, in the $YbPt_{0.98}In$ data (full symbols). These transition temperatures are marked by the vertical dotted lines for the former compound, and by one dashed line for the latter. It can be seen that the corresponding resistivity measurements

(Fig.9.2b) show changes in slope around the respective transition temperatures. Another noticeable difference between YbPtIn and $YbPt_{0.98}In$ manifests in the resistivity values (Fig.9.2b and 9.3) with the ones for the former compound being approximately three times smaller in the latter one. The error bars shown for the lowest temperature ρ values give a caliper of the uncertainty in estimating the resistivity values for the two compounds, further confirming the aforementioned difference. The larger residual resistivity in $YbPt_{0.98}In$ is consistent with the additional disorder (*i.e.*, site disorder) or presence of additional vacancies in this type of crystals.

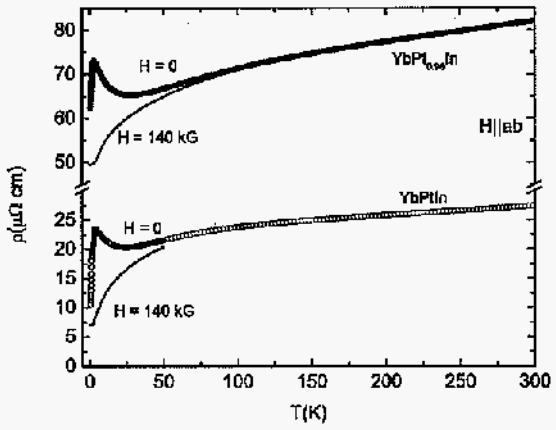

Figure 9.3 Temperature-dependent resistivity for $YbPt_{0.98}In$ and YbPtIn, for H = 0 (symbols) and H = 140 kG (solid lines).

Thus the zero-field measurements indicate a dramatic effect of the small Pt-deficiency on the ordered state in YbPtIn: the upper transition is shifted down in temperature in the Pt-deficient compound, whereas a second one is clearly identifiable only in YbPtIn. In order to explore the differences between these two samples more thoroughly, a systematic study of the field-dependence of $\rho(T)$ and $C_p(T)$ was undertaken.

9.2.3 High magnetic field measurements: YbPtIn

9.2.3.1 $H \parallel ab$

The low-temperature specific heat data for the on-line grown compound YbPtIn is shown in Fig.9.4a, for various values of the applied field. As already seen, two sharp peaks present in the H = 0 data can be associated with magnetic phase transitions at T = 3.4 K and 1.4 K. As the applied field is increased, these transitions (indicated by small arrows in Fig.9.4a) move to lower temperatures, and eventually drop below 0.4 K around 20 kG, and 60 kG respectively. Trovarelli *et al.* (2000a) have reported similar measurements up to 80 kG, which are consistent with our data; however, their study did not include a systematic analysis of the H - T phase diagram or the potential quantum critical behavior in this compound.

The magnetic component of the specific heat is defined as $C_m = C_P(\mathrm{YbPtIn}) - C_P(\mathrm{LuPtIn})$, and is shown in Fig.9.4b as C_m / T *vs.* T^2, for the same field values as before. From the linear extrapolation of the zero-field C_m / T data from T ~ 5 K down to T = 0 (inset, Fig.9.4b), the electronic specific heat coefficient γ can be roughly estimated as $\gamma \simeq 500$ mJ / mol K^2.

When the magnetic specific heat is plotted in C_m /T vs. ln T coordinates (Fig.9.5), a reduced region of logarithmic divergency (non-Fermi liquid NFL behavior) is apparent; however this linear region in C_m /$T(lnT)$ is more ambiguous than in other heavy fermion compounds displaying NFL behavior (*e.g.*, $YbRh_2Si_2$ (Trovarelli, 2000b) and YbAgGe (Bud'ko, 2004). Because of a downturn in the high field data (H $\geq$ 50 kG [Fig.9.5b]) around 5 K for H = 50 kG, the largest logarithmic divergency which occurs for H ~ 60 kG, is limited to only a fraction of a decade in temperature (1.5 K < T < 6.5 K). The above observations suggests that a QCP may exist around a critical field value H_c^{ab} just above 60 kG, but the presence of a NFL region at intermediate field values is less clearly defined than in the previously studied Yb-based heavy fermion compounds.

One of the expressions considered in the scaling analysis at a QCP (Tsvelik, 1993) is the cross-over function $[C(H) - C(H=0)]$ / T *vs.* H/T^{β}. In the case of $YbRh_2Si_2$ (Paschen, 2004) and YbAgGe (Bud'ko, 2005), the H/T^{β} range over which universal scaling was observed in high fields corresponded to 1/T < 3 K^{-1}, and 1.2 K^{-1} respectively (with $\beta > 1$). Due to

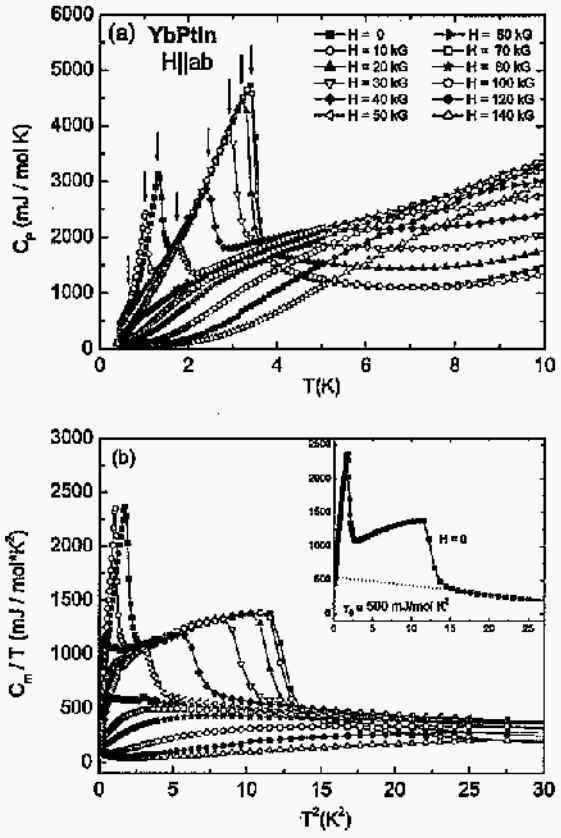

Figure 9.4 (a) Low-temperature specific heat curves for YbPtIn, for H $\parallel$ ab; arrows indicate the peak positions, associated with magnetic phase transitions. (b) low-temperature part of the $C_m/T(T^2)$ curves for various values of the applied field; inset: the H = 0 $C_m/T(T^2)$ curve, with its linear fit below 5 K (dotted line) extrapolated down to T = 0 to provide a rough estimate of the electronic specific heat coefficient $\gamma \simeq 500$ mJ / mol K^2.

the slightly enhanced magnetic ordering temperature $T_{ord} = 3.4$ K in YbPtIn, the analogous 1/T range is drastically reduced ($1/T < 0.3$ K^{-1}), making the unambiguous determination of the critical exponent β essentially impossible.

Low-temperature resistivity curves for different values of the applied magnetic field are

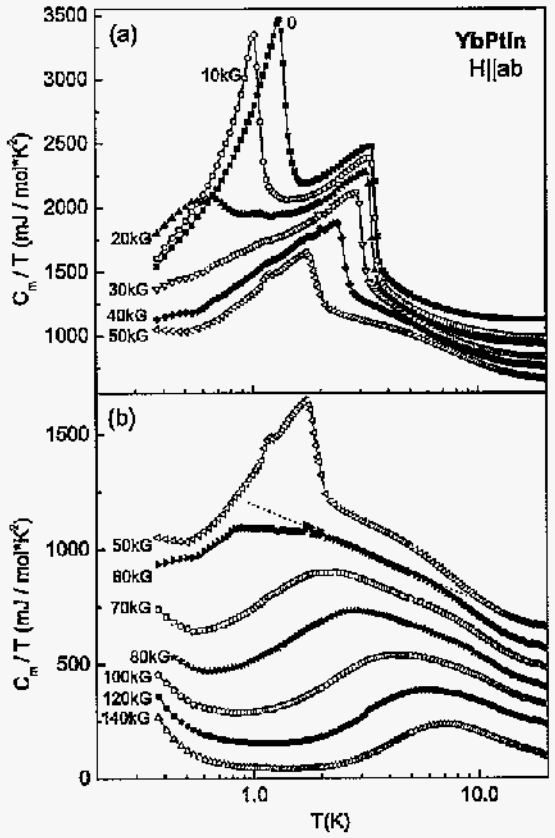

Figure 9.5 Semi-log plot of C_m/T *vs.* T for (a) H = 0 - 50 kG and (b) H = 50 - 140 kG. All curves (except for the H = 140 kG one) are shifted up by multiples of 100 mJ/mol K^2. The dotted line (for H = 60 kG) is a guide to the eye for the largest region of logarithmic divergency of C_m/T.

shown in Fig.9.6. The $\rho(T)\mid_H$ data are consistent with the presence of two magnetic phase transitions at low fields; the small arrows indicate these transition temperature values, as determined from maxima in the $d\rho/dT$. Both these transitions are suppressed by increasing applied field. Whereas the upper transition persists for 50 kG< H < 60 kG, a field of about 20 kG is sufficient to drive the lower one below our base temperature of 0.4 K. It is worth noting that the critical field $H_c^{ab} \sim 60$ kG, determined from the ρ(T,H) data as the field required to

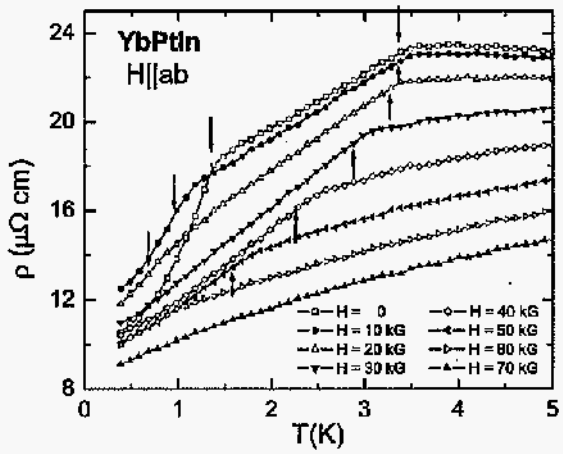

Figure 9.6 Low-temperature resistivity data for YbPtIn taken at different applied fields, for H $\parallel$ *ab*; the small arrows indicate the magnetic transition temperatures.

suppress the magnetic ordering, is close to the position of the QCP as inferred based on the C_P data (Fig.9.4).

At intermediate field values (60 kG< H < 70 kG), no clear NFL regime ($\rho \propto T$) can be identified in the resistivity data (Fig.9.7), as it is unclear whether linear regions exist at low T, for either ρ(T) or $\rho(T^2)$. However, for H > 70 kG the low-T resistivity data is possibly indicating Fermi liquid-like FL behavior (Fig.9.7b,c), as it can be described by $\rho(T) = \rho_0 + A\,T^2$. On the ρ *vs.* T^2 plot, the upper limit of the linear regions are marked with small arrows for each field value. These maximum temperatures appear to become larger as the applied field is being increased, despite the scattering of the data towards low T, which increases the error bars on these cross-over temperature values.

When magnetoresistance measurements ($\rho(H)\,|_T$) are performed (Fig.9.8) three features are apparent at very low temperatures, as indicated for T = 0.4 K by the small arrows. The inset shows ρ(H) at T = 0.8 K, to exemplify how these transition temperatures were inferred from these data. For T $\geq$ 1 K, the two lower transitions merge and the resulting one is still

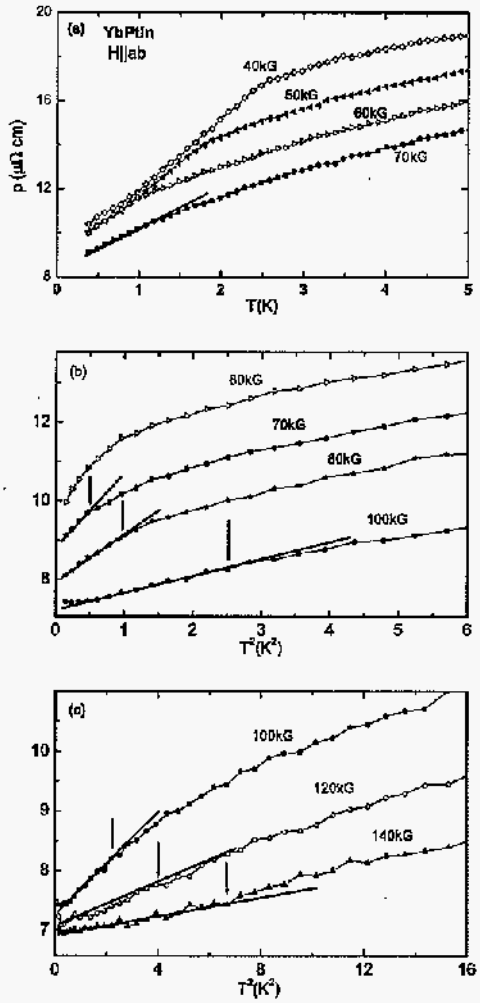

Figure 9.7 Low-temperature part of the (a) ρ(T) data for H = 40, 50, 60 and 70 kG, and $\rho(T^2)$ for (b) H = 60, 70, 80 and 100 kG and (c) H = 100, 120 and 140 kG, with their respective linear fits at very low T (solid lines). The arrows indicate the temperatures at which deviations from the T^2 behavior occur. Note: for H = 70 kG linear fits are shown on both ρ(T) (a) and $\rho(T^2)$ (b), given the big uncertainty of the T-dependence of resistivity at this field value.

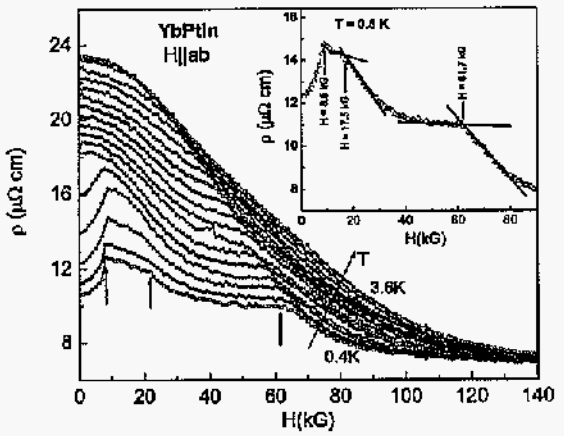

Figure 9.8 ρ(H) isotherms for YbPtIn, for H $\parallel$ ab and T = 0.4 - 3.6 K, ΔT = 0.2 K; the arrows point to the transition fields at the lowest temperature, with the inset exemplifying how these critical fields are determined for T = 0.8 K.

distinguishable up to approximately 1.4 K. The upper transition moves down towards zero field as the temperature approaches T_N = 3.4 K.

Based on the above field- and temperature-dependent thermodynamic and transport measurements, a $T - H$ phase diagram for $H \parallel ab$ can be constructed (Fig.9.9): in zero magnetic field, two magnetic phase transitions can be observed, around T_N = 3.4 K and T_m = 1.4 K. Increasing magnetic field splits the lower transition into two separate ones around H $\sim$ 10 kG; one of these phase lines drops towards our lowest temperature at almost constant field, whereas the second one has a slower decrease with field, such that it approaches T = 0.4 K around H = 20 kG. In a similar manner, the upper transition is driven down towards 0 around H_c = 60 kG.

Upon further increasing the applied field, another line emerges around the $H_c^{ab} \approx$ 60 kG critical field value. The points on this line represent a crossover between a possible non-Fermi liquid-like NFL regime (high temperatures), and a Fermi liquid like FL regime (for low temperatures). This is analogous, even though less clear (as indicated by the large error bars)

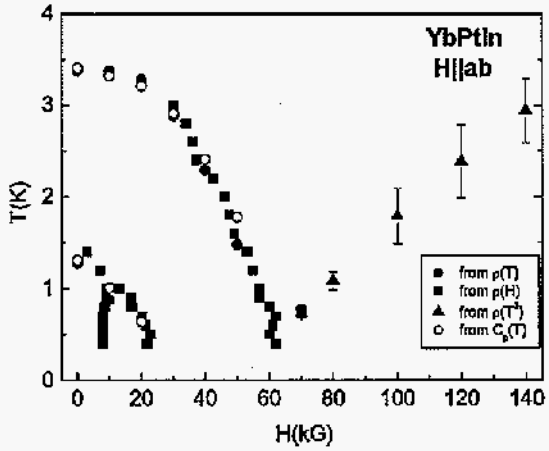

Figure 9.9 H || ab T - H phase diagram for YbPtIn, as determined from resistivity (full symbols) and specific heat (open symbols) data. Note the error bars on the high-field points representing the uncertainty in determining the cross-over temperatures.

to the coherence line (Continentino, 1989) previously observed in $YbRh_2Si_2$ (Paschen, 2004) and YbAgGe (Bud'ko, 2005). Although measurements below 0.4 K would be necessary for a better estimate of the quantum critical point QCP in this field orientation, Fig.9.4-9.9 suggests that $H_c^{ab} \approx 60$ kG.

9.2.3.2 $H \parallel c$

Fig.9.10 presents specific heat data for YbPtIn, $H \parallel c$, for fields up to 80 kG. High torques on this sample for this orientation of the field prevented us from completing these measurements up to 140 kG. Moreover, as will be shown below, there are significant discrepancies between the transition temperatures determined even from the intermediate-field specific heat data and the transport measurements (*i.e.*, for H $\geq$40 kG). This observation prompts us to suspect that significant torques may have changed the sample orientation for the specific heat measurements, even for fields significantly lower than 80 kG.

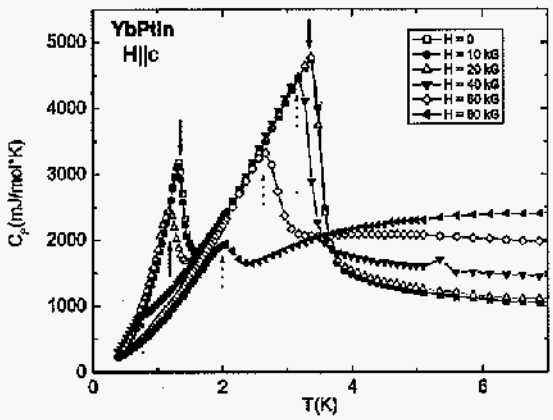

Figure 9.10 $H \parallel c$ specific heat data for YbPtIn, for H = 0, 10, 20, 40, 60 and 80 kG; small arrows indicate the positions of peaks possible associated with magnetic phase transitions (dotted arrows: peaks on $C_P(T)$ data for possibly torqued sample [see text]).

In zero field, we can confirm the two magnetic transitions observed before, at $T_N = 3.4$ K, and $T_m = 1.4$ K respectively; as the small arrows indicate, the lower-T transition is driven down in field, and falls below 0.4 K for H $>$ 40 kG, whereas the upper transition persists above 80 kG.

The temperature and field dependent resistivity data (Fig.9.11-9.12) indicate a much slower suppression of the magnetic order with the applied field. In Fig.9.11a, $\rho(T)$ curves are shown, with the arrows indicating the transition temperatures as determined from $d\rho/dT$. Fig.9.11b presents a subset of these derivatives, to illustrate the criteria for determining the temperatures: for the lower transition, a peak in $d\rho/dT$ broadens as field is increased, and disappears for H $>$ 80 kG; the upper transition is marked by a step in these derivatives, which also broadens as H increases. At the highest measured field (*i.e.*, 140 kG) we are unable to distinguish between a very broad step (with a possible transition temperature marked by the small arrow) or a cross-over in corresponding $d\rho/dT$. The field-dependent resistivity data (Fig.9.12) are

indicative of a low temperature transition consistent with that seen in $\rho(T)$, with the critical fields determined from on-sets.

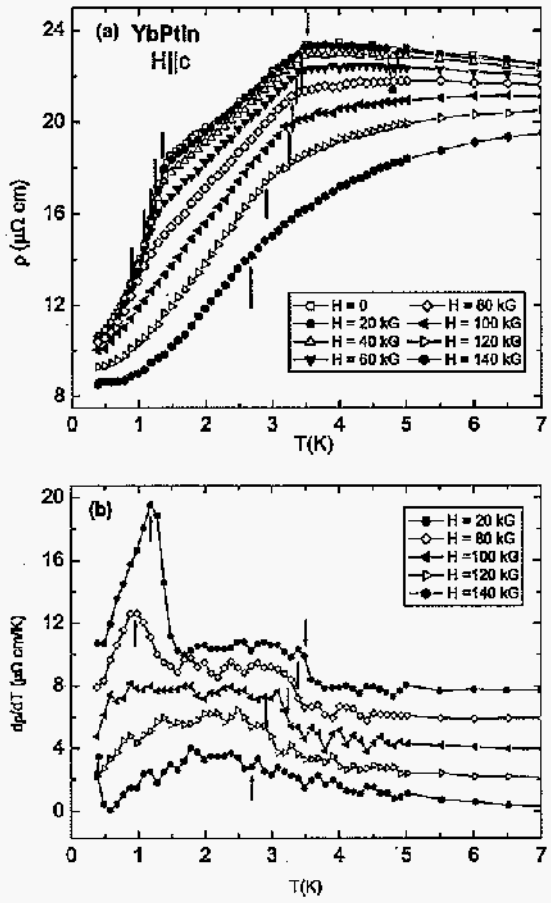

Figure 9.11 (a) Low-temperature ρ(T) data for YbPtIn taken at different applied fields, for H $\parallel$ *c*. (b) $d\rho/dT$ curves for H = 20, 80, 100, 120 and 140 kG. On both plots, the small arrows indicate the magnetic transition temperatures.

Given the above C_P(T,H) and ρ(T,H) data, we suspect that magnetic fields H > 20 kG deform the four wires supporting the He-3 specific heat platform used for the C_P(T,H) measurements, whereas the resistivity sample appears to be well held in place by grease on the

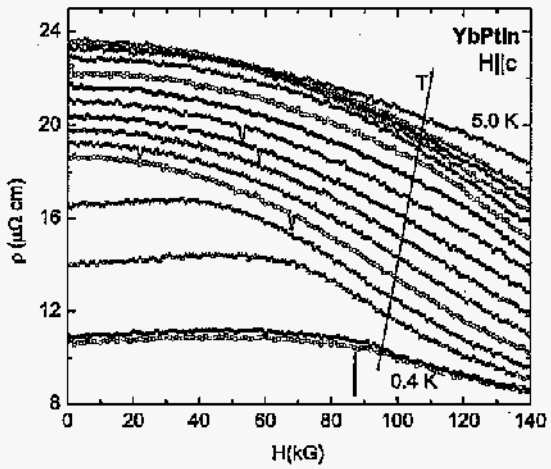

Figure 9.12 ρ(H) isotherms for T = 0.4, 0.5, 1 - 4 K (ΔT = 0.25 K) and 5 K. Small arrow indicates the critical field position at the lowest temperature (T = 0.4 K).

rigid platform. Consequently, at high fields, the two sets of data (C_P(T,H) and ρ(T,H)) may not correspond to the same orientation of the field ($H \parallel c$), yielding different transition temperature values for the corresponding applied fields.

As a result, in constructing the T - H phase diagram for H$\parallel$ c (Fig.9.13), we will consider the T_c values as determined from the ρ(T,H) data up to H = 140 kG, and only the H $\leq$ 20 kG ones based on specific heat measurements. Also shown are error bars for points determined from ρ(T) data at several field values (*i.e.*, for H = 20, 80, 100, 120 and 140 kG), and for the point obtained from ρ(H) at our minimum temperature (T = 0.4 K); these give a caliper of the errors bars in determining the points on this phase diagram for the whole field and temperature range. Two transitions can be observed in Fig.9.13, at low fields, around 3.4 K, and 1.4 K respectively. As H is being increased, the low temperature line slowly approaches T = 0 around H $\sim$ 85 kG. The step in $d\rho/dT$ associated with the upper transition (Fig.9.11b) broadens as the field increases, resulting in increasingly large error bars in determining these transition temperatures. As already mentioned, it is uncertain if the transition persists up to

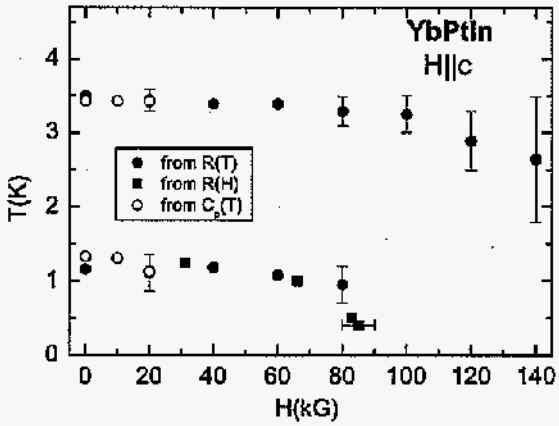

Figure 9.13 H ∥ c T - H phase diagram for YbPtIn, as determined from resistivity (full symbols) and specific heat (open symbols) data. Error bars on points from ρ(T) data at H = 20, 80, 100, 120 and 140 kG, and from ρ(H) at T = 0.4 K shown as a caliper of the errors in determining the points on this phase diagram.

H = 140 kG, or if cross-over occurs between 120 and 140 kG.

9.2.4 High magnetic field measurements: $YbPt_{0.98}In$

9.2.4.1 $H \parallel ab$

Given the differences between YbPtIn and $YbPt_{0.98}In$ evidenced by both thermodynamic and transport data (Figs.9.1-9.3), it is desirable to compare similar measurements on the two compounds, and to study the effect of the small stoichiometry change on the field-induced QCP.

Consequently, in Fig.9.14 we present the low-temperature specific heat data of $YbPt_{0.98}In$, for various values of the applied field H ∥ ab. A well-defined peak at T = 2.1 K in the H = 0 data may be associated with the magnetic ordering of this compound. As the applied magnetic field is increased, this transition (indicated by small arrows) moves to lower temperatures, and eventually drops below 0.4 K around 35 kG. By plotting the magnetic specific heat data

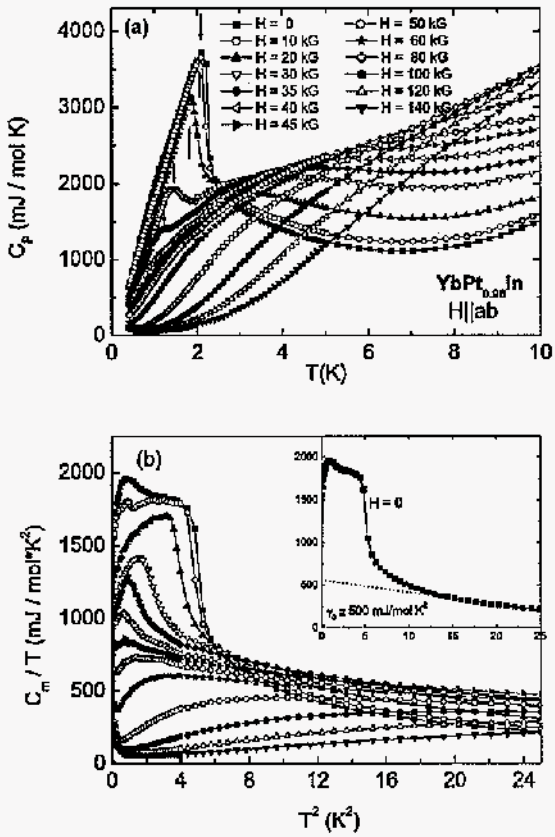

Figure 9.14 (a) Low-temperature specific heat curves for $YbPt_{0.98}In$, for H $\parallel$ *ab*; arrows indicate the positions of the peaks associated with magnetic ordering. (b) low-temperature part of the $C_m/T(T^2)$ curves for various values of the applied field; inset: the H = 0 $C_m/T(T^2)$ curve, with its linear fit below 5 K (dotted line) extrapolated down to T = 0 to provide a rough estimate of the electronic specific heat coefficient $\gamma \simeq 500$ mJ / mol K^2.

$C_m = C_P(YbPt_{0.98}In) - C_P(LuPtIn)$ as C_m / T *vs.* T^2 (Fig.9.14b), we can estimate the electronic specific heat coefficient γ: the linear extrapolation of the H = 0 data from T $\sim$ 5 K down to T = 0 (inset, Fig.9.14b), gives $\gamma \approx 500$ mJ / mol K^2.

Fig.9.15 shows the magnetic specific heat as C_m / T *vs.* ln T, for the same field values as

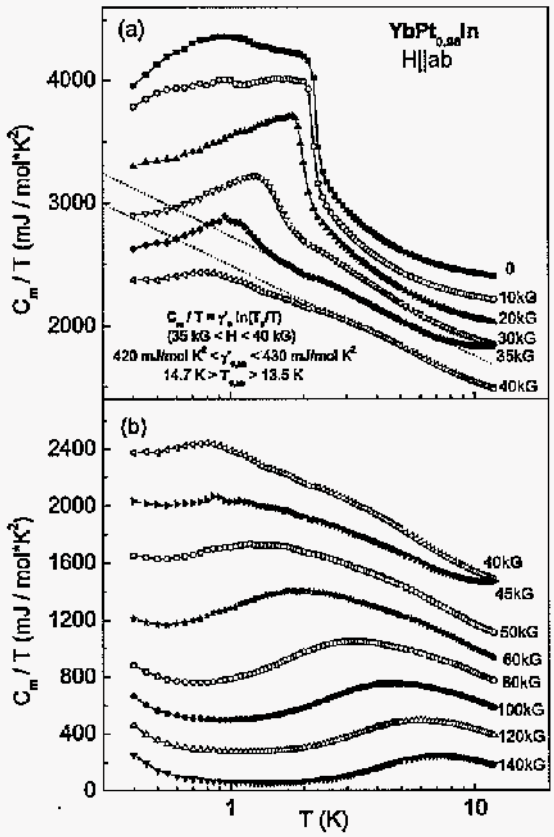

Figure 9.15 Semi-log plot of C_m/T *vs.* T for (a) H = 0 - 40 kG and (b) H = 40 - 140 kG. All curves (except for the H = 140 kG one) are shifted up by multiples of 200 mJ/mol K^2. The dotted lines (for H = 35 and 40 kG) are guides to the eye for the linear regions on the C_m/T curves for H possibly just above and below H_c^{ab} (see text).

before. A logarithmic divergence can be observed in these data, with the largest temperature region where C_m / $T(lnT)$ occurring around H = 35 kG (dotted line). However, on the next measured curve (*i. e.*, for H = 40 kG) the linear region extends over a comparable temperature interval, at slightly larger temperatures than in the H = 35 kG case. It thus appears that the largest temperature region (close to a decade) for the logarithmic divergency of the C_m/T

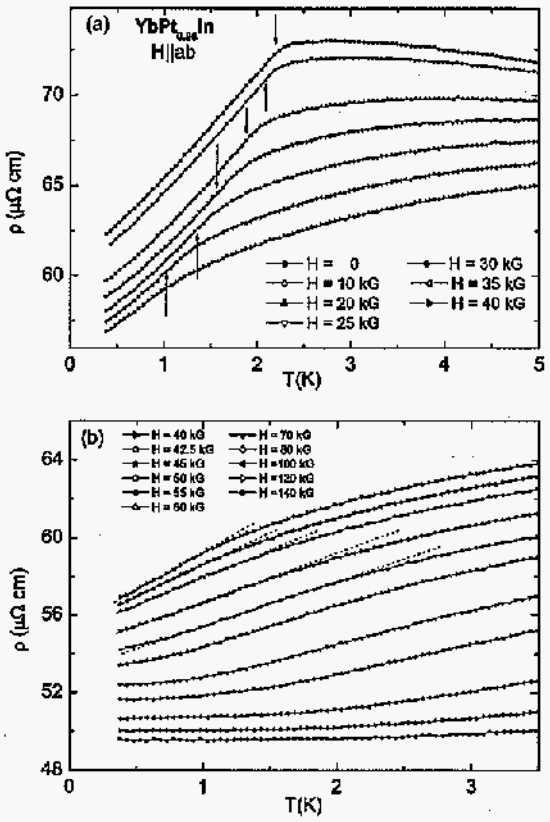

Figure 9.16 $YbPt_{0.98}In$ low-temperature resistivity data for H $\parallel$ ab, for (a) H = 0, 10, 20, 25, 30, 35 and 40 kG and (b) H = 42.5, 45, 50, 55, 60, 70, 80, 100, 120 and 140 kG. In (a) small arrows indicate the possible ordering temperatures, whereas dotted lines in (b) are guides to the eye pointing out the regions of linear $\rho(T)$ (or the departure from linearity at low T for the H = 55 kG curve [see text]).

data may occur for some intermediate field value (35 kG < H < 40 kG). These data could be described as C_m / T = $\gamma_0' \ln(T_0/T)$, with the ranges for γ_0' and T_0 determined from the linear fits on the H = 35 and 40 kG curves: 420 mJ/mol K^2 < γ_0' < 430 mJ/mol K^2, and 14.7 K > T_0 > 13.5 K. The above observations seem consistent with a QCP in this compound with critical field above 35 kG.

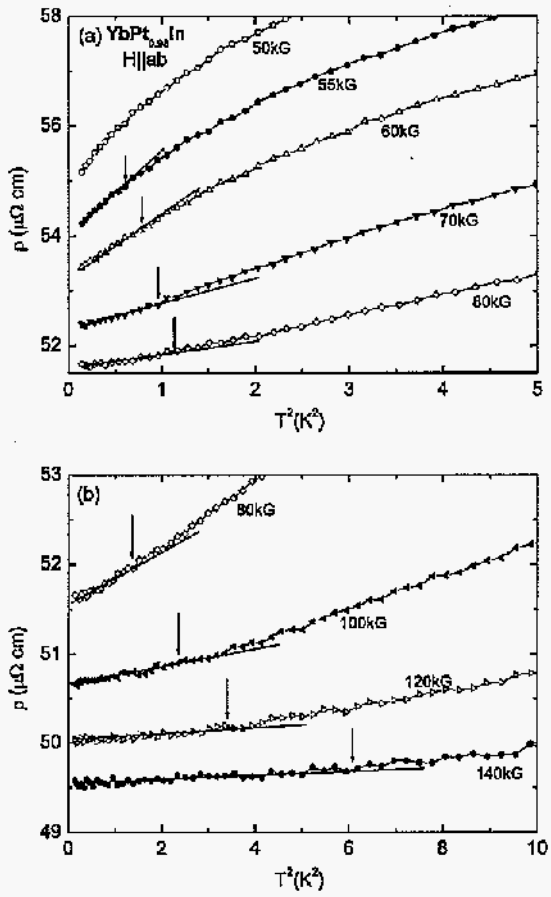

Figure 9.17 Low-temperature part of the $YbPt_{0.98}In$ $\rho(T^2)$ data, for (a) H = 50, 55, 60, 70 and 80 kG and (b) H = 80, 100, 120 and 140 kG, with their respective linear fits at very low T (solid lines). The arrows indicate the temperatures at which deviations from the T^2 behavior occur.

Fig.9.16 shows the low-temperature resistivity data for various values of the applied magnetic field. A maximum in $d\rho/dT$, associated with the magnetic ordering can be identified at T = 2.1 K in the H = 0 data, and is indicated by small arrow in Fig.9.16a; this transition temperature appears to drop below 0.4 K as field is increased above 35 kG (Fig.9.16b), consistent with the specific heat data. For applied fields between 40 kG and 50 kG, the resistivity

appears to be linear in temperature down to our base temperature, as indicated by the dotted lines in Fig.9.16; a dotted line for the H = 55 kG curve is also shown on the same plot, to emphasize the non-linear temperature dependence towards low T of the respective $\rho(T)$ curve.

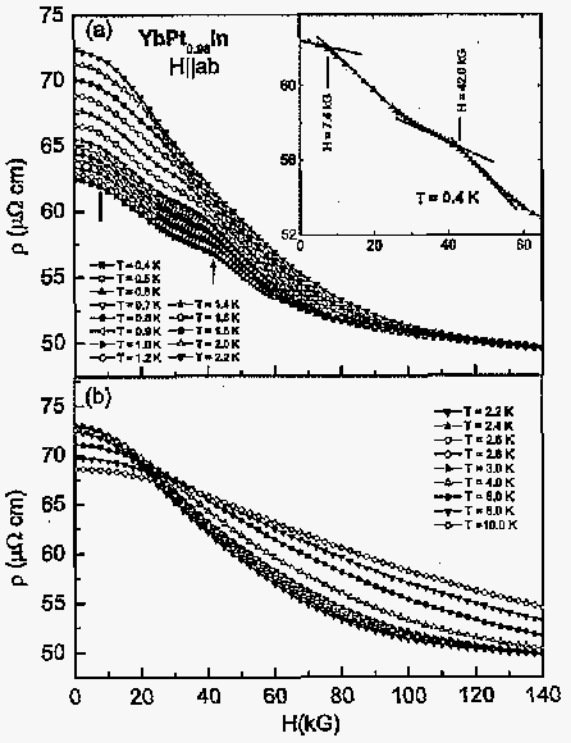

Figure 9.18 ρ(H) isotherms for $YbPt_{0.98}In$, for H $\parallel$ ab and (a) T = 0.4 - 1.0 K (ΔT = 0.1 K), 1.2 - 2.2 K (ΔT = 0.2 K), and (b) T = 2.2 - 3.0 K (ΔT = 0.2 K), 4, 6, 8 and 10 K; the arrows point to the transition fields at T = 0.4 K, with the inset exemplifying how these critical fields were determined.

As the field is increased above 55 kG, the low-temperature resistivity can be described as $\rho(T) = \rho_0' + AT^2$ (Fig.9.17), up to some maximum temperature values marked by small arrows. These temperatures mark the cross-over from the non-Fermi liquid NFL region observed at intermediate fields (40 kG < H < 50 kG), to a Fermi liquid-like FL regime at low temperatures for H $\geq$ 55 kG, consistent with the specific heat data. Similar to the case

of YbPtIn, the linear range observed in $\rho(T^2)$ increases with increasing field, whereas the A coefficient is decreasing with H.

Transverse magnetoresistance measurements were taken at constant temperatures ranging from 0.4 K to 10 K. As shown in Fig.9.18, two different temperature regimes can be identified in these data: for T = 0.4 – 1.8 K (Fig.9.18a), two transitions can be distinguished. The small arrows mark the positions for these two transitions for T = 0.4 K, whereas the inset illustrates how these critical field values were determined. As the temperature increases up to about 1.8 K, the upper transition moves down in field and broadens, whereas the position of the lower one seems almost unaffected by the change in temperature. For temperatures higher than 2 K (Fig.9.18b), the magnetoresistance isotherms display only a broad feature that looks more like a cross-over rather than a transition.

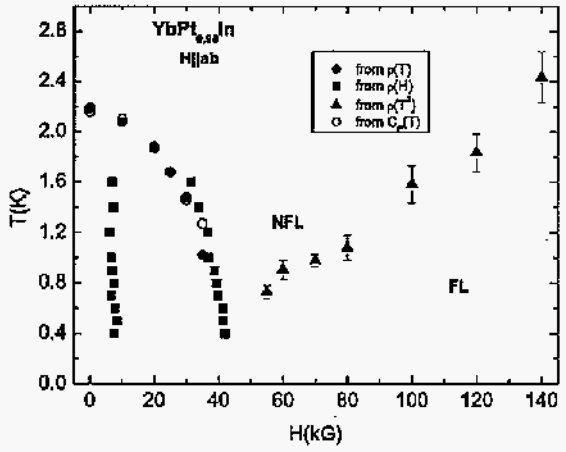

Figure 9.19 H ∥ *ab* phase diagram for $YbPt_{0.98}In$, as determined based on specific heat (open symbols) and transport (full symbols) data. The error bars on the high-field points represent the uncertainty in determining the cross-over temperatures.

Using the detailed C_P(T,H) and ρ(T,H) measurements discussed above, the $YbPt_{0.98}In$ T - H phase diagram for H ∥ *ab* can be constructed. As can be seen in Fig.9.19, it is qualitatively

similar to the corresponding T - H phase diagram for the stoichiometric compound (Fig.9.9): in $YbPt_{0.98}In$ magnetic ordering occurs at around 2.1 K. An almost field independent phase line is apparent in the $\rho(H)\ |_T$ data around 8 kG, and it appears to persist close to the magnetic ordering temperature. Increasing applied field drives the higher transition towards T = 0 at a critical field values between 35 and 55 kG. At intermediate field values, signatures of NFL behavior occur in the temperature-dependent resistivity ($\Delta\rho(T) \sim T$) and specific heat ($C_m/T \sim -lnT$) for this compound. As field is increased above 55 kG, the FL regime is apparently recovered, as the resistivity becomes quadratic in T (Fig.9.17).

9.2.4.2 $H \parallel c$

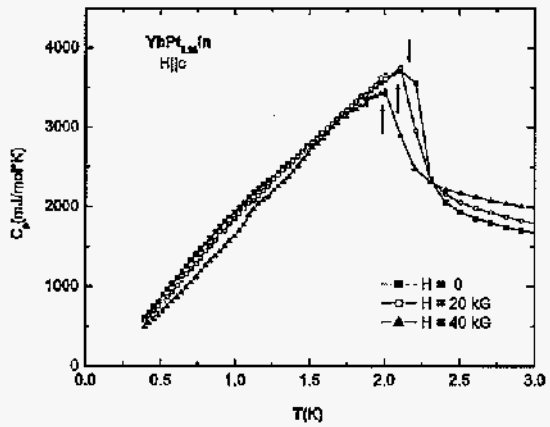

Figure 9.20 $H \parallel c$ specific heat data for $YbPt_{0.98}In$, for H = 0,20 and 40 kG; small arrows indicate the positions of peaks possibly associated with the magnetic phase transition.

The similarities observed previously between YbPtIn and $YbPt_{0.98}In$ are also present for the $H \parallel c$ direction, as the C_P(T,H) and ρ(T,H) measurements indicate. As in the case of the stoichiometric compound, significant torques on the specific heat platform and sample for H $\geq$ 50 kG may be the cause of the different transition temperature values, as determined by

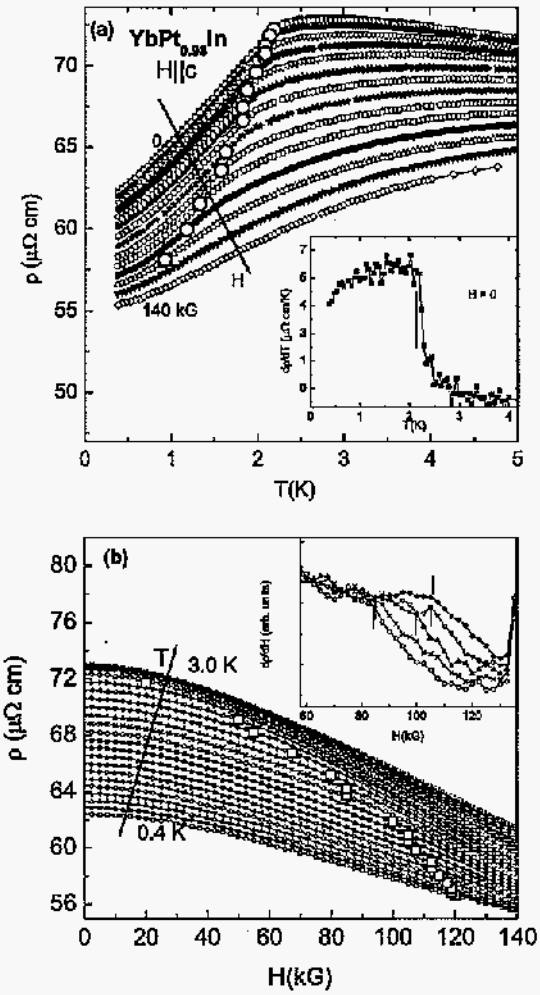

Figure 9.21 (a) $YbPt_{0.98}In$ low-temperature resistivity data for H $\parallel$ c, for H = 0 - 140 kG (ΔH = 10 kG), with the large dots marking the possible magnetic ordering temperature; inset: H = 0 dρ/dT, with the small arrow marking the transition temperature. (b) ρ(H) isotherms for T = 0.4 - 3.0 K (ΔT = 0.1 K). The critical fields for the possible phase transition were determined as local maxima in dρ/dH (as illustrated in the inset for T = 1.2 - 1.6 K), and are shown as large squares.

the two data sets mentioned above. Therefore we will only take into consideration C_P(T,H) data for H < 50 kG (Fig.9.20). Similar to the $H \parallel ab$ measurements (Fig.9.14), the $H \parallel c$ C_P curves reveal a magnetic transition around 2.1 K for H = 0 (Fig.9.20), which drops to ~ 2 K for H = 40 kG, before the sample torques significantly; small arrows indicate the position of the transition temperature for the three curves shown in Fig.9.20.

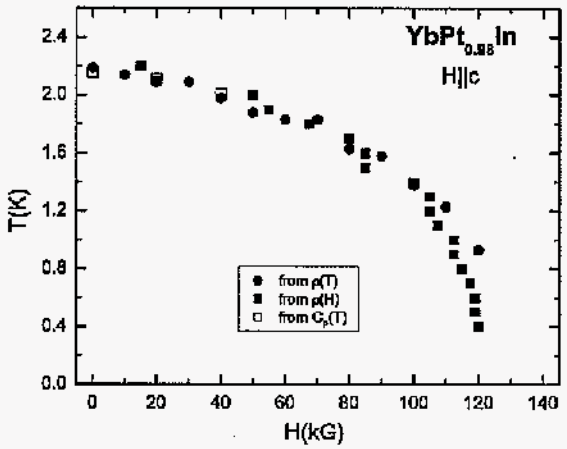

Figure 9.22 T - H phase diagram for $YbPt_{0.98}In$ ($H \parallel c$), as determined from the specific heat (open symbols) and resistivity (full symbols) measurements.

The temperature and field dependent resistivity data (Fig.9.21) indicate a slow suppression of the magnetic order with the applied field. Fig.9.21a shows the ρ(T) curves in various applied fields, with the large circles marking the phase transition as determined from $d\rho/dT$; the inset illustrates how the transition temperature was determined for H = 0. Whereas at H = 0 the transition temperature is consistent with the value determined from C_P data ($T_{ord} \sim 2.2$ K), the critical field required to suppress this transition below our base temperature appears to be around 120 kG. Given the limited temperature range at these high fields, for H = 130 and 140 kG we were unable to distinguish a linear or quadratic temperature dependence of the resistivity. The magnetoresistance isotherms are presented in Fig.9.21b, and the large squares

on this plot also indicate the high-T magnetic phase transition; in the inset, a few $d\rho/dH$ curves are shown to illustrate how the critical field values for the transition were determined.

Based on the C_P(T,H) and ρ(T,H) presented above, the $H \parallel c$ T - H phase diagram for $YbPt_{0.98}In$ can be obtained, as shown in Fig.9.22. At low fields, this T - H phase diagram is consistent with the in-plane one for this compound: a magnetic transition is apparent around 2.1 K, but the possible second one around 1.0 K is not visible in the H‖c measurements; the T $\simeq$ 2.1 K transition is driven down in temperature by increasing applied fields, and it approaches our base temperature (*i.e.*, 0.4 K) around 120 kG. Lack of measurements below 0.4 K limits our ability to probe the existence of a QCP in this orientation, similar to the one at $H_c^{ab} = 35$ kG for $H \parallel ab$.

9.2.5 Hall resistivity measurements in $YbPt_{0.98}In$: H‖ab

Based on the low temperature thermodynamic and transport measurements, YbPtIn and $YbPt_{0.98}In$ can be regarded as Yb-based heavy fermion compounds with long range, possibly reduced moment ordering that can be driven through a field-induced quantum critical point, similar to the previously studied Yb-based HF systems, $YbRh_2Si_2$ (Paschen, 2004) and YbAgGe (Bud'ko, 2005). In the latter two compounds, Hall effect measurements served as additional tools for characterizing the QCP and its effects on the finite-temperature properties of these materials.

In order to further explore the field-induced QCP our Yb-based compounds, field-dependent Hall resistivity measurements were performed for temperatures up to 300 K. However, the data on the stoichiometric compound was noisy, given the limited (small) crystal size, and meaningful Hall resistivity data could only be collected for the solution-grown compound for H $\parallel$ ab. These measurements are shown in Fig.9.23.

We determined the Hall coefficient R_H for $YbPt_{0.98}In$ in the low-field (H < 30 kG) and high-field (H > 60 kG) regimes, as the slopes of the $\rho_H(H)$ data shown in Fig.9.23 for various T. (This alternative definition for the $R_H(T)$ was preferred to $d\rho_H$ / dH due to the scattering of the data at low fields as seen later in Fig.9.25b). The results are shown in Fig.9.24 on

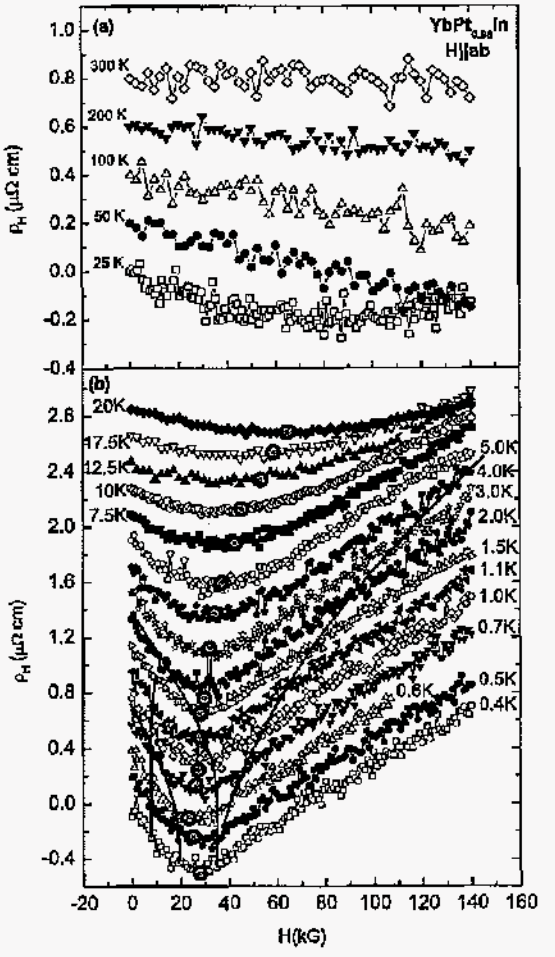

Figure 9.23 Field-dependent Hall resistivity for $YbPt_{0.98}In$ ($H \parallel ab$) for (a) T = 25 - 300 K and (b) T = 0.4 - 20 K (except for the T = 0.4 K and 25 K, all curves are shifted up by multiples of 0.2 $\mu\Omega$ for clarity). The lines represent the phase transitions from the phase diagram in Fig.9.19; the large diamonds indicate the ρ_H minima.

a semi-log scale. The high-H points (squares) show the expected levelling off of $R_H(T)$ as $T \longrightarrow 0$, whereas the low-T data appear to have a larger variation with T. At temperatures higher than 25 K, the two data sets merge (as the $\rho_H(H)$ data become roughly linear for the whole field range [Fig.9.23a]). These data indicate that the field-dependent Hall resistivity will be non-trivial and potentially of interest at low temperatures.

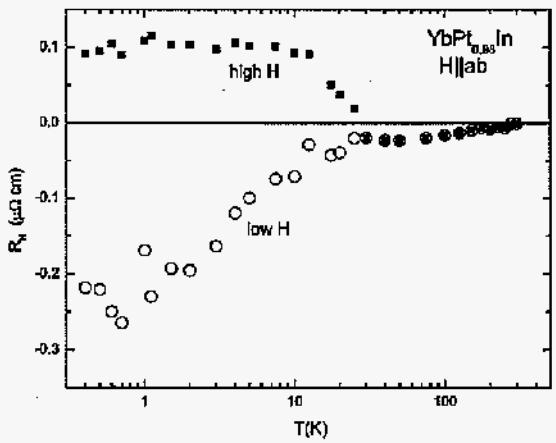

Figure 9.24 Temperature-dependent Hall coefficient of $YbPt_{0.98}In$ (H $\parallel$ ab), with low-field (open symbols) and high-field (full symbols) points determined as described in the text.

In the field-dependent Hall resistivity measurements shown in Fig.9.23, two possible regimes can be distinguished: a high-T regime (T $>$ 25 K), where a monotonic (average) decrease with field can be observed, despite the scattering of the data (Fig.9.23a), and a low-T regime (T $\leq$ 25 K), for which a minimum in the ρ_H(H) data appears and sharpens as the temperature decreases (Fig.9.23b). For T = 5 $-$ 25 K, the Hall resistivity curves show a fairly broad minimum (Fig.9.23b), marked by the large gray dots, which moves down in field with decreasing temperature. Below 5 K, this minimum is more and more pronounced, as emphasized by large dots, and is almost unaffected by the change in temperature.

Coleman *et al.* (Coleman, 2001) have indicated that R_H(C) data (where C is a control

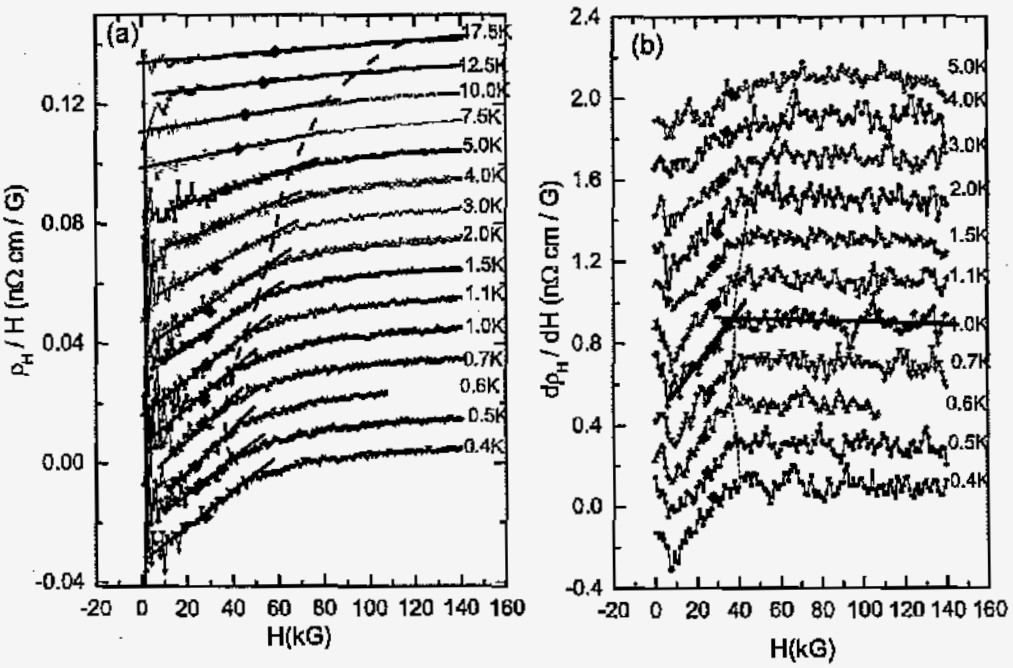

Figure 9.25 Alternative definitions of the Hall coefficient of $YbPt_{0.98}In$ (H $\parallel$ *ab*): (a) $R_H = \rho_H / H$ and (b) $R_H = d\rho_H / dH$, measured at various temperatures. Except for the T = 0.4 K ones, all other curves are shifted for clarity, by multiples of (a) 0.01 nΩ cm /G and (b) 0.2 nΩ cm /G. The large dots are the ρ_H minima shown in Fig.9.23, and the dotted line represents the cross-over line, determined by the maximum-H on the low field linear fits (see text).

parameter, *i.e.*, H in our case) can be used to distinguish between two possible QCP scenarios: diffraction off of a critical spin density wave SDW (manifesting as a change in the slope of $R_H(C)$ at C_{crit}) or a breakdown of the composite nature of the heavy electron (signaled by the divergence of the slope of $R_H(C)$ at C_{crit}). In our case, it is not clear what definition of the Hall coefficient should be used for comparison with the theory (*i.e.*, either $R_H(C) = \rho_H/H$ or $R_H(C) = d\rho_H / dH$) since the magnetic field H is itself the control parameter C. Therefore

in Fig.9.25 we are presenting the R_H(H) curves determined using both of the aforementioned definitions. When $R_H(H) = \rho_H / H$ (Fig.9.25a), the Hall coefficient is linear up to a field value which varies non-monotonically with T, as indicated by the dashed line. This line is shifted to higher field values with respect to the Hall resistivity line (Fig.9.23b), marked here by the large diamonds. When using the $R_H(H) = d\rho_H / dH$ definition for the Hall coefficient (Fig.9.25b), the maximum-H points on the low-field linear fits could be used as the criterium for defining the Hall line (indicated by the dotted line).

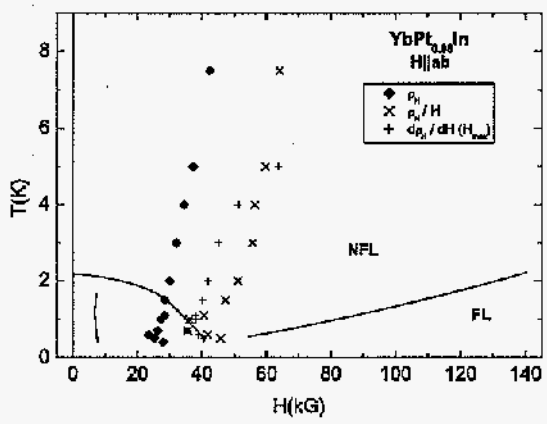

Figure 9.26 Revised $YbPt_{0.98}In$ phase diagram (H $\parallel$ ab). The solid lines correspond to the phase lines from the T - H phase diagram in Fig.9.19, and the symbols delineate the new phase line as determined from the Hall resistivity data, using various criteria as described in the text.

Regardless of what criterium is being used, the Hall measurements define a new phase line, distinct from any of the ones inferred from either the C_P(T,H) or the ρ(H,T) data. Fig.9.26 shows the $T - H$ phase diagram with the phase lines discussed before (lines), also showing the Hall line inferred from the various definitions (symbols). The line resulting from the Hall resistivity ρ_H data (diamonds) seems to persist even below T_{ord}, down to our lowest T. However, the other two criteria used for the definition of the Hall line ($R_H(H) = \rho_H / H$ or

H_{max} for the linear fit of $R_H(H) = d\rho_H / dH$) mark yet another distinct line, which resembles more the Hall line observed for either $YbRh_2Si_2$ (Paschen, 2004) and YbAgGe (Bud'ko, 2005) as it appears to converge with the "coherence" line, and the high-T magnetic ordering phase boundary, at the QCP, around H_c^{ab}.

9.3 Discussion

For both the YbPtIn and $YbPt_{0.98}In$ compounds a number of similar properties, as well as systematic differences, could be distinguished. First, the small stoichiometry difference was apparent from single crystal x-ray measurements, which also resulted in slightly reduced lattice parameters and unit cell volumes in the YbPtIn system. Furthermore, the resistivity values were shifted towards higher values in the Pt-deficient compound (Figs.9.2b-9.3) for the whole temperature (T = 0.4-300 K) and field ranges (H = 0-140 kG) of our measurements. High enough fields suppressed the magnetic order in both systems, at least for field applied within the basal plane; in a similar manner to the T-scale in these compounds, the critical field value was reduced in $YbPt_{0.98}In$ by comparison to the analogous one in YbPtIn. For the c direction, the field values required to suppress the magnetic order in $YbPt_{0.98}In$ and YbPtIn were close to, or respectively higher than our maximum available field (*i.e.*, 140 kG); this precluded us from studying the low temperature properties of the two compounds outside the ordered state, for this orientation of the field.

However, for $H \parallel ab$ NFL-like behavior occurs in $YbPt_{0.98}In$ for intermediate field values and above the ordering temperatures, as indicated by the logarithmic divergence of the C_m /T data (Fig.9.15a) and the linear resistivity (Fig.9.16a). In YbPtIn the NFL region is less clearly defined, as no linear region could be unambiguously identified in the resistivity (Fig.9.6), whereas the logarithmic divergence of the specific heat was limited to a small temperature range by a downturn in the $C_m /T(\ln T)$ data (Fig.9.5) towards high T.

At low temperatures, and for $H > H_c^{ab}$ where a QCP is apparent for each of the two systems, the FL-like behavior is recovered, as the resistivity shows a $\Delta\rho \sim AT^2$ functional dependence, more clearly defined in the Pt-deficient compound than in the stoichiometric one.

All these observations lead us to believe that, whereas a QCP exists in both compounds around $H_c^{ab} \approx 35 - 45$ kG for $YbPt_{0.98}In$, and 60 kG for YbPtIn, the small disorder in the former system in addition to the applied magnetic field induces a NFL regime in this compound, more clearly than in the latter one.

To further study the nature of the field-induced QCP in the two systems, we analyze the field dependence of the electronic specific heat coefficient γ, and of the coefficient A in the $\Delta\rho \sim AT^2$ resistivity.

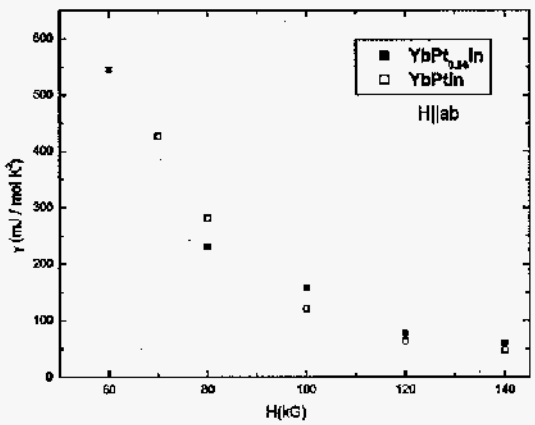

Figure 9.27 The H $\parallel$ *ab* field-dependent electronic specific heat coefficient γ of YbPtIn (open symbols) and $YbPt_{0.98}In$ (full symbols).

The field-dependent electronic specific heat coefficient γ could be estimated at low T, outside the ordered state, and these values are shown in Fig.9.27. For both compounds, $\gamma(H)$ was taken as the corresponding C_m/T value at T $\approx$ 1.3 K, such as to avoid the low-T upturn in the highest field data. A drastic decrease of γ (almost an order of magnitude) can be observed in Fig.9.27 for both compounds, for fields above their respective H_c^{ab}.

The field dependence of the coefficient A of the quadratic resistivity is shown in Fig.9.28a,b for YbPtIn and $YbPt_{0.98}In$ respectively. A 1 / $(H - H_{c0}^{calc})$ divergence can be observed for both compounds, with H_{c0}^{calc} estimated from the fit as 64.4 kG for YbPtIn, and 56.0 kG for

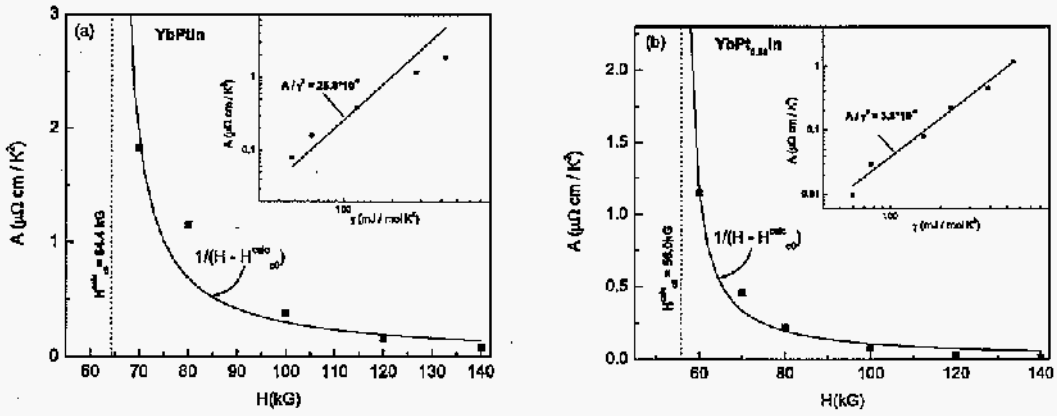

Figure 9.28 The H $\parallel$ *ab* T^2-resistivity coefficient A as a function of field, for (a) YbPtIn and (b) $YbPt_{0.98}In$ (symbols); the solid line represents a $1/\ (H\ -\ H_{c0}^{calc})$ fit, from which the expected critical field values H_{c0}^{calc} were estimated (see text). Inset: log plot of A vs. γ (symbols), with a linear fit (solid line) used to estimate the A / γ^2 ratio.

$YbPt_{0.98}In$. This critical field value for the former system is consistent with the $H\ \parallel\ ab$ specific heat and resistivity data (Figs.9.4-9.9), which suggested that $H_c^{ab}\ \approx 60$ kG. In the case of $YbPt_{0.98}In$, where NFL behavior was observed between 35 kG and 45 kG, the critical field value can only be determined to a range within the above two field values; the $H_{c0}^{calc}\ \approx$ 56 kG determined from the A *vs.* $1\ /\ (H\ -\ H_{c0}^{calc})$ fit (Fig.9.28b) is within the above field range, thus consistent with the specific heat and resistivity data (Figs.9.14-9.26).

The proportionality $A\ \sim\ \gamma^2$ between the resistance coefficient A and the electronic specific heat coefficient γ is emphasized by the logarithmic plots in the insets in Fig.9.28. In the case of the YbPtIn compound (Fig.9.28a, inset), the solid line represents the Kadowaki-Woods ratio $A\ /\ \gamma^2\ \approx\ 2.6\ *\ 10^{-5}\ \mu\Omega$ cm / (mJ / mol K)^2. Such a value is close to that observed for many heavy fermion systems (Kadowaki, 1986), but slightly higher than the $A\ /\ \gamma^2$ ratio reported for $YbRh_2Si_2$ (Gegenwart, 2002); this, in turn, was larger than the values observed for most Yb-based intermetallic compounds (Tsujii, 2003). The corresponding value was larger still in YbAgGe (Bud'ko, 2004), and it would appear that this is a common feature of Yb-based

materials with field-induced NFL-like behavior.

When we turn to the Pt-deficient compound (Fig.9.28b, inset), a smaller A / γ^2 ratio is indicated by the solid line: A / γ^2 $\approx$ $0.4 * 10^{-5}$ $\mu\Omega$ cm / (mJ / mol K)^2. This value is again one order of magnitude larger than that expected for many Yb-based compounds (Tsujii, 2003), and several times smaller than the ratio observed for the stoichiometric YbPtIn compound (Fig.9.28a). In light of observations of suppression of the A coefficient due to site disorder (Tsujii, 2003; Lawrence, 1985), we may have to consider the A / γ^2 ratio for $YbPt_{0.98}In$ as a reduced value from the enhanced ratio observed for the ordered compound.

9.4 Conclusions

The detailed field- and temperature-dependent measurements presented here allowed us to confirm that YbPtIn is a heavy fermion compound, as has been presented by Trovarelli et al. (2000a). In addition, we showed that a field-induced QCP exists in this material, at least for $H \parallel ab$, with $H_c^{ab} \approx 60$ kG. In addition to the magnetic field used as a tuning parameter, we showed that a small Pt-deficiency introduced in this system had effects consistent with positive pressure applied to Yb-based heavy fermion compounds. Thus, in the $YbPt_{0.98}In$ compound we also see a suppression of the magnetic ordering by applied magnetic field; in addition, the small disorder also suppresses the ordered state (both T_{ord} and H_c have smaller values in this compound than the similar ones in YbPtIn), and gives raise to a NFL region characterized by linear resistivity and logarithmic divergency of the specific heat, as also seen in the previously studied HF systems with field-induced NFL behavior, $YbRh_2Si_2$ and YbAgGe. As the critical field required to suppress the magnetic order in the c direction appeared to exceed our maximum field, experiments to higher fields would be desirable in order to extend the comparison with $YbRh_2Si_2$ and YbAgGe to the effects of anisotropy on the field-induced QCP.

CHAPTER 10. Summary and conclusions

The present work was initially motivated by the desire to continue the study of complex metamagnetism in relation to the crystal structure of various compounds; this study already included tetragonal compounds like $HoNi_2B_2C$ (Canfield 1997b; Kalatsky 1998) and $DyAgSb_2$ (Myers 1999), in which the rare earths occupy unique tetragonal positions. We intended to find hexagonal systems suited for such a study, with complex metamagnetic properties, and the search for extremely anisotropic hexagonal compounds turned into a rewarding exploration.

We identified and grew most of the heavy rare earth members of two isostructural series, RAgGe and RPtIn, both belonging to the hexagonal Fe_2P family of materials. In each of these series we found one compound, TmAgGe, and TbPtIn respectively, that was suitable for a simple study of angular dependent metamagnetism: they had three rare earth ions in the unit cell, positioned at a unique crystallographic site with orthorhombic point symmetry. The magnetization of both TmAgGe and TbPtIn was extremely anisotropic, with larger values for the in-plane orientation of the applied field than in the axial direction. Complex metamagnetic transitions existed for field within the ab-plane, and, similar to the case of the tetragonal compounds RNi_2B_2C and $DyAgSb_2$, they depended on the field orientation within the basal plane. We were thus able to develop a two-dimensional model, *the three co-planar Ising-like systems model*, which described well the angular dependence of the metamagnetic transitions in the TmAgGe and TbPtIn hexagonal compounds. Having three magnetic moments in the hexagonal unit cell, in orthorhombic point symmetry positions, added to the complexity of the analysis compared to the case of tetragonal compounds having one rare earth atom per unit cell, in tetragonal point symmetry. However, *the three co-planar Ising-like systems model* yielded complex, but intelligible angular dependencies of the critical fields and locally saturated

magnetizations for the various metamagnetic transitions observed experimentally. Having found two systems with different rare earth ions (Tm and Tb) and different ligands (Ag, Ge and Pt, In) gives us some confidence that this behavior may be generic to the Fe_2P-based compounds, and potentially even more widely applicable. Furthermore, we generalized this model to a *three non-planar Ising-like systems model*, in an attempt to understand the nature of the magnetic order in the non-planar magnetic RPtIn compounds (R = Dy - Tm); even though a more detailed analysis is needed to optimize it, this three-dimensional model could also be developed into a useful tool for characterizing hexagonal compounds with orthorhombic point symmetry of the rare earth site.

In addition to these extremely anisotropic compounds, the R = Yb members of each of the aforementioned series proved to be heavy fermion HF compounds; the apparently small or reduced moment ordering in YbAgGe and YbPtIn corresponded to an increase in the ordering temperature from 1 K in the former system, to 3.4 K in the latter one. In addition, a small Pt-deficiency in YbPtIn yielded a very different transition temperature ($\sim$ 2.1 K) in the flux-grown $YbPt_{0.98}In$ compound. In all three compounds a field-induced QCP was observed; for the two flux-grown ones (*i.e.*, for YbAgGe and $YbPt_{0.98}In$), signatures of field-induced NFL behavior could also be identified, which were less obvious in the YbPtIn compound. A remarkable feature of the YbAgGe compound is the extended relevant field- and temperature-ranges are enhanced compared to $YbRh_2Si_2$ (Trovarelli, 2000b; Gegenwart, 2002; Ishida, 2002; Paschen, 2003; Paschen, 2003), making the physical properties of this compound experimentally more accessible, and the extended T = 0 non Fermi liquid-like regime. These observations made YbAgGe and YbPtIn extremely interesting. Once more, having two examples of isostructural heavy fermion materials, with very different ligands (which greatly affect the hybridization in these systems) allowed us to analyze their individual properties, and also to compare similar effects in compounds with very different ligands. Moreover, having $YbPt_{0.98}In$ single crystals, in addition to the stoichiometric YbPtIn, offered the possibility of analyzing the effect of disorder on its properties in comparison to those of the stoichiometric system.

We can thus conclude that the RAgGe and RPtIn series of compounds presented in this

work cover a rich spectrum of physical properties. The anisotropy and metamagnetism are particularly interesting in light of the crystal structure of these compounds, a hexagonal unit cell with unique rare earth site in orthorhombic point symmetry. The *four position clock model* (Kalatsky 1998) developed for tetragonal systems with the magnetic moments in tetragonal point symmetry, together with the *three Ising-like systems model* for hexagonal unit cell with moments in orthorhombic point symmetry, should provide useful tools for further studies of metamagnetism in other systems with planar symmetry. Further work should be devoted to finding tetragonal compounds with rare earths in orthorhombic point symmetry, which might be similar to TmAgGe and TbPtIn, or hexagonal systems with the magnetic moments occupying unique trigonal or hexagonal point symmetry positions, with the latter resembling more $HoNi_2B_2C$ and $DyAgSb_2$. Also, more detailed measurements and a more complex version of the *three non-planar Ising-like systems model* might further our understanding of metamagnetism in less anisotropic compounds. Finally, it is desirable to continue the search for Yb-based heavy fermion compounds, given the limited number of existing stoichiometric such systems, in which QC phase transitions and NFL behavior can be induced by the application of magnetic field.

Bibliography

Andraka, B. and A. M. Tsvelik, Phys. Rev. Lett. **67** 2886 (1991).

Ashcroft, N. W., and N. D. Mermin, *Solid State Physics*, W. B. Saunders, Philadelphia, (1976).

Ball, A. R., D. Gignoux, F. E. Kayzel, D. Schmitt and A. de Visser, J. Magn. Magn. Matter. **110** 53 (1992).

Ball, A. R., D. Gignoux and D. Schmitt, J. Magn. Magn. Matter. **119** 96 (1993).

Baran, S., M. Hofmann, J. Leciejewicz, B. Penc, M. Ślaski and A. Szytuła, J. Alloys Comp. **281** 92 (1998).

Beyermann, W. P., P.C. Canfield, S.L. Bud'ko, A. Lacerda, Bull. Am. Phys. Soc. **43**(1), C31-8, 115 (1998).

Borombaev, M. K., R. Z. Levitin, A. S. Markosyan, V. A. Reimer, E. V. Sinitsyn and Z. Smetana, Sov. Phys.-JETP **66** 866 (1987).

Boutron, P., Phys. Rev. B, **7** 3226 (1973).

Bud'ko, S. L., Z. Islam, T. A. Wiener, I. R. Fisher, A. H. Lacerda and P. C. Canfield, J. Magn. Magn. Matter. **205** 53 (1999).

Bud'ko, S. L., E. Morosan and P. C. Canfield, Phys. Rev B **69** (2004), 014415.

Bud'ko, S. L., E. Morosan and P. C. Canfield, Phys. Rev B **71** (2005), 054408.

Canfield, P. C., P. L. Gammel and D. J. Bishop, Phys. Today, **51** 40 (1998).

Canfield, P. C. and S. L. Bud'ko, J. Alloys Comp. **262-263** 169 (1997a).

Canfield, P. C., S. L. Bud'ko, B. K. Cho, A. H. Lacerda, D. Farrell, E. Johnston-Halperin, V. A. Kalatsky and V. L. Pokrovsky, Phys. Rev. B **55** 970 (1997b).

Canfield, P. C. and I. R. Fisher, J. Cryst. Growth **225** 155 (2001).

Canfield, P. C. and Z. Fisk, Phil. Mag., **65** 1117 (1992).

Canfield, P. C., E. Morosan and S. L. Bud'ko, Bull. Am. Phys. Soc. **48**(1) 1373 (2003).

Chien, C. L. and C. R. Westgate, *The Hall Effect and Its Applications*, Plenum Press, New York and London (1980).

Cho, B. K., B. Harmon, D. C. Johnston and P. C. Canfield, Phys. Rev. B **53** 2217 (1996a).

Cho, B. K., P. C. Canfield and D. C. Johnston, Phys. Rev. B **53** 8499 (1996b).

Cho, B. K., P. C. Canfield, L. L. Miller and D. C. Johnston, Phys. Rev. B **52** 3684 (1995).

Coleman, P., C. Pépin, P. W. Anderson and T. V. Ramakrishnan, Phys. Rev. Let. **55** 414

(1985).

Coleman, P., C. Pépin, Q. Si and R. Ramazashvii, J. Phys.: Cond. Matt. **13** R723 (2001).

Continentino, M. A., Phys. Rep. **239** 179 (1994).

Continentino, M. A., *Quantum Scaling in Many-Body Systems* World Scientific Singapore (2001).

Continentino, M. A., cond-mat/0307518 (2003) (unpublished).

Continentino, M. A., G. M. Japiassu and A. Troper, Phys. Rev B **39** 9734 (1989).

Cooper, B. R., Phys. Lett. **22** 244 (1966).

Custers, J., P. Gegenwart, H. Wilhelm, K. Neumaier, Y. Tokiwa, O. Trovarelli, C. Geibel, F. Steglich, C. Pépin and P. Coleman, Nature (London) **424** 524 (2003).

Daybell, M. D., *Magnetism*, edited by H. Suhl (Academic, NY) **5** 129 (1973).

Desgranges, H. U. and K. D. Schotte, Phys. Lett. A **91** 240 (1982).

Doniach, S., Physica B **91** 231 (1977a).

Doniach, S., *Valence Instabilities and Related Narrow-Band Phenomena*, edited by R. D. Parks, Plenum Press, New York and London, 168 (1977b).

Doukouré, M. and D. Gignoux, J. Magn. Magn. Matter. **30** 111 (1982).

Dunlap, B. D., J. Magn. Magn. Matter. **37** 211 (1983).

Elliott, R. J., *Magnetic properties of rare earth metals*, London, New York, Plenum Press, (1972).

Elwell, D. and H. J. Scheel, *Crystal Growth from High-Temperature Solutions*, Academic Press, London (1975).

Ferro, R., R. Marazza and G. Rambaldi, Z. Anorg. Allg. Chem. **410** 219 (1974).

Fert, A. and P. M. Levy, Phys. Rev. B, **36** 1907 (1987).

Fisher, M. E., Phil. Mag. **7** 1731 (1962).

Fisher, M. E. and J. S. Langer, Phys. Rev. Lett. **20** 665 (1968).

Fisher, I. R, J. R. Cooper and R. J. Cava, Phys. Rev. B **52** 15086 (1995).

Fisk, Z. and M. B. Maple, J. Alloys Comp. **183** 303 (1992).

Fisk, Z. and J. P. Remeika, *Handbook of the Physics and Chemistry of Rare Earths* **12** 53 (1989).

Fujita, T., K. Satoh, Y. Maeno, Y. Uwatoko and H. Fujii, J. Magn. Magn. Matter. **76-77** 133 (1988).

Galadzhun, Y. V., V. I. Zaremba, H. Piotrowski, P. Mayer, H. D. Hoffmann and R. Pöttgen,

Z. Naturforsch. B **55** 1025 (2000).

Garlea, O., E. Morosan, S. L. Bud'ko, J. L. Zarestky, P. C. Canfield and C. Stassis, J. Appl. Phys **95** 6921 (2004).

Gasser, U., P. Allenspach, F. Fauth, W. Henggeler, J. Mesot, A. Furrer, S. Rosenkranz, P. Vorderwisch and M. Buchgeister, Z. Phys. B **101** 345 (1996).

Gegenwart, P., J. Custers, C. Geibel, K. Neumaier, T. Tayama, K. Tenya, O. Trovarelli, and F. Steglich, Phys. Rev. Lett **89** 056402 (2002).

Gibson, B, R. Pöttgen, R. K. Kremer, A. Simon and K. R. A. Ziebeck, J. Alloys Comp. **239** 34 (1996).

Gignoux, D., D. Schmitt, in: K. A. Gschneider Jr., L. Eyring (Eds.), *Handbook of the Physics and Chemistry of Rare Earths*, Elsevier, Amsterdam, **138** 293 (1995)

Gignoux, D., D. Schmitt, in: K. H. J. Buschow (Ed.), *Handbook of Magnetic Materials*, Elsevier, Amsterdam, **2** 239 (1997).

Gignoux, D., D. Schmitt and M. Zerguine, J. Magn. Magn. Matter. **66** 373 (1987).

Gschneidner Jr., K. A. and F.W. Calderwood, Bull. Alloy Phase Diagrams, **6**(1), (1985).

Hadžić-Leroux, M., A. Hamzić, A. Fert, P. Haen, F. Lapierre and O. Laborde, Europhys. Lett. **1** 579 (1986).

Heuser, K., E.-W. Schneidt, T. Schreiner and G. R. Stewart, Phys. Rev. B **58** R15959 (1998).

Hewson, A.C., *The Kondo Problem to Heavy Fermions*, Cambridge University Press, Cambridge UK (1997).

Hundley, M. F., A. Malinowski, P. G. Pagliuso, J. L. Sarrao and J. D. Thompson (cond-mat/0402076) (2004).

Hurd, C. M., *he Hall Effect in Metals and Alloys*, Plenum Press, New York and London, (1972).

Hutchings, M. T., Solid State Phys. **16**, 227 (1964).

Ishida, K., K. Okamoto, Y. Kawasaki, Y. Kitaoka, O. Trovarelli, C. Geibel and F. Steglich, Phys. Rev. Lett **89** 107202 (2002).

Iwata, N., K. Honda, T. Shigeoka, Y. Hashimoto and H. Fujii, J. Magn. Magn. Matter. **90-91** 63 (1990).

Jensen, J. and A. R. Mackintosh, *Rare Earth Magnetism* (Oxford University Pres, Oxford) 1991.

Kaczorowski, D., B. Andraka, R. Pietri, T. Cichorek, V. I. Zaremba, Phys. Rev. B. **61** 15255 (2000).

Kadowaki, K. and S. B. Woods, Solid State Commun., **58** 507 (1986).

Kalatsky, V. A. and V. L. Pokrovsky, Phys. Rev. B **57** 5485 (1998).

Kasuya, T., Progr. Theor. Phys. **16** 45 (1956).

Katoh, K., Y. Mano, K. Nakano, Y. Niide and A. Ochiai, J. Magn. Magn. Matter. **268** 212 (2004).

Knopp, G., A. Loidl, R. Caspary, U. Gottwick, C.D. Bredl, H. Spille, F. Steglich and A. P. Murani, J. Magn. Magn. Mater. **74** 341 (1988).

Koerner, S., E.-W. Schneidt, T. Schreiner, K. Heuser and G. R. Stewart, J. Low Temp. Phys. **119** 147 (2000).

Kondo, J., Prog. Theor. Phys. **32** 37 (1964).

Kurisu, M., T. Takabatake and H. Fujii, J. Magn. Magn. Matter. **90-91** 469 (1999).

LapierreF., P. Haen, R. Briggs, A. Hamzić, A. Fert and J. P. Kappler, J. Magn. Magn. Mat **63-64**, 338 (1987).

Lawrence, J. M., J. D. Thompson and Y. Y. Chen, Phys. Rev. Lett **54** 2537 (1985).

Lea, K. R., M. J. M. Leask and W. P. Wolf, J. Phys. Chem. Solids **23** 1381 (1962).

Lenkewitz, M., S. Corsepius, G.-F.v. Blanckenhagen and G. R. Stewart, Phys. Rev. B **55** 6409 (1997).

MacKeown, P. K. and D. J. Newman, *Computational Techniques in Physics*, Adam Hilger, Bristol, (1987).

Mandal, P. and K. Winzer, Solid State Comm. **107** 679 (1997).

Massalski, T. B, H. Okamoto, P. R. Subramanian and L. Kacprzak, *Binary Alloys Pahe Diagrams*, ASM International, Materials Park, OH, 1522 (1990).

Mattis, D. C., *The Theory of Magnetism, Vol. I: Statics and Dynamics*, Springer-Verlag Series, Berlin-New York, (1981).

McEwen, K. A., G. J. Cock, L. W. Roeland and A. R. Mackintosh, Phys. Rev. Lett. **30** 287 (1973).

Meissner, W. and B. Voight, Ann. Phys. **7** 761 (1930).

Mihály, N. and A. Zawadowski, J. de Phusique Lett. **39** L483 (1978).

Morosan, E., S.L. Bud'ko, P.C. Canfield, M.S. Torikachvili and A.H. Lacerda, J. Magn. Magn. Matter. **277** 298 (2004)

Morosan, E., S. L. Bud'ko and P. C. Canfield, Phys. Rev. B **71** 014445 (2005a).

Morosan, E., S. L. Bud'ko, Y. A. Mozharivskyj and P. C. Canfield, Phys. Rev. B **72** 014425 (2005b).

Müllmann, R., B. D. Mosel, H. Eckert, G. Kotzyba and R. Pöttgen, J. Solid State Chem **137** 174 (1998).

Myers, K. D., P.C. Canfield, V.A. Kalatsky and V.L. Pokrovsky, Phys. Rev. B **59** 1121 (1999a).

Myers, K. D., S. L. Bud'ko, I. R. Fisher, Z. Islam, H. Kleinke, A. H. Lacerda and P. C. Can-

field, J. Magn. Magn. Mater. **205** 27 (1999b).

Narozhnyi, V. N., V. N. Kochetkov, A. V. Tsvyashchenko and L. N. Fomicheva, Solid State Comm. **109** 549 (1999).

Nimori, S., G. Kido, D. X. Li, Y. Haga and T.Suzuki, J. Magn. Magn. Mater. **140-144**(2) 1167 (1995).

Noakes, D.R. and G.K.Shenoy, Phys.Lett. **91A** 35 (1982).

O'Handley, R. C., in C. L. Chien and C. R. Westgate (Eds.): *The Hall Effect and Its Applications*, Plenum Press, New York and London, 417 (1980).

Olesinski, R.W. and G.J. Abbaschian, Bull. Alloy Phase Diagrams **9**(1), (1988).

Overhauser, A. W., Phys. Rev. Lett. **3** 414 (1959).

Pamplin, Brian R., *Crystal Growth*, Pergammon Press Ltd,. Oxford, (1975).

Paschen, S., T. Luehmann, C. Langhammer, O. Trovarelli, S. Wirth, C. Geibel and F. Steglich, Acta Phys. Pol. B **34** 359 (2003).

Paschen, S., T. Luehmann, S. Wirth, P.Gegenwart, O. Trovarelli, C. Geibel, F. Steglich, P. Coleman and Q. Si, Nature **432** 881 (2004).

Pogorelov, Y. G. and V. R. Shaginyan, Pis'ma Zh. Exp. Teor. Fiz. **76** 614 (2003) [JETP Lett. **76** 532 (2003)].

Pöttgen, R., Z. Krist. **211** 884 (1996).

Pöttgen, R., B. Gibson and R. K. Kremer, Z. Krist. **212** 58 (1997).

Rajan, V. T., Phys. Rev. Lett. **51** 308 (1983).

Ruderman, M. A. and C. Kittel, Phys. Rev. **96** 99 (1954).

Sampathkumaran, E. V., K. Sengupta, S. Rayaprol, K. K. Iyer, Th. Doert and J. P. F. Jemetio, Phys. Rev. Lett **91** 36603 (2003).

Samolyuk, G. (private communication) (2004).

Satoh, K., T. Fujita, Y. Maeno, Y. Uwatoko and H. Fujii, J. Phys. Soc. Japan, **59** 692 (1990).

Shannon, R. D., Acta Crystallographica A **32** 751 (1976).

Stevens, K. W. H., Proc. Phys. Soc., **A65** 209 (1952).

Stewart, G. R., Rev. Mod. Phys. **56** 755 (1984).

Stewart, G. R., Rev. Mod. Phys. **73** 797 (2001).

Suzuki, H., D. Gignoux, D. Schmitt, T. Shigeoka, P.C. Canfield and C. Detlefs, J. Magn. Magn. Matter. **251** 16 (2002).

Takayanagi, S., Y. Ōnuki, K. Ina, T. Komatsubara, N. Wada, T. Watanabe, T. Sakakibara and T. Goto, J. Phys. Soc. Jpn. **58** 1031 (1989).

Takimoto, T. and T. Moryia, Solid State Commun. **99** 457 (1996).

Taylor, K. N. R. and M. I. Darby, *Physics of Rare Earth Solids*, Chapman and Hall, London, (1972).

Thompson, J.D. and J.M.Lawrence,in: K.A.Gschneidner (Ed.), *Handbook on the Physics and Chemistry of Rare Earths*, **19** (Elsevier, Amsterdam) 383 (1994).

Trovarelli, O., C. Geibel, R. Cardoso, S. Mederle, R. Borth, B. Buschinger, F. M. Grosche, Y. Grin, G. Sparn, F. Steglich, Phys. Rev. B **61** (2000a), 9467.

Trovarelli, O., C. Geibel, S. Mederle, C. Langhammer, F. M. Grosche, P. Gegenwart, M. Lang, G. Sparn and F. Steglich, Phys. Rev. Lett 85 626 (2000b).

Tsvelik, A. M. and M. Reiser, Phys. Rev. B 48 R9887 (1993).

Tsujii, N., K. Yoshimura and K. Kosuge, J. Phys: Condens. Matter **15** 1993 (2003).

Umeo, K., K. Yamane, Y. Muro, K. Katoh, Y. Niide, a. Ochiai, T. Morie, T. Sakakibara and T. Takabatake, J. Phys. Soc. Jpn., **73** 537 (2004).

Wang, Y. L., Phys. Lett. A **35** 383 (1971).

Watson, K. C, J. Crangle, K.-U. Neumann and K.R.A. Ziebeck, J. Magn. Magn. Matter. **140-144** 883 (1995).

Wilson, K. G., Rev. Mod. Phys., **47** 773 (1975).

Yamaguchi, Y., J. Sakurai, F. Teshima, H. Kawanaka, T. Takabatake and H. Fujii, J. Phys: Cond. Mat., **2** 5715 (1990).

Yatskar, A., N.K. Budraa, W.P. Beyermann, P.C. Canfield and S.L. Bud'ko, Phys. Rev. B **54** R3772 (1996).

Yoshii, S., K. Kindo, K. Katoh, Y. Niide, A. Ochiai, J. Magn. Magn. Matter. **272-276** e99 (2004).

Yoshimori, A., J. Phys. C **15** 5241 (1976).

Yosida, K., Phys. Rev. **106** 893 (1957).

Zaremba, V. I., Y. V. Galadzhun, B. D. Belan, A. Pikul, J. Stepien-Damm, D. Kaczorowski, J. Alloys Comp. **316** 64 (2001).

Ziman, J. M., *Electrons and Phonons*, Oxford University Press, Oxford (1967).

Acknowledgements

Ames Laboratory is operated for the U.S. Department of Energy by Iowa State University under Contract No. W-7405-Eng.-82. This work was supported by the Director for Energy Research, Office of Basic Energy Sciences. Work at NHMFL - Los Alamos Facility was performed under auspices of the National Science Foundation and the U.S. Department of Energy.